UNIVERSITÀ
DI TRENTO

Dipartimento di
Ingegneria Industriale

XXXII cycle

Doctoral School in Materials, Mechatronics and Systems Engineering

SOLAR CONCENTRATION FOR THE ENVIRONMENT INDUSTRY: PHOTOCATALYTIC MATERIALS AND APPLICATION TECHNOLOGIES

Murilo Alexandre Fendrich

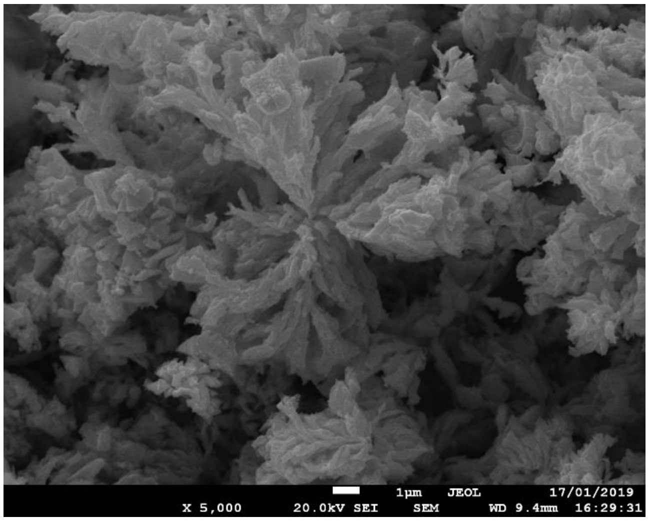

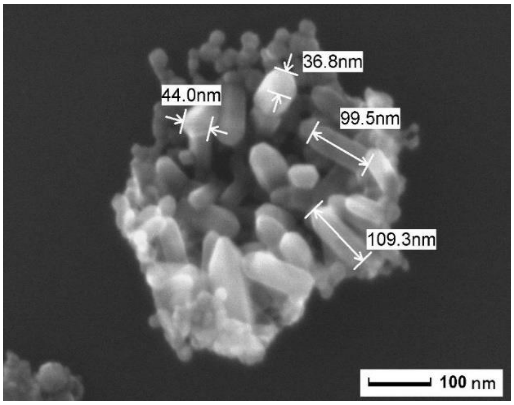

January 2021

SOLAR CONCENTRATION FOR THE ENVIRONMENT INDUSTRY: PHOTOCATALYTIC MATERIALS AND APPLICATION TECHNOLOGIES

Murilo Alexandre Fendrich

Approved by:	**Committee of final defence:**
Professor Alberto Quaranta, Tutor Department of Industrial Engineering *University of Trento, Italy.*	Professor Francesco Parrino, Department of Industrial Engineering *University of Trento, Italy.*
Professor Antonio Miotello, Co-tutor Department of Physics *University of Trento, Italy.*	Professor Chiara Maurizio, Department of Physics and Astronomy, *University of Padova, Italy.*
External Referees:	Professor Elti Cattaruzza, Department of Molecular Sciences and Nanosystems *Ca' Foscari University of Venice, Italy.*
Professor Chiara Maurizio, Department of Physics and Astronomy *University of Padova, Italy.*	
Professor Serena Berardi, Department of Chemical and Pharmaceutical Sciences *University of Ferrara, Italy.*	

University of Trento, Italy
Department of Industrial Engineering

January 2021

University of Trento - Department of Industrial Engineering

Doctoral Thesis

Murilo Alexandre Fendrich - 2021
Published in Trento (Italy) – by University of Trento

To my dear family

Cover image from top left clockwise: SEM image of PLD produced WO_3 photocatalyst in flower shape-like nanostructure, quartz glass lid under concentrated sunlight irradiation performing water purification, SEM image of green-synthesized ZnO in nanorod shape, parabolic dish solar concentrator apparatus (lab. IdEA, physics dept., UNITN).

Abstract

This thesis presents the achievements pursued during the doctoral course. The work was carried out in the context of the project ERiCSol (*Energia RInnovabile e Combustili SOLari*), as part of the University of Trento strategic plan for the years 2017-2021. The project was conceived to establish an interdepartmental area to promote the challenge of developing scientific research and technological innovation to increase the competitiveness of Trento at national and international level in the areas of energy and environment. Among all the goals of the project, this work dedicates special attention to 1) development of novel materials for solar photocatalytic reactions and 2) use of renewable energy to push forward applications in water remediation.

To accomplish these goals, the research brings a full collection of experimental activities regarding the employment of solar concentration for the environment industry and therefore this document is organized in 9 chapters.

In chapter 1, it is presented the introduction outlining the overview of the environment industry, the employment of solar light as energy source and the general and specific objectives.

Chapter 2 presents a literature review regarding the last 30 years of applications correlating the use of solar light towards wastewater purification. The chapter reviews the engineering features of solar collectors, photocatalyst materials employed and the panorama of the pollutants investigated up to the present date in solar photocatalysis, presenting comparisons between models and real wastewater approaches.

Chapter 3 details the experimental techniques and characterizations employed to sustain the investigation proposed in the thesis. The first part of the chapter explains the features of parabolic dish solar concentrator designed and manufactured by the IdEA group at the physics department of the university of Trento. After, it is presented the pulsed laser deposition, a thin films fabrication technique employed to produce the photocatalysts used on water purification experiments. The second part of the chapter presents the description of the characterization techniques used to reveal the fabricated photocatalyst materials properties.

Based on the review on the fundamentals of solar photocatalysis and the experimental techniques, chapters 4 and 5 present a discussion in the field of novel photocatalytic materials capable to operate under concentrated sunlight irradiation. Chapter 4 in special presents the investigation regarding the fabrication of tungsten trioxide (WO_3) thin film coatings, bringing the

novelty of using pulsed laser deposition as the fabrication method and the evaluation of this material in photocatalysis for the degradation of methylene blue dye model pollutant. Chapter 5 instead, presents the development on Zinc Oxide (ZnO) nanoparticles, bringing an innovative point of view on a “green-synthesis” approach and the material immobilization in film for heterogeneous photocatalysis routes.

Chapters 6 and 7 discuss solar photocatalysis aiming to shift applications from model pollutants to real wastewater remediation conditions. Important comparisons are performed and discussed regarding the advantages and existing drawbacks. To fulfill this purpose, chapter 6 presents an application case of solar photocatalysis to the degradation of a surfactant-rich industrial wastewater whereas chapter 7 presents the approach focused on the remediation of organic lead contaminants present on a local water well site in the city of Trento.

The last experimental approach of concentrated solar light is presented on chapter 8, dedicated to the application of concentrated sunlight towards waste biomass valorization. Conversely to the application on water previously described, this chapter presents the activity on designing, fabricating and coupling a hydrothermal reactor with concentrated sunlight using it as the driving force to promote degradation of grape seeds evolving into hydrochars with possible valorization of the carbonized material.

Lastly, chapter 9 presents the conclusions and suggestions, this item expresses the final considerations on the results of the experimental investigations, advantages and limitations observed, and suggests possible actions for future works.

Contents

List of figures

List of tables

List of abbreviations and acronyms

3D – Tridimensional
AD – As deposited
AISI – American Iron and Steel Institute
AN200 – Annealed at 200°C
AN400 – Annealed at 400 °C
AN600 – Annealed at 600 °C
AOP – Advanced oxidation process
APPA – *Agenzia Provinciale per la protezione dell'ambiente*
ASTM – American Society for Testing and Materials
BG – Bandgap
BROC – Bio-recalcitrant organic compounds
BSE – Back-scattered electrons
CB – Conduction band
CDRH – Center for Devices and Radiological Health
CEC – Contaminants of emerging concern
CPC – Compound parabolic collector
DEL – Diethyl lead
EBD – Electron beam deposition
EDDS – Ethylenediamine-N,N'-disuccinic acid
EDTA – Ethylenediaminetetraacetic acid
EDXS – Energy-dispersive X-ray spectroscopy
EIT – European Institute of Technology
EPA – Environmental Protection Agency
EY – Energy yield
FEG – Field emission gun
FESEM – Field emission scanning electron microscope
FWHM – Full width at half maximum
GC-MS – Gas chromatography – Mass spectrometry
HHV – Higher heating value
HTC – Hydrothermal carbonization
IdEA – *Idrogeno, Energia e Ambiente*
IEP – Isoelectric point
IPC – Inclined plate collector
IPCA – Integrated photocatalyst adsorbent
IR – Infrared
JCPDS – Joint-Committee on Powder Diffraction Standards
LASER – Light amplification by stimulated emission of radiation
MB – Methylene blue
MONO – Monomethyl lead
NIR – Near infrared
NP – Nanoparticle
NS – Nanostructure
NR – Nanorod
NW – Nanowire

OECD – Organization for Economic Cooperation and Development
PA – Polyamide
PC – Photocatalysis
PCA – Photocatalytic activity
PDC – Parabolic dish concentrator
PDMS – Polydimethylsiloxane
PFAS – Per- and polyfluoroalkyl substances
PhD – Doctor of philosophy
PLD – Pulsed laser deposition
PPM – Part per million
PTC – Parabolic trough collector
PTR – Parabolic trough reactor
PVC – Polyvinyl chloride
PZC – Point of zero charge
RPM – Rotation per minute
RT – Room temperature
SE – Secondary electrons
SEM – Scanning electron microscope
SME – Small and medium enterprises
SLOI – *Società Lavorazioni Organiche Inorganiche*
SODIS – Solar disinfection
SP7 – 7th International Conference on Semiconductor Photochemistry
SPME – Solid-phase microextraction
SY – Solid yield
TEL – Tetraethyl lead
TFFBR – Thin film fixed bed reactor
TOL – Total organic lead
TREL – Triethyl lead
UN – United Nations
UNITN – University of Trento
USA – United States of America
UV – Ultraviolet
VB – Valence band
VIS – Visible
WWTP – Wastewater treatment plant
XRD – X-ray diffraction
YAG – Yttrium aluminum garnet

List of symbols

α – Alpha
α-Fe_2O_3 – Hematite
Å – Angstrom
A – Ampere
A – Proportionality constant
Ag-$BiVO_4$ – Silver doped bismuth vanadate
β – Beta
β-Bi_2O_3 – Beta bismuth (III) oxide
Bi_2WO_6 – Bismuth tungstate
B/W – Dry biomass to water ratio
°C – Degree Celsius
C – Concentration
C_0 – Initial concentration
$CaCl_2$ – Calcium chloride
$(CH_3CH_2)_4Pb$ – Tetraethyl lead
$(CH_3CH_2)_3Pb^+$ – Triethyl lead
$(CH_3CH_2)_2Pb^{2+}$ – Diethyl lead
$(CH_3CH_2)Pb^{3+}$ – Monomethyl lead
cm – Centimeter
cm^{-1} – Per centimeter
cm^2 – Square centimeter
CdS – Cadmium sulfide
CO – Carbon monoxide
CO_2 – Carbon dioxide
Co_3O_4 – Cobalt oxide
CuO – Cupric oxide
Cu_2O – Cuprous oxide
e^- – Electron
e^-_h – Electron-hole
Eg – Optical bandgap
eV – Electron volt
$FeCl_3$ – Iron chloride
Fe_2O_3 – Iron oxide
$Fe_2(SO_4)_3$ – Iron (III) sulfate
GaP – Gallium phosphide
ɣ – Gamma
h – Hour
h – Planck constant
h^+ – Positive hole
H_3BO_3 – Boric acid
$H_2C_2O_4$ – Oxalic acid
HO_2^- – Hydroperoxyl radical
H_2O – Water
H_2O_2 – Hydrogen peroxide

H_2SO_4 – Sulfuric acid
Hz – Hertz
Id – Direct irradiance
J/cm^2 – Joule per square centimeter
K – Degradation kinetics
keV – Kilo electron volt
K_2HPO_4 – Dipotassium phosphate
KrF – Krypton fluoride
Kg – Kilogram
KWh – Kilowatt hour
λ – Lambda
L – Liter
M – Molar
m – Meter
m – Angular coefficient
m^2 – Square meter
mA – Milliampere
mbar – Millibar
mg – Milligram
MJ – Megajoule
ml – Milliliter
mm – Millimeter
m-WO_3 – Monoclinic phase of tungsten trioxide
Mg_2SO_4 – Magnesium sulfate
µm – Micrometer
$m_{HC,dry}$ – Mass of dry hydrochar
$m_{bio,\ dry}$ – Mass of dry biomass
min – Minute
min^{-1} – Per minute
NaCl – Sodium chloride
$Na_2S_2O_5$ – Sodium metabisulfite
$Na_2S_2O_8$ – Sodium persulfate
nm – Nanometer
ns – Nanosecond
ν – Nu
O_2 – Oxygen
O_2^- – Superoxide
$OH^\bullet$ – Hydroxil radical
OH^- – Hydroxide ion
Pa – Pascal
% – Per cent
π – Pi
P25 – Evonik commercial titanium dioxide nanopowder
PC 100 – Evonik commercial titanium dioxide nanopowder
PC 500 – Evonik commercial titanium dioxide nanopowder
r – Radius

R^2 – R square
Rd – Diffuse reflectance
Rs – Specular reflectance
R_{tot} – Total reflectance
s – Second
δ – Sigma
θ – Theta
SnO_2 – Tin (IV) oxide
t – Time
T – Transmittance
Tc – Thermodynamic critical point
TiO_2 – Titanium dioxide
WO_3 – Tungsten trioxide
$Zn(NO_3)_2$ – Zinc nitrate
ZnO – Zinc Oxide
ZnS – Zinc sulfide
v – Frequency
W – Watt
WB – Tungsten boride
X – Per

Chapter 1 - Introduction

Environmental activities such as cleanup and reuse are probably as old as the advent of the first human settlements. However, the habits of managing these activities truly began with the second industrial revolution, at the end of the nineteenth century in response to dreadful living conditions and recurrent epidemics in overcrowded growing cities. In the last decades, connected to the context of globalization, technological change, and new political priorities, policy makers have expressed a strong interest in a so-called environmental goods and services industry. This has been a new growth sector, generating wealth and creating jobs as well as playing a major role in the transition of economies towards sustainable development [1].

In order to formalize the economical operations of the waste resources, the Organization for Economic Cooperation and Development (OECD) introduced the definition of the environmental goods and services industry hereinafter referred as the Environment Industry, as the *"activities which produce goods and services to measure, prevent, limit, minimize or correct environmental damage to water, air and soil, as well as problems related to waste, noise and ecosystems"*. This industry includes cleaner technologies, products and services that reduce environmental risk and minimize pollution and resource use in addition to activities related to resource management, resource exploitation and natural hazards. Hence, the activities covered by the environment industry are defined and classified into three main groups, being: 1) pollution management, 2) cleaner technologies and products, and 3) resource management. In particular, item 2) details*: "Production of equipment, technology, specific materials or services for cleaner or resource-efficient technologies and processes"* [2,3].

Considering the OECD details for the environment industry, and the last few decades efforts to improve the industrial applications that propose increased performance with decreased environmental damage allied to cleaner and sustainable use of natural resources, one of the key strategies are the applications benefiting from the energy provided by sunlight. Focus to energy conversion for generating electricity and thermal processes have been under increased attention and investments [4].

Regarding the possibilities of using the sunlight to drive industrial processes and the broad knowledge in the development of engineering configurations for solar energy devices, interesting purposes have gained attention to couple solar collectors to promote water purification.

Approaches of solar disinfection towards direct photolysis to reduce bacterial levels on drinking water were the first published in the solar wastewater remediation field [5]. Years after, the use of metal ions and semiconductors such as TiO_2 gained strong attention on promoting the development of photocatalysis having the sunlight as the irradiation source for degrading complex molecules observed in industrial and urban areas wastewaters. Therefore, as the effectiveness of conventional wastewater treatment processes has been increasingly challenged by the growth of industrial activities, the demand for low-cost and low-impact treatments emerged. Important observations that also contribute for the concern about water are the increase in the chemical complexity of the pollutants and the insufficient efforts on life cycle assessments in some situations neglect sub byproducts that should be taken into consideration ending up on water wells. In the other hand, limitations appear when the majority of semiconductor materials employed are capable to operate only in the UV range and thus increasing the complexity needed in solar systems to benefit of only this range of solar irradiation, reducing then the economic interest for such applications [6].

To become the employment of wastewater treatments cost-effective, the development of semiconductor materials, capable to operate under the near UV-Visible irradiation, and produced from abundant raw materials sources, could overcome the limitations on applications of solar wastewater remediation. Designing as integral or modular part for industrial purposes could improve the quality of treated waters in companies or urban areas. Possible solutions are represented by systems coupling solar concentration technology with advanced oxidation processes with catalysts in homogenous or heterogeneous mechanisms. A solar system, employed as a preliminary stage in wastewater treatment plants or as a small-scale stand-alone operated by small-medium enterprises, could reduce the environmental and economic impact of wastewaters.

Lastly, apart from solar water purification systems, the use of the concentrated sunlight acting as the free-energy source for thermochemical process also takes an important place for biomasses valorization. The conversion of organic waste materials by means of hydrothermal carbonization can add value and retake wastes back to contribute on a circular economy.

1.2 Objectives

1.1.1 General objective

The present work has the general objective to develop novel photocatalytic materials for applications on solar wastewater remediation and the approach for solar hydrothermal carbonization as a contribution for the advancement of environment industry.

1.1.2 Specific objectives

To accomplish the general objective, the following specific objectives are proposed:

- An up-to-date literature review on the use of solar concentration for wastewater remediation, identifying the state-of-the art in terms of engineering configurations of solar systems, photocatalyst materials, mechanisms employed, and the pollutants investigated;
- Production of tungsten trioxide (WO_3) photocatalyst thin film coatings by pulsed laser deposition, characterization of the properties and study of the heterogeneous photocatalytic activity under concentrated sunlight;
- Production of zinc oxide (ZnO) photocatalyst particles by a green-synthesis method and additionally study the immobilization on fixed films, characterization of the properties and study of the heterogeneous photocatalytic activity under concentrated sunlight comparing with alternative synthesis methods;
- Application of the produced materials for solar photocatalysis towards the degradation of surfactant-rich industrial wastewater;
- Application of the produced materials for solar photocatalysis towards the degradation of organolead compounds contaminated wastewater;
- Design and production of a hydrothermal carbonization reactor thermodynamically activated by concentrated sunlight for waste biomass valorization.

Chapter 2 – Solar concentration for wastewaters remediation: A review of materials and technologies

Preview: this chapter brings to light an up-to-date literature review of the solar collector systems and catalysts applied to wastewater purification, promoting a position of the field to applications, its limitations and future perspectives. As the first activity of the PhD career, it was a fruitful starting point allowing the possibility to develop a deep collection of literature works about engineering configurations, advanced oxidation processes, process comparisons between homogeneous and heterogeneous photocatalysis routes as well as information about the water contaminant substances investigated. The chapter resulted in an extensive comprehension about the broad possibilities for the employment of sunlight for wastewaters remediation and face the existing limitations.

The content of this chapter was adapted from:
Fendrich, M.A.; Quaranta, A.; Orlandi, M.; Bettonte, M.; Miotello, A. Appl. Sci. **2019**, *9*(1), 118; https://doi.org/10.3390/app9010118

2.1 Introduction

The demand for clean water sources has been rapidly increasing in recent decades, led by industrialization, the expansion of agriculture and, especially, population growth. Access to safe water supplies has thus become an issue of global significance [7]. Moreover, the health risk associated with polluted water resources is projected to become a major global issue within the next few decades [8]. Among the various practical strategies and solutions proposed for more sustainable water management, wastewater reuse and recycling stands out as the most economically-viable and environmentally-friendly [9].

Presently, the most common wastewater treatments are based upon a combination of mechanical, biological, physical and chemical processes such as filtration, flocculation, chemical or biological oxidation of organic pollutants.

A common problem for current technologies is the poorly biodegradable organic pollutants, the so-called bio-recalcitrant organic compounds (BROCs). A class of treatments capable of tackling BROCs is known as advanced oxidation processes (AOPs), relying on the formation of highly-reactive transient (e.g., superoxide, peroxide, hydroxyl radical) chemical species that can convert BROCs into more biodegradable compounds or, ideally, into inorganic carbon [10]. Among the most efficient AOPs are those based on hydroxyl radicals $OH^{\bullet}$, a powerful oxidant. These methods are generally based on the dissociation of hydrogen peroxide in water, either by direct absorption of ultraviolet (UV) photons or by mediation with metal ions (Fe and Co are among the most studied) through Fenton and photo-Fenton reactions [11–13]. In addition, and equally or even more important, is the possibility of generating $OH^{\bullet}$ radicals by the interaction, in water, of artificial or natural light with semi-conductors. This process is commonly described as photocatalysis [14].

In recent decades, the photocatalytic degradation of several organic compounds has received growing attention as a water purification process. Irradiating semi-conductors, for example TiO_2, in the form of micro- or nano-sized particles, on fixed supports or in aqueous suspensions, creates a redox environment that is reactive towards most organic species [15]. A number of reports have shown that surfactants, pesticides and dyes can be effectively converted into less dangerous products like carbon dioxide and hydrochloric acid. In 1998, the United States Environmental Protecting Agency (EPA) published a detailed list of molecules capable of being degraded by AOPs [16].

In photocatalysis, photons can be seen as reactants and/or co-catalysts, hence playing a critical role in the process. On this basis, considerable research effort has been made since the 90s to employ solar radiation as an abundant, renewable and potentially zero-cost light source. In this approach, solar photons are collected and directed into a photoreactor where they power catalytic reactions. Traditionally, solar collector systems are broadly classified as concentrating or non-concentrating, according to their concentration factor or to the temperature which can be reached by the system [17].

Combining wide versatility, potentially low cost and the capability of total conversion to non-toxic products, the use of solar-powered AOPs for the treatment of urban and industrial wastewaters is likely the most promising application of AOP technology [18,19].

The application of solar disinfection (SODIS) has also been recently demonstrated on real wastewater samples with the possibility of integrating SODIS technology to an urban wastewater treatment plant (WWTP) [20,21]. Nanofiltration in combination with tertiary processes, including solar photocatalysis, is also the object of considerable research interest; however, it has presented uncertain results [22,23]. Another material-oriented approach that is still at an early stage in terms of literature reports, suggests the use of a combination between a photocatalyst and adsorbents. It is termed integrated photocatalyst adsorbent (IPCA), and is based on an adsorbent which has the ability to degrade organic matter in the presence of sunlight [24].

The investigation of different catalyst materials and the comparison of homogeneous versus heterogeneous catalysis routes are also crucial points and are hence the object of intense discussion. In this chapter it is brought together the collector designs which have been employed for solar photocatalysis to date. In addition, the reviewed literature is organized according to the pollutant or pollutants investigated, and to whether the application is to model or real wastewaters. This angle of analysis seeks to highlight the importance of moving towards the investigation of real wastewaters.

Specifically, the first part details solar collector designs and their components. The second part focuses on the catalyst materials employed for solar AOPs. As the development of photocatalysts is a vast field, it is considered only the materials which have already been investigated in combination with a solar collector. Finally, the last section reports case studies on both model solutions and on real wastewater samples.

2.2 Solar Collector Systems Employed for Wastewater Treatment

The starting point for the use of solar collectors in wastewater remediation can be traced back to parabolic systems, originally developed for thermal energy applications, and then adapted in 1989 in Albuquerque, New Mexico—USA for water purification. Immediately afterwards, in 1990, a dedicated facility started operations at the *Plataforma Solar de Almeria* — Spain. Ten years later, dedicated research on wastewater treatments started to be effectively performed [25]. Solar collectors can be concentrating or non-concentrating systems. The former can be classified depending on the principle adopted for focusing sunlight and based on whether they use a fixed or moving receiver [26], while the latter generally consists of flat panels which can be fixed or movable, i.e., following the sun. While in thermal solar applications all wavelengths of the sunlight spectrum are concentrated onto an absorber to produce an increase in temperature, for a solar AOP, the most effective photons are those on the high-energy side of the spectrum, in the UV or near UV range (300–400 nm wavelength), due to the prevalent use of wide band-gap semiconductors as catalyst materials. Wavelengths up to 600 nm are, to date, effectively exploited only by photo-Fenton reactions or by emerging catalyst materials designed ad-hoc for visible light absorption [6].

This is therefore an opportunity and a challenge for the materials science field. The use of light at wavelengths higher than 400 nm would also allow the use of silvered mirrors, which are simple and robust, but which present poor UV reflectance.

In fact, given that, to date, the range between 300 and 400 nm has been considered to be of exceptional importance, conventional silver mirrors have not been considered suitable as reflectors. This is mainly due to their low average reflectance in this wavelength interval, with a minimum at around 320 nm related to an interband transition [27]. Furthermore, the glass covering commonly present on silver mirrors contains iron impurities, which further contribute to reductions in UV radiation**.**

Mirrors based on aluminum are generally considered a better option when working with processes requiring UV photons [28]. In fact, their reflectance is high (around 93%) and almost constant in the 300–400 nm range. As proposed in previous works [29,30], the best reflective surface for solar AOPs should be: (i) efficient in the UV range, (ii) weather resistant and (iii) reasonably cheap. At present, the benchmark solution is based on anodized and electro-polished aluminum surfaces. An available alternative is using aluminum mirrors protected with acrylic resin coating [31].

The design of a solar AOP system requires consideration of a number of factors: the mirror materials and shaping, the catalyst, wastewater loading method (batch or once-through), flow type and rates, pressure drops, eventual pretreatment, eventual oxidant loading method, pH control and the use of a tracking system to enhance the direct solar radiation [6]. These criteria are presented in Table 2.1.

Table 2.1: Design factors for a solar wastewater remediation AOP.

Component	Feature
Mirror design	Parabolic/Dish/Plane/Fresnel
Tracking system	Automatic/Manual/Fixed
Catalyst	Dissolved/Suspended/Supported
Reactor configuration	Single/Parallel/Series
Wastewater loading	Once-through/Batch
Flow rate	Volume per time/On-Off
System pressure	Pumping employed
Pretreatment	Present/Absent
Oxidant loading method	Once/Periodically dosed
pH control	Acidic/Neutral/Basic

Most existing literature reports are based on different combinations of these factors, giving rise to a variety of configurations. Some of the main design choices for both concentrating and non-concentrating systems are reviewed in the following sections.

2.3 Concentrating Solar Systems

Concentrating solar collector systems are those which focus incident sunlight through a reflective surface—generally a polished metal, metalized glass or plastic. Solar concentrators can also present tracking systems with one or more axis to follow the position of the sun during the day [32–34].

The advantages of concentrating systems are: (1) potentially small reactor tube area, thus allowing for easier handling of the wastewater; (2) a limited reactor area is also more compatible with supported catalysts and turbulent flows, thus avoiding the issue of catalyst sedimentation; and (3) the evaporation of volatile compounds can be controlled.

Furthermore, it has been shown that degradation rates are generally improved by an increase of radiation intensity within given limits. This was clearly established for both photo-Fenton reactions and direct photocatalysis for SODIS applications [35–37], where a range of linear dependency between rates and irradiance was found and a minimum solar dose identified.

On the other hand, they present disadvantages such as the use of only (or primarily) direct solar radiation, possible high cost, and water overheating [25].

Among the concentrating systems, 5 are of particular interest in the context of wastewater remediation: (1) the parabolic through collectors (PTCs), which concentrate sunlight in a line; (2) compound parabolic collectors (CPCs), a design variant of PTCs; (3) the parabolic dish, designed to focus on a specific spot; (4) Fresnel concentrators, that can be designed to both single spot or line systems; and (5) optical fiber photoreactors, which are presented as a possible solution for reaching remote and difficult-access contaminated water sources.

2.3.1 Parabolic Trough Collectors (PTC)

Early solar photoreactor designs for photochemical applications were mounted on parabolic trough concentrators (PTCs), which were adapted from installations employed for thermal energy generation. PTCs can be defined as parabolic reflective surfaces that concentrate the radiation of the sun on a focal line, where the wastewater flows in a tubular reactor [38]. PTCs are constructed by bending a sheet of reflective or highly polished material, generally reflective silver or polished aluminum, into a parabolic shape. Figure 2.1 shows the schematic drawing of a PTC and an image of a constructed collector [39]. To increase the efficiency of direct solar radiation collection, the platform can work with one or two motor tracking systems, thereby keeping the aperture plane perpendicular to the incident radiation [19]. PTC applications are different depending on aperture areas, and can be divided in two fields according to temperature range [40]: the first for temperatures in the range between 100 and 250 °C and the second between 300 and 400 °C [41–43]. Examples include solar water heating [44], desalination [45,46], and water disinfection [47].

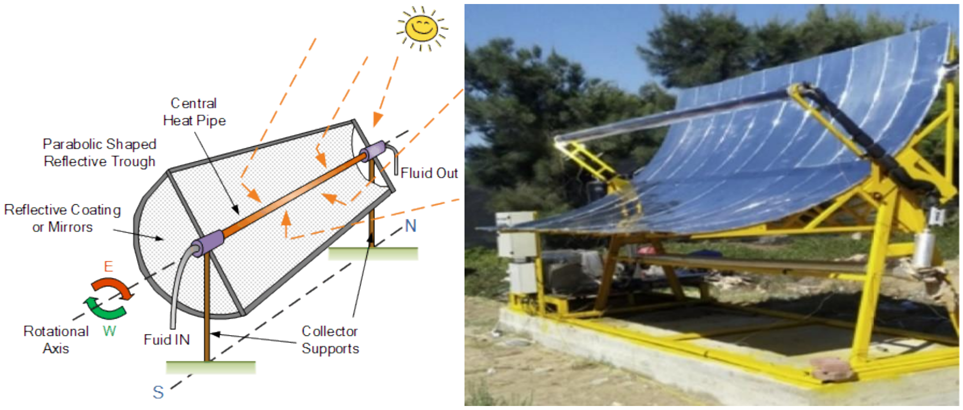

Figure 2.1: Schematic drawing of a parabolic trough collector [48].

Considering the applications of PTC to wastewater purification, early examples consisted of solar thermal parabolic-trough collectors where wastewaters flowed in a borosilicate glass tube placed on the focal line [6,49]. *Pyrex*$^{®}$ or *Duran*$^{®}$ borosilicate glass was chosen because of the necessity to have low levels of iron impurities. A tubular shape for the photoreactor configuration is considered optimal for sustaining the pressure and flow levels required by circulation systems [25].

2.3.2 Compound Parabolic Collectors (CPC)

A variant of the PTC concentrator described in the previous section is the CPC. With respect to PTCs, they offer the advantage of concentrating on the receiver all the radiation that arrives at the collector within a determined angle of acceptance, thus exploiting also part of the diffuse radiation. The concentration factor (C_{CPC}) of a two dimensions CPC is related to the angle of acceptance, as per Equation (1):

$$C_{\mathrm{CPC}} = \frac{1}{\sin \theta a} = \frac{a}{2\pi r} \qquad (1)$$

where θa is the angle of acceptance, a is the mirror aperture and r is the reactor tube radius. Previous investigations point that a reactor diameter between 25 and 50 mm is optimal [25] and the design of a CPC-based system and an example picture are shown in Figure 2.2.

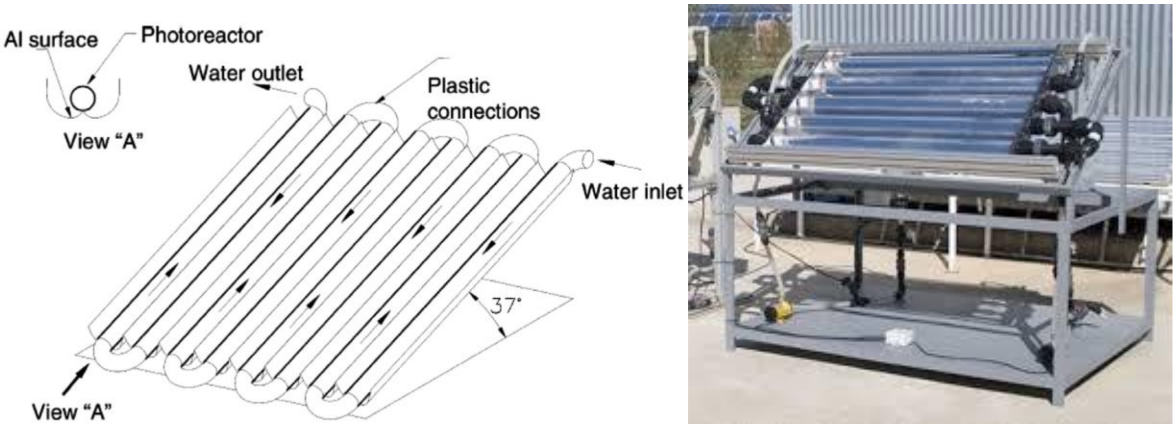

Figure 2.2: Schematic drawing and picture of a compound parabolic collector [32,50].

Several CPC type configurations have been realized and tested by companies and have been central to recent research projects [51]. Finally, it is worth mentioning an extremely simplified version of the CPC, the compound triangular collector, consisting of two reflective surfaces forming a V-shape. This configuration is of very simple construction and easy maintenance, but it nonetheless recently demonstrated good performance in the treatment of bacterial contaminants in municipal wastewaters [52].

2.3.3 Parabolic Dish Concentrators (PDC)

PDCs are widely studied and applied for converting solar energy into electrical or chemical energy and are accepted as those of highest efficiency in terms of concentration factors. The work of John Ericsson, dating back to the 1880s [53], is recognized as being among first examples of solar energy conversion and the coupling of a PDC to a Stirling engine. A PDC is a type of concentrator which reflects the solar rays onto an absorber installed on its spot-like focus. It consists primarily of a support frame equipped with a sun-tracking system, a reflective concave parabolic dish, and an absorber [54]. In this case, tracking the sun is a necessity, since PDCs only work with direct radiation, and a two-axis tracker is commonly employed.

PDCs offer the possibility of being installed in hybrid operation plants in combination with distinct types of solar concentrators [55]. The solar dish system can achieve, if temperature is of interest, high values due to high concentration factors. Figure 2.3 presents a schematic drawing and an image of a parabolic module in use at the laboratories of the physics department from the University of Trento - Italy. This collector is based on an innovative process to manufacture parabolic mirrors, resulting in potentially very low production costs [56,57].

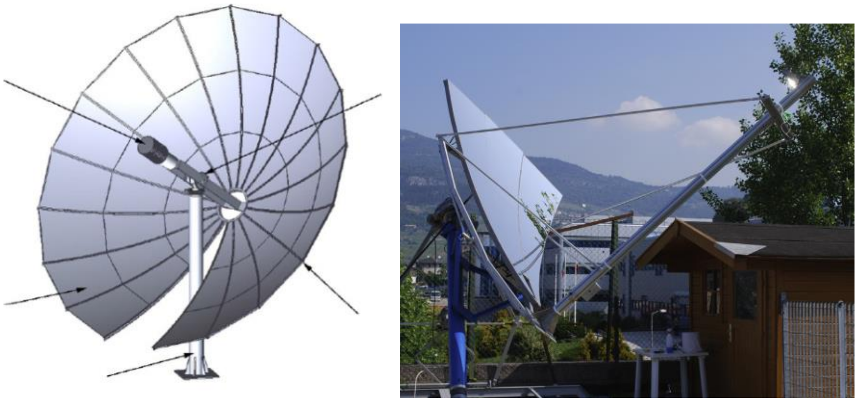

Figure 2.3: Schematic drawing and picture of a parabolic dish [56,57].

In solar wastewater purification, the selection of a PDC is motivated by specific needs. Being the most effective concentrators reaching concentration ratios that can be higher than 2000 suns they can provide an advantage in cases where a very high photon density and/or thermal processes enhance pollutant degradation, for example, when the rapid abatement of a high content of pollutant is needed.

2.3.4 Fresnel Solar Concentrators

Fresnel solar collectors have been developed and applied for solar energy production, and can be found in both a line or point-focus design. They can work in two basic configurations exploiting either mirrors or lenses to produce the concentration effect. Usually they are ground-mounted with flat or nearly flat surfaces tracking the sun and concentrating onto a focal receiver which, for wastewater treatment, is usually of tubular design and is equipped with secondary reflectors [58].

Compared to PTCs, Fresnel configurations offer two distinct advantages: (1) the receiver is fixed and usually with a larger collection area, which can lead to a simpler photoreactor design; (2) mirrors can be smaller and flat or nearly flat and are thus of simpler and cheaper fabrication. However, due to a greater distance between the receiver and the mirror array, they suffer from lower optical efficiency and are particularly prone to tracking errors [59].

Figure 2.4 presents the schematic drawing and an actual installation of Fresnel reflectors. This example shows the most common configuration, with evenly-placed, identical mirrors, a convenient design in terms of simplicity, but not necessarily the most efficient [60].

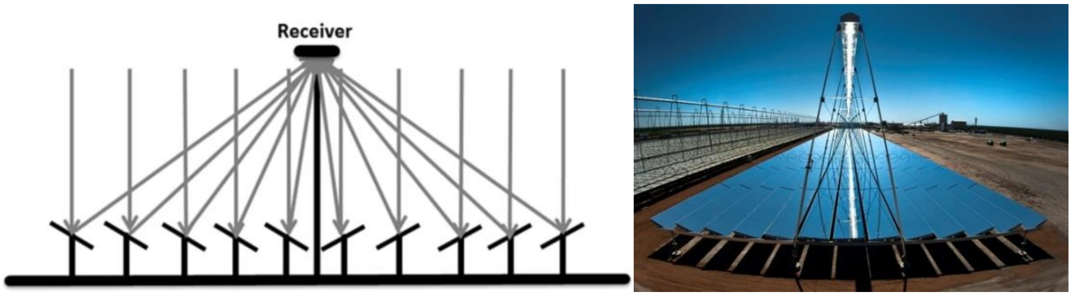

Figure 2.4: Schematic drawing of a Fresnel lens receiver [59].

A few applications to wastewater purification can be found in the literature. For example, Fresnel transmitting concentrators, which employ lenses instead of mirrors, were recently investigated. The lenses were made of an acrylic material with a transmittance of 0.92 in the range 400–1100 nm [61,62]. Despite the drawback of difficulties of concentrating UV light (<400 nm), results evidenced a possible reasonable option if used with low costs catalysts to accelerate the degradation of organic molecules in water models as a comparison of solely using direct solar radiation. A scheme of Fresnel lens transmitter concentrator is presented in Figure 2.5.

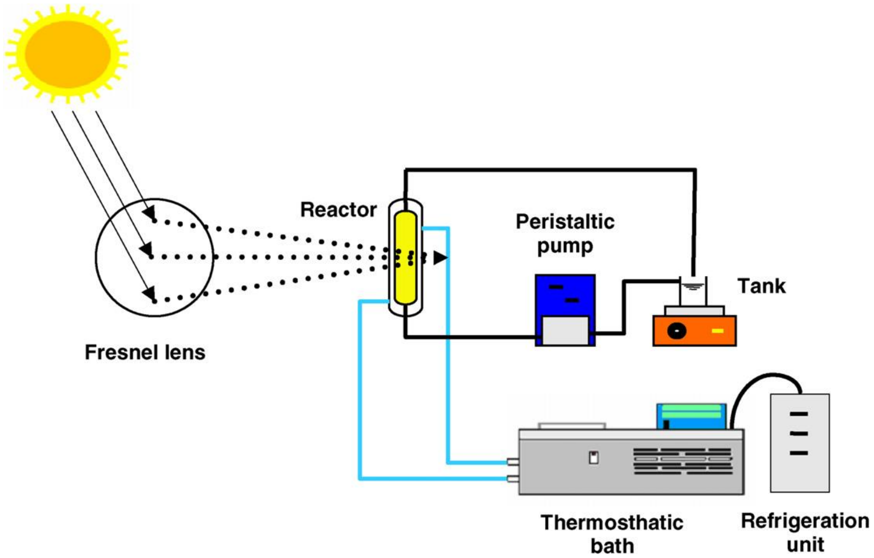

Figure 2.5: Fresnel lens transmitter concentrator scheme [63].

2.3.5 Optical Fiber Photoreactors

Optical fiber photoreactors have recently been studied for water remediation. The basic principle is based on the use of optical waveguides, usually in the form of optical fibers, to convey photons into the bulk of a wastewater. An interesting possibility is that of using a photocatalyst directly supported on the waveguides to achieve very high surface area to volume ratios. Some reports show values even higher than for a conventional photoreactor with suspended photocatalysts [64]. The use of optical fibers as waveguides has been investigated mostly with artificial light [65,66]. Extending the concept for use with sunlight would be much more complicated, with the need for a very accurate reflectors/tracking system to compensate for the movement of the sun.

The main advantage of this design is that the distance between the light collection system and the photoreactor can be great and non-linear, thanks to the properties of optical fibers. This would make it possible to reach otherwise inaccessible wastewater reservoirs, for example within buildings or subterranean reservoirs [67]. To date however, its complexity and low efficiency makes this design still impractical [38].

2.4 Non-Concentrating Solar Systems

Non-concentrating collectors usually consist of flat mirrors oriented to the equator line with a predetermined inclination angle depending on the installation place latitude. They can be static or movable systems and are generally on a single axis.

Their main advantages are: (1) simple design and low fabrication cost when compared to curved mirrors [68], and (2) they work with both direct and diffuse radiation. Also, they present high optical and quantum efficiency but usually do not heat water efficiently, which can be an advantage depending on the application. The main drawback is that they are generally designed for laminar flows, for which mass transfer rates are known to be suboptimal [25]. Among the non-concentrating systems, two deserve particular attention: (1) inclined plate collectors (IPC) and (2) water-bell photoreactors.

2.4.1 Inclined Plate Collectors (IPC)

Inclined plate collectors (IPC) are flat or corrugated panels over which a thin (typically <1 mm) laminar flow (usually 0.15–1.0 L/min) of wastewater is sustained. It is probably the simplest available design and offers the advantage of a large surface to support the photocatalyst material, in a configuration known as thin film fixed bed reactor (TFFBR). It is to be noted that water heating is not an issue with this design, with temperature typically between 70 and 95 °C [69]. IPCs are considered to be particularly suitable for small-scale applications [70]. Figure 2.6 presents an image and a scheme of an IPC.

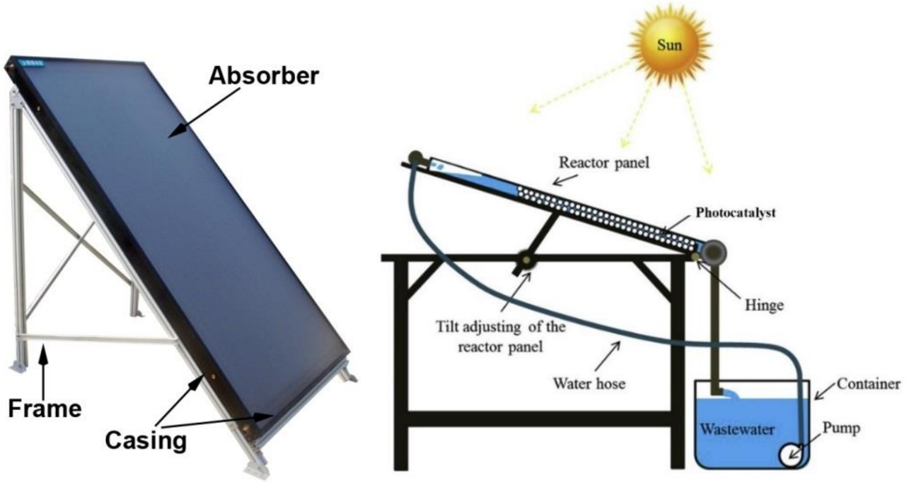

Figure 2.6: Examples of inclined plate collectors [71].

2.4.2 Water-Bell Photoreactors

This type of photoreactor, as shown in Figure 2.7, is similar in general design to the IPC reactor. The main differences are as follows: (1) the water film is generated by ejecting the fluid through nozzles with the shape of a water-bell, and (2) the photocatalyst is dispersed in powder form in the liquid phase. As positive points, it permits a turbulent flow [72,73] and avoids sedimentation of the catalyst due the constant pumping of liquid through the nozzles [74]. High flow rates can provide intense mixing and avoid dead zones in the system. On the other hand, the advantages provided by supported photocatalysts, as in the IPC design are lost.

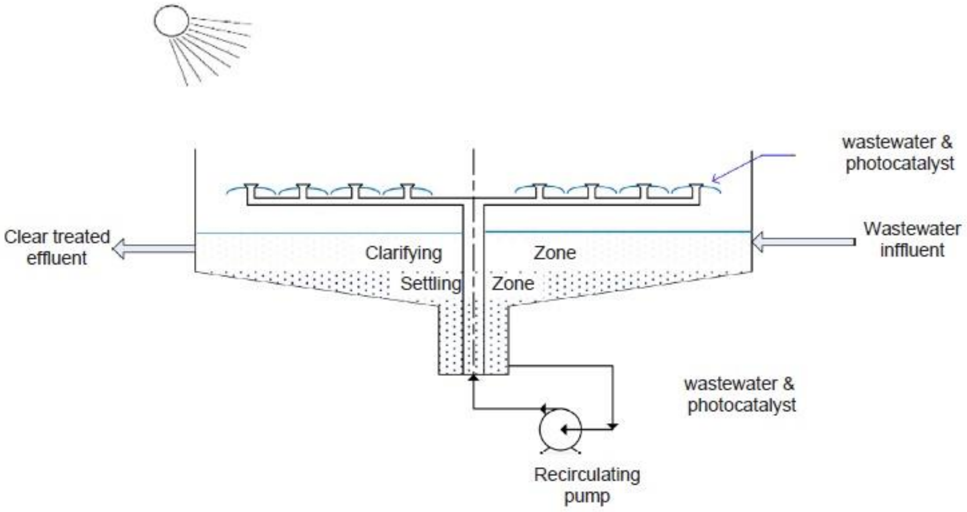

Figure 2.7: Schematic drawing of a water-bell photoreactor [75].

2.5 Advanced Oxidation Processes and Photocatalysis

AOPs are commonly defined by the chemistry and chemical engineering community as water treatments aimed at the removal of pollutants via oxidation by highly reactive radicals, such as the hydroxyl ($OH^\bullet$) or others (e.g., superoxide, peroxide, sulphate). In wastewater remediation, the most common process employs hydrogen peroxide (H_2O_2) as the hydroxyl radical source, activated by UV light. Although oxidation reactions by $OH^\bullet$ have been known for more than a century, with the use of Fenton's reagent in analytical chemistry, the application to wastewater remediation was only considered when evidence of $OH^\bullet$ generation in "sufficient quantity to carry out water purification" was given in the late 1980s [76]. Even though AOPs are of special interest for several applications, among which aromatics and pesticides degradation in water purification processes [77], oil derivatives, and volatile compounds [78], they have not yet been employed for large-scale commercial use. AOPs offer important advantages in water remediation, such as the possibility to effectively eliminate organic compounds in the aqueous phase, rather than collecting or transferring pollutants into another phase. Indeed, the contaminants can, in principle, be converted by complete oxidation into inorganic compounds, such as carbon dioxide and this process is called mineralization. Also, $OH^\bullet$ can, in principle, react with almost every organic aqueous pollutant without discriminating, potentially targeting a wide variety of compounds. A notable exception is that of Perfluorinated compounds, which are not attacked by $OH^\bullet$ radicals due to the stability of the C-F bond [79]. Some heavy metals can also be precipitated as $M(OH)_x$ [80]. AOPs currently have a number of serious drawbacks, affecting cost and limiting their large-scale application. For example, a constant input of reagents is usually necessary to keep an AOP operational, because the quantity of hydroxyl radicals in solution needs to be high enough to react with all the target pollutants at useful rates. Scavenging processes can occur in the presence of species which react with OH radicals without leading to degradation, for example, bicarbonate ions (HCO_3^-) [81] and chlorides [82] should be removed by a pre-treatment or the AOPs are compromised. In particular, the interference role of bicarbonate, chloride and dissolved silica anions has been recently studied in depth [83–85]. Finally, most existing processes rely on TiO_2 as the catalyst material. Although it offers important advantages in terms of stability, robustness and catalytic activity, it also has the serious limitation of requiring activation by UV light [86]. As such, it is mostly employed with artificial UV-sources, which are expensive, have short operational lifetimes, and require a high energy input.

For these reasons, it is not economically reasonable to use only AOPs to treat large amounts of wastewater, but AOPs can be conveniently integrated with conventional treatments as a final or intermediate step [87]. In this context, the use of solar radiation to promote AOPs could contribute to greatly reduce costs by relying on a free and renewable source of photons, even if the cost problems mentioned above must be mitigated in order to have an efficient and competitive water purification technology. This possibility, along with increasing efforts towards the implementation of water reuse worldwide, are currently accelerating research towards the implementation of large-scale AOPs [88].

2.5.1 Principles of Solar Photocatalysis

Solar photocatalysis currently plays a minor role, since the growth of research focusing on solar systems applied therein has shown a smaller increase compared to overall photocatalysis research, as demonstrated on Figure 2.8. This information points to the opportunity to dedicate efforts to this clean technology connected to the abundant solar energy source.

Major types of photocatalysis include heterogeneous photocatalysis, where the catalyst and substrates are in different phases, and homogeneous photocatalysis, where they are in the same phase and this classification is adopted for the following sections.

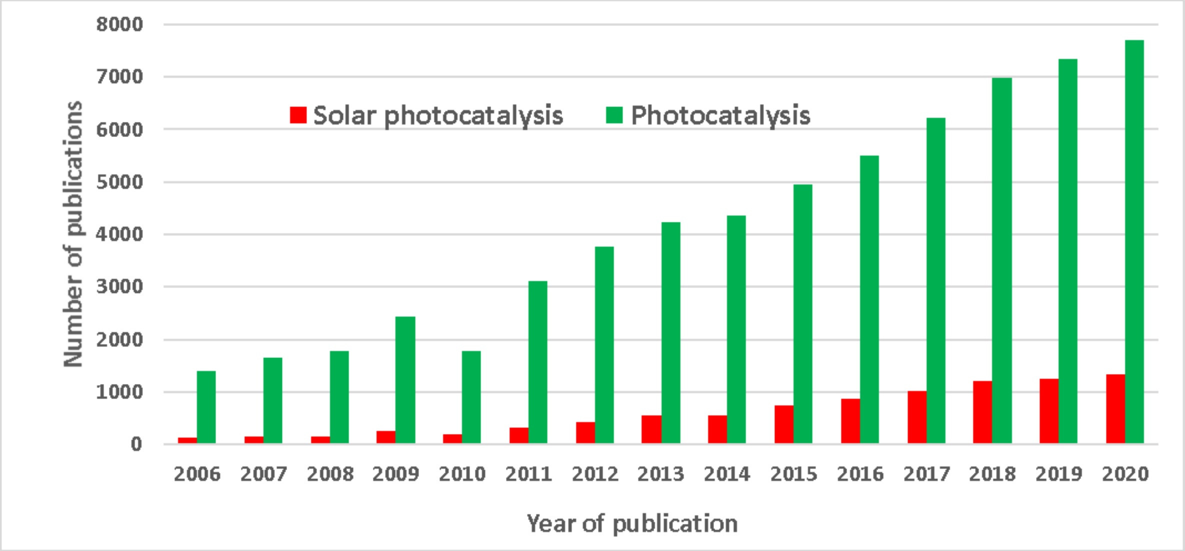

Figure 2.8: Publications on photocatalysis compared to those on solar photocatalysis. Data from Scopus in December 2020 comparing "photocatalysis" with "solar AND photocatalysis" as search terms within the "article title, abstract, keywords" search document field.

2.5.2. Heterogeneous Photocatalysis

In heterogeneous photocatalysis processes, the catalyst is generally a semiconductor material activated by absorption of UV or UV-Visible photons. Several semiconductors have been investigated as catalysts, such as TiO_2, Fe_2O_3, CdS, GaP, Co_3O_4, ZnS. Among these, TiO_2 has received the most investigation efforts since its good photocatalytic properties under UV irradiation were already known in the early 1970s. However, novel types of catalysts focused to solar applications are rapidly emerging, especially those which are able to efficiently absorb visible light.

Heterogeneous photocatalysis by semiconductors can be explained in the framework of the band theory for the electronic structure of solids. In Figure 2.9 the first step is shown, where an electron (e^-) in the valence band (VB) is excited to the vacant conduction band (CB) by absorption of a photon of energy $h\nu$ equal to or greater than its optical band gap, leaving a positive hole (h^+) in the VB. The excited electrons can reduce available acceptor species, such as oxygen in proximity of the surface, while holes are often powerful oxidants. The photo-generated electrons and holes can thus drive redox reactions with species for which the involved redox potentials are an appropriate match. However, the electrons and holes can also recombine without participating in any redox process, in a competing deactivation event. This is a major issue in the design of materials and is the reason why the time scale of the recombination process must be kept as large as possible.

In the case of TiO_2 photocatalysis in water with UV photons of energy ≥3.2 eV for anatase and 3.0 eV for rutile (corresponding to about 387 and 413 nm wavelength respectively), photo-generated electron-hole pairs at the solid-liquid interface can promote redox reactions with adsorbed water and dissolved oxygen. This process results in the formation of $OH^•$ and O_2^- radicals respectively, which are powerful oxidant species capable of reacting with most organic substances. The two most common configurations for heterogeneous photocatalytic reactors are: (1) reactors where the photocatalyst is in powder form suspended in water - colloid, and (2) reactors where the photocatalyst is immobilized on a surface – thin film coating. The first configuration is more explored, due to the simplicity of synthesis methods for powders; however, it needs an additional separation step, generally sedimentation and/or filtration, to recover the catalyst material. In the case of TiO_2, commercial products such as Evonik P25 and P100 are the most commonly employed in the literature. Catalyst separation and recovery is a major drawback for large-scale applications [1]; thus, it is possible to identify an open space on the research field aimed at the immobilization of the photocatalyst. This is highlighted by emerging manufacturing technologies, as exemplified by the use of pulsed laser deposition (PLD) for the production of thin film nanocatalysts with controlled properties [89,90]. Discussions highlighting the use of TiO_2 catalysts with sunlight on PTR and IPC reactors can be found in the literature [91,92]. Also, advances in photocatalyst immobilization for TiO_2, to be used with concentrated sunlight, present alternatives as mesoporous clays, nanofibers, nanowires, nanorods, membranes and surface doping modifications [7]. The possibility to produce glasses or polypropylene tubes with supported TiO_2 has also been reported [50]. In practice, however, novel applications of TiO_2 have been hindered due to their wide optical band gaps allowing only little or no absorption of visible-light [93,94]. The use of doping has been extensively investigated with the goal of increasing the catalyst absorption in the visible range, among which modifications of TiO_2 by W [95], Pt [96], N, V and V-N [97], Cu and N [98], Co and B [99], and Ag [100] showed promising results for the photocatalytic degradation of organic compounds. Many studies have also been devoted to the design of other metal oxide photocatalyst materials, such as perovskite-type oxides, which can work under visible light illumination [24,101,102]. Other catalysts investigated for wastewater purification with sunlight are Bi_2WO_6 and Ag-$BiVO_4$, for their absorption closer to the visible range (420 nm) [103]. In a theoretical work, density functional theory (DFT) calculations explored the modification of a β-Bi_2O_3 photocatalyst with 32 elements to design visible-light-responsive photocatalysts. Based on this, a series of photocatalysts were identified as good candidates for the reduction of chlorinated organic compounds in water [104]. Recently, Co_3O_4 hierarchical urchin-like structures were produced by PLD and tested on model dyes, raising great interest in the synthesis of hierarchical 3D nanostructures for applications in water purification [89]. Iron oxide-based nanostructures have also been fabricated by PLD and studied for photocatalytic water purification [105]. Other catalysts such as SnO_2, and ZnS have also been reported which can operate either via the reductive pathway (ZnS) or the oxidative one (SnO_2) [106,107].

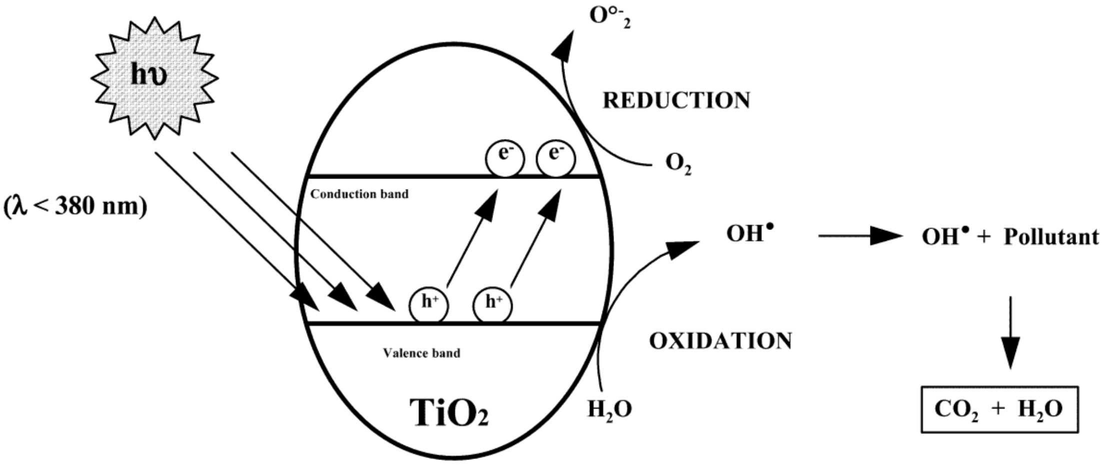

Figure 2.9: General mechanism of the heterogeneous photocatalysis [14].

An interesting study employed volcanic ashes in a solar photocatalytic reactor. The volcanic ashes are rich in titanomagnetite, labradorite, augite and ferrous magnesium hornblende capable of performing photocatalysis in the visible-NIR ranges [108]. Reports of novel materials focusing on visible light response catalysts are rapidly emerging and are increasingly successful. Their application to solar concentration for wastewater purification appears to represent an interesting opportunity to advance the field. Table 2.2 below shows a selection of references implementing the design strategies discussed above.

Table 2.2: Selected references for catalyst materials. Selection is based on two criteria: materials developed for visible light absorption and materials introducing an advancement over benchmark TiO_2.

#	Reference	Catalyst Material	Characteristics	Major Results	Solar *
1	Sacco et al., 2018 [52]	N-doped TiO_2	N-doped TiO_2 particles immobilized on polystyrene spheres	Inactivation of *E. coli* in municipal wastewaters	Yes
2	Wang et al., 2015 [84]	TiO_2 with fly ashes	Sol-Gel coating of TiO_2 on ashes xenospheres	MB dye degradation under visible light	No
3	Edla et al. 2015 [89]	Co_3O_4	PLD synthesized Co oxide urchin-like particle-assembled coating	Enhancement of MB dye degradation under visible light by hierarchical nanostructuring	No
4	Mecha et al., 2018 [92]	doped TiO_2	Calcinated powders and ozonation	SODIS of municipal wastewater	Yes
5	Patel et al., 2014 [97]	V-N-codoped TiO_2	RF- sputtering of thin films	Enhanced MB dye degradation under visible light	No
6	Jaiswal et al., 2015 [98]	Cu-N codoped TiO_2	Sol-gel thin films	Degrade MB dye and p-Nitrophenol solution under UV-VIS light	No
7	Jaiswal et al., 2016 [99]	Co-B-codoped TiO_2	Sol-gel thin films	Degradation of organic pollutants (p-nitrophenol and rhodamine B dye) under visible light	No
8	Varma et al., 2016 [100]	Ag-doped TiO_2	TiO_2 decorated with Ag nanocomposites	Degradation of p-nitrophenol (PNP) and MB dye under visible light	No
9	Jing et al., 2014 [101]	Cu_2O	Nanocrystals integrated photocatalyst adsorbent (IPCA)	Maximum adsorption capacity evaluation to examine the removal of organic pollutants (HA, CR and MO).	No
10	Malato et al., 2016 [103]	TiO_2	Particles in suspension	Strategies to improve quantum yield	Yes
11	Niu et al., 2016 [104]	Bi_2O_3	Nanoparticles (tens to hundreds of nanometers)	Pentachlorophenol (PCP), trichloroethylene (TCE), and hexachlorocyclohexane	No

12	Edla et. al., 2017 [105]	Fe_2O_3	PLD synthesized Fe oxide urchin-like particle-assembled coating	Enhancement of MB dye degradation under visible light by hierarchical nanostructuring	No
13	Fenoll et al., 2012 [106]	ZnO, TiO_2, WO_3, SnO_2	Micrometric scale particles in suspension	Photodegradation of fenamiphos (pesticide)	Yes
14	Borges et al., 2017 [108]	Volcanic ashes	Grinded and sieved in the range 1.40–1.80 mm and 500–850 µm	MB dye degradation	Yes
15	Sano et al., 2004 [109]	Pt doped TiO_2	Pt loaded TiO_2 synthetized at elevated temperatures	Photocatalytic degradation of volatile organic compounds (VOCs)	Yes
16	Vela et al. 2018 [110]	TiO_2 and $Na_2S_2O_8$	Commercial nanopowders with an electron acceptor in solution	Degradation of bisphenols, diamylphthalate, butyl benzylphthalate, methylparaben and ethylparaben in wastewater model	Yes
17	Rodriguez et al., 2010 [111]	TiO_2 and Ferri-carboxilate	Ferricarboxilates and commercial TiO_2 in combination	Degradation of Bisphenol A in model wastewater	Yes
18	Muradov, 1994 [112]	Pt doped TiO_2	Construction of a plate type photoreactor with immobilized TiO_2	Nitroglycerine and Rhodamine dye models degradation	Yes
19	Villén et al., 2006 [113]	Ru(II) complex	Ruthenium trischelate complex immobilized onto porous silicone	Inactivation of *Escherichia coli/faecalis*	Yes
20	Bansal et al., 2018 [114]	Composite Fe-TiO_2	Spherical beads with average diameter of 1.5 cm	Pharmaceutical wastewaters decontamination	Yes

* research performed with a solar collector as the light source.

2.5.3 Homogeneous Photocatalysis

In the homogeneous photocatalysis process, important efforts were devoted to the investigation of the Fenton reaction in an aqueous solution containing metal ions and hydrogen peroxide, capable of providing hydroxyl radicals. When UV/visible radiation (wavelength ≤ 600 nm) is introduced in the process, it becomes catalytic; this is known as “photo-Fenton”

[13,115,116]. In the photo-Fenton reaction, the metal ion initially reacts with the H_2O_2 added to the contaminated water, producing $OH^{\bullet}$ radicals (Equation (2)):

$$\text{Metal}^{2+} + H_2O_2 \rightarrow \text{Metal}^{3+} + OH^{-} + OH^{\bullet} \quad (2)$$

$$\text{Metal}^{3+} + OH^{-} + h\nu \rightarrow \text{Metal}^{2+} + OH^{\bullet} \quad (3)$$

The absorption of a photon (Equation (3)) then not only restores the initial Metal^{2+}, the crucial catalytic species for the Fenton reaction, but also produces additional radicals that can contribute to the oxidation of organic pollutants [117].

Though less interesting from an industrial point of view due to the difficulty of separating and recovering the catalyst, a photo-Fenton process in the homogeneous route has been recently demonstrated for SODIS technology, using ethylendiamine-N′,N′-disuccinic acid as a complexing agent to prevent iron precipitation as ferric hydroxide [118].

2.5.4 Homogeneous Versus Heterogeneous Photocatalysis

Among the major solar photoreactor system design issues are whether to use a homogeneous route with a dissolved catalyst or a heterogeneous one with a suspended or supported catalyst. This decision is greatly affected by the availability of facile and cost-effective fabrication methods. A large part of the investigations performed so far have used suspended particles in the contaminated water, which, as with the case of a dissolved catalyst, demands a final extra step to separate and recover the catalyst. A solution to this problem is the use of supported catalyst configurations, but this has, to date, been hindered by higher costs due to more complex synthesis procedures. Thus, research efforts on improved manufacturing techniques, such as the use of PLD, will likely offer possible solutions to this issue [89,105,119–122].

A supported-catalyst design also needs to take into account several additional problems. As the catalyst dispersion is not optimal, the greatest possible surface area is needed to ensure a good contact between active sites and target substrates, and an effective irradiation geometry must be identified. A good adhesion with the supporting material is also critical, as it dictates the capability of withstanding the mechanical wear from the water flow, and thus, the durability and operational lifetime of the catalyst coating. All these issues can, however, be addressed by careful design and improvements in coating technology.

Overall, the heterogeneous route to photocatalytic water treatments with supported semiconductors is a more promising technology when compared to its suspended catalyst counterpart or to the homogeneous route, mainly due to the necessity of easy industrial handling and replacement of the materials.

2.6 Wastewaters

Since investigations dedicated to water purification with the use of sunlight began, several types of pollutants have been investigated. These have generally been model compounds, while real wastewaters, due to their greater complexity, are still less explored. In the following sections, research papers investigating important model and real wastewaters are presented in tables organized by the main class of pollutant considered.

2.6.1 Model Pollutants

In the initial studies of the solar concentration for wastewaters research field, several types of model pollutants were investigated using concentrated sunlight and AOPs [123]. The United States Environmental Protecting Agency (EPA) made an inventory of more than 800 molecules that can be degraded by advanced oxidation processes [16]. In Table 2.3, works that investigated BROCs from the industrial general chemical products sector are presented. The investigations collected were performed from 1999 until today are representative of the importance of solar collectors to the wastewater purification field. Among the pollutants tested on the water models, substances such as phenols, amines, gaseous toluene and acetaldehyde, detergents, trichloroethylene, phenolate, diverse acids and phosphates deserve attention. In terms of the solar collector employed, special emphasis was devoted to the PTC and CPC configurations (12 reports), IPC (5 reports), optical fiber (2 reports), and PDC (1 report). In terms of catalysts, all the investigations primarily reported on the use of TiO_2 as a catalyst material, with variations in terms of the supporting system, doping element and particle structure. As a solid catalyst, TiO_2 was consequently employed in the heterogeneous route for catalysis.

Table 2.3: BROCs model wastewaters (Industrial general chemical products).

#	Reference	Pollutant Tested	Solar Collector	Catalyst Material	Catalysis Type
1	Fernandez-Ibanez et al., 1999 [124]	4-chlorophenol	PTC/CPC	TiO_2 supported and suspended	Heterogeneous
2	Sano et al., 2004 [109]	Gaseous toluene and acetaldehyde	PTC	Pt-TiO_2 supported	Heterogeneous
3	Klare et al., 2000 [125]	Amines	PTC	TiO_2 (P-25) TiO_2 (AK1) TiO_2 (UV 100) Pt-TiO_2 (synth) suspended	Heterogeneous
4	Oyama et al., 2004 [126]	Commercial Detergents	PDC	TiO_2 (P-25) suspended	Heterogeneous
5	Mehos et al., 1992 [81]	Trichloroethylene	PTC	TiO_2 (P-25) suspended	Heterogeneous
6	Minero et al., 1996 [127]	Sodium pentachlorophenolate	PTC	TiO_2 (P-25) suspended	Heterogeneous
7	Bandala et al., 2004 [128]	Oxalic acid	PTC/CPC	TiO_2 suspended	Heterogeneous
8	Malato et al., 1997 [129]	2,4-dichlorophenol	PTC/CPC	TiO_2 (P-25) suspended	Heterogeneous
9	Noorjahan et al., 2003 [130]	H-acid	IPC	TiO_2 supported	Heterogeneous
10	Feitz et al., 2000 [131]	Phenol dichloroacetic acid	IPC	TiO_2 supported	Heterogeneous
11	Chan et al., 2003 [132]	Benzoic acid	IPC	TiO_2 (P-25) supported	Heterogeneous
12	van Well et al., 1997 [133]	Dichloroacetic acid	IPC	TiO_2 (UV 100) suspended	Heterogeneous
13	Dillert et al., 1999 [68]	Dichloroacetic acid	IPC/CPC	TiO_2 (P-25) TiO_2 (UV 100) suspended	Heterogeneous
15	Peill and Hoffmann, 1997 [67]	4-chlorophenol	Opt. fiber	TiO_2 (P-25) supported	Heterogeneous

16	Xu et al., 2008 [134]	4-chlorophenol	Opt. fiber	TiO_2 (synth.) supported	Heterogeneous
17	Tanveer and Tezcanli Guyer, 2013 [32]	Alkanes, alcohols, carboxylic acids, aromatics, polymers and surfactants	CPC	TiO_2 (P-25/PC 500/UV 100/TTP/PC 10/PC 50/Rhodia)	Heterogeneous
18	Barwal and Chaudhary, 2016 [9]	Urea, ammonium chloride, sodium acetate, peptone, magnesium hydrogen ortho-phosphate trihydrate, potassium dihydrogen orthophosphate, ferrous sulphate, starch, glucose, yeast and trace nutrients	PTC	TiO_2	Heterogeneous
19	Vela et al., 2018 [110]	Bisphenol A, bisphenol B, diamylphthalate, butyl benzylphthalate, methylparaben and ethylparaben	CPC	TiO_2 alongside an electron acceptor like $Na_2S_2O_8$	Heterogeneous
20	Rodriguez et al., 2010 [111]	Bisphenol A	CPC	Ferricarboxilate, TiO_2 (P25), combinations thereof	Heterogeneous and homogeneous
21	Kositzi et al., 2004 [135]	Peptone, Meat extract, Urea, K_2HPO_4, NaCl, $CaCl_2.2H_2O$, Mg_2SO_4 $7H_2O$	CPC	TiO_2 (P-25) suspended Fe(III)/H_2O_2 photo-Fenton process	Heterogeneous and homogeneous

Table 2.4 presents the published papers dedicated to the investigation of model waters containing dyes as the main pollutant. The first studies were reported in 1994 and continue to receive interest to the present day. Dyes such as methyl-orange, Remazol red B, rhodamine, indigo carmine, methylene blue, and reactive black 5, among others, were studied by employing either CPC or IPC solar collectors. Also, 3 investigations were performed using the homogeneous route with ferrous salts solutions, and the majority with the heterogenous one.

Table 2.4: BROCs model wastewaters (Dyes).

#	Reference	Pollutant Tested	Solar Collector	Catalyst Material	Catalysis Type
1	Augugliaro et al., 2002 [136]	Methyl-orange (azo-dye) Orange II (azo-dye)	CPC	TiO_2 (P-25) suspended	Heterogeneous
2	Selva Roselin et al., 2002 [137]	Remazol red B (azo-dye)	IPC	ZnO supported	Heterogeneous
3	Muradov, 1994 [112]	Nitroglycerine Rhodamine dye	IPC	TiO_2 (P-25) Pt-TiO_2 supported	Heterogeneous
4	Thu et al., 2005 [138]	Formetanate Indigo carmine (indicator dye)	IPC/CPC	TiO_2 (PC 500) supported and suspended	Heterogeneous
6	Rodríguez-Chueca et al., 2014 [8]	Synthetic wool dying in different colors (yellow, blue and red)	CPC	TiO_2	Heterogeneous
7	Sutisna et al., 2017 [71]	Methylene blue dye	IPC	TiO_2	Heterogeneous
8	Cabrera-Reina et al., 2019 [139]	Acid Red 1, Acid Yellow 17, Reactive Black 5 and Reactive Orange 1	CPC/IPC	Fe (II)	Homogeneous
9	Monteagudo et al., 2009 [140]	Orange II dye	CPC	Ferrioxalate in solution	Homogeneous
10	García-Montaño et al., 2008 [141]	Procion Red H-E7B and Cibacron Red FN-R (azo-dyes)	CPC	Fe(II)/H_2O_2 photo-Fenton processs	Homogeneous

Table 2.5 instead presents the use of solar photocatalysis, mostly under the heterogenous route with IPC and CPC solar collectors, to investigate the degradation of pesticides as model pollutants. In this segment of pollutants, investigations have gained attention since the year 2000. Eight miscellaneous pesticides (ethoprophos, isoxaben, metalaxyl, metribuzin, pencycuron, pendimethalin, propanil and tolclofos-methyl) were studied. Initial investigations on this sector have paved the way for further research on real water sources from extensive agriculture areas.

Table 2.5: BROCs model wastewaters (Pesticides).

#	Reference	Pollutant Tested	Solar Collector	Catalyst Material	Catalysis Type
1	Fenoll et al., 2012 [106]	Fenamiphos pesticide	CPC	TiO_2, ZnO	Heterogeneous
2	Berberidou et al., 2017 [142]	Lontrel 100AS commercial herbicide	IPC	Ferrioxalate/TiO_2	Heterogeneous and homogeneous

A last BROC contaminant reported in the literature was a pharmaceutical product, as reported in Table 2.6. In 2005, a CPC solar collector using commercial P-25 TiO_2 as the catalyst and heterogeneous photocatalysis was utilized to investigate the degradation of the antibiotic Lincomycin.

Table 2.6: BROCs model wastewaters (Pharmaceuticals).

#	Reference	Pollutant Tested	Solar Collector	Catalyst Material	Catalysis Type
1	Augugliaro et al., 2005 [143]	Lincomycin (antibiotic)	CPC	TiO_2 (P-25) suspended	Heterogeneous

In another field of application of solar collectors applied for wastewater purification, solar disinfection (SODIS) was employed to study the removal of bacteria as E. Coli, faecalis and Salmonella and fungi, such as fusarium spores as shown in Table 2.7. Investigations were mostly developed with CPC solar collectors. Both—heterogeneous and homogeneous routes are represented, with a prevalence of TiO_2 catalyst for the former and of ferrous solutions for the latter.

Table 2.7: SODIS model wastewaters (Bacteria and Fungi).

#	Reference	Pollutant Tested	Solar Collector	Catalyst Material	Catalysis Type
1	Sichel et al., 2007 [36]	*Escherichia coli*	CPC	TiO_2 (P-25) supported from colloid	Heterogeneous
2	Fernández et al., 2005 [50]	*Escherichia coli*	CPC	TiO_2 (P-25) suspended and support	Heterogeneous
3	Villén et al., 2006 [113]	*Escherichia coli/faecalis*	CPC	RDP2+ (dye) supported	Heterogeneous
4	McLoughlin et al., 2004 [144]	*Escherichia coli*	PTC/CPC	TiO_2 (P-25) supported	Heterogeneous

5	Freudenhammer et al., 1997 [145]	Simulated bacterial municipal wastewater	IPC	TiO_2 (P-25) supported	Heterogeneous
6	Polo-López et al., 2012 [146]	Fusarium spores	CPC	Ferrous sulfate heptahydrate	Homogeneous
7	Nahim-Granados et al. 2018 [147]	*E.coli* O157:H7 and Salmonella enteritidis	IPC	Ferrous sulphate heptahydrate and ferric nitrate	Homogeneous
8	Aguas et al. 2017 [148]	agricultural pathogenic fungi (Curvularia sp.)	CPC	Ferrous sulfate heptahydrate	Homogeneous
9	Rodríguez-Chueca et al., 2014 [8]	*E.coli*, coliform Enterococcus faecalis	CPC	ferrous sulfate in slurry	Homogeneous

2.6.2 Real Pollutants

The investigation of real wastewaters samples has taken place mainly in the last decade. Anyhow, the increasing importance of this approach demonstrates a constant switch from model investigations to real wastewater sources with the aim of solving the critical situation of pollution worldwide. Table 2.8 shows real industrial effluents already investigated such as olive mill wastewater, effluents from the beverage industry, micropollutants in municipal effluents and metallic wastes, mostly with CPC solar collectors. Both heterogeneous and homogeneous routes were used.

Table 2.8: Real wastewaters (Industrial general chemical products).

#	**Reference**	**Pollutant Tested**	**Solar Collector**	**Catalyst Material**	**Catalysis Type**
1	Ruzmanova et al., 2013 [149]	Olive mill wastewater	CPC	TiO_2 suspended	Heterogeneous
2	Durán et al., 2015 [150]	Beverage industry effluents	CPC	Ferrioxalate, oxalic acid	Homogeneous
3	Brienza et al., 2016 [151]	Municipal effluents with 53 micropollutants detection	IPC	HSO^{-5} /Fe^{+2} and TiO_2	Heterogeneous and homogeneous
4	Onotri et al., 2017 [152]	copper, iron, zinc and EDDS	CPC	TiO_2 suspended	Heterogeneous

Residual dyes from the textile industry were studied in 2015 as shown in Table 2.9 under homogeneous route using CPC solar collectors and ferrous solutions as catalyst.

Table 2.9: Real wastewaters (Dyes).

#	Reference	Pollutant Tested	Solar Collector	Catalyst Material	Catalysis Type
1	Manenti et al., 2015 [153]	Textile dyes	CPC	ferric–organic ligand complexes such as oxalic acid, citric acid and EDDS, ferrioxalate	Homogeneous

Table 2.10 shows investigation of real wastewater sources contaminated with pesticides containing Chlorpyrifos, lambda-cyhalothrin and diazinon using CPC or IPC solar collectors, employing homogeneous and heterogeneous photocatalysis routes.

Table 2.10: Real wastewaters (Pesticides).

#	Reference	Pollutant Tested	Solar Collector	Catalyst Material	Catalysis Type
1	Gar Alalm et al., 2015 [154]	Chlorpyrifos, lambda-cyhalothrin, and diazinon as major contaminants on pesticides	CPC	Ferrous sulfate hydrate and TiO_2	Homogeneous and heterogeneous
2	Pichat et al., 2004 [155]	Pesticides	IPC	TiO_2 (PC 500) supported	Heterogeneous

Municipal wastewaters contaminated with pharmaceuticals were treated and results are reported on the publications in Table 2.11. Among the contaminants, presences of acetaminophen, antipyrine, atrazine, carbamazepine, diclofenac, flumequine, hydroxy biphenyl, ibuprofen, isoproturon, ketorolac, ofloxacin, progesterone, sulfamethoxazole and triclosan were investigated. Novel Fe-TiO_2 composite catalysts with the objective of performing both photocatalysis and photo-Fenton have been studied for the treatment. Their degradation performances were evaluated in a CPC reactor under the homogeneous and heterogeneous route.

Table 2.11: BROCs real wastewaters (Pharmaceuticals).

#	**Reference**	**Pollutant Tested**	**Solar Collector**	**Catalyst Material**	**Catalysis Type**
1	Méndez-Arriaga et al., 2009 [156]	pharmaceuticals present in real wastewater sources	CPC	TiO_2 suspended	Heterogeneous
2	Bansal et al., 2018 [114]	Pharmaceutical wastewaters	IPC	Composite Fe-TiO_2	Heterogeneous
3	Foteinis et al., 2018 [157]	Pharmaceutical wastewaters, i.e., antipyrine	CPC	Ferrous sulfate, oxalic acid	Homogeneous
4	Ferro et al., 2015 [158]	multidrug (namely ampicillin, ciprofloxacin and tetracycline)	CPC	Ferrous sulfate and TiO_2	Homogeneous and heterogeneous
5	Almomani et al., 2018 [159]	antibiotics, estrogens	CPC	Iron (III) perchlorate hydrate and TiO_2	Homogeneous and heterogeneous

In terms of SODIS, as shown in Table 2.12, application to real wastewater sources, municipal effluents were mostly used to investigate the inactivation of bacteria and fungi using the homogeneous and heterogeneous routes. CPC solar collectors were used and ferrous salts and TiO_2 were used as catalysts.

Table 2.12: SODIS real wastewaters (Bacteria and Fungi).

#	**Reference**	**Pollutant Tested**	**Solar Collector**	**Catalyst Material**	**Catalysis Type**
1	Miralles-Cuevas et al., 2017 [160]	Municipal effluents	CPC	$Fe_2(SO_4)_3$	Homogeneous
2	Ortega-Gómez et al., 2014 [161]	E. coli and total coliforms inactivation	CPC	Ferrous sulfate heptahydrate	Homogeneous
3	Polo-López et al., 2014 [162]	phytopathogen fungi spores	CPC	Ferrous sulphate heptahydrate, ferric nitrate and TiO_2	Homogeneous and heterogeneous
4	Sacco et al., 2018 [52]	Escherichia coli	CPC	Nitrogen-doped TiO_2	Heterogeneous

All the analyzed studies present relevant information about degradation rates and the processes involved in the use of solar light for the degradation of pollutants in wastewaters. In particular, a relevant quantity of pollutants was tested, and the development of low-cost solar systems evolved. Also, it is observed that TiO_2 is a very well-established catalyst for use in solar wastewater degradation, but new catalysts and possible cost reductions offer interesting opportunities for research.

2.7 Conclusions and Perspectives

Although solar water treatments have produced significant interest in research, they have not yet reached commercialization; there are only a few examples of medium to large-scale solar wastewater processing plants in industry. However, recent literature results demonstrate that solar wastewater treatment has the potential to be successfully employed both as a cheaper and more environmentally friendly alternative to conventional processes, or integrated in existing plants, thereby increasing efficiency and reducing operating costs. However, further research towards industrialization is needed. Two directions emerge as particularly promising: advances in materials science towards immobilized photocatalysts, which can effectively use sunlight, and switching to the investigation of real, rather than model, wastewaters.

Regarding the former, photocatalysts working with UV-visible light would make it possible to better harness sunlight and ease the design requirements for solar collectors and photoreactors. For example, by eliminating the need for UV radiation, it would be possible to use conventional mirrors, which are significantly less expensive and more durable than UV-reflecting mirrors.

Regarding wastewaters, investigations which initially began with water models have turned to real wastewater sources in recent years. These are much more complicated samples, generally containing a variety of species which can interfere with the treatment. This complexity needs to be tackled by directed research efforts, particularly by the chemistry and chemical engineering community, in order to progress towards industrial application.

Chapter 3: Experimental techniques and characterizations

3.1 Experimental techniques

This section presents the experimental techniques employed in the development of the work. It is presented the details of the solar concentrator used for the practical experiments of wastewater treatment and the pulsed laser deposition (PLD), a thin film fabrication technique that was extensively used for obtaining the novel catalyst materials proposed for application on wastewater treatment.

3.1.1 Solar concentrator – Parabolic Dish Collector (PDC) apparatus

The experiments were performed using the solar concentrator available at the physics department of the University of Trento. The solar concentrator employed is an apparatus designed, built and patented by the IdEA group [56]. It consists of a PDC with 5 m diameter, with the focus located at 2.5 m distant from the mirrors. It was designed to assemble a maximum of 24 coated silver glass mirrors in individual segments (each of 0.76 m^2 area comprising in a complete assemble a total area of 18.24 m^2). The setup has reduced fabrication, maintenance and operation costs (Appendix A). Figure 3.1 presents the schematic drawing and a picture example of the device configured with 3 mirrors.

The system is equipped with a polar-equatorial axis solar tracker, capable to ensure a constant alignment with the sun throughout the daylight. The mirrors are mounted in a metal support driven by a stepper motor coupled with a gearmotor resulting in an angular speed of 0.004167°/s [163]. The rotation main axis is parallel to the axis of Earth. The solar declination angle is compensated via manual adjustments. Depending of the configuration of the experiment, either one single or a joint of three sections of mirrors can be mounted.

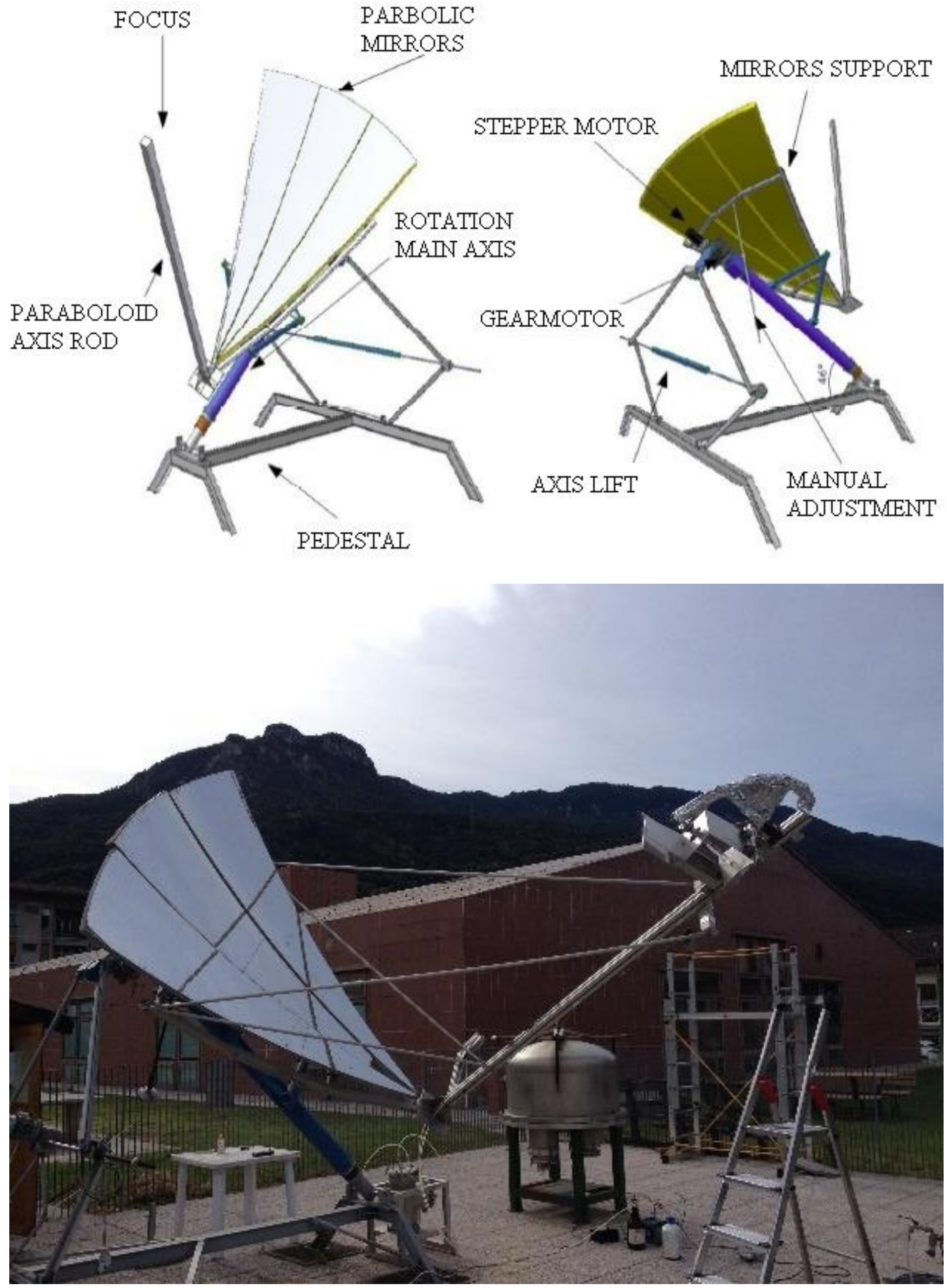

Figure 3.1: Schematic drawing (up) and an image of assembled solar concentrator apparatus (down) for experiments used in this work.

Each mirror module has a 0.8 mm thick silver coated glass (FAST GLASS®). They are mechanically reinforced with a fiberglass layer, a PVC panel and a second fiberglass layer in order to improve stiffness to the whole structure and to sustain the curvature over time.

The mirrors optical reflectance property feature reflectivity higher than 90% on the measured range between 450 and 1200 nm and a strong decrease for wavelengths lower than 400 nm, evidencing a strong decrease in the reflection properties for the near-UV light range. The reflectance curve is shown on figure 3.2 and the measurements were done with an UV-Visible-NIR spectrophotometer (Varian Cary 5000).

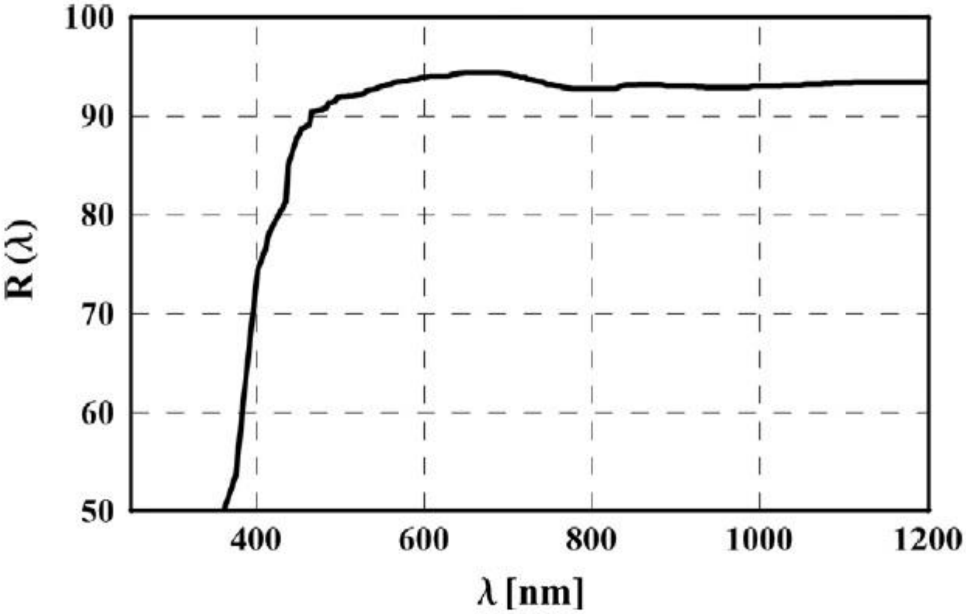

Figure 3.2: Reflectance as function of wavelength of the silver coated mirror employed on this work [57].

Simulation and measurement studies evaluated the power profile of the concentrated solar spot promoted by the apparatus. Figure 3.3 presents the spot characterization from a single mirror module, the shape of the spot is close to a Gaussian distribution with a peak flux of 70 W/cm^2, taking into account the central area of the peak, it corresponds to concentration factor of nearly 870x in a circular spot with a diameter of approximately 5.8 cm.

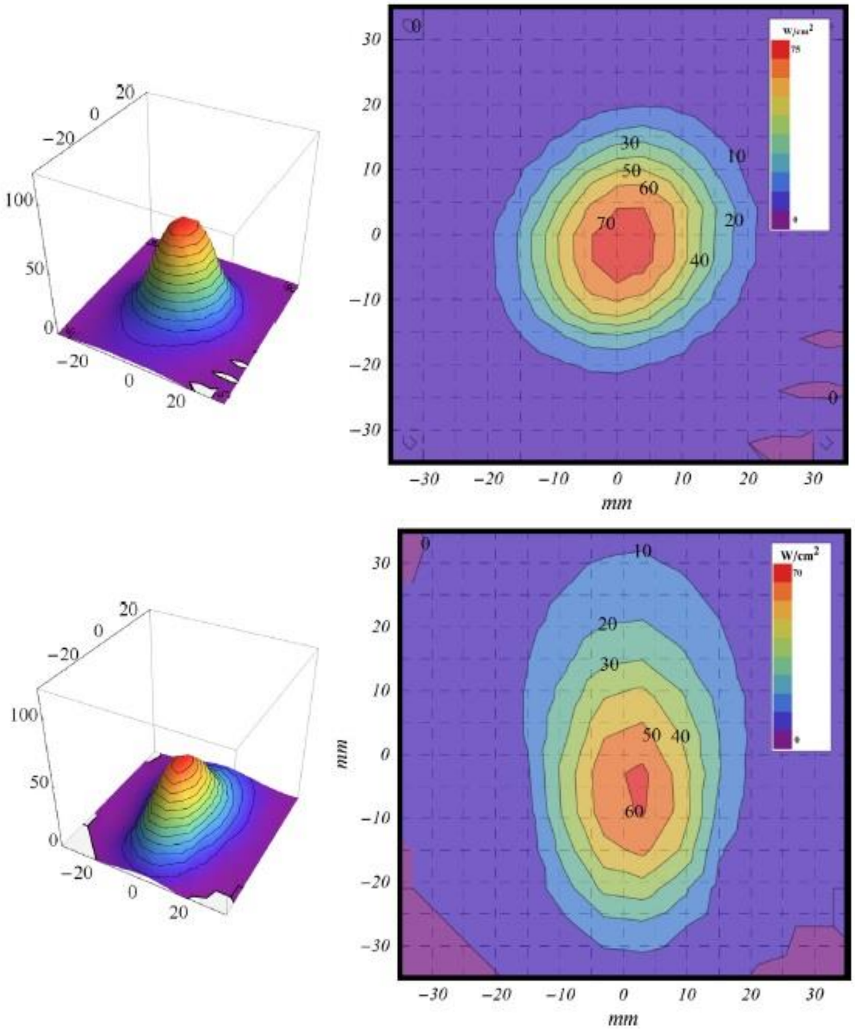

Figure 3.3: simulated (up) and measured (down) solar spots of the solar concentrator used in this work [57].

The solar direct and reflected spectra on the PDC solar apparatus was acquired in a sunny clear day condition for the near UV-Visible range. The spectra presented in figure 3.4 are related to the direct pointing of a portable spectrophotometer (Ocean Optics USB4000, software Spectra Suite) towards the sun and pointing against one module of the mirror reflecting the solar light. The spectra were not corrected for the detection system spectra responsivity. As can be observed the mirror reproduces very well the solar spectrum without any distortion.

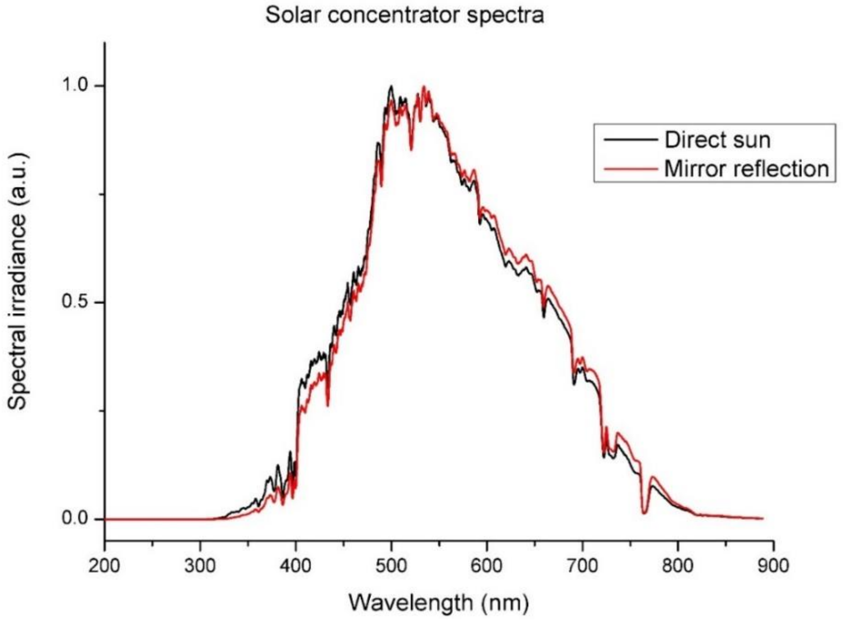

Figure 3.4: Solar spectra measured on the PDC solar concentrator: direct sun light incidence and radiation reflected by the mirror.

For the photocatalysis experiments in the solar concentrator, the volume of the circulated water was 2 L, the liquid was circulated from a reservoir in the ground to the solar spot, where was positioned a quartz glass tube of approximately 150 ml volume used as the reactor for the solar concentrator. The quartz tube was sealed at one end and closed by a three-port lid on the other end. One port hosted a thermocouple for temperature monitoring, and the other two ports are the inlet and outlet for the liquid circulation. A pumping system was used to promote the circulation of the solution provided by a diaphragm dosing pump (Hanna instruments, model BL5 with volume flow rate of 5 L/h at 7 bar of pressure), the tubing circuit was assembled with polyamide pipes with 8 mm external and 6 mm internal diameters. For cooling purposes, the piping system was passed thru a water chiller reservoir with a volume of 20 L that kept the temperatures constant during all the experiments. Figure 3.5 shows the schematic drawings of the quartz glass system, inlet, outlet and thermocouple for temperature monitoring and an image of the assembled glass quartz tube that receive the reflected concentrated solar light.

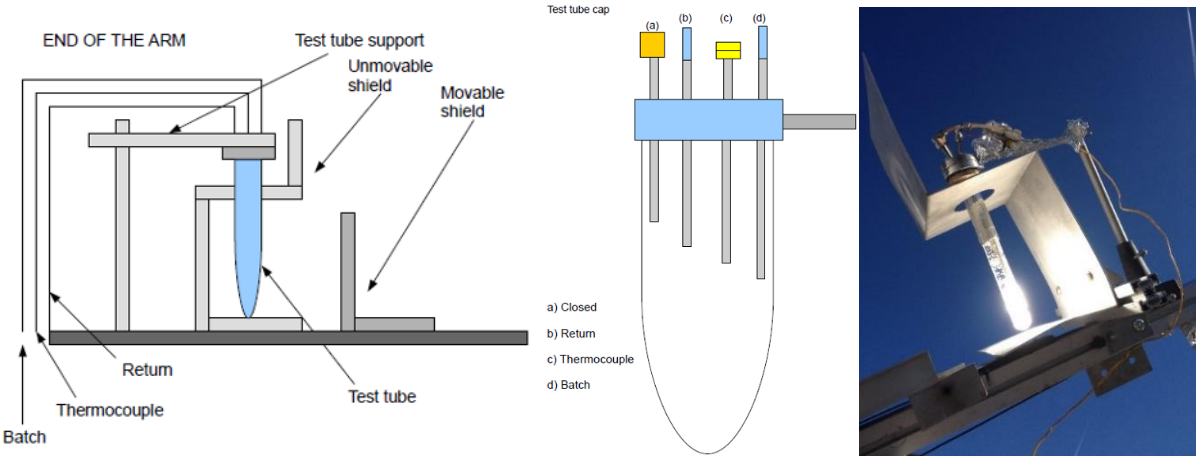

Figure 3.5: schematic drawings of the quartz glass for the concentrated solar light receiver (left and center) [164] and a picture of the quartz glass lid use to expose the wastewaters to the concentrated sunlight (right).

During all the experimental procedures presented in the following chapters the solar intensity was constantly measured using a pyrheliometer (Kipp & Zonnen CHP1) with an aperture angle of 5° mounted on the axis rod positioned towards the parallel direction of the sunlight. The solar concentration scheme is represented by figure 3.6. The mirror pointed towards the sun reflects the light to a spot where the quartz lid is installed. The glass lid can have inside a catalyst and is under constant circulation of the liquid object of study.

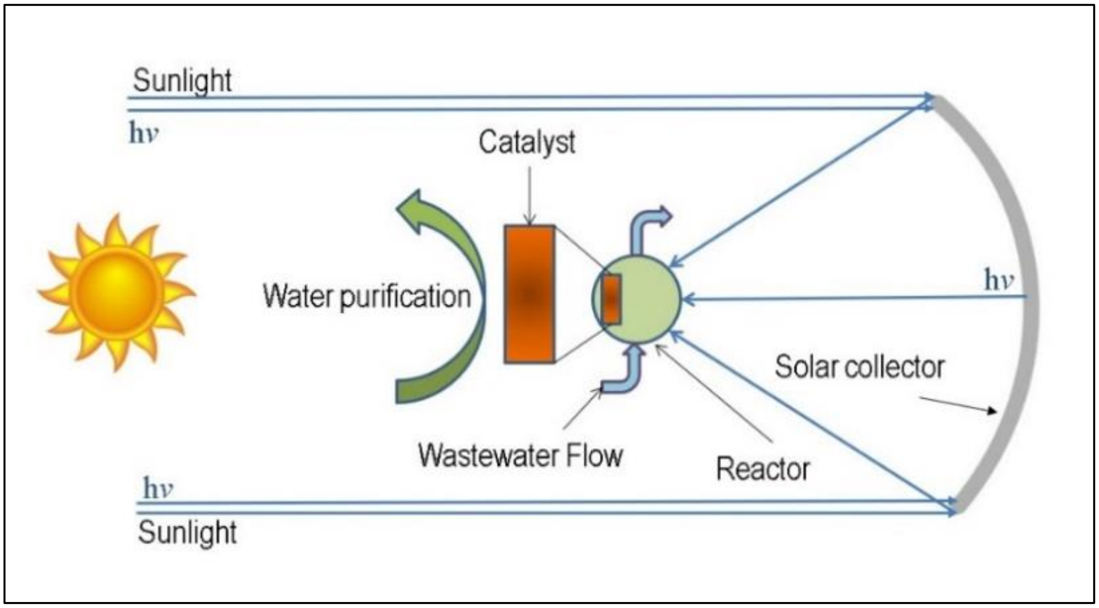

Figure 3.6: Concentration scheme

3.1.2 Thin film coatings fabrication - Pulsed laser deposition (PLD)

Pulsed laser deposition (PLD) is a thin film fabrication technique belonging to the physical vapor deposition field, in a close observation reveals a complex nature that results in coating materials with particular properties. The process comprising PLD is based on focusing a laser beam towards an evacuated chamber with a target inside. Under the emission of a high energy density, the material from the target hit by the laser beam is ablated, evolving into a plasma plume, which expands along the normal direction of the target surface. Figure 3.7 presents the PLD working scheme, as a general rule, the laser beam is delivered inside the chamber in an angle of 45° and thus the substrate is placed in a position in front of the target. Other important characteristics of the PLD process are the possibility to control the temperature of the substrate as well as the condition to apply movement to the target, in order to avoid being hit repeatedly in the same position.

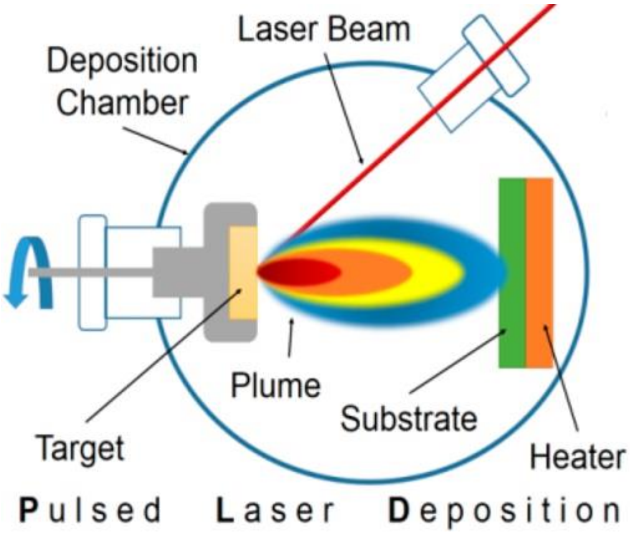

Figure 3.7: PLD working scheme

The PLD technique is reported employing different types of lasers such as Nd:YAG, excimer and Ti:Sapphire for instance, emitting particular wavelengths and under distinct conditions for pulse time duration (from nano to femtoseconds), revealing then diverse phenomena [165–167].

Regarding the phenomena involving the PLD process, the energy hitting the target material on the deposition increases the electron energy and as consequence the energy is transferred to the target lattice through electron-phonon interaction [168].

The energy provided by the laser is high enough to submit the outer layers of the target material to reach temperatures above the melting point with heating rates that can reach values of 10^{12} K/s [169]. In this condition of heating above the melting point of the material, can be evidenced the emergence of a metastable liquid [170]. If the temperature of the metastable liquid reaches value close to the thermodynamic critical point (Tc), thermal density fluctuations promote homogeneous nucleation in a remarkably fast kinetics. Being the energy fluence high enough, the surface of the target breaks into a condition with the combined presence of liquid droplets and vapor phase and this is named as phase explosion, also predicted in target temperatures in the range of 0.9 Tc [171].

Sequent to the phase explosion, the liquid droplets and the vapor phase of the material are ejected from the target surface and adiabatically expand forming a plasma plume due to the ionization by the high temperature and the laser irradiation. Given the conditions, if in vacuum, the plume takes a free shape from the adiabatic expansion and alternatively, if the expansion is under a specific chosen gas and pressure, the plume expansion can be slowed depending on the possible collisions, braking into components or scattering orders [172].

The gas and pressures employed on the deposition chamber play a relevant role on the final film material properties. They perform the activities of cooling and condensing as well as the gas can act as a compressive strain to the deposited film. Also, influencing on the chemistry of the film depends on the reactive condition of the gas, such as metallic film being ablated in a rich oxygen atmosphere, resulting in a metal oxide over the substrate surface. All the materials synthesized by PLD presented in the next chapters had a metal target, either in powder or solid forms and were ablated in oxygen (O_2) atmosphere with the aim to generate the according metal oxides to be employed as photocatalysts materials.

From the flight regarding the laser heating the target and the plume formation, the next step is regarding the film formation. The growth of the film depends on the parameters adjusted to promote the process, normally the adjustments are substrate temperature, background gas type, and pressure. A strong advantage is that the phase explosion can generate directly nanoclusters from the target surface to be direct to the substrate. Also, the flexibility to propose mixtures of materials in terms of composites in the target can lead to novelties and advances in technological materials with specific tuned properties. Moreover, the geometrical film condition in terms of porous and compact can be chosen by determining the pressure in the chamber. In the other hand, thickness is dependable on the number of pulses emitted by laser, distance from target to substrate, gas pressure, laser energy fluence and spot area. Normally, the growth rate has the range between 0.001 to 1 Å per pulse. Under these controlled conditions, uniform films can be produced adding movements of the target for a uniform erosion.

In this work, a KrF nanosecond pulsed laser (lambda Physik, model LPX 220i) was used as the tool for the fabrication of photocatalysts from chapters 4 to 7, the main parameters of the laser are presented on table 3.1.

Table 3.1: Main parameters of the laser lambda Physik (LPX 220i) employed in this work.

Parameter	**Value**
Wavelength	248 nm
CDRH Class	IV
Pulse Energy (at low repetition rate of 5 Hz)	450 mJ
Max Repetition Rate	200 Hz
Average Power (at max repetition rate)	80 W
Nominal Pulse Duration (FWHM)	20 ns
Pulse-to-Pulse Stability (based on 90 % of all pulses)	± 3%
Beam Dimension (FWHM)	5 – 12 x 23 mm^2
Beam Divergence (FWHM)	1 x 3 mrad

The energy density or laser fluence is measured in terms of J/cm^2 and can be modulated by means of varying the voltage provided by the laser power supply resulting in the emitted energy and the distance of the focal length to the target.

Figure 3.8 presents the schematic 3D view of the system, comprising the beam delivery system inside the chamber, the movement apparatus and the fixing both of the target and the substrate.

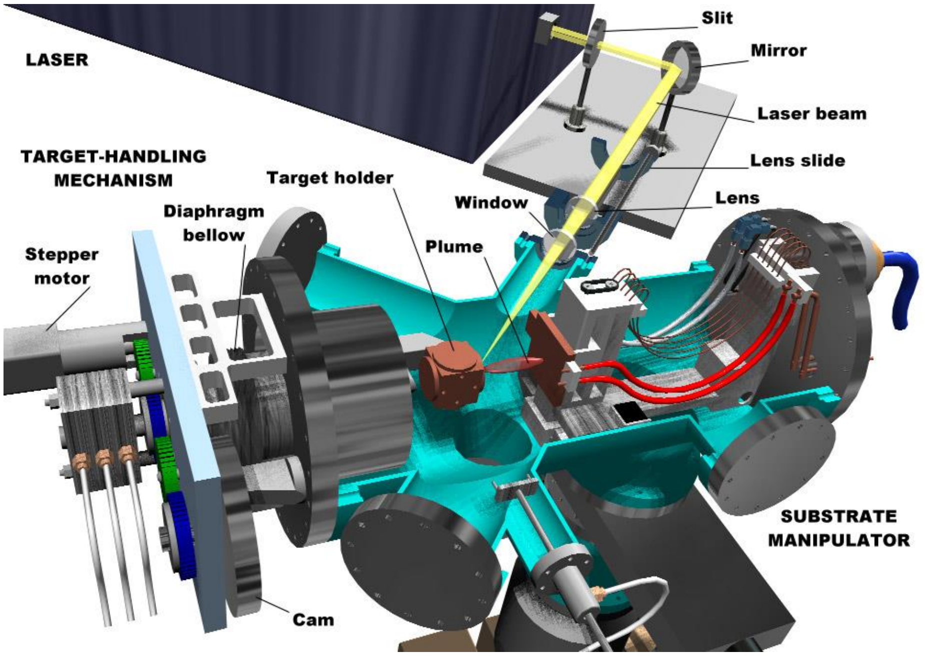

Figure 3.8: schematic 3D view of the laser deposition apparatus employed in this work [173].

Figure 3.9 presents the scheme for the vacuum system of the chamber. It is composed by a mechanic diaphragm pump as auxiliary to a turbomolecular pump, with the capacity to achieve values of vacuum up to 10^{-6} mbar. The apparatus is provided by a safety system using a by-pass valve, pressure sensors and a gate valve.

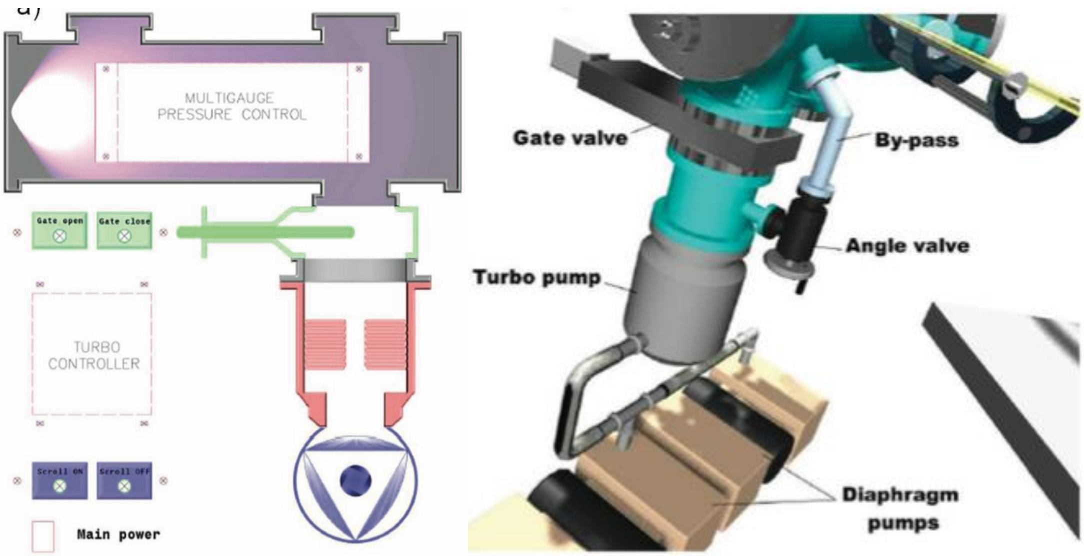

Figure 3.9: schematic view of the evacuation system (left) and the schematic 3D view of the existing vacuum mechanism (right) [173].

A key challenge to PLD is to scale in industrial process and commercial exploitation of the technique. Installations available already can produce films in a substrate with up to 300 mm diameter or run a continuous cover up to 10 m^2 tape [174]. Designing innovative larger areas of thin film coatings by PLD seems to be a matter of time, running in parallel the comprehension of the physics of film formation and the scaling-up of mechanical systems and vacuum technology for the laser fabrication.

3.2 Characterization techniques

This section presents the characterization techniques used to reveal the properties of the developed materials, the characterizations were performed in terms of scanning electron microscopy, X-Ray diffraction, Micro-Raman spectrometry and UV-Vis-NIR spectrophotometry, they are detailed in the next items.

3.2.1 Scanning Electron Microscopy (SEM)

The scanning electron microscope (SEM) is an instrument that aims to investigate the microstructural characteristics of solid specimens like morphology, surface topography and composition in the micrometer and sub micrometer range. It can reach a resolution of about 5-10 Å under optimal conditions, higher than that achievable with an optical microscope, which is limited by the wavelength of visible light at 0.1 - 0.2 mm.

The SEM technique is based on the emission of an electron beam by thermoionic effect (Tungsten cathode and Lanthanum Hexaboride) or by field emission, which is accelerated through a series of focusing lenses and apertures arrangement and impinges the sample. This arrangement has the purpose of decreasing the beam spot diameter to the range of 30 Å and the current to a few picoamperes. The final lens assembly allows the deflection movement of the beam in the directions X and Y in order to allow the rastering over a rectangular surface of the sample. The interaction between the constituent atoms and incident electrons produces a variety of signals related to reflected electrons, secondary electrons, *Auger* electrons, transmitted electrons, cathodoluminescence and X-Rays. Essentially, three signals are acquired: secondary electrons (SE), back-scattered electrons (BSE) and X-Rays for the cases a detector is available.

The SE electrons are generated from inelastic collision between the electrons in the beam and the atomic electrons of the sample. The beam can transfer to the atomic electrons an amount of energy sufficient to be ejected from the atoms. The energy is between 5 and 10 eV and for this reason only the electrons produced near the surface can escape from the samples. The SE provides information on the material topography and the main cause of the image contrast observed is the existing angle between the incident beam and the surface [175].

Back-scattered electrons (BSEs) are produced by the collision of the electrons from the beam with the atom nucleus of the specimen. The scattering phenomena is an elastic collision and the electrons exit from the surface with a high energy. BSE contains information on chemical composition of the elements in the specimen. The number of BSEs increase with the atomic number Z of the atoms, so a material with a high Z appears brighter on the image than a material having a lower Z [175].

On SEMs with X-Rays detection devices installed, they arise from two different mechanisms: *Bremsstrahlung* and fluorescence. In the first case the incident electrons are deaccelerated by the electric field of the atoms emitting X-rays. This signal features a continuous spectrum and therefore are not useful for the analysis purpose. In the other hand, in the fluorescence mechanism an electron of the beam is inelastically scattered by an inner-shell electron in the specimen. The latter acquires a sufficient energy to escape from the atom leaving a vacancy in its inner shell. The electrons than fill that vacancy emit an X-ray and the energy is characteristic for each element and each atomic transition of the element. Hence, an energy-dispersive spectrometer (EDS) in the SEM chamber measures the number and the energy of the emitted X-rays. The EDS spectrum contains information on the elemental composition of the sample and on the concentration of each element in the specimen. The schematic diagram of a SEM is showed in figure 3.10.

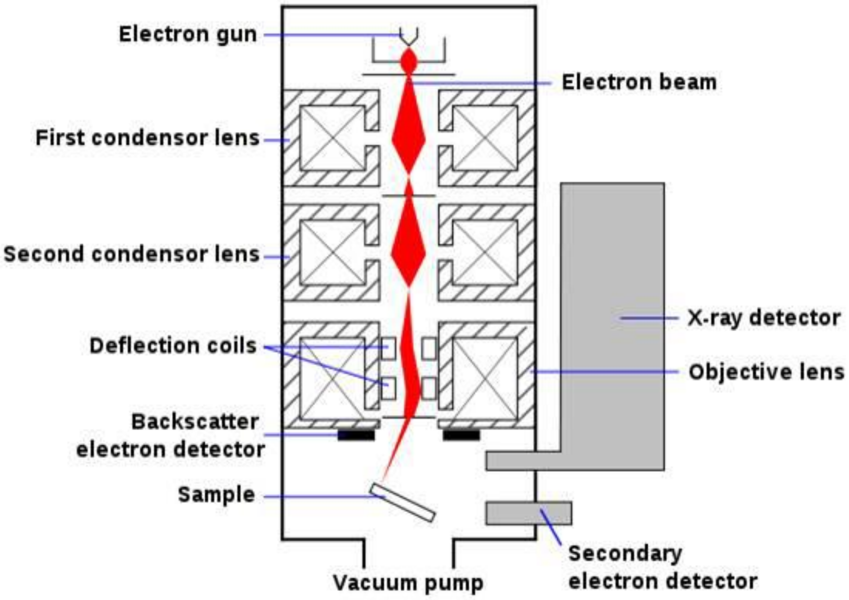

Figure 3.10: Schematic diagram of a SEM [176].

In this work a scanning electron microscope (SEM-FEG, JSM 7001F, JEOL) with 20 keV electron beam energy equipped with energy dispersive spectroscopy analysis (EDS, INCA PentaFET-x3) was used for examining the particles sizes and surface morphologies of all the samples prepared. They were deposited over silicon and placed in a support fixed with carbon tape.

3.2.2 X-Ray diffraction (XRD)

The X-ray diffraction (XRD) is a bulk characterization technique used to measure the average spacing between different crystalline planes, determine the orientation of a single crystal or grain, study the crystal structure of an unknown material and measure the size, shape and internal stress of small crystalline regions. Since the wavelength of X-Rays is in the range of the distance between the atoms in a crystal lattice, a special interference phenomenon of diffraction can provide information about the distance between the atoms. X-Ray wavelengths vary from about 10 nm to 0.001 nm.

The X-Ray process consists in a beam hitting an atom, the electrons absorb the energy and oscillate around their mean positions. Since the energy is not enough for the electrons to be ejected from the atom, the electrons emit the energy in the form of X-Rays. This process is called as elastic scattering. A generic crystal is composed by several ordered planes of atoms, and for this reason huge number of X-Rays are emitted due to the interaction of each atom with the incoming X-Ray beam. An interference pattern can be produced by the superposition of the emitted waves. This pattern depends on the wavelength and on the incident angle of the incoming beam. A positive or constructive interference occurs when the path difference between the two incident rays is equal to an integer multiple of the wavelength. This relation is called *Bragg's* law and is represented on figure 3.11.

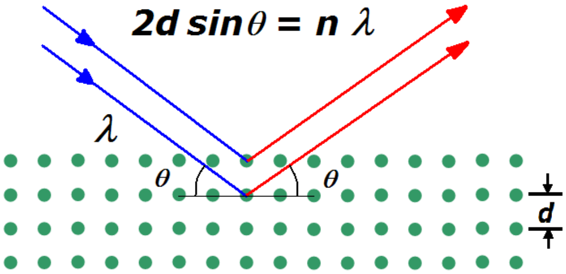

Figure 3.11: schematic diagram of Bragg's law [177].

A typical XRD pattern is obtained by varying the angle of incidence of the X-Ray beam and measuring the intensity of the emitted radiation. A number of peaks are observed in the pattern corresponding to diffraction from different atomic planes of the material. By identifying the peaks in the diffraction pattern and comparing with the standard peaks for different crystalline materials it is possible to identify the phase of the material under study. A typical X-Ray diffractometer has three basic components: X-Rays source, a sample stage and a detector as shown in figure 3.12. The angle between the plane of the sample and the incident X-Ray beam is the Bragg angle and identified as θ. On the other hand, the angle between the detector and the projection of the source beam is identified as 2θ. The diffractometer geometry is therefore called as θ-2θ, or Bragg-Brentano geometry. The X-Ray source is usually fixed, and the specimen is moved by means of θº/min while the detector measures the output radiation at 2θº/min with respect to the source path.

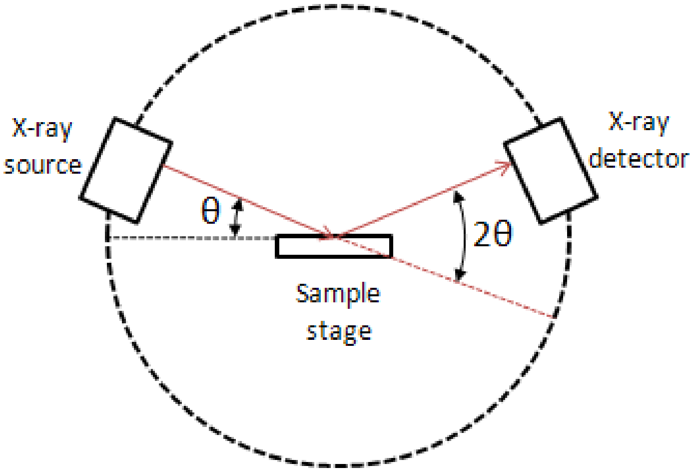

Figure 3.12: Block diagram of a typical X-Ray diffractometer [178].

Structural characterization in small angle and wide-angle was performed using a XRD equipment (model X'Pert PRO, Panalytical) with Cu Kα radiation (λ = 1.5414 Å) in Bragg-Brentano (θ–2θ) configuration with a step size of 0.05 ° and a scan rate of 1 °/min to evaluate the crystallinity of the bulk materials.

3.2.3 Micro-Raman spectrometry

This spectroscopy technique deals with elastic and inelastic interaction. The first indicates that an incident photon is absorbed and emitted without any loss of kinetics energy. This process is nominated as Rayleigh scattering. The second means that the incident absorbed photon and the one emitted by the atom/molecule after the transition present different frequencies. This is due to the atom/molecule does not return in the same stable state after the emission. If the final vibrational state of the molecule is more energetic than the initial state, the inelastically scattered photon will possess a lower frequency for the total energy of the system to remain balanced. This shift in frequency is designated as a Stokes shift. On the contrary, if the final vibrational state is less energetic than the initial state, then the inelastically scattered photon will possess a higher frequency, which is designated as an anti-Stokes shift. A schematic diagram presenting the features of Rayleigh and Stokes scattering is present on figure 3.13.

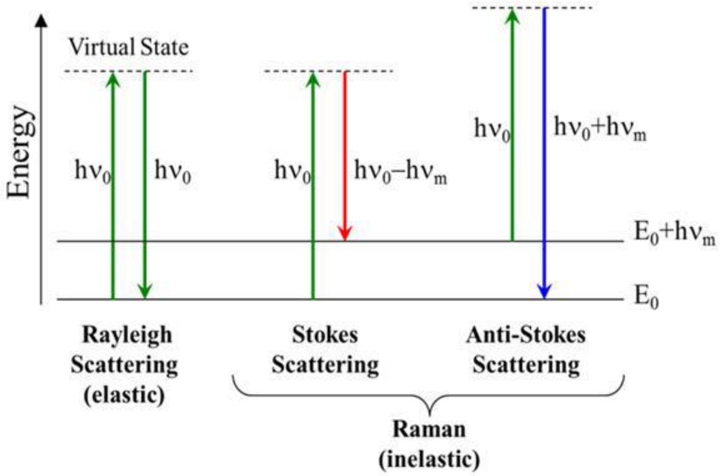

Figure 3.13: A schematic diagram explaining the Rayleigh and Raman (Stokes) scattering [179].

The Raman technique is used to identify the chemical bonding of materials and provides information about the vibrational structures of the specimen, the crystallographic orientation of a sample along with other applications in solid state physics.

A typical Raman spectroscopy apparatus consists of a monochromatic light (laser) illumination system, focusing lenses, optical filter, detectors and computer control software. The laser beam is irradiated on the sample and the scattered photons are filtered by a notch filter which blocks the elastically scattered photons and transmit the low intensity Raman scattered photons (around 0.001% of total intensity). The Raman scattered photons are dispersed by the grating followed by amplification and then detected by a CCD detector. To acquire a large spectrum of the scattered light the grating alignment is varied. The output signal is processed using a specific software to display the Raman spectra for the given specimen. Figure 3.14 shows a schematic representation of Raman spectroscopy apparatus.

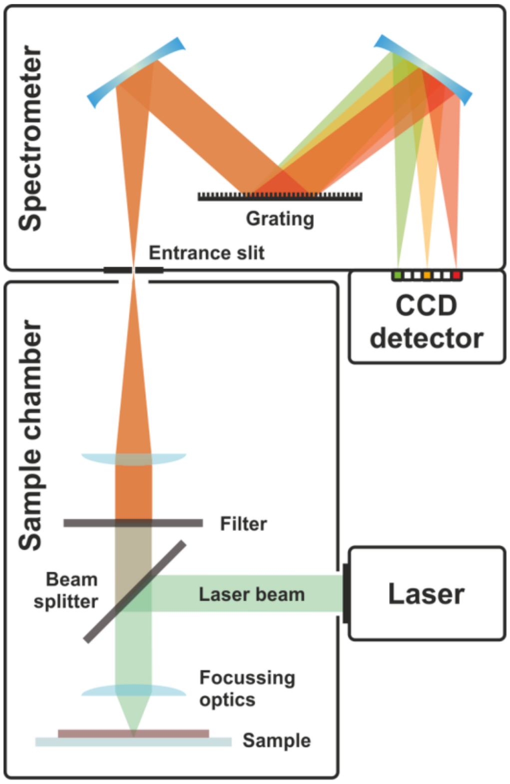

Figure 3.14: Raman spectroscopy apparatus schematic diagram [180].

In this work, Micro-Raman spectroscopy was performed using a LabRAM Aramis Jobin-Yvon Horiba μ-Raman system equipped with a He-Ne laser source (632 nm) for the analysis of the phases of surface or just below via inelastic scattering of surface radiation.

3.2.4 UV-Vis-NIR spectrophotometry

The Ultraviolet-Visible-Near Infrared spectroscopy is a non-destructive analysis technique employed to study the optical properties of materials based on the electronic transitions induced by the absorption of incident photons. The absorption spectroscopy is normally acquired in the ranges of UV (10 - 200 nm), near UV (200 - 380 nm), visible light (380 - 780 nm) and eventually in near the IR spectrum (780 - 3300 nm).

The absorption is possible only if the photons have the required energy for electrons to have transition from a lower energy level to a higher energy level. The absorption bands are very narrow and characteristic for each molecule. However, a real absorption spectrum shows broadened peaks, because of the superposition of vibrational and rotational energy levels of the molecule on the electronic energy level.

In case of molecules, the total energy is given by the sum of three contributions:

$$E_{total} = E_{electronic} + E_{vibrational} + E_{rotational}$$

The transition between electronic states is caused by the absorption of visible-UV light (10 - 700 nm). The transition between the vibrational states is due to the absorption of infrared radiation (700 nm - 1 mm) and the rotational states are typically promoted by microwave radiation (1mm-1m).

When light passes through a sample, the amount of light absorbed is the difference between the incident radiation (I_0) and the transmitted radiation (I). The amount of light absorbed is expressed as either transmittance or absorbance. Transmittance usually is given in terms of a fraction of 1 or as percentage and is defined as follows:

$$T = I/I_0$$

Or

$$\%T = I/I_0 * 100 \qquad (1)$$

Absorbance is defined as the negative of log T and is written as,

$$A = -\log T$$

Or

$$A = \log[I_0/I] \qquad (2)$$

The *Beer-Lambert* law states that the amount of light absorbed by the solution is directly proportional to the molar concentration of the absorbing species in the solution and the optical length of the solution:

$$I = I_0\, e^{-\varepsilon l C} \qquad (3)$$

where ε is the molar absorption coefficient, l the optical length of the sample and C the concentration. Substituting equation (3) in the definition of the absorbance on equation (2), the Beer-Lambert law becomes,

$$A = \varepsilon l C \qquad (4)$$

Knowing the thickness and the molar absorption coefficient of the sample under study, it is possible to obtain the concentration of the solute in the solution.

A typical UV-VIS-NIR spectrophotometer consists of a light source, a monochromator, a beam splitter, two holders (one for the sample and one for the reference), and two photodiode detectors as shown on figure 3.15. Light from a source is focused onto a monochromator which separates the light emitted by the source into its component wavelengths. To achieve a constant light intensity over a wide spectrum, two sources are used: a deuterium arc lamp (for the UV region) and a tungsten-halogen lamp (for the visible range). The obtained monochromatic beam is then split into two beams by a beam splitter: this way the light from the source reaches both the sample and the reference. The light at the end of the two paths is collected by the two photodiode detectors and the ratio of the two beams is displayed.

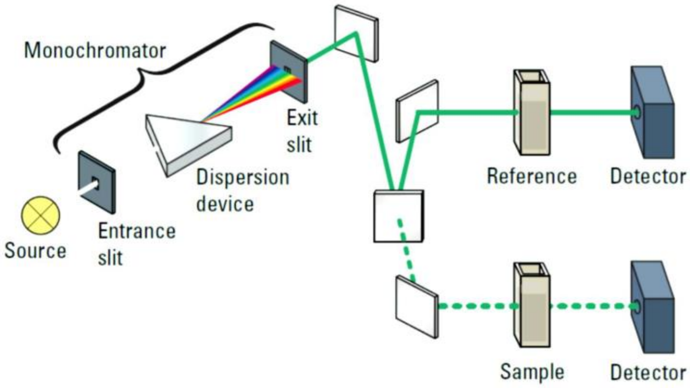

Figure 3.15: schematic representation of a UV-VIS-NIR spectrophotometer [181].

Spectra were obtained with a Varian Cary 5000 UV-VIS-NIR absorption spectrophotometer with readings between 200 and 800 nm, which is the wavelength range where electronic transitions due to absorption occur.

In the photocatalytic studies presented in chapters 4 and 5 where methylene blue (MB) dye was employed as the model pollutant, the UV-Vis spectra was analyzed considering the absorption on the characteristic peak of this dye at 664 nm at different experiment times as it is exemplified in the graphic from figure 3.16.

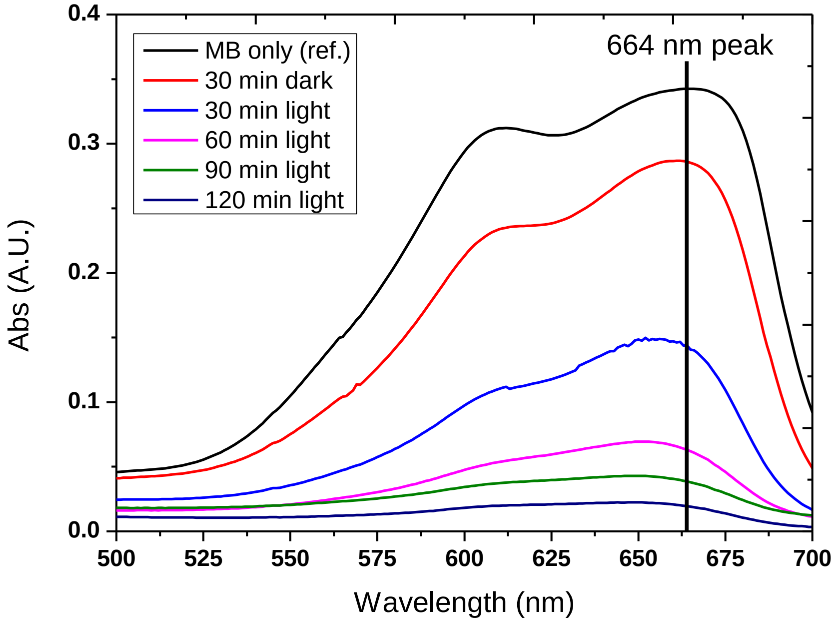

Figure 3.16: UV-Vis absorption example graphic for methylene blue dye.

The relative degradation values were calculated based on the quotient relation from equation (5), between the absorption of the sample at a determined time and the reference initial model solution, where *C0* and *C* are the initial and final concentrations of the dye solution respectively:

$$\text{Relative degradation} = \frac{C}{C0} \qquad (5)$$

The relative degradation values were then plotted as a function of time. The kinetic rate constant (K) for each experimental condition was calculated by plotting an interpolation curve using a pseudo-first order kinetic model proposed by Langmuir–Hinshelwood [182]. The choice of using this model was due to one of the reactants is a catalyst and therefore its concentration is in theory considered constant, being the concentration of MB in the solution the single variable for the experiments. The model is described by equation (6), where K corresponds to the slope of the interpolation curve. The K value results in a time related information (min^{-1}) and thus the error bars are based on the R^2 value resulting from the fitting of the curve.

$$C = C0e^{-Kt} \qquad (6)$$

Figure 3.17 presents an example of the relative degradation values calculated from the observed absorption data from figure 3.16. The curve fitting equation is described, being the K constant the value of 0.018 min^{-1} and the R^2 value of 0.9838.

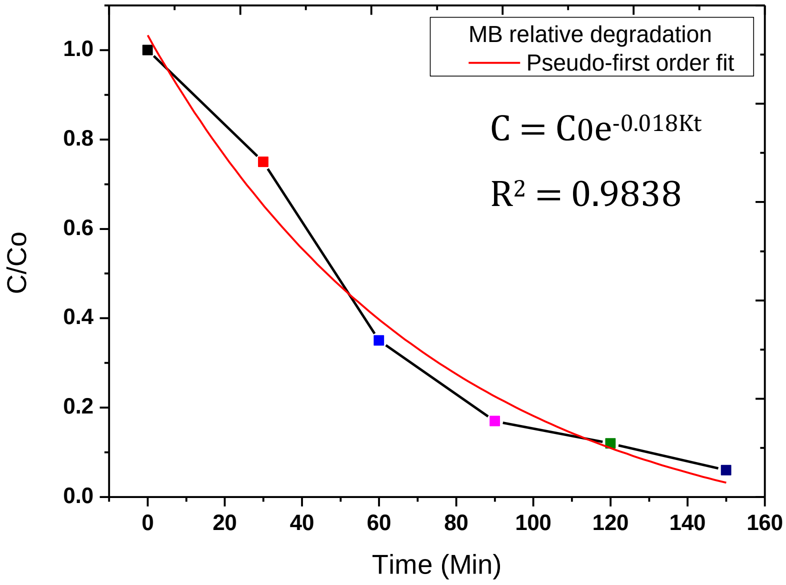

Figure 3.17: Relative degradation of MB dye example showing the pseudo-first order fitting curve.

Chapter 4: Pulsed laser deposition of nanostructured tungsten oxide films: A catalyst for water remediation with concentrated sunlight

Preview: The increasing interest for addressing photocatalyst materials towards an effective application with sunlight is an important topic in materials science. This chapter presents a novel investigation of tungsten trioxide (WO_3) coatings fabricated by pulsed laser deposition (PLD) with the aim of providing a nanostructured photocatalyst capable to operate with concentrated sunlight and exhibiting good stability in mild acidic environment. As the main author of this investigation, my contribution includes the synthesis of the WO_3 films, performing the solar photocatalytic measurements along with all the material characterizations, analyzing the data of the results obtained. Finally, the drafting of the manuscript and submission for publication.

The content of this chapter was adapted from:
Fendrich, M.; Popat, Y.; Orlandi, M.; Quaranta, A.; Miotello, A.. Mater. Sci. Semicond. Process. **2020**, 119, 105237; https://doi.org/10.1016/j.mssp.2020.105237

4.1 Introduction

The population growth and the consequent increase of industrial activities have been directly affecting the environmental behavior [70,118]. Water quality is a matter of important concern due to the decrease in the number of available potable water sources [162]. Precautions and strong environmental actions such as forests restructuring, and conservation have been attempting to sustain weather equilibrium and water quality [23,183,184]. On the other hand, contaminated water residuals from industrial activities require constant development of remediation methods as far as new chemical processes are employed [185,186]. The most common wastewater treatments are based upon a combination of mechanical, biological, physical and chemical processes such as filtration and flocculation.

In terms of contaminated water remediation, during the last years, an industrial research field was based on the development of advanced oxidation processes (AOP) for the removal of organic recalcitrant contaminants and hence persistent agents present in water [187]. Solutions in terms of AOPs have received special attention to applications using heterogeneous photocatalysis which are capable of generating oxidizing radicals by light exposure [10,86]. Heterogeneous routes are interesting solutions due to the enhanced possibility of controlling reaction rates using a supported catalyst, which can be inserted or removed immediately during a reaction, thereby demonstrating advantages when compared to homogeneous routes, which require post processing treatments for the catalyst removal [7].

The possibility to use semiconductor materials as catalysts has been investigated with special attention. For example, TiO_2 as a catalyst material [93,94] in anatase form, presents high photoactivity in presence of UV light in the wavelength range between 300 to 388 nm [103]. Nevertheless, the requirement regarding the use of UV light, such as the employment of UV lamps as artificial light sources to activate the photocatalytic effect is reported as a disadvantage, turning the decontamination process economically inefficient [84]. In this framework engineering configurations for solar mirrors were also developed in terms of concentrating and non-concentrating solar systems [25]. Also, remarkable efforts to explore different photocatalysts apart from TiO_2 using solar light as the activation source have been reported with other materials such as Fe_2O_3, CdS, GaP, Co_3O_4, ZnS [24,101,104,106].

Semiconductors with promising possibilities to be employed as photocatalysts capable of being activated by sunlight and explored in a variety of applications in the literature are tungsten oxide-based materials [188–192]. They are activated in the visible and near-UV light range, since the reported bandgap of tungsten oxide (WO_3) is 2.6 eV, meaning photoactivation at 472 nm wavelength. Other important properties are the isoelectric point (IEP) between 0.4 and 1 and point of the zero charge (pH_{PZC}) of 0.43. Pourbaix diagrams presented for tungsten oxides demonstrate a stable catalytic activity under acidic pH conditions, which is a general rule in industrial processes [193].

Important investigations published on WO_3 based structures as photocatalysts for water remediation are reported in literature [107,194–199]. Among the different fabrication methods, pulsed laser deposition (PLD) can lead to novelties, with respect to chemical synthesis procedures [200], in terms of material crystallinity, larger film area, thickness control and morphology along with the possibility of obtaining 3D hierarchical nanostructures [201–206] by varying the parameters such as the laser fluence and ambient gas in deposition chambers. The combined innovation of producing photocatalysts in the form of coatings with controlled properties and its use with a natural visible free source of photons provides an opportunity to explore the scalability of AOPs in water remediation with solar irradiation, under a reasonable economic investment. Moreover, the wastewater purification technologies that can avoid the increasing use of chemical supplies is advantageous to address water purification of emerging contaminants in an eco-friendly direction.

This chapter proposes the fabrication by PLD of a monoclinic nanostructured "flower-shape like" tungsten oxide (WO_3) coating operating under near UV-visible light, stable in acidic environments and capable of working with solar concentration. The film deposition was performed in oxygen atmosphere from a compressed powder target. The deposited samples were thermally annealed to induce the growth of the monoclinic WO_3 phase. The m-WO_3 coatings were characterized and tested as photocatalysts for degradation of the Methylene Blue (MB) dye as a model pollutant under photo-Fenton-like conditions. The experiments were divided in 2 steps, first in labscale (30 ml of MB solution volume) with artificial visible light lamps to understand the effectiveness of the produced coating and, in the second step, the MB solution volume was scaled up to 2 L and the photocatalytic performance under concentrated sunlight evaluated.

4.2 Materials and methods

4.2.1 Synthesis

A powder mixture of 1.5 grams of metallic tungsten (W, Alfa Aesar average particle size, 1-5 micron, 99.9% purity) and 2.5 grams of boric acid (H_3BO_3 Sigma Aldrich, >99.5%) was prepared and compressed in the form of a disc to be used as a target for the PLD fabrication of the tungsten oxide coatings. Boric acid was used as a dispersing agent to obtain mechanically stable compressed powders targets. The PLD deposition was performed by the apparatus described previously in chapter 3. Pulse duration of 25 ns and repetition rate of 20 Hz was chosen for deposition. The fluence of the laser was always maintained at 4.5 J/cm^2 for the target ablation. The PLD chamber was evacuated up to a base pressure of 1 x 10^{-6} mbar prior to all the depositions. The fabrication of the coatings was carried out in an oxygen (O_2) atmosphere at pressure of 1.5 x 10^{-2} mbar. The target to substrate distance was fixed at 4.5cm with the substrate positioned parallel to the target and the number of pulses used were 10.000. The coatings were deposited at room temperature on glass slides measuring 2.5 × 7.5 cm^2 and on Si plates, the weight of the catalyst reached 4 mg on each as deposited glass slide (AD) measured in a precision scale with resolution of 10^{-2} mg. Thermal annealing of the deposited coating was carried out in air at the temperatures of 200, 400 and 600ºC for 8 h with a heating rate of 5 ºC/min (AN200, AN400 and AN600, respectively) to investigate the growth mechanism of m-WO_3.

4.2.2 Characterization

Based on the characterization techniques described in chapter 3, SEM was used for examining the surface morphologies and the cross section of all the samples prepared by PLD. Structural characterization was performed using X-Ray Diffractometry to evaluate the crystallinity of the bulk material. Micro-Raman spectroscopy was performed for the analysis of the surface or just below via inelastic scattering of surface radiation. Lastly, absorption spectra were obtained with UV-VIS-NIR absorption spectrophotometry.

4.3 Labscale photocatalytic measurements

The photocatalytic activity of the synthesized samples was evaluated in labscale by studying the degradation of 30 ml (10 ppm) model MB dye solutions in neutral condition (pH 7) at: (1) in presence of light only, (2) with added H_2O_2 and light, (3) with WO_3 catalyst and light, and (4) combination of all three (H_2O_2, light and WO_3 catalyst). When employed, 1ml of H_2O_2 (1M), as an oxidizing agent, in an aqueous solution, was used for degradation by photo-Fenton-like reaction. The catalyst coatings prepared on glass slides were dipped in the above prepared MB dye solution and kept in the dark for 30 mins at constant stirring with *Reynolds* number (Re) of 2000 and 400 rpm rotation to establish equilibrium between the solution and the catalyst surface. Adsorption is the major prerequisite condition for any heterogeneous catalytic reaction. After dark reading, 3 bulbs of halogen lamps (Osram HALOPAR 30, 75 Watts each, and aperture angle of 30°), comprising a total of 225 W total irradiated non-concentrated power emitting mostly visible light were used as the light source. They were placed on top of the magnetic stirrer at a height of 40 cm above the MB solution. 1 ml of MB dye solution was collected after fixed intervals of 30 mins during the reaction to study the amount of degradation by measuring the UV-Vis absorption spectra and analyzing the characteristic peak of MB at 664 nm. The degradation rate and the K constants were plotted and calculated using the relations expressed on chapter 3.

All the photocatalytic experiments were performed in a controlled temperature range between 20 and 30 °C using a water circulation cooling serpentine around the reactor vessel. CO_2 evolution was followed in selected experiments by an IR sensor (COZIR GSS 5% model and data acquisition by Gaslab software) placed at 3 cm proximity of the solution surface. Since the reactor is open, the measurement is not quantitative, but can only qualitatively evidence a variation in the atmospheric level of CO_2 on the reservoir experiment surrounding. Lastly, a set of experiments was performed varying pH. The WO_3 catalyst and 1M of H_2O_2 were added to the MB solution under neutral (pH 7), mildly acidic (pH 4) and strongly acidic (pH 1) conditions obtained by adding sulfuric acid (H_2SO_4, 1M stock). The use of acidic conditions aimed to investigate the catalyst performance and stability in these frequently occurring industrial wastewaters [107].

4.4 Solar Concentrator photocatalytic measurements

The solar scaling-up experiment was performed by studying the degradation of MB dye as model pollutant in the same concentration, measurement spectra and time as the labscale experiments. At this stage, instead of a 30 ml volume, degradation of 2 L of 10 ppm MB dye solution was tested for each of the four different solar experimental conditions: (1) concentrated sunlight exposure only, (2) concentrated sunlight and 0.6 ml of H_2O_2, (3) concentrated sunlight and WO_3 catalyst, and (4) combination of concentrated sunlight, WO_3 catalyst and 0.6 ml of H_2O_2 (corresponding to a concentration of 0.1M) as the oxidizing agent for photo-Fenton-like reaction. Regarding the use of H_2O_2, the concentration used in solar concentrator experiments was 1 order of magnitude lower (0.1M) than in the labscale experiments, because of the observed direct photocatalysis of H_2O_2 by solar photons otherwise masking all other reactions. The WO_3 catalyst material was deposited on glass slides at the same conditions as that employed for labscale experiments. The glass slides were inserted inside the quartz glass tube that was used as the reactor for the solar concentrator with the features described in chapter 3.

Figure 4.1 presents the working setup used in the work. The solar intensity was constantly measured with value readings between 650 and 750 W/m^2 during all the experiments time. The experiments were performed in the months of March and April in Trento – Italy, hours of the day between 10:00 and 15:00.

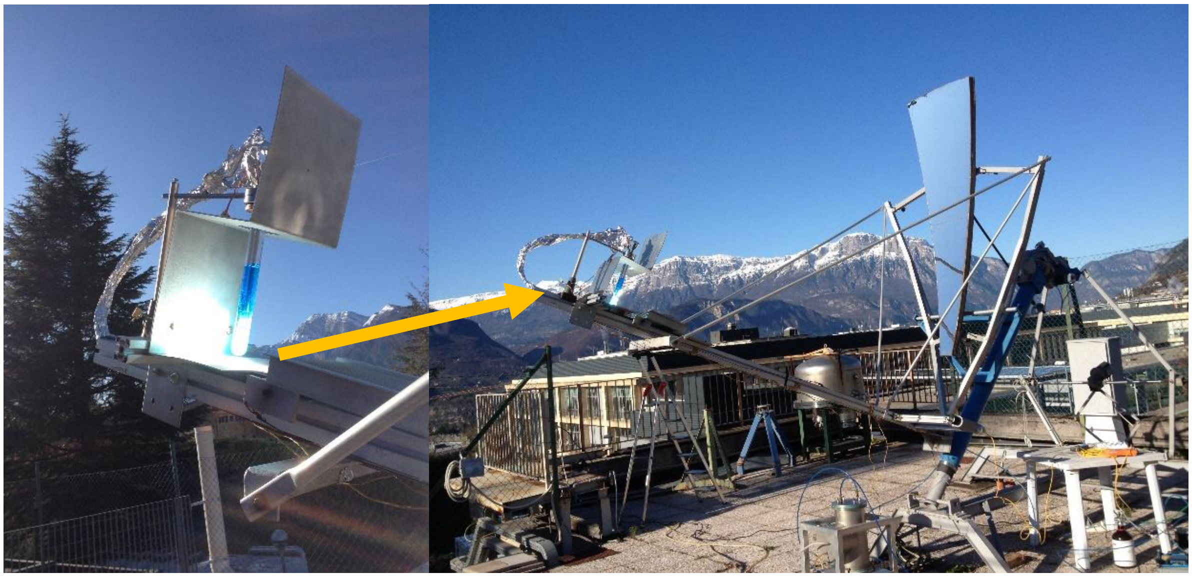

Figure 4.1: PDC solar apparatus for solar water purification used in this work.

In this study, due the high energy provided by the concentration of sunlight over the focus, only one mirror module was mounted on the system. As the volume in the solar concentrator experiment was increased, the circulating pipes passed inside an engineered cooling vessel to keep the temperature range controlled in the same condition as in the labscale experiments, the solution temperature was always between 20 and 30 °C as well.

4.5 Results and Discussions

Surface SEM pictures of the sample AD are shown in figure 4.2 (a and b) show a particle-like morphology with particle size ranging from tens of nanometer to few micrometers. This kind of morphology is expected owing to the phase explosion process occurring close to the thermodynamic critical temperature upon irradiating with high laser fluence [207]. AN200 samples are shown in figure 4.2 (c and d) show similar morphology as the AD samples, highlighting that this annealing temperature threshold is insufficient to promote a relevant oxidation and morphology change on the deposited samples [208]. Differently, the AN400 samples on figure 4.2 (e and f) show a cracking of the deposited particles, which indicates a possible phase change due to the oxidation process. After further increase in the annealing temperature, the AN600 sample from figure 4.2 (g and h) shows the particle like morphology evolved into flower-like structures depicting completely different morphology from the initial AD sample [209].

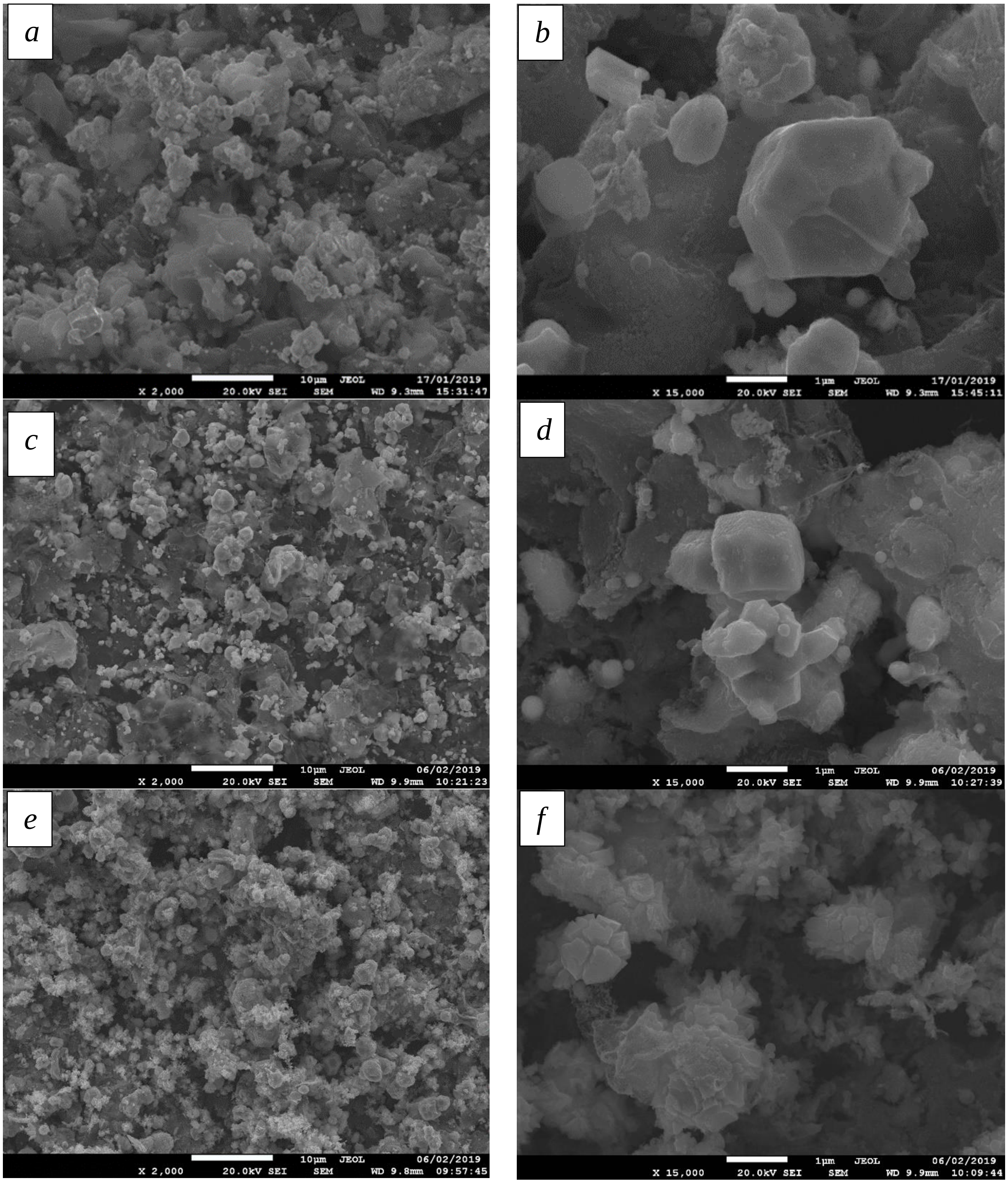
a
b
c
d
e
f
10µm JEOL 17/01/2019
X 2,000 20.0kV SEI SEM WD 9.3mm 15:31:47
1µm JEOL 17/01/2019
X 15,000 20.0kV SEI SEM WD 9.3mm 15:45:11
10µm JEOL 06/02/2019
X 2,000 20.0kV SEI SEM WD 9.9mm 10:21:23
1µm JEOL 06/02/2019
X 15,000 20.0kV SEI SEM WD 9.9mm 10:27:39
10µm JEOL 06/02/2019
X 2,000 20.0kV SEI SEM WD 9.8mm 09:57:45
1µm JEOL 06/02/2019
X 15,000 20.0kV SEI SEM WD 9.9mm 10:09:44

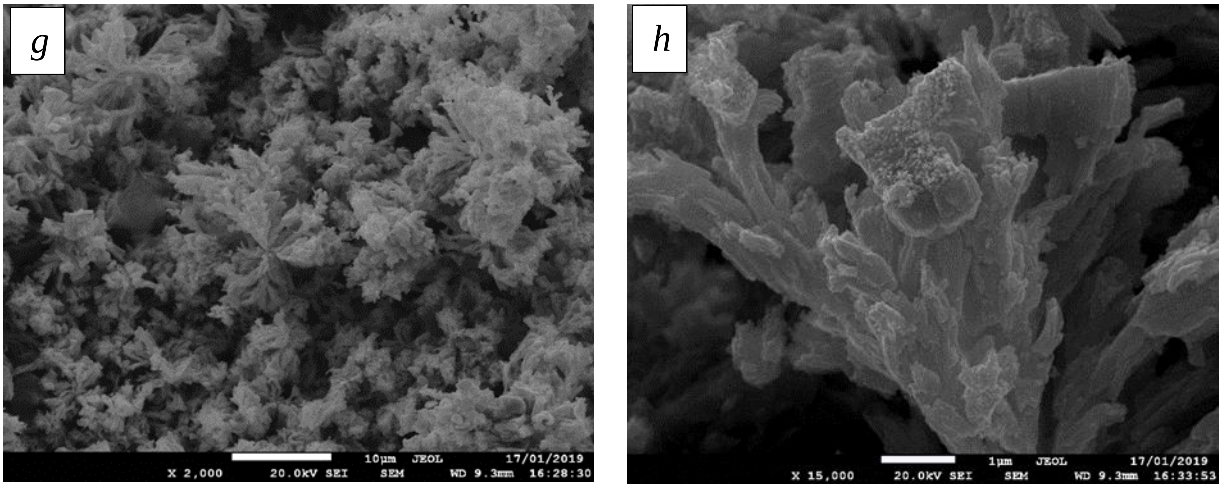

Figure 4.2: Surface SEM images of (a & b) as-deposited [AD] samples, (c & d) AN200, (e & f) AN400 and (g & h) of AN600 samples. Magnifications of 2000x (left column) and 15000x (right column).

Cross-section SEM images are shown in figure 4.3. Following the above observations regarding the morphology changes, it can be also inferred the thickness of the fabricated samples, which showed small variations at the different annealing temperatures, the thickness in all samples is on the range of 10 µm. In the AN600 some vertical individual growths of the flower-shape like morphology in figure 4.3 (g) overpassing the value of 10 µm can be also seen, but these are not representative of the overall thickness.

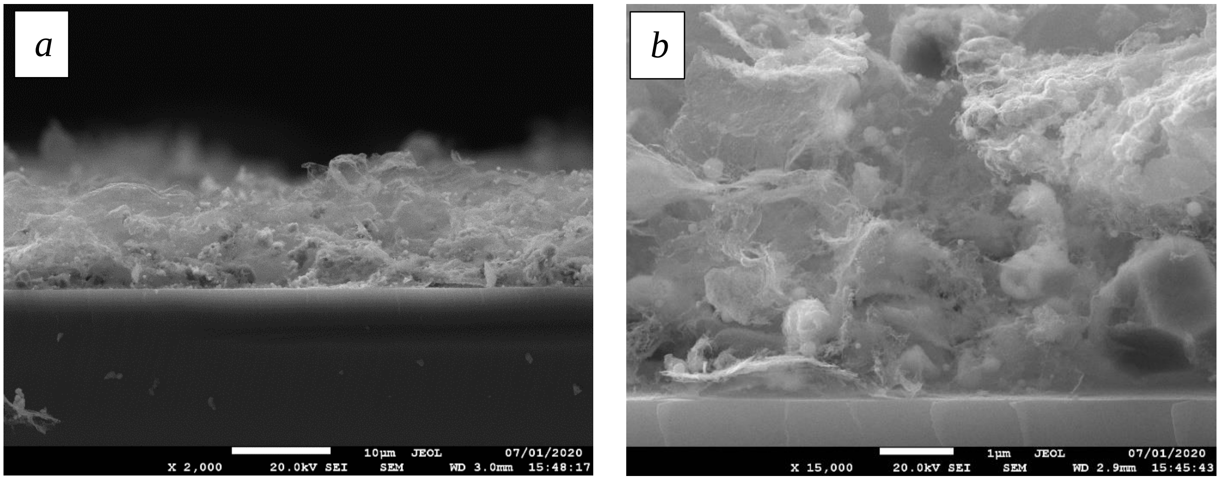

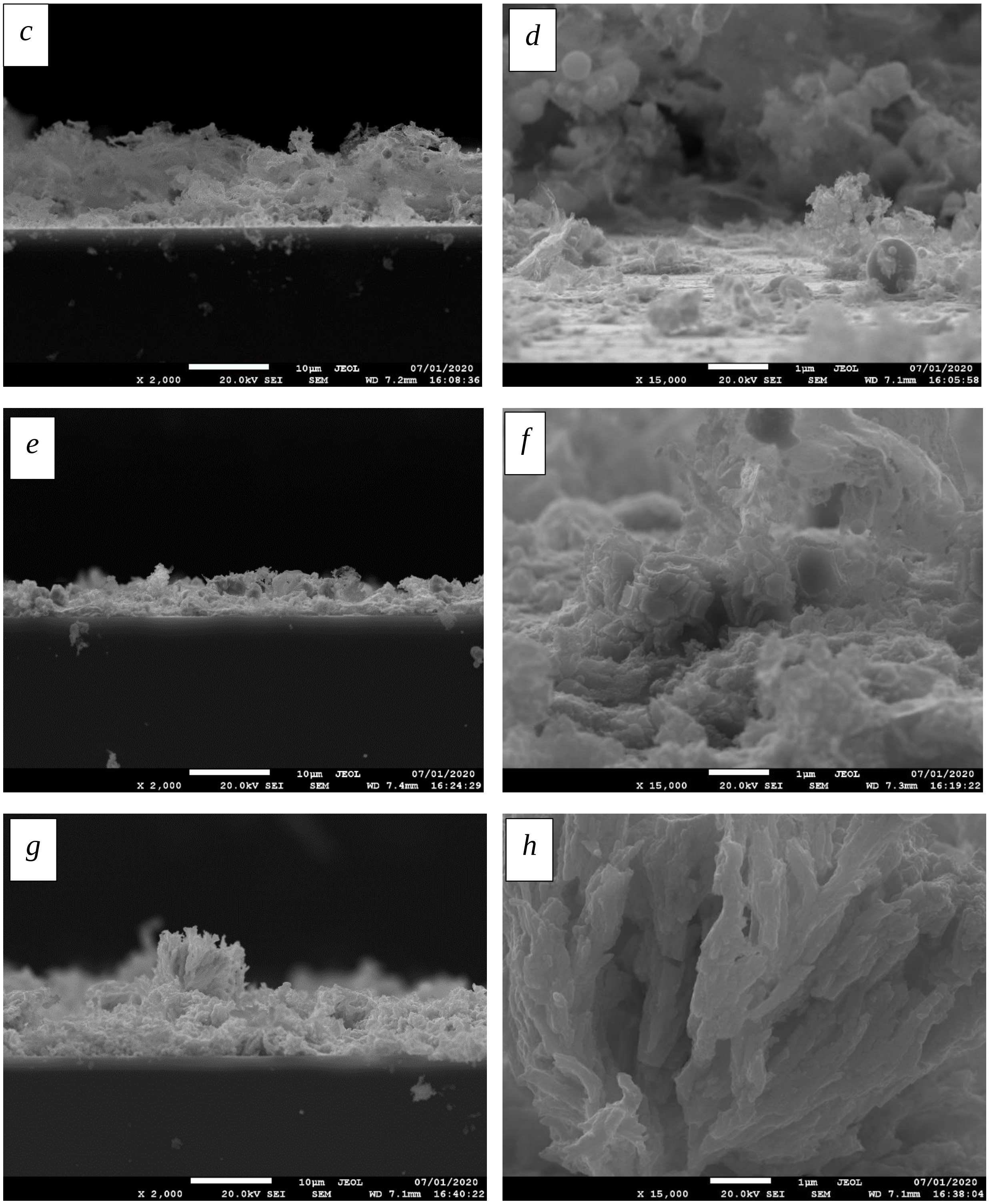

Figure 4.3: Cross-section SEM images of (a & b) as-deposited [AD] samples, (c & d) AN200, (e & f) AN400 and (g & h) of AN600 samples. Magnifications of 2000x (left column) and 15000x (right column).

XRD spectra on samples AD, AN200, AN400 and AN600 are shown in figure 4.4. The XRD pattern from AD coating shows the prevalence of metallic tungsten (W), with peaks at 2θ = 40, 44 and 58° corresponding to the tungsten planes (110), (211) and (200) respectively and a cluster of convoluted peaks centered at roughly 15° assigned to the tungsten boride (WB) alloy, referred to the boride planes (101), (103), (105), (112) and (008) [210,211]. The peak at 28° refers to the silicon substrate plane (111). On the AN200 sample the boride cluster around the region of 15° disappeared, suggesting a decomposition of the boride phase, the permanence of the peaks at 40, 44 and 58° confirm the remaining presence of metallic tungsten phase. A cluster peak region at 24 and a new peak at 33° suggests the development of oxidation [212]. At the annealing temperature of 400 °C (AN400), a combined presence of metallic tungsten (peaks at 40 and 58°) and an increase in tungsten oxide (peaks at 24 and 33°) can be observed. Finally, the XRD pattern for the AN600 sample, which presents sharp diffraction peaks at 2θ = 23.1, 23.6, 24.2, 26.6, 28.8, 33.4, 33.8, and 34° is associated to the monoclinic phase of WO_3, with lattice parameters of a = 7.297 Å, b = 7.5439 Å, c = 7.688 Å and α,ɣ = 90°, β = 90.91° (JCPDS Card No. 43-1035) [213,214].

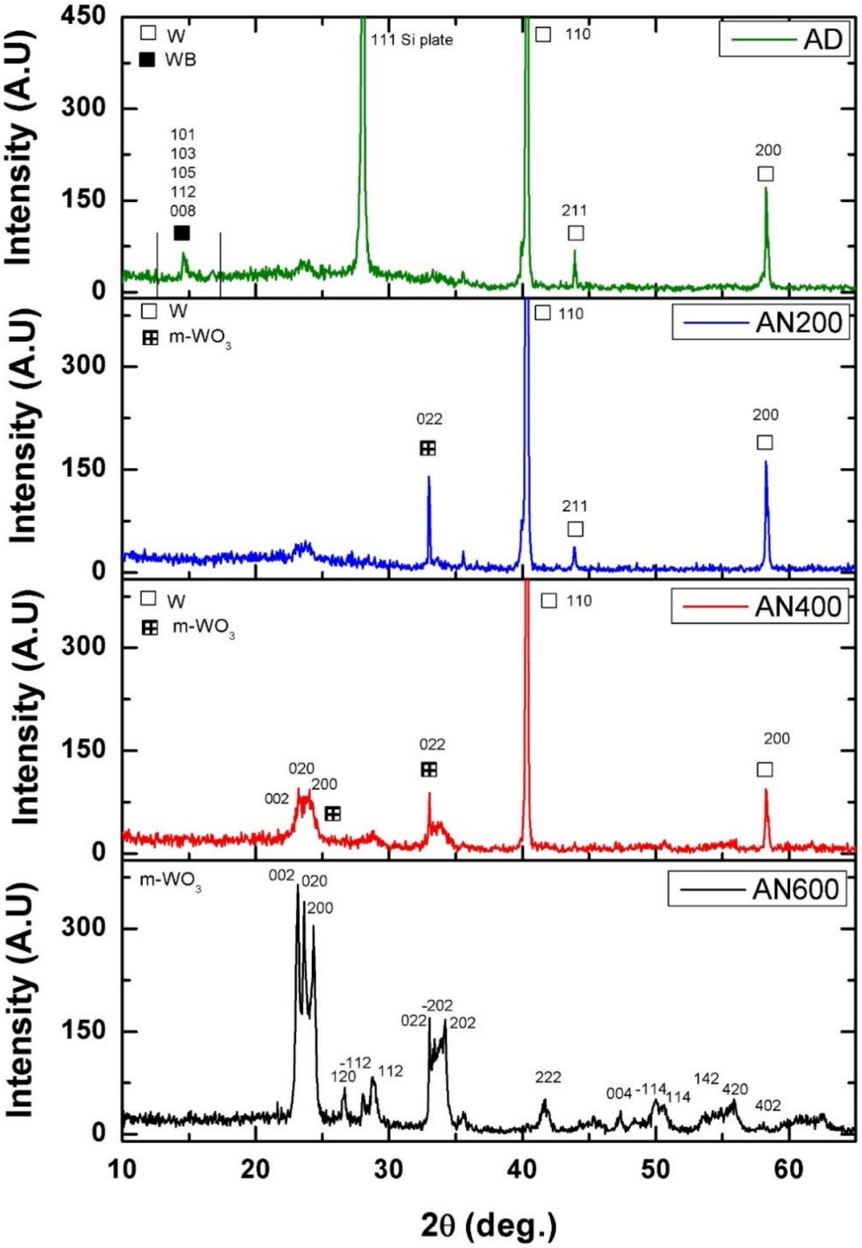

Figure 4.4: XRD spectra as-deposited [AD], AN200, AN400 and AN600 samples.

Micro-Raman spectra for AD, AN200, AN400 and AN600 samples are shown in figure 4.5 in the range of 100 to 1000 cm^{-1}. The broad shape of the peaks with low intensities between the range of 130 and 400 cm^{-1}, and a minor signal on 806 cm^{-1}, indicate a small partial surface oxidation for the AD sample. Upon annealing at 200, 400 and 600°C, the peaks become gradually sharper and well resolved as the values of temperature increase, until they are well matched with the monoclinic phase of WO_3. In particular, the peak at 134 cm^{-1} is the lattice mode, 271 and 327 cm^{-1} are due to bending vibration δ(O-W-O) and 711 and 806 cm^{-1} correspond to the ν(O-W-O) mode of WO_3 [215–217].

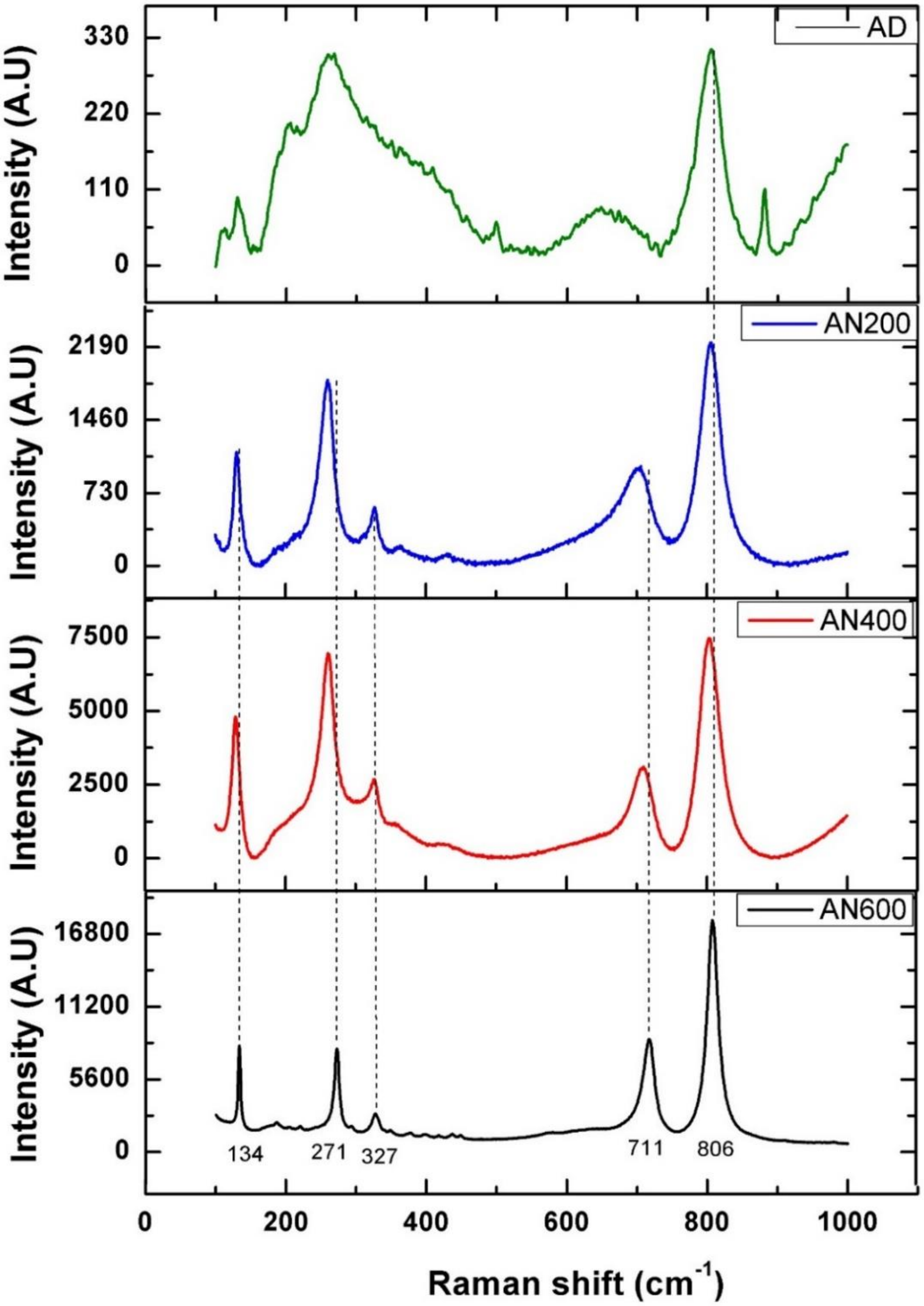

Figure 4.5: Raman spectra for the as-deposited [AD], AN200, AN400 and AN600 samples.

Optical absorption spectra were acquired for AD and AN600 (WO_3) samples in the range of 350-600 nm (Figure 4.6). AN600 (WO_3) sample confirms a clear absorption edge around 472 nm, which corresponds to the absorption of WO_3 samples reported in literature [200,218,219]. While AD sample, due to the mostly metallic nature of the film, only shows an unstructured absorption increasing in the UV part of the spectrum (<400 nm).

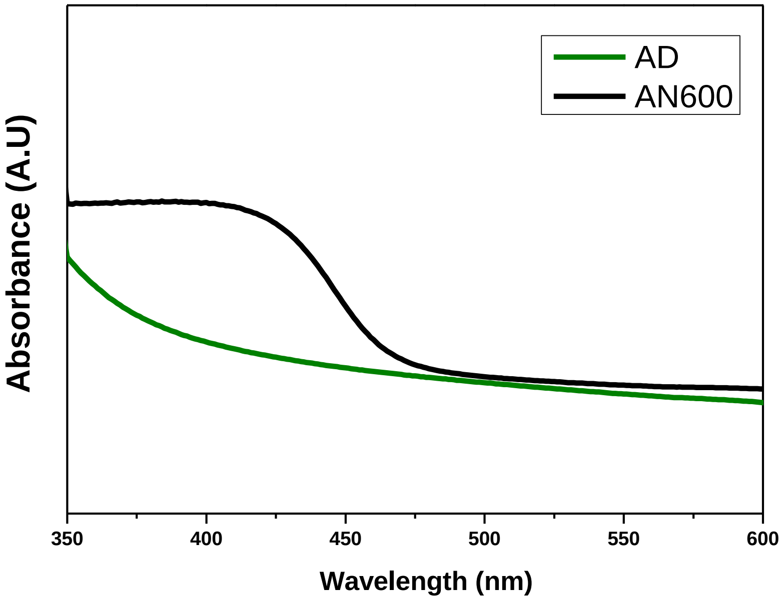

Figure 4.6: Absorption spectra for as-deposited (AD) and AN600 samples.

The energy of the optical band gaps can be determined by applying the *Tauc* model in the high absorption region**.** The direct and indirect bandgap energies were estimated as shown in figure 4.7. The linear region of the plot is extrapolated to intersect the x-axis, thus giving *Eg*.

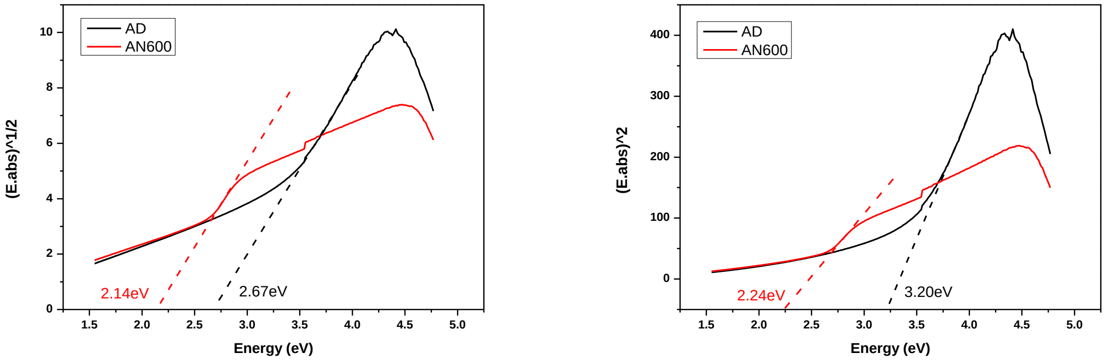

Figure 4.7: Plots of indirect (left) and direct (right) bandgaps of the investigated WO_3 photocatalyst.

Because AD coating presents only the features of a metallic tungsten film and borides with no formation of WO_3, and samples AN200 and AN400 did not exhibit a complete oxidation from metallic tungsten, hence, only AN600 coatings were selected for evaluation of photocatalytic activity in labscale and solar experiments. Additionally, the AD, AN200 and AN400 film samples were not mechanically stable under stirring and/or water flow conditions: after a few minutes the film was lost due to detachment, flaking and poor adhesion. The effectiveness of the AN600 film as a photocatalyst was studied by using it for degradation of model MB dye through a photo-Fenton-like reaction involving H_2O_2.

The photocatalytic degradation performed on MB dye, (1) in presence of light only, (2) with added H_2O_2 and light, (3) with coating annealed at 600°C (AN600) and light, and (4) combination of all three (H_2O_2, light and AN600 catalyst) are presented in figure 4.8. A photochemical reaction pathway is known to be accessible for MB under visible light, leading to products which are still toxic but not absorbing in the visible spectrum anymore [220]. This effect was evaluated by experiment, in blank conditions (no catalyst and no radical source). In 120 mins, the degradation of MB dye under visible light illumination is only 34% (1) and increases to 51% (2) after addition of H_2O_2. In agreement with previous reports, the decomposition of MB is observed to be a markedly faster process than without H_2O_2 added [221]. The catalyst coating AN600 under light illumination in absence of H_2O_2 can degrade 74% (3) of the dye, with interesting performance comparing to powder disperse solutions reported in other works [218]. Finally, in presence of the AN600 coating along with H_2O_2 and light illumination the degradation reaction is almost completed at 96% (4). In principle, any metal oxide semiconductor for which the conduction band is reducing enough to transfer an electron to H_2O_2 can be used to initiate a Fenton-like process:

$$M^{n} + H_2O_2 \text{ -> } M^{n+} + HO° + HO^{-} \qquad (1)$$

Since the number of conduction band electrons is restored by photon absorption, the process is also catalytic under light and can be defined as a photo-Fenton-like process [6]. These conditions are satisfied by the electronic structure of WO_3 [222], thus a photo Fenton like behavior can be expected in presence of H_2O_2. This indicates that the catalyst coating likely improves the degradation process through the photo-Fenton-like reaction by generation of $OH^{\bullet}$ radicals by dissociation of H_2O_2 [223]. Importantly, the result also evidences that the tungsten oxide film (AN600) alone works as a pure photocatalyst which might be able to generate hydroxide radicals from adsorbed H_2O on the surface. Although the involvement of H_2O_2 is very useful, the catalyst coating can be however also utilized without H_2O_2. The results explained previously are expressed in figure 4.9 that presents the kinetic constants for the reactions. In accordance to the degradation rates exposed, the values obtained are 0.003, 0.005, 0.012 and 0.024 min^{-1} respectively. To summarize:

a) a partial (34%) photochemical reaction of MB under light only occurs;
b) introducing H_2O_2, its dissociation promotes the availability of $OH^{\bullet}$ radicals determining and increase of the degradation (51%);
c) applying the AN600 catalyst itself with artificial visible illumination, it works also purely as a photocatalyst, with even higher degradation than only H_2O_2 (74%);
d) a photo-Fenton-like reaction occurs by adding AN600 catalyst + H_2O_2 under light, as indicated by the increment in degradation (96%).

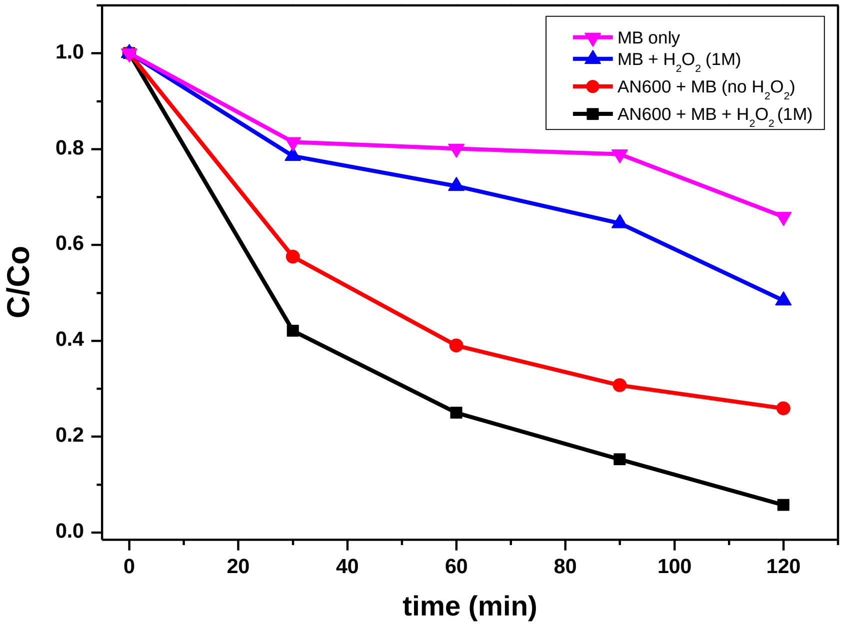

Figure 4.8: Relative concentration of MB dye after 120mins in presence of AN600 coating, H_2O_2 (1M) and visible light, labscale experiment, neutral condition during the experiment (pH 7).

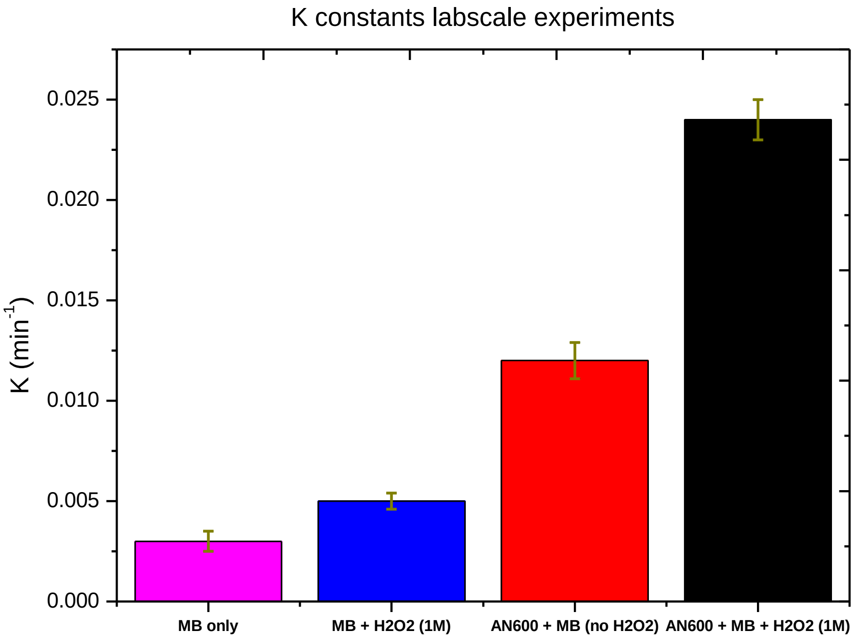

Figure 4.9: Kinetic constants (K) for the experiments performed in labscale, neutral condition during the experiment (pH 7).

CO_2 emission measurements were also done for the experiments involving the catalyst (with and without H_2O_2) and the graphs are reported in figure 4.10 (a and b). The confirmation of the activation of the photo-Fenton-like reaction and photocatalysis processes without H_2O_2 are clearly given by the evolution of CO_2 as soon as light is irradiated on the catalyst coating. The $OH^{\bullet}$ radicals generated in both the cases possibly mineralize the MB dye giving rise to the formation of CO_2 as by-product.

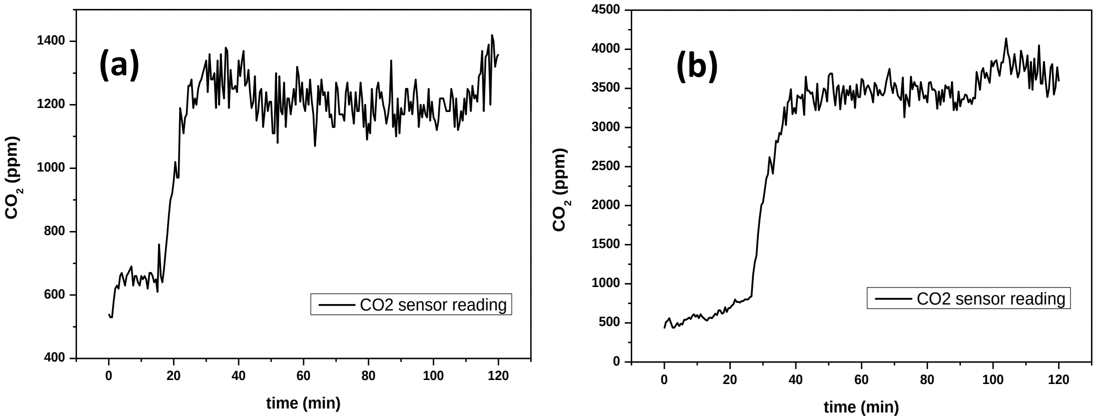

Figure 4.10: CO_2 evolution during MB degradation by AN600 sample (a) in presence of visible light without H_2O_2 (b) in presence of H_2O_2 and visible light, labscale experiment.

The photocatalytic degradation promoted by the AN600 coating of MB dye in different pH was also tested and the results are shown in figure 4.11. The best activity was observed at pH 4. The experiments were done at either neutral, mildly acidic (pH 4) or highly acidic (pH 1) pH. The results are in accordance with Pourbaix diagram for tungsten oxide, which presents this material stable in slightly acidic conditions, comparable to neutral [193,224]. On the other hand, the highly acidic condition (pH 1) did not promote enhanced photoactivity, as the increased acidity led to mechanical instability of the catalyst over the glass slide surface and removal of the coating. Figure 4.12 presents the kinetics constants for the performed pH experiments, resulting in 0.022, 0.024 and 0.01 min^{-1} for the pH 7, 4 and 1 respectively.

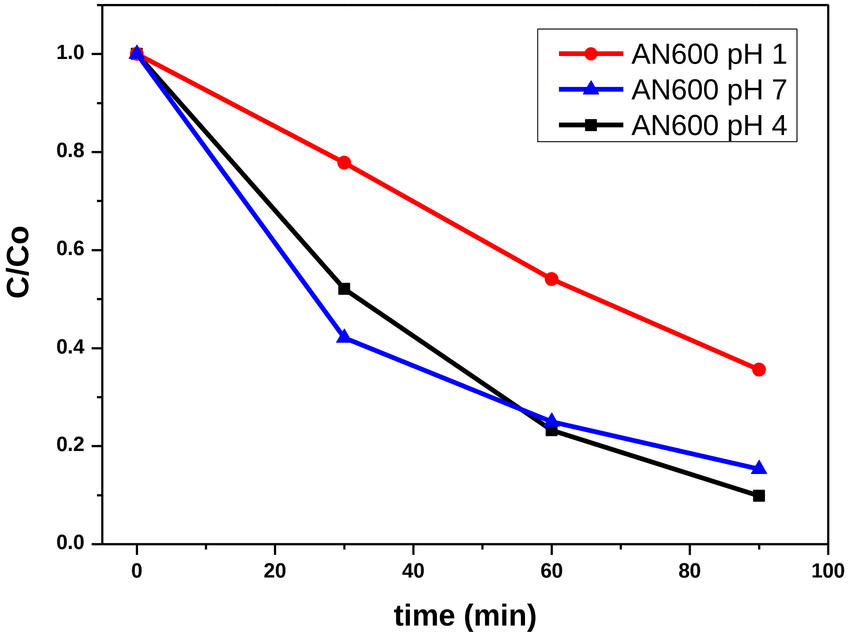

Figure 4.11: Effect of pH on photocatalytic degradation of MB by AN600 sample in presence of H_2O_2 (1M) and visible light, labscale experiment. Obs: the referred pH values were kept along the experiment.

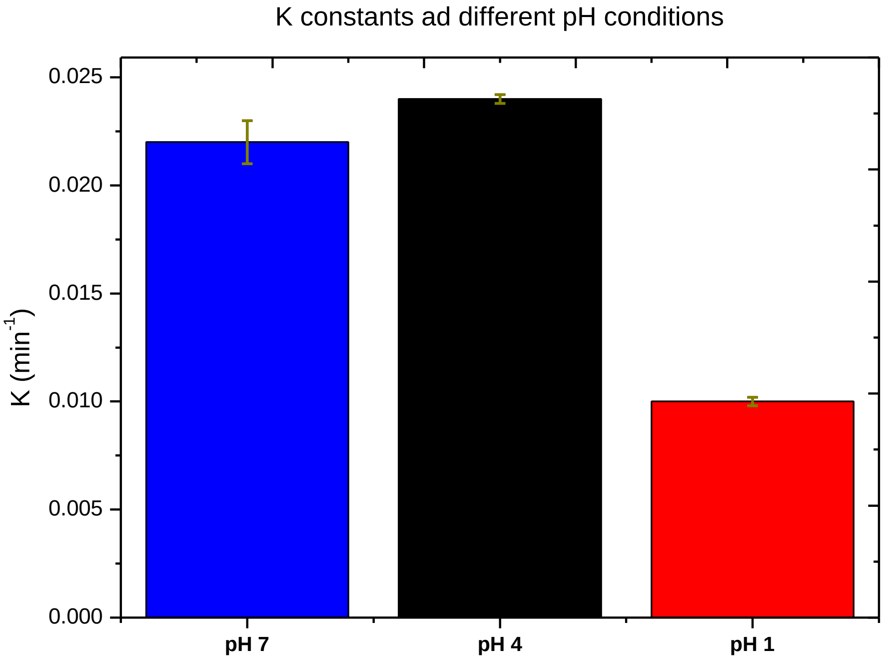

Figure 4.12: Kinetic constants (K) for the experiments performed in labscale in different pH conditions at labscale, AN600 sample in presence of H_2O_2 (1M) and visible light.

In the solar concentrator experiment setup, the role of light, H_2O_2 and catalyst, on catalytic degradation was evaluated in the same time frame as in the lab scale by performing the degradation of MB dye, (1) in presence of concentrated light only (blank), (2) with combination of H_2O_2 and concentrated light, (3) with coating annealed at 600˚C (AN600) and concentrated light, and (4) combination of all three (H_2O_2, concentrated light and AN600 coating). Figure 4.13 presents the results and in 120 mins, the degradation of MB dye in light is about 54% (1) which increases to 63% (2) after inclusion of H_2O_2 confirming the direct photolysis promoted by the high concentration factor of the solar spot. Adding AN600 without the presence of H_2O_2, degradation observed in 120 mins is 59% (3), which does not allow to imply significant changes in results from the effects of only direct photolysis. Finally, with AN600 along with H_2O_2 and light, the degradation occurs significantly higher with about 85% (4) degradation in 120 mins. Figure 4.14 presents the kinetic constants for the solar concentration experiments, corroborating the reported degradation results and having values of: 0.006, 0.008, 0.007 and 0.015 min^{-1} respectively.

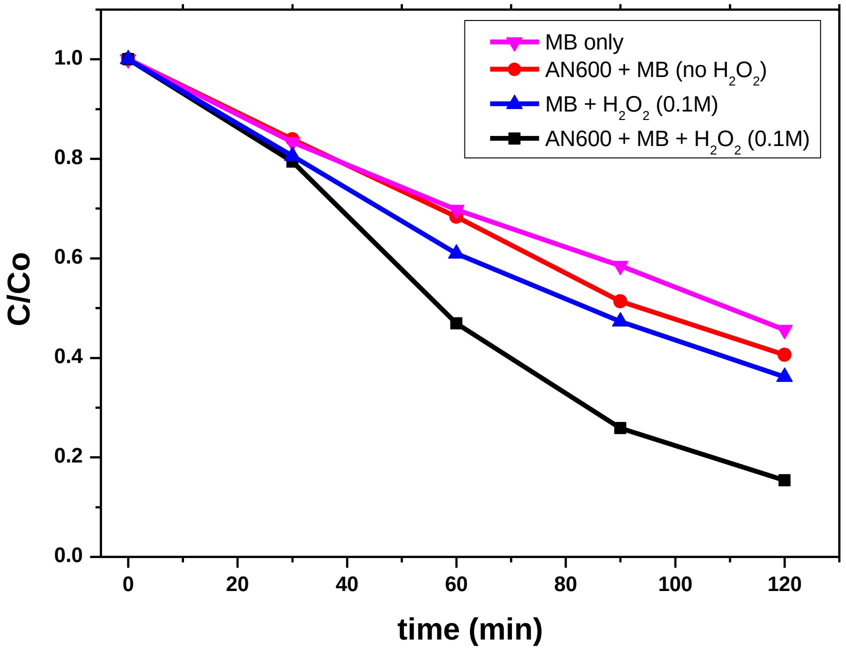

Figure 4.13: Relative concentration of MB dye after 120mins under concentrated sunlight in presence of AN600 coating and H_2O_2 (0.1M), solar concentrator experiment, neutral condition during the experiment (pH 7).

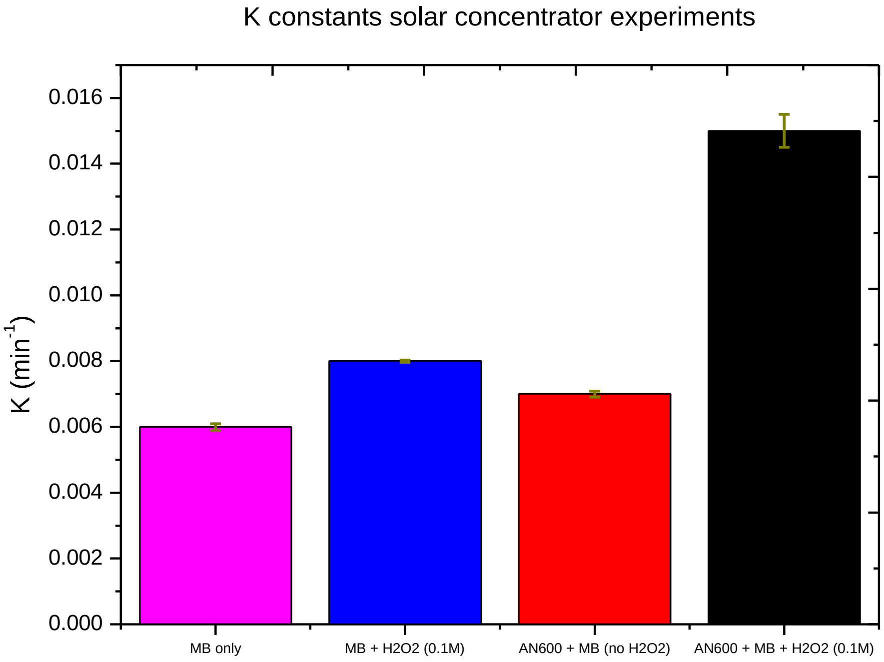

Figure 4.14: Kinetic constants (K) for the experiments performed in the solar concentrator, neutral condition during the experiment (pH 7).

It is worth to point out that experiments performed in labscale and in the solar concentrator apparatus are not directly comparable. The reasons rely on the fact that the labscale experiments were performed with the total volume of 30 ml MB dye solution being exposed to the artificial light source during all the 120 mins experiment. In the other hand, in the solar apparatus the volume of the solution was scaled up for 2 L circulated volume and only 150 ml of the total was exposed directly to the concentrated sunlight during circulation using a 5 L/h pumping system. These parameters affect the result due to a decrease of the residence time of the solution exposed to the combination of photocatalyst and sunlight. Also, strong photolysis effect can be observed by the exposition to sunlight solely, capable of degrading nearly 54% of the 2 liters solution, whilst the lamp in labscale can degrade only 34% of the 30 ml solution. Another important difference is the decrease by one order of magnitude on the H_2O_2 concentration, resulting in minor availability of OH radicals in the solution (Appendix B). This is reflected by the only modest increase in degradation between the light-only condition and the light+H_2O_2 condition (experiments 1 and 2). An overview of this section is presented on table 4.1 collecting all the results obtained on this work.

Table 4.1: summary of the conditions tested and of results for the WO_3 PLD produced AND600 catalyst film.

Photocatalyst condition	**Source of irradiation**	**pH**	**Solution volume**	**MB degradation (%) in 120 min.**	**Kinetic constant (K, min^{-1})**
No catalyst	Halogen lamps	7	30 ml	34	0.003
H_2O_2 (1M)	Halogen lamps	7	30 ml	51	0.005
AN600	Halogen lamps	7	30 ml	74	0.012
AN600 + H_2O_2 (1M)	Halogen lamps	7	30 ml	96	0.024
AN600 + H_2O_2 (1M)	Halogen lamps	7	30 ml	82	0.022
AN600 + H_2O_2 (1M)	Halogen lamps	4	30 ml	90	0.024
AN600 + H_2O_2 (1M)	Halogen lamps	1	30 ml	62	0.01
No catalyst	Conc. Sunlight	7	2 L	54	0.006
H_2O_2 (0.1M)	Conc. Sunlight	7	2 L	63	0.008
AN600	Conc. Sunlight	7	2 L	59	0.007
AN600 + H_2O_2 (0.1M)	Conc. Sunlight	7	2 L	85	0.015
*H_2O_2 (1M)	Conc. Sunlight	7	2 L	88	0.016
*AN600 + H_2O_2 (1M)	Conc. Sunlight	7	2 L	83	0.015

***** Data presented on appendix B

4.6 Conclusions

m-WO_3 nanostructured films were prepared by the PLD fabrication technique for application on solar photocatalytic wastewater remediation for the first time. PLD targets were prepared by a mixture of metallic W and H_3BO_3. The as-deposited (AD) samples were thermally annealed at 200, 400 and 600 °C for the comprehension on the formation of monoclinic phase “flower-shape like” nanostructured WO_3 coating. The film showed complete formation of the oxide after annealing at 600 °C (AN600) and for this reason it was chosen to be tested for heterogeneous photocatalysis on MB dye degradation. The coatings showed enhanced photocatalytic degradation of MB dye under photo-Fenton-like conditions. The enhanced photoactivity can be attributed to the surface morphology that provides high surface area thereby acting as an efficient adsorber that allows enhanced interaction between the dye molecules and the active sites for photocatalytic reactions as well as the confirmation of appropriate performance in acidic pH.

Solar scaling-up experiments were employed to eliminate the use of an artificial source of light thereby making the whole process economically efficient for low-cost industrial applications. Even though some parameters adjustments in terms of the need for circulation system and consequent decrease in the residence time between the catalyst and the solution were necessary, the m-WO_3 coatings showed positive results in the solar PDC setup under both direct photocatalysis and photo-Fenton-like conditions thus expanding the outreach of the synthesized coatings.

Chapter 5 – Colloidal and immobilized ZnO nanostructures synthesized by a green method for water remediation via concentrated sunlight photocatalysis

Preview: The possibility of using an eco-friendly combination of green-synthesized material and solar concentration technology for advanced oxidation processes (AOPs) presents important potential applications in water remediation. Zinc Oxide (ZnO) nanostructures (NSs) were prepared via a green synthesis method using plant extract of garlic bulbs (Allium Sativum) (ZnO-Green), resulting in crystalline (wurtzite) nanorods (NRs). Comparisons were made using chemical and PLD synthesis of ZnO. The fabricated materials were compared in solar photocatalytic experiments. As the second author of this work, this investigation was developed in a collaboration with the University of Sousse in Tunisia, enabling possibilities to introduce a low-cost solar concentrator in favorable sunny areas as well as developing photocatalysts from natural biological sources.

The content of this chapter was submitted to the *Journal of Environmental Management* on November 18th, 2020.

5.1 Introduction

In the past centuries, water has often been used in a careful and sustainable way. However, now, freshwater resources are more and more dwindling due to a significant increase in consumption as a result of technological progress and in particular the population growth [225]. The problem is intensified by significant pollution related to agricultural, domestic and industrial discharges [226]. Wastewater contains microorganisms (viruses, helminths, and bacteria), inorganic pollutants (Mercury, Chromium, Arsenic, Titanium, Copper, Cobalt, Nickel, Lead, and Zinc), and organic pollutants (polychlorinated biphenyls, hydrocarbons, polycyclic aromatic compounds, dyes, phenolic compounds, and pesticides). In many cases, the poor biodegradability and high toxicity lead to serious hazards to human health, as well as to the natural environment [227]. Conventional methods for water remediation (e.g. adsorption, filtration, and ozonation) present economic constraints due to the requirement of strong investments and often still yield toxic by-products, requiring additional treatment [228]. In the last 20 years, photocatalysis has shown to be an important strategy for wastewater remediation [89,229]. Photocatalysis is classified as an advanced oxidation process (AOP) that uses light for the partial or total mineralization of harmful organic pollutants and its performance is measured by means of photocatalytic degradation activity (PCA) [230]. Recent research focus on the production of materials which are capable to efficiently harvest solar irradiation~~s~~ and use it in favor of green wastewater purification processes. [231]. Currently, several types of semiconductor-based photocatalysts, like metal oxides in nanoscale forms, (i.e. TiO_2, Fe_2O_3, and ZnO) have been applied in water treatment [88,232,233]. Zinc oxide (ZnO) which is a direct band gap (BG)(II-VI), n-type semiconductor, has emerged as a promising candidate for environmental applications thanks to some important properties: 1) it is capable of generating powerful oxidants such as the hydroxyl and superoxide radicals [234–236], 2) it has low toxicity and high chemical and thermal stability, thus exhibiting an optimal environmental compatibility [237] and 3) it is a potentially cheaper alternative to the benchmark TiO_2 [238].

In order to enhance the performance in photocatalysis, efficient transport of the generated charge carriers to the surface is highly required. Notwithstanding this aspect, high surface area with a large number of active sites giving favorable catalytic kinetics is also important. Different morphological nanostructures (NSs) such as porous nanowires, nanosheets, nanorods (NRs) and 3D-urchin like solid zinc oxides were already reported to enhance the surface reactivity [233,239,240]. The different methods investigated for the preparation of ZnO NSs include physical and chemical techniques, but both requiring multistep procedures, long-lasting synthesis processes , high vacuum conditions as well as costly precursors. Nowadays, research efforts to develop clean, non-toxic and eco-friendly methods for nanostructures synthesis are ongoing. In this regard, green methods have recently been investigated to produce nanoparticles (NPs) using biological sources, that act as stabilizers and reducing agents, favoring the development of specific NSs [241,242].

This chapter reports on a new strategy to produce ZnO NRs using garlic extract (Allium Sativum) as a reagent. Comparatively, the green synthesis used in this work provides an advancement over other methods as it is simple, cost-effective, eco-friendly and relatively reproducible [243]. Moreover, this approach is advantageous considering the potential for large-scale production.

For water remediation purposes, suspended nanoparticle powders are remarkably effective considering that they have a high surface area and can be easily dispersed in the contaminated solution. However, the post-processing removal of the NPs from the liquid solution can be an inefficient additional process step [244]. From an industrial perspective working with photocatalysts immobilized as coatings is thus an improvement. For this reason, immobilization of the ZnO NRs by spin coating was performed, to be employed in heterogeneous solar photocatalysis processes. The comparisons were made against ZnO coatings produced by pulsed laser deposition (PLD). Several techniques are available for ZnO thin films production, like chemical vapor deposition [245], sputtering [246], and the sol-gel method [247]. The PLD method was chosen for its versatility, allowing to control structure and morphology parameters and, accordingly, influence electrical, physico-chemical, mechanical, and optical properties of films [105,248]. It is proposed the investigation of the photocatalytic activity (PCA) of ZnO in form of colloidal suspension and thin films. Finally, an economic analysis (appendix C) aimed at providing cost estimates for the remediation experiments was produced, taking into account installation costs and operation costs for a process using either ZnO-Green or ZnO-Chem.

5.2 Synthesis of ZnO NSs

5.2.1 Green-synthesis of ZnO NRs using an aqueous extract of Allium Sativum (garlic) bulbs

The green-synthesis used Allium Sativum (garlic) bulbs as the precursor. The method comprised 2 steps: preparation of vegetable extract and synthesis of ZnO NRs. The procedure was carried out using a modified version of synthesis published in previous report [249]. In particular, 20 grams of thinly sliced bulbs of Allium Sativum were boiled in 100 ml of deionized water at 75–80 °C under magnetic stirring at 900 rpm for 20 minutes resulting in a plant extract. The obtained plant extract was then cool ed down in air to room temperature (RT) and filtered with filter paper (Whatman n° 1) for the NPs synthesis. For the synthesis, 60 ml of the garlic extract was heated at 60 °C under magnetic stirring at 400 rpm, followed by adding 6 grams of zinc nitrate ($Zn(NO_3)_2.6H_2O$) and the mixture was kept Stirring for 20 minutes. The obtained mixture was dried in air atmosphere oven at 110 °C for 6 hours. The product was an intermediate, which was further washed with deionized water and isopropanol, then calcinated at 500 °C for 4 hours to reach the final product containing the ZnO NSs (hereinafter referred as ZnO-Green).

5.2.2 Chemical Synthesis of ZnO NPs using coprecipitation process

For a comparative evaluation with the green method presented above, ZnO NPs were also chemically prepared by coprecipitation process [227]. $Zn(NO_3)_2.6H_2O$ and oxalic acid ($H_2C_2O_4.2H_2O$) were firstly dissolved in deionized water forming a solution with 0.4 mol/L concentration. $Zn(NO_3)_2.6H_2O$ solution was dropped (in a flow rate of approximately 0.1ml/sec) into $H_2C_2O_4.2H_2O$ solution under stirring at 300rpm. Then, the mixture was kept for 19 h at RT to develop the precipitates and cooled in an ice bath for 45 minutes. The precipitates were filtered with Whatman filter paper n° 1 and rinsed with deionized water and isopropanol. The obtained product was subsequently dried at RT and calcinated at 425°C for 90 min, resulting in a powder featuring a white color (hereinafter referred as ZnO-Chem).

5.3 Immobilization of green-synthetized ZnO NRs by spin coating

The second part of the investigation focused on the immobilization of the green-synthesized ZnO NRs in the form of coating. To achieve this goal, polyethylene glycol (0.27 g) was dissolved in deionized water (5 ml) and sonicated until the formation of a clear solution. ZnO-Green NPs (~20mg/2ml) were added and the suspension obtained was stirred for 45 minutes and sonicated for a further 15 minutes in order to obtain a homogenous dispersion, which was then spin-coated with a KV-4A Spin Coater over a glass slide substrate measuring 75 mm x 26 mm under rotation of 600 rpm for 3 minutes. After every spin coating cycle the glass slide was preheated at 80 °C for 1 hour, then annealed at 500 °C for 2 hours. The spin coating cycles were repeated (1 and 5 cycles) in order to obtain 2 samples of immobilized ZnO-Green on the surface of the glass substrate with measured material masses of 0.6 mg, and 1.9 mg respectively.

5.4 PLD synthesis of ZnO coatings

For the comparative evaluation on photocatalysis with the spin coated films present in the item 5.3, ZnO thin films were fabricated by the PLD technique both on glass slides and silicon (Si) substrate using a solid metallic zinc (Zn) target in a reactive oxygen (O_2) atmosphere at RT. The PLD system used in the fabrication consisted of a KrF excimer laser detailed on chapter 3, using a repetition rate of 10 Hz, and a pulse duration of 20 ns. The deposition chamber was initially evacuated through a turbo molecular pump to a base pressure of 1 x 10^{-6} mbar before all the depositions. During the deposition process, the O_2 pressure was maintained at 1.5×10^{-2} mbar. The laser beam was focused on the target to ablate it at a constant energy density of 3 J/cm^2. The substrate to target distance was set to 4.5 cm, with the substrate position parallel to the target, and the number of pulses was fixed to 4000. The deposited coatings were then submitted to annealing in oven under air atmosphere at 600 °C during 6 hours with a heating rate of 5 °C/min in order to evolve the ZnO nanostructure (hereinafter referred as ZnO-PLD). The weight of the coating resulted from PLD deposition process (0.7 mg) is comparable to that used for the spin coated ZnO film.

5.5 Characterization methods of ZnO particles and films

All ZnO samples were characterized by UV-VIS optical absorbance, and X-Ray Diffraction measuring the diffracted intensity in the 2θ range between 30 and 100. The particle morphologies and thicknesses were investigated using the SEM technique described on chapter 3, item 3.2.

5.6 Solar photocatalytic (PC) experiments

The ZnO samples prepared as reported in the previous items were investigated in solar photocatalysis experiments. Two groups of tests have been carried out by using: 1) a colloidal solution prepared by dispersing the green-synthesized powders (ZnO-Green) in different concentrations; the pertinent PC results were compared with that of the chemically synthesized ones (ZnO-Chem), and 2) ZnO-Green immobilized by spin coating and ZnO film deposited by PLD were compared in the heterogeneous photocatalysis route. Absorbance spectrum regarding the discoloration of MB dye as model pollutant was the method chosen to evaluate the performance of the catalysts.

Regarding the first set of experiments, the PC activity of ZnO NSs generally depends on the load of the catalyst under investigation. Thus, to determine the optimal concentration of the green-synthesized ZnO catalyst towards the efficient oxidation, the experiments were conducted by varying the concentration of the catalyst under concentrated solar light.

The volume of the circulated model solution was 2L with a MB concentration of 10 ppm under the following conditions: 1) Concentrated sunlight + ZnO-Green powder catalyst, in concentrations of 0.1, 0.3, 0.6 g/L and 0.6 g/L of ZnO-Chem which can be considered the optimized concentration under the evaluated concentrations; 2) Concentrated sunlight exposure only as a blank. The concentrated solar light was directed into a quartz glass tube of approximately 150 ml volume that was used as the reactor. The quartz tube was sealed at one end and closed by a three-port lid on the other end. One port hosts a thermocouple for temperature monitoring, and the other two ports are the inlet and outlet for the MB solution circulation. A pumping system was used to promote the circulation of the solution provided by a diaphragm pumping system with a volume flow rate of 5 L/h. The tubing circuit was made of polyamide pipes connected to a cooler with monitored temperature.

In the second step of MB degradation experiments, the green-synthesized NSs, immobilized over the glass slides, were compared with the ZnO coating fabricated by PLD, in two conditions: 1) Concentrated sunlight + immobilized green-synthetized NSs with 0.6 and 1.9 mg in weight and PLD coating with 0.7 mg in weight, and 2) Concentrated sunlight exposure only as a blank.

The solar concentrator apparatus setup employed was the one described on chapter 3, and an image of the configuration with 1 mirror module is presented on figure 5.1. The solar radiance readings for the experiments were always between 600 and 700 W/m^2 during the months of November and December. In this study only one module of mirror was used. 1 ml of MB dye in circulation solution was collected every 30 minutes, and in the case of the colloidal solutions, the sample was centrifuged to prevent the catalyst scattering and then absorbance was recorded using spectrophotometry at 663 nm to evaluate the degradation rate. The relative degradation and the K constants were calculated using the equations 1 and 2 presented on chapter 4, where C_0 and C are the initial and final concentrations of the dye respectively. The same procedure was used for all the different concentrations of the ZnO catalyst (0.1, 0.3, 0.6 g/L) and immobilized coatings photocatalysis experiments, keeping constant the concentration of dye and the % degradation was determined [250]. All the experiments were performed at a controlled temperature range between 27 and 38 °C.

Figure 5.1: Solar concentrator configuration used for this investigation.

5.7 Colloidal photocatalysis - Properties of the synthesized ZnO particles

5.7.1 UV-Visible spectrophotometry

UV-vis absorption spectrum was obtained in order to evaluate the optical absorbance behavior for the synthesized ZnO as depicted in figure 5.2. The absorption peaks observed for both ZnO-Green and ZnO-Chem at the wavelength of about 373 nm reflect the ZnO NPs formation [251]. The characteristic absorption band at 373 nm can be assigned to the intrinsic absorption of the BG of ZnO NSs due to electron (e^-) transition from the VB to the CB, i.e. (O2p-Zn3d) [252]. The energy of the optical BG (*Eg*) can be determined by the *Tauc* model in the high absorption range. In the case of a direct gap of a semiconductor like ZnO, the following relation links the absorption coefficient α to the photon energy hυ [253]:

$$\alpha h\upsilon = A\,(h\upsilon - Eg)^{1/2} \qquad (2)$$

Where h is the Planck constant, A is a proportionality constant, Eg is the optical BG energy (eV) and the 1/2 exponent applies to direct allowed optical transitions. The direct BG energy was estimated as shown in figure 5.2. The linear region of the plot is extrapolated in order to intersect the x-axis, thus giving Eg. The BG for ZnO-Green and the ZnO-Chem samples are 2.8 eV and 2.9 eV respectively, which are in good agreement with the reported value for ZnO [241]. The value of the BG energy corresponding to the ZnO-Green sample is smaller than that of ZnO-Chem. The decrease in the BG energy can be possibly explained by the metal ions content present in the plant extract.

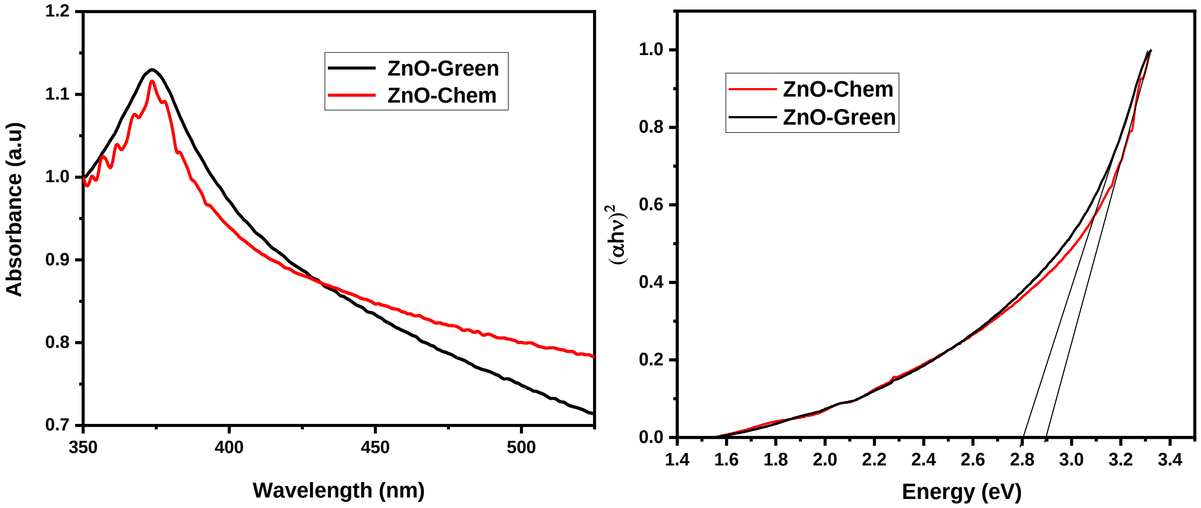

Figure 5.2: UV-Visible spectra of both ZnO-Green and ZnO-Chem (left) and Plot of $(\alpha h\upsilon)^{2}$ versus photon energy for the ZnO-Chem and ZnO-Green samples (right).

5.7.2 X-Ray diffraction (XRD) analysis

XRD patterns of ZnO NSs produced by both green (ZnO-Green) and chemical (ZnO-Chem) synthesis are presented in figure 5.3. The diffraction peaks from both samples indicate the nanocrystalline structure. Further, the diffraction peaks at angles (2θ) around 31°, 34°, 36°, 47°, 56°, 62°, 66°, 67°, 69°, 72°, 76° indexed to the (100), (002), (101), (102), (110), (103), (200), (112), (201), (004) and (202) crystal planes respectively belong to the ZnO wurtzite crystalline phase confirmed from JCPDS card No. 36-1451. The produced ZnO NPs showed high purity and crystallinity being all the X-ray diffraction peaks related to the ZnO wurtzite crystalline phase. The crystalline size of ZnO was estimated by Scherrer's equation: [254]

$$d = \frac{K\lambda}{\beta \cos\theta} \qquad (3)$$

Where, K is a constant (K=0.9), λ is the wavelength of X-rays and β is the value of full width at half maximum (FWHM). The average crystallite size of the green-synthesized ZnO results of 19 nm, whereas the crystallite average size for the ZnO chemically synthesized was 26 nm. Hence, we can suggest that bioactive secondary metabolites in the plant extract play a role in reducing particle size. This aspect will be subject of further investigation.

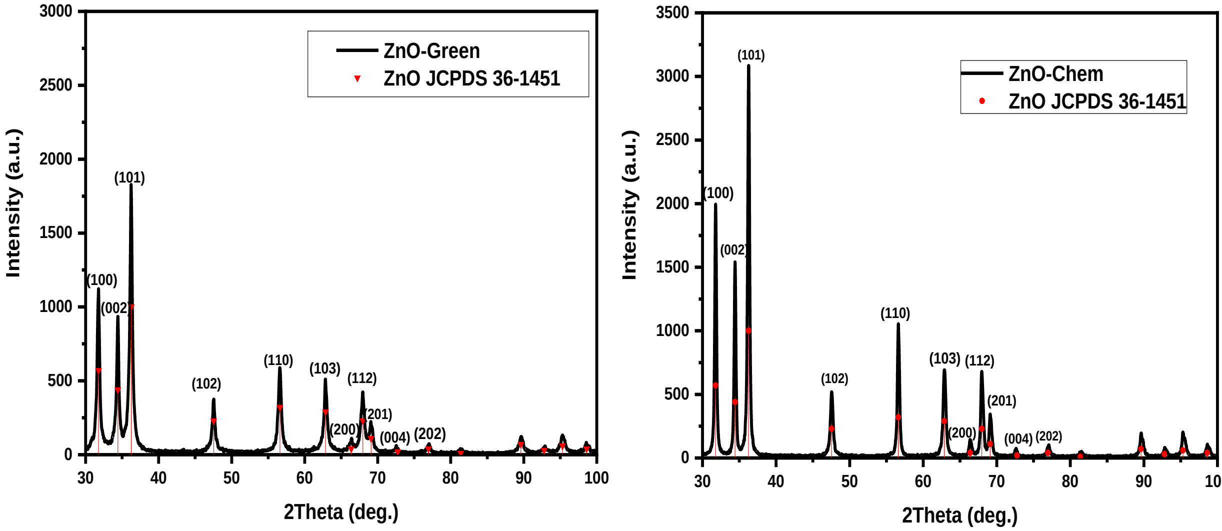

Figure 5.3: XRD patterns of ZnO-Green (left) and ZnO-Chem NSs(right).

5.7.3 FESEM analysis of synthesized ZnO particles

Figure 5.4 shows the FESEM analysis of ZnO. The images clearly illustrate the formation of nanocrystalline structures that have different morphology and sizes depending on the synthesis method. Figure 5.4a shows that the chemically synthesized ZnO NPs (ZnO-Chem) assemble into aggregates of elongated shape, in line with other literature reports [238]. In Figure 5.4b, ZnO-Green shows instead vertically aligned nanorods having an average diameter of ~30-40 nm and length of ~100-200 nm, and each individual ZnO NRs has well-developed hexagonal facets. This result is likely due to the effect of the plant extract promoting a specific structure of ZnO NRs.

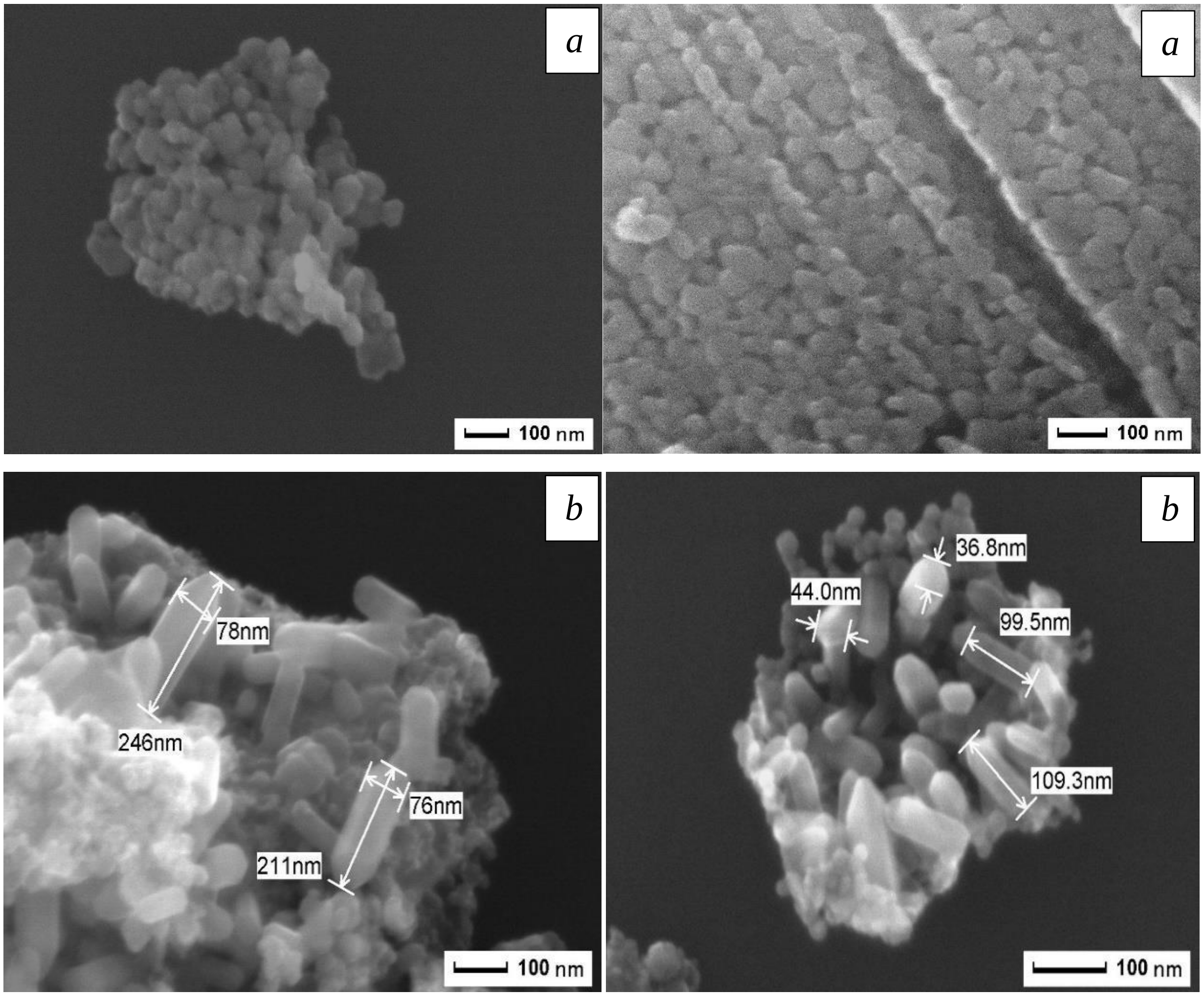

Figure 5.4: FESEM images of a) ZnO chemically synthesized (ZnO-Chem), and b) ZnO synthesized using plant extract (ZnO-Green).

The elemental composition of the samples determined by means of EDXS analysis is presented in figure 5.5. The presence of Zn and O peaks (Fig. 5.5a) confirms that the NPs synthesized by the chemical method are primarily made of ZnO. Figure 5.5b suggests the presence of ZnO and other elements typically contained in garlic extract (ZnO-Green) [255].

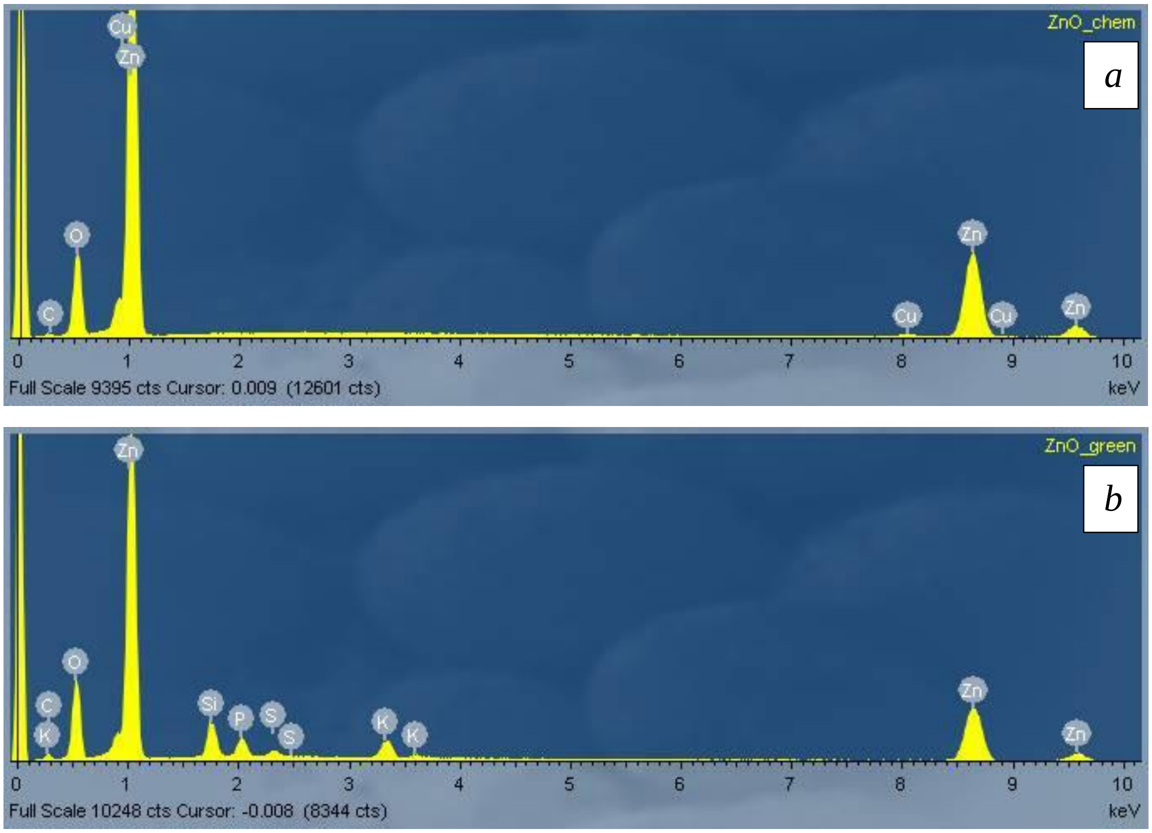

Figure 5.5: Energy dispersive X-ray spectroscopy spectrum of (a) ZnO-Chem and (b) ZnO-Green.

5.8 Heterogeneous solar photocatalysis (PC) - colloidal suspension

The PC efficiency of ZnO is generally assigned to a smaller size, a uniform morphology, [256] effective migration of photo produced electron-hole (e^--h^+) pairs toward the surface [257] as well as the high absorption of light due to oxygen vacancies. These last narrow the NPs BG and provides a transient trapping state for the photo-generated e^-, which inhibits their recombination [258–260]. Further, better absorption of oxygen from water with high surface oxygen vacancies, ensuing in the generation of a greater number of reactive radicals ($OH^{\cdot}$ and O^{2-}) [261].

PC processes involving ZnO in MB solution produce radicals that could then act as reactive species to degrade the adsorbed organic pollutants [262]. More specifically [263]:

$$ZnO + \mathbf{h\upsilon} \rightarrow ZnO\ (h^+_{VB} + e^-_{CB}) \quad (4)$$

$$H_2O + h^+_{VB} \rightarrow OH^{\cdot} + H^+ \quad (5)$$

$$O_2 + e^-_{CB} \rightarrow O_2^{-\cdot} \quad (6)$$

$$O_2^{-}.+ H^{+} \rightarrow HO_2^{\cdot} \ (7)$$

$$HO_2^{-} + H^{+} \rightarrow H_2O_2 \ (8)$$

$$H_2O_2 + \mathbf{h\upsilon} \rightarrow 2OH^{\cdot} \ (9)$$

Harmful compounds that are in interaction with $OH^{\cdot}$ or O^{2-} → Intermediates → harmless product (10)

The PC degradation mechanism of MB is illustrated on figure 5.6.

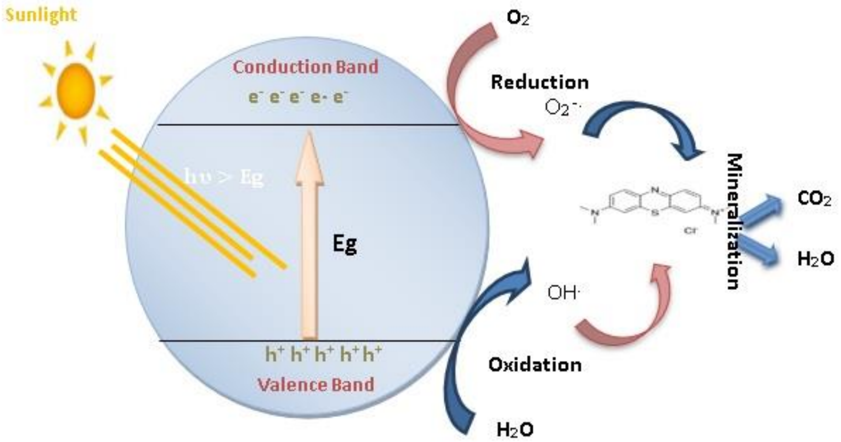

Figure 5.6: PC mechanism occurring over ZnO.

The plot of C_0/C vs time for the MB relative degradation using the synthesized ZnO NSs under sunlight irradiation in colloidal suspension is shown in figure 5.7. The decolorization of MB was insignificant in the absence of ZnO catalyst and in dark condition. Hence, MB decolorization engenders mainly from the PCA of photoexcited ZnO NSs.

As can be seen, 0.1, 0.3 and 0.6 g/L concentrations are effective for the degradation of MB along 120 minutes solar photocatalysis experiment presenting degradations of 78%, 94% and 94%. With solely concentrated solar light (only sun experiment) the degradation is indeed only 55%. It can be also inferred that 0.6 and 0.3 g/L concentrations reach the same final result in the end of the 120 min experiment, however 0.6 g/L concentration shows an initial superior performance in the degradation with estimated kinetic parameters as given in figure 5.7a. The PC degradation was modeled by the pseudo-first order model expressed in chapter 3, defined by Langmuir–Hinshelwood for low concentration of MB solution. [264]. Figure 5.7b presents the compared results of the NSs performance of the ZnO-Green and ZnO-Chem under the same concentration of

0.6 g/L. The data clearly show that the ZnO NRs synthesized from green method gives higher PCA than the ZnO nanocrystals synthesized by chemical method. This suggests that the photodegradation rate is higher for smaller crystalline sizes of NRs as obtained by green method with the charge carrier recombination effect greatly reduced in NRs architecture [182].

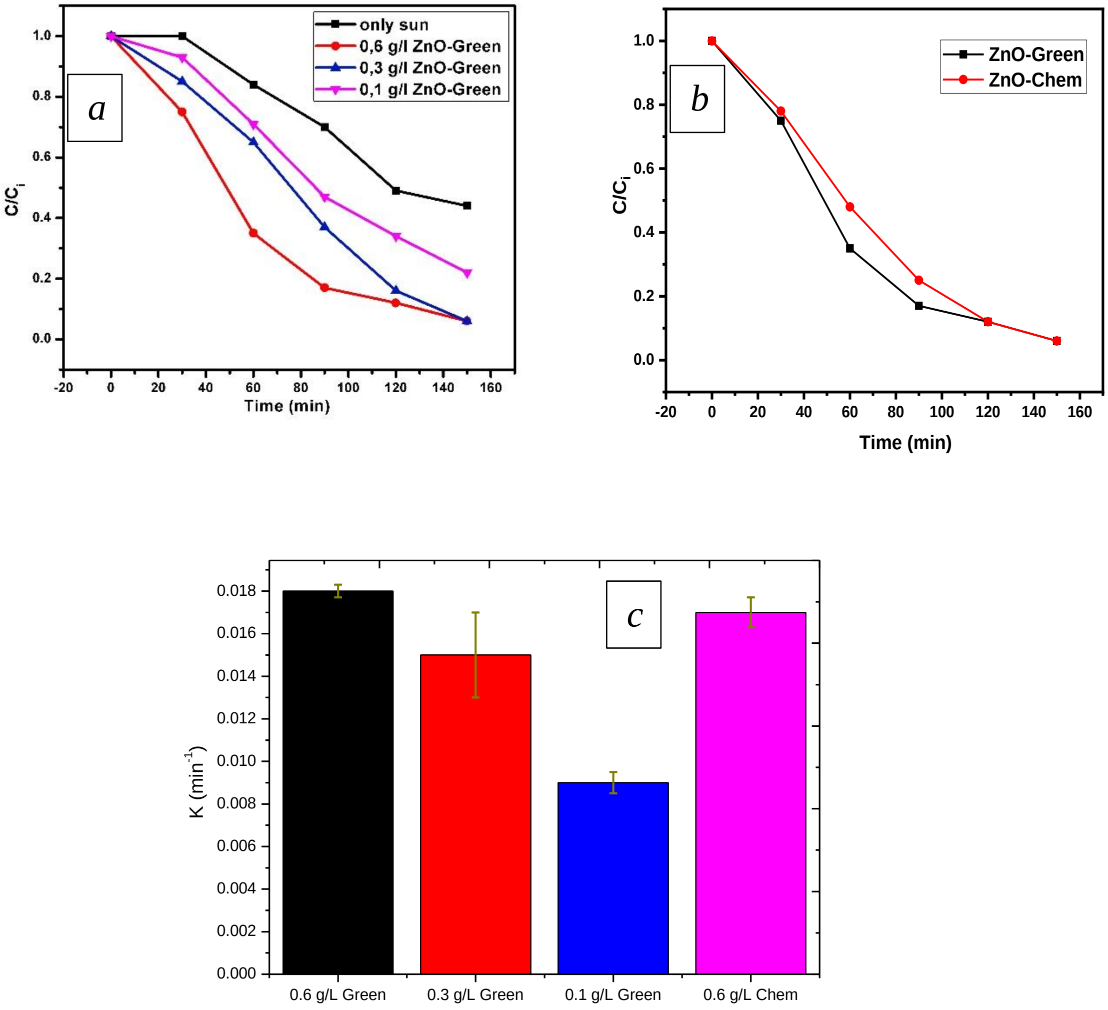

Figure 5.7**:** a) Photodegradation of 10 ppm MB dye under sunlight irradiation at different photocatalyst concentrations, b) comparison of the PCA between ZnO-green and ZnO-Chem, and c) kinetic constants for photodegradation of MB dye under sunlight irradiation.

Table 5.1 presents a comparison of our results with ZnO prepared by other biomaterials as well as chemically synthesized ZnO used for PC degradation of MB dye.

Table 5.1: Comparison of PCs from previous works with ZnO based catalyst for MB degradation.

Synthesis method	**Irradiation**	**MB concentration**	**Catalyst load**	**Degradation (%)**	**Rate constant k (min^{-1})**	**Ref.**
Green synthesis	Visible light	6 ppm	1g/L	96% in 420 min	-	[265]
Green synthesis	UV light	15 ppm	1 g/L	84 % in 120 min	-	[266]
Chemical method	UV light	10ppm	1g/L	80% in 240min	0.0208	[267]
Precipitation	UV light	20 ppm	0.25 g/L	81% in 180 min	0.0084	[268]
Sol-gel				92% in 180 min	0.0124	
Green synthesis	UV light	5 ppm	1 g/L	90% in 150 min	0.0130	[269]
Green synthesis	UV light	16 ppm	0.8 g/L	74 % in 180 min	0.0073	[270]
Green synthesis	UV light	10 ppm	0.24 g/L	85% in 120 min	0.0175	[271]
	Sunlight			92% in 120 min	0.0190	
Green synthesis	Sunlight	25 ppm	0.5 g/L	90% in 120 min	-	[272]
Green synthesis	Sunlight	20 ppm	0.5 g/L	88%in 270 min	0.0100	[273]
Green synthesis	**Sunlight**	**10 ppm**	**0.6 g/L**	**94% in 120 min**	**0.0183**	**This Work**
Co-precipitation				**94% in 120 min**	**0.0172**	

5.9 Coatings photocatalysis - Properties of the synthesized ZnO films

5.9.1 XRD analysis

Figure 5.8 shows the XRD diffraction peaks of the as deposited and annealed ZnO films produced by PLD on silicon substrate. The XRD pattern of the ZnO-PLD film annealed at 600°C reveals a textured crystalline nature, exhibiting the (002), (101), (100) and (110) diffraction peaks with (002) preferred orientation of crystal growth thus showing hexagonal wurtzite structure. The as-deposited sample mainly has a (002) oriented texture not evidencing a full crystalline structure, possibly because of the amorphous nature of films produced by PLD. The crystallite size of the prepared ZnO samples was estimated through Debye Scherrer formula using the FWHM value of (002) crystallographic plane. The average grain sizes of as deposited and annealed ZnO films are 10.4 and 22.3 nm, respectively.

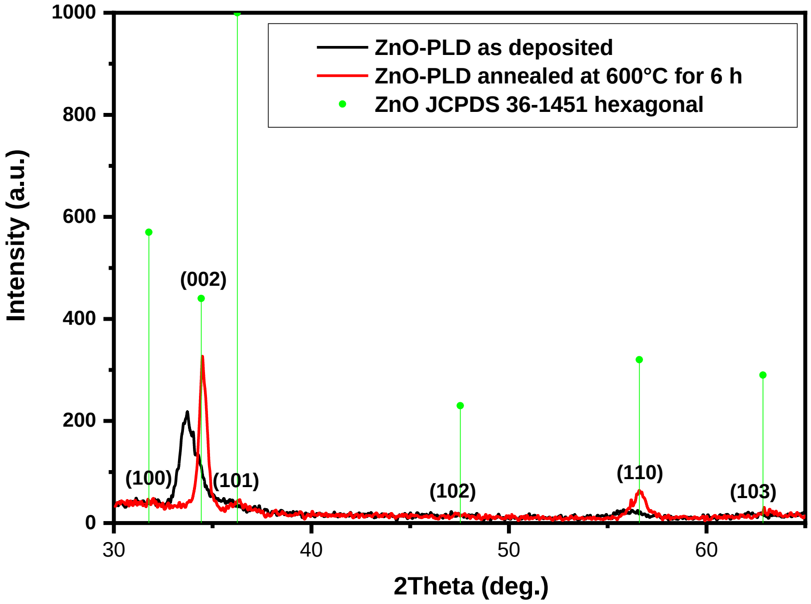

Figure 5.8: XRD diffraction peaks of the as-deposited and annealed ZnO films grown by PLD.

5.9.2 FESEM analysis of the coatings

FESEM images of as grown and annealed ZnO-PLD thin films are illustrated in figure 5.9. Figure 5.9. (a-b) show FESEM images of cross-section cut of ZnO films grown on Si (100) with a thickness of 114 nm for the as deposited sample and of 135 nm for the sample annealed at 600 °C. Figure5.9 (c-d) shows surface morphologies for both samples. The annealing temperature of 600 °C (Fig. 5.9d) led to an evolution of the initial structure to a uniform and compact film with a nanostructured surface of increased roughness.

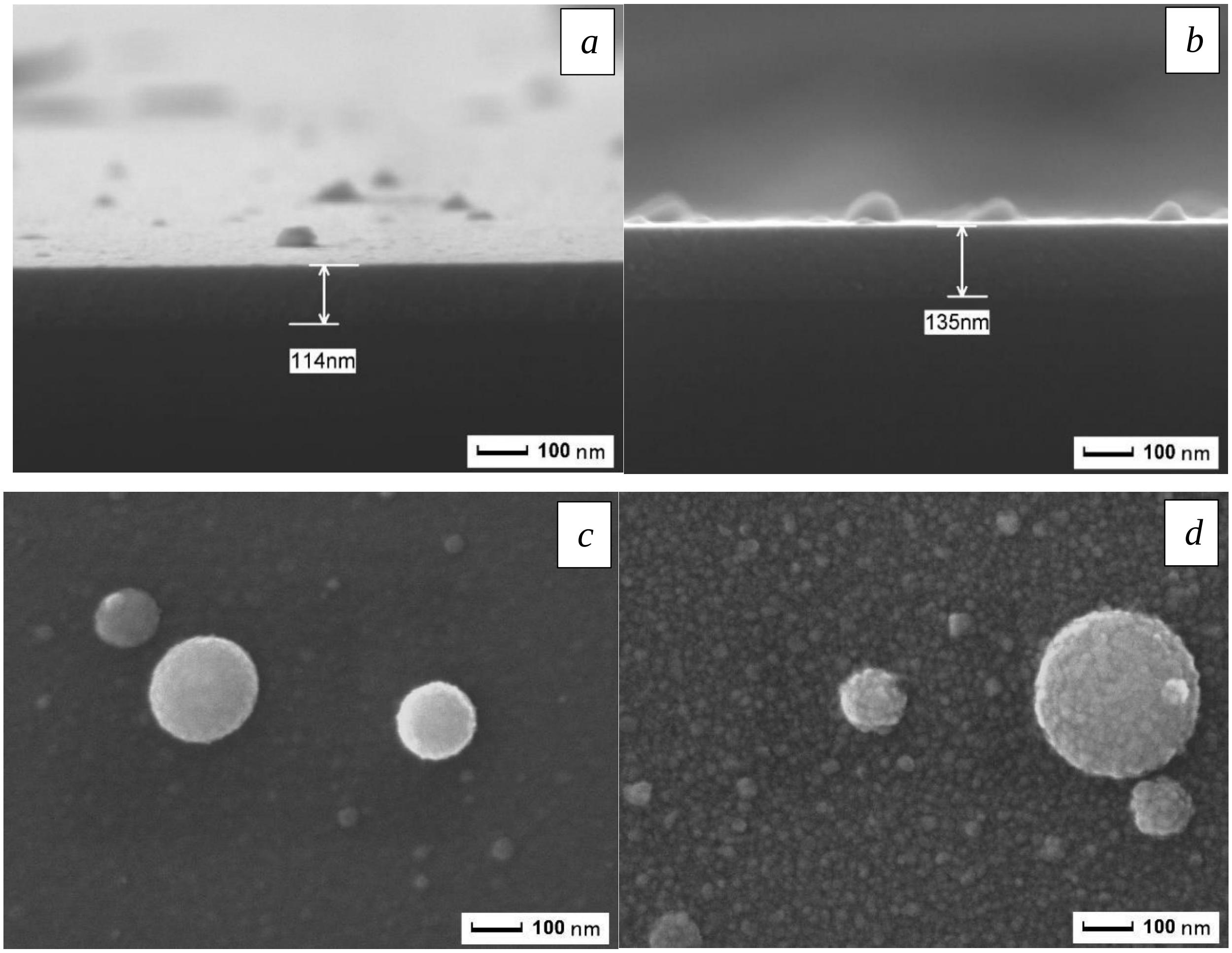

Figure 5.9: FESEM images of the as-deposited (a,c) and annealed (b,d) ZnO films grown by PLD.

Figure 5.10a) shows FESEM images of the green-synthesized ZnO thin film coated on a silicon wafer surface. Agglomeration of the particle in grains led to a porous morphology of densely packed particles. The energy dispersive spectroscopy (EDXS) spectrum of the ZnO-Green coating in figure 5.10b) indicates that the ZnO thin film is composed mainly of Zn and O, in line with the composition of the ZnO-Green powder used to produce the coatings.

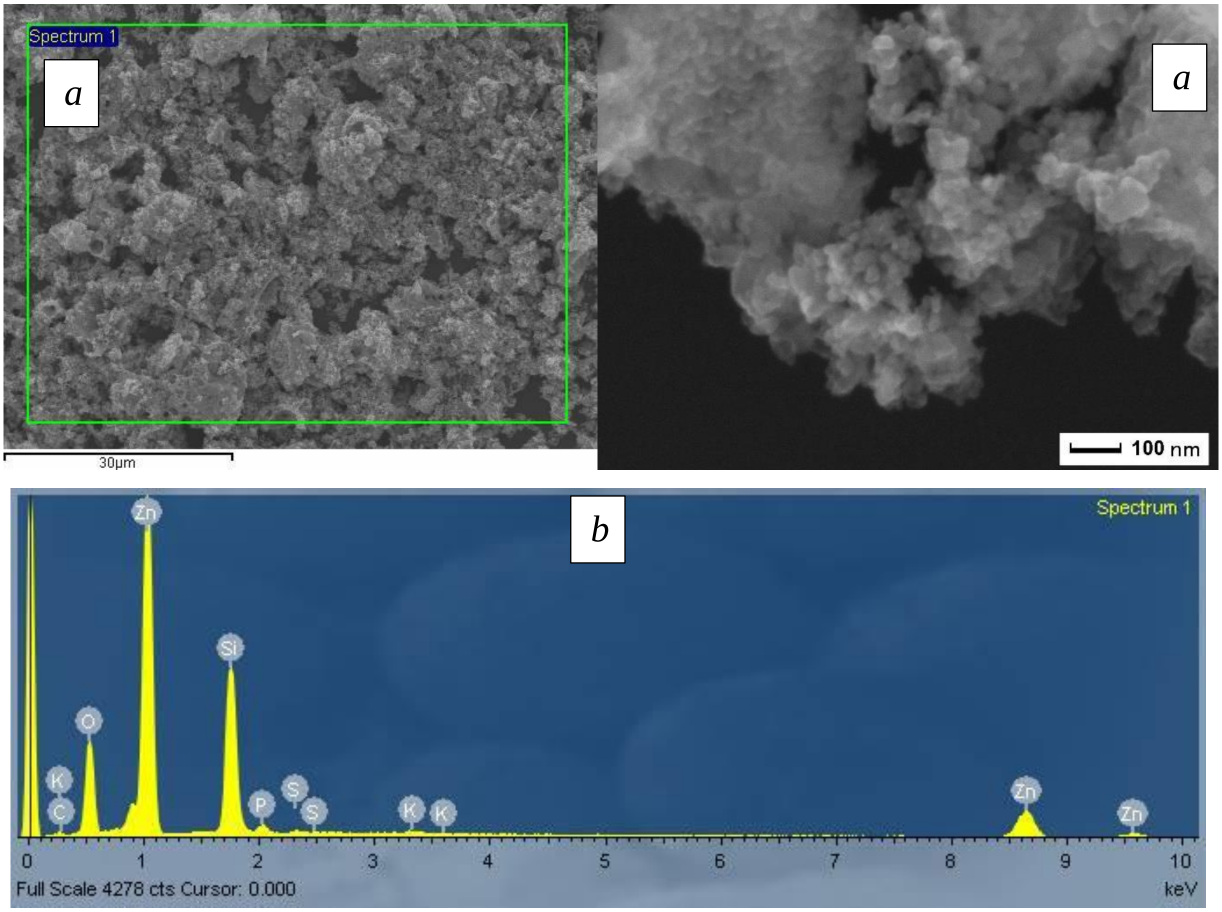

Figure 5.10: a) FESEM images of ZnO-Green coating, and b) the energy dispersive spectroscopy (EDXS) spectrum.

5.10 Heterogeneous solar photocatalysis - immobilized ZnO coatings

Figure 5.11(a) depicts the time-dependent PCA of the ZnO-Green and the PLD ZnO coatings towards MB degradation. The ZnO-PLD film induced a MB degradation of 73% and the ZnO-Green samples resulted in values of nearly 69% degradation for both the coating weights (0.6 and 0.9mg) after120 minutes of experiment. For only sun experiment, the degradation was 55%. The photo-degradation rate (Fig 5.11b) resulted in 9.77 $\times 10^{-3}$, 7.37×10^{-3}, and 7.54×10^{-3} min^{-1} for the PLD ZnO film, ZnO-Green coating with 0.6 mg, and ZnO-Green coating with 1.9 mg respectively. This proves that it is possible and easy to produce, through green path, ZnO thin films with PCA efficiency comparable to the ZnO film grown by PLD.

By evaluating the degradation response, it can be noticed that the increase in the weight and consequently the thickness of the biosynthesized ZnO coating, does not lead to a significant enhancement in the PC performance. This result can be understood because the PC reaction occurs at the interface between the ZnO catalyst surface and MB pollutant, [274] and so further increase in ZnO film thickness does not enhance the PCA of the material despite a higher amount of photocatalyst [275,276].

On the other hand, this technique can produce highly porous ZnO films having a large surface area [277], thus overcoming the problem of the limited surface area usually associated to supported catalysts. Finally, it is observed that the green route synthesis gives coatings having comparable PCA efficiency as that of ZnO films fabricated by PLD.

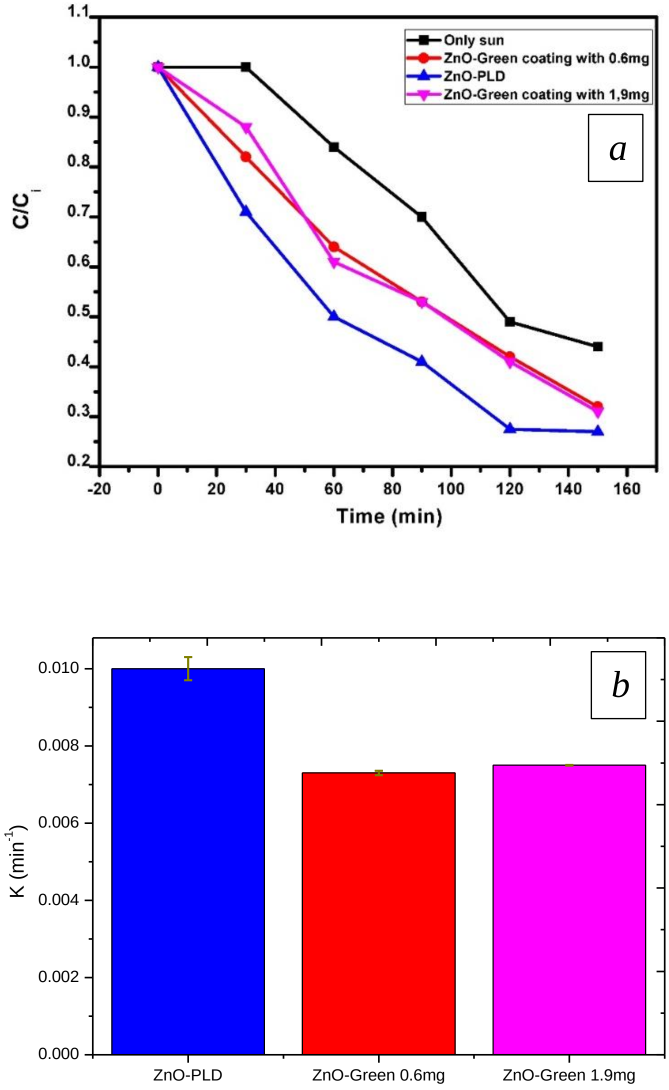

Figure 5.11: a) PCA efficiency on the ZnO-PLD film, ZnO-Green coating (0.6mg), ZnO-Green coating (1.9mg) and b) kinetic constants for photodegradation of MB dye under sunlight irradiation

The reaction rate constant and the degradation efficiency values obtained in this work are compared with previously reported ones using different techniques of deposition in table 5.2.

Table 5.2: Comparison of PCAs from previous reported works with ZnO based films as catalyst toward MB degradation.

Synthesis method	**Source of irradiation**	**MB concentration**	**Degradation (%)**	**Rate constant K (min^{-1})**	**Ref.**
Sol-gel	UV-light	10 ppm	67% in 4h	0.005	[276]
Wet Chemical route	UV light	3 ppm	92% in 2h	-	[278]
Electrospinning	UV –A light	-	80% in 4h	0.006	[279]
Pyrolysis spray	UV-light	8 ppm	99% in 3h	0.024	[280]
RF Magnetron Sputtering	UV-light	3 ppm	95.6 % in 5h	0.01	[281]
Grown by CBD on a 3 nm seed layer deposited by ALD	UV-light	4.8 ppm	100% in 4 h	0.043	[275]
Sol-gel method and deposited by the Doctor Blade method	Visible light	10 ppm	2.7% in 2 h 44.8% in 2h	0.0002 0.041	[282]
PLD	**Concentrated sunlight**	**10 ppm**	**73% in 2h**	**0.01**	**This work**
coating with 0.6mg **coating with 1.9mg**			**68% in 2h** **69% in 2h**	**0.0073** **0.0075**	

The data reported on table 5.2 leads to the conclusion that the reaction rate and the degradation efficiencies achieved in this study are competitive with respect to other literature results. To estimate the stability of the prepared ZnO nanostructured thin films, catalyst samples were weighted again after the 120 min experimental run and resulted in a 25%, 10% and 0% loss of material for ZnO-Green coatings with 0.6 mg, ZnO-Green coatings with 1.9 mg and the ZnO-PLD film respectively. The enhanced stability of the PLD film is likely due to its more compact morphology and to intrinsically better adhesion given by the PLD technique. The loss of material for the ZnO-Green coatings, though limited, will be investigated by further optimization of the spin-coating procedure to maximize adhesion and mechanical stability.

5.11 Conclusions

In this research work we reported the PCA of ZnO photocatalysts (particles and films) synthesized through either a green, a conventional chemical, and a PLD process. ZnO nanorods were produced via green synthesis using natural extract as reducing and stabilizer agent, hence playing a significant role towards structural evolution. The results reveal that green ZnO, both in the form of thin films and in the form of suspension, can be fruitfully used for PC application. Indeed, the PC efficiency of green-synthesized ZnO NRs deposited by spin-coating is almost equivalent to that ZnO films grown by PLD. This means that the green method-based technique can produce environmentally friendly ZnO NRs to achieve high PC performance towards MB dye degradation. Economic evaluation of the costs (appendix C) highlights that the green-synthesis is also cost-effective, reducing the photocatalysts-associated cost by 35%. A further contribution is given by the lowest operating cost of the solar concentrator. These findings pave the way for the application of ZnO-based solar photocatalysis in wastewater treatments at large scale.

Chapter 6 – Treatment of surfactant-rich industrial wastewaters with concentrated sunlight: toward solar wastewater remediation

Preview: this chapter reports the work developed on the application of a photo-Fenton process powered by concentrated sunlight for the treatment of surfactant-rich industrial wastewaters. This approach fulfills the interest for the development of low-cost/high-yield real wastewater treatment process. As a general overview, employing as a stage in wastewater treatment plants or as a small-scale stand-alone operated by small-medium enterprises could reduce the environmental and economic impact of wastewaters. As one of the authors of this article, my contribution includes the synthesis of iron oxide photocatalyst coatings and performing the experimental campaign.

The content of this chapter was adapted from:
Orlandi, M.; Filosa, N.; Bettonte, M.; Fendrich, M.; Girardini, M.; Battistini, T.; Miotello, A.. Int. J. Environ. Sci. Technol. **2019**, 16. https://doi.org/10.1007/s13762-018-2099-7

6.1 Introduction

Despite great advancements in the last decades, both in terms of technology and of regulations, the extensive use of surfactants still raises major environmental concerns [283,284]. Broadly defined as substances which lower the surface tension of the medium in which they are dissolved [285], surfactants have a wide range of applications, ranging from detergents to pharmacy, resulting in large quantities of contaminated waters. Their inherently high solubility also means that they can be present in wastewaters at very high concentrations, posing a challenge to otherwise effective conventional, e.g., biological removal methods [286]. Furthermore, while an extensive body of the literature exists on their toxicity and biodegradation routes [287,288], the effects on humans and the environment of their degradation products are less well established [289]. Aside from environmental considerations, the economic context needs also to be considered. In most advanced economies, surfactant concentrations in wastewaters are regulated [290] and treatment of these pollutants is often mandatory and provided by specialized companies as a service. This translates into a cost for manufacturing companies, especially important for small-medium enterprises (SMEs) which often do not possess their own treatment facilities. In countries where surfactants are not regulated, they are not only a serious threat to the environment, but also exacerbate the conflict of use between industry, agriculture and domestic needs, limiting industrial development. A possibility to overcome these problems is offered by advanced oxidation processes (AOP). These are innovative water treatment technologies, based on the in situ generation of highly reactive transitory species (e.g., hydroxyl radical, superoxide radical) [10]. Among the AOPs, photocatalysis has demonstrated its efficiency in degrading a wide range of pollutants [11], but its industrial application has been limited to special cases only, where conventional methods are not viable. This is due mainly to the very high cost imposed by the use of artificial UV radiation as the preferential light source. Indeed, UV lamps are expensive, have a short operational lifetime and require a high energy input. This chapter reports the investigation on a treatment method based on an AOP in the form of a photo-Fenton reaction powered by concentrated sunlight. The treatment is directed at the abatement of large quantities of common surfactants, rather than targeting a specific molecule. This motivates the choice of a photochemical reactor based on photo-Fenton, a well-established process for generating hydroxyl radicals; these species are powerful oxidants and react with a wide range of organic compounds in water [12,13,115,116]. Furthermore, the combination of a photo-Fenton reactor and a solar concentrator allows to take advantage of the UV–visible portion of the solar spectrum, thus effectively exploiting a large density of near-UV radiation through a renewable, carbon-free and potentially zero-cost energy source.

6.2 Materials and methods

For the experiments, three mirror modules were mounted on the solar concentrator providing a concentration factor of nearly 2500X on a circular (5.8 cm diameter) focus. It can be noted that while a portion of UV photons ($\lambda < 330$ nm) is lost with respect to sunlight, the remaining part ($325 < \lambda < 400$ nm) is concentrated within the range of 2500X ratio, thus acting as an effective near-UV light source. The reactor was the quartz tube (150 ml volume) reported in chapter 3 and an image with the experiment configured for the surfactant-rich wastewater is shown in figure 6.1. Forced circulation of the sample between the reactor and a 2 L reservoir was provided by an independent pumping system (volumetric flow rate 5 L/h). This setup was used for the treatment of industrial wastewaters provided by the company Aquaspace spa (Rovereto, Italy). The samples contained high quantities (5–20 g/L) of the most common surfactants used as detergent. All the data reported are from experiments with comparable solar irradiance. Two kinds of samples were treated: (1) wastewaters as received at the plant were subjected to a heterogeneous photocatalytic process, using an iron-based nanocatalyst [105] and (2) wastewaters extracted from the Aquaspace plant physico-chemical treatment unit, after the addition of known amounts of $FeCl_3$, employed as a coagulant, were subjected to homogeneous catalysis. H_2O_2 concentrations were chosen, according to recent the literature reports [158,291], to provide a quantity of radicals sufficient to degrade all the surfactants and to limit OH radicals scavenging by other organic species. Since the focus is on large quantities, no specific surfactant was followed. A photometric method for the determination of the total quantity was chosen instead. This is already extensively employed in water treatment plants for routine analysis. Thus, surfactants concentrations were determined before and after each treatment by use of commercial photometric evaluation kits (Hach Lange), LCK 334, LCK 331 and LCK 333, respectively, for total anionic surfactants, total cationic surfactants and total nonionic surfactants. Errors in the surfactant determination are negligible (0.2 mg/L) and thus not reported in the data tables. An important feature of photocatalytic AOPs is the possibility of pollutants mineralization, defined as the conversion of organic carbon into inorganic species. In particular, the conversion to CO_2 allows for the removal of the pollutant avoiding the risk of formation of potentially toxic partial oxidation products. To verify this, CO_2 evolution during the most effective treatments was followed by an IR sensor (COZIR Wide range 100) placed in the headspace of the reservoir.

Figure 6.1: PDC configured with 3 mirror modules (left) and quartz glass lid circulating the surfactant-rich wastewater (right).

6.3 Results and discussion

6.3.1 Heterogeneous catalysis

For these series of experiments, the photocatalyst was introduced in the reactor as a thin layer deposited on a 75 mm x 25 mm glass slide, with catalyst weight kept constant at about 20 mg. This quantity was chosen to ensure complete surface coverage. The iron-based catalyst (3D hierarchical nanostructured α-Fe_2O_3 coatings on glass substrate) fabricated by PLD was chosen for several reasons: (1) it absorbs a good portion of the sunlight spectrum, (2) it is a non-toxic and non-hazardous material, (3) it is cheap and easily fabricated and (4) it is active toward the photo-Fenton reaction. A previous paper details the catalyst fabrication, characterization and catalytic activity [105]. Indeed, this material showed very promising photoactivity toward degradation of a model dye (MB), along with remarkable stability and reusability. These properties are attributed to enhanced surface area and synergy effects between the spatially organized nanostructured features composing the surface: urchin-like particles with radially growing nanowires and nanorods and flower-like particles with nanosized flakes shown in figure 6.2. The main drawbacks are sub-optimal intrinsic catalytic properties, due mainly to the very short mean diffusion length (2-4 nm) for holes in α-Fe_2O_3 [86], resulting in only a very thin layer (< 5 nm) contributing to photoactivity. Stability in acidic-to-neutral pH, another known issue for α-Fe_2O_3 [292], is however found to be enhanced in this material. A wastewater stock with total surfactant concentration of about 20 g/L was divided into a batch of 1L volume samples and treated according to the following scheme:

(a) reference: not treated, kept in the dark;
(b) blank: treated for 1 h with concentrated solar light;
(c) catalyst: treated for 1 h with concentrated solar light in presence of photocatalyst only;
(d) H_2O_2: treated for 1 h with concentrated solar light in presence of H_2O_2 1 M (without catalyst);
(e) H_2O_2 + catalyst: treated for 1 h with concentrated solar light in presence of H_2O_2 1 M and photocatalyst.

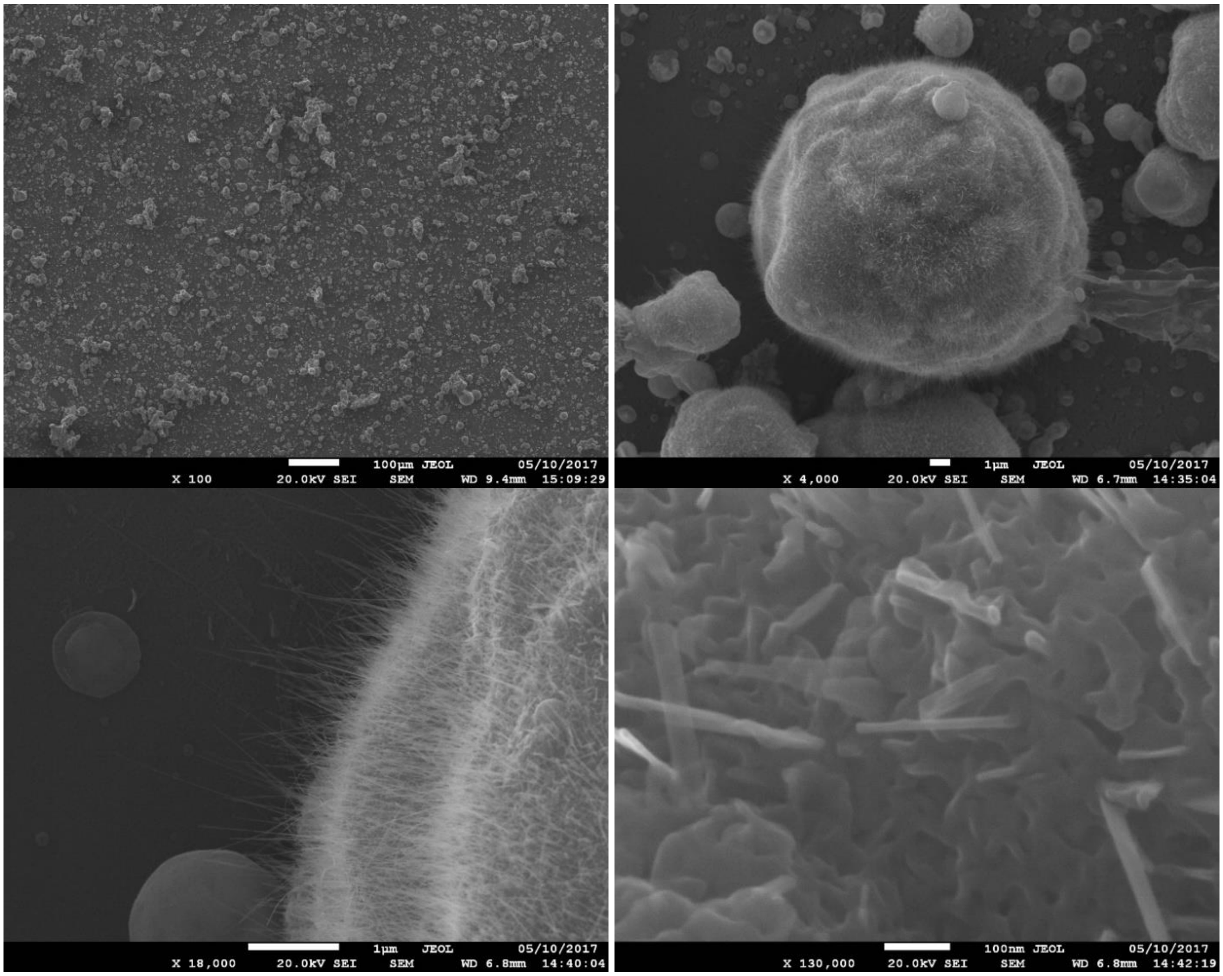

Figure 6.2: Iron oxide (hematite, α-Fe_2O_3) fabricated by PLD used in the heterogenous photocatalysis treatment. From top-left clockwise, magnifications of 100X, 4000X, 18000X and 130000X respectively.

The pH was not adjusted before or during treatment to keep it constant: it is neutral for (a), (b) and (c) and mildly acidic (pH 5) for (d) and (e). Given that the distribution of species for iron does not significantly change in the pH range 5–8, as can be seen from the *Pourbaix* diagram [292], this does not compromise comparison between experiments. An advantage of the use of solar energy, especially if concentrated, is the possibility to maintain near boiling temperatures without additional energy costs. In view of a potential application, this is expected to help the degradation of thermolabile surfactants. However, in our case the samples were kept at 30 ± 10 °C for the duration of the treatment, to minimize thermolysis in order to simplify data interpretation. Results are reported in Table 6.1. In the case of experiment (b) where only light is present, the degradation of surfactants could be ascribed to photochemical reactions [293]. The higher values in presence of the catalyst (c) could be attributed to trapping by the highly structured surface, increasing the amount of time for which the pollutant is exposed to concentrated sunlight, combined with surface reactions such as oxidation by the valence band holes of the material. In the case of (d), reactivity is likely due to OH° radicals generated by the homolytic decomposition of H_2O_2 by UV photons. While the molar extinction coefficient values for H_2O_2 in water are low (1 at 300 nm and 0.01 at 360 nm, with intermediate values in between) they're not negligible, especially considering that light in our system is concentrated with an 870X ratio. The hypothesis of OH° radicals' production from UV absorption for (d) is thus a reasonable one. The analysis results are instead compatible with a photo-Fenton reaction for experiment (e). In this case, the absolute quantity of degraded surfactants (4.5 g, 23.5% of the total) is remarkable, all the more considering the amount of catalyst (20 mg). Figure 6.3 shows the CO_2 evolution, is also significant for case (e), the photo-Fenton reaction, showing a saturation of the headspace in just a few minutes, while it is negligible in absence of H_2O_2. It has to be noted here that these data are in no way quantitative, since the system is not airtight. However, though qualitative, they indicate clearly that pollutants conversion to CO_2 takes place.

Table 6.1: Surfactants concentration and degradation yield in heterogeneous catalysis conditions.

	(a) Reference	**(b) Blank**	**(c) Cat.**	**(d) H_2O_2**	**(e) H_2O_2 + cat.**
Concentration (mg/L)					
Anionic	14,800	14,400	13,500	13,000	12,000
Cationic	780	270	332	323	242
Nonionic	3370	3250	3350	2315	2245
Degradation[a] (mg/L)					
Anionic		400	1300	1800	2800
Cationic		510	448	457	538
Nonionic		120	20	1055	1125
% Degradation[a]					
Anionic		2.7	8.8	12.2	18.9
Cationic		65.4	57.4	58.6	69.0
Nonionic		3.6	0.6	31.3	33.4
% Total		**5.8**	**9.3**	**17.5**	**23.5**

[a] Considered as the missing mass

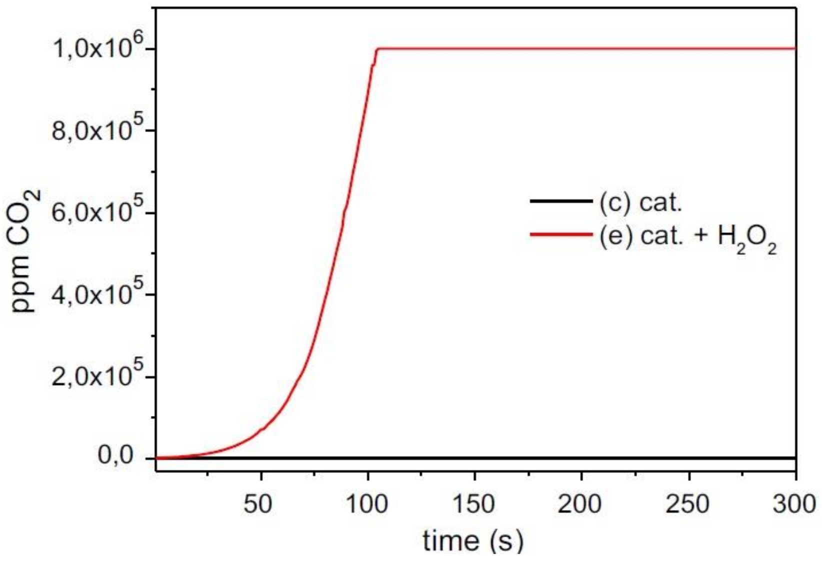

Figure 6.3: CO_2 evolution in heterogeneous catalysis conditions

6.3.2 Homogeneous catalysis

In this case, no catalyst was introduced in the system, since the wastewaters already contain $FeCl_3$, added as part of the routine physico-chemical stage operation of the plant. $FeCl_3$ provides the iron ions to enable the photo-Fenton reaction, although it is not an ideal source, since chloride ions are known inhibitors for this process [82]. A wastewater stock with total surfactants concentration of 4.9 g/L and $FeCl_3$, 9×10^{-3} M was divided into a batch of 1L volume samples and treated according to the following scheme:

(a) reference: not treated, kept in the dark;
(b) blank: treated for 10 min with concentrated solar light;
(c) Fenton blank 0.2: treated for 10 min with H_2O_2 0.2 M under dark;
(d) Fenton blank 0.5: treated for 2 min with H_2O_2 0.5 M under dark;
(e) photo-Fenton 0.2: treated for 10 min with H_2O_2 0.2 M with concentrated sunlight;
(f) photo-Fenton 0.5: treated for 2 min with H_2O_2 0.5 M with concentrated sunlight.

Upon H_2O_2 addition, reactions were observed to be very intense and accompanied by vigorous bubbling. This is attributed to the occurrence of a Fenton process, which was then evaluated with experiments (c) and (d). The H_2O_2 concentration was reduced to 0.5 and 0.2 M and shorter treatment times (10 min or 2 min vs 1 h) were necessary to keep temperature in the 25–45 °C range, again to minimize the possible thermolysis. Results are shown in Tables 6.2 and 6.3. As for the heterogeneous case, exposition to concentrated sunlight only (b) yields a limited degradation, which is, however, not accompanied by CO_2 evolution. The addition of H_2O_2 activates a Fenton process which, as seen from (c) and (d), already leads to significant surfactants degradation. However, the most remarkable results are obtained when switching to a photo-Fenton process: in the best case (f) 89% of the total (4.3 g) is degraded with an exposition time of 2 min only. Interestingly, a lower H_2O_2 concentration in (e) also leads to good results as 3.14 g, 64%, of the total surfactants are degraded with a 10 min exposition. In Figure 6.4 again, CO_2 evolution leads to headspace saturation in a few minutes under the photo-Fenton conditions, proving that a degree of conversion to inorganic carbon occurs.

Table 6.2: Surfactants concentration and degradation yield in homogeneous catalysis conditions: 10 min. treatments.

	(a) Reference	**(b) Blank 10 min.**	**(c) Fenton blank 0.2M 10 min.**	**(e) Photo- Fenton 0.2 M H_2O_2 10 min.**
Concentration (mg/L)				
Anionic	3820	3175	2475	1480
Cationic	227	236	85	66
Nonionic	858	882	723	218
Degradation[a] (mg/L)				
Anionic		645	1345	2340
Cationic		0b	142	161
Nonionic		0b	135	640
% Degradation[a]				
Anionic		17	35	61
Cationic		0b	63	71
Nonionic		0b	16	75
% Total		**13**	**33**	**64**

[a] Considered as the missing mass, [b] the small apparent increase could arise from a slightly higher temperature of (b), improving solubility.

Table 6.3: Surfactants concentration and degradation yield in homogeneous catalysis conditions: 2 min. treatments.

	(a) Reference	**(d) Fenton blank 0.5 2 min.**	**(f) Photo-Fenton 0.5 M H_2O_2 2 min.**
Concentration (mg/L)			
Anionic	3820	2500	488
Cationic	227	98	< 40
Nonionic	858	795	24
Degradation[a] (mg/L)			
Anionic		1320	3332
Cationic		129	>187
Nonionic		63	834
% Degradation[a]			
Anionic		35	87
Cationic		57	>82
Nonionic		7	97
% Total		**31**	**89**

[a] Considered as the missing mass, [b] the small apparent increase could arise from a slightly higher temperature of (b), improving solubility.

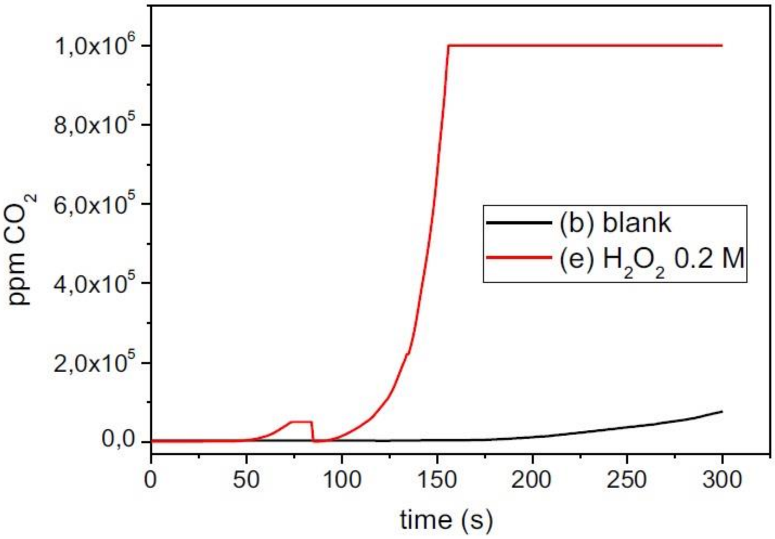

Figure 6.4: CO_2 evolution in homogeneous catalysis conditions

6.4 Conclusions

Coupling a solar concentrator to a photo-Fenton-based reactor proves to be a very effective way to abate high surfactants levels in industrial wastewaters samples, with yields of 89% in 2 min for the best homogenous and 23% in 1 h for the best heterogeneous condition. In both cases, CO_2 evolution measurements indicate conversion of organic to inorganic carbon. From this preliminary investigation and due also to the complexity of real samples, it is not possible to extract a clear picture of the degradation mechanism: This likely works via a combination of direct photolysis and photo-Fenton reactions. A dedicated investigation, possibly on model solutions, will be needed to clarify this point, but reasonable hypothesis are already advanced in the discussion section. The degradation yield for heterogeneous catalysis, though not exceptional, is already interesting, since it was obtained in nonoptimized conditions. A simple way to enhance it would be to increase the irradiated catalyst geometric area, which currently is smaller than the concentrator spot diameter. This can be done at low cost, since the catalyst itself is prepared from cheap and earth-abundant materials (Fe and B) [105]. While heterogeneous catalysis is generally more relevant industrially, mostly because of the ease of separation of reactants from products and catalysts, homogeneous catalysis is particularly interesting in our case, since it employs $FeCl_3$ as the catalyst, which is used anyway in the water treatment plant. Based on these results, it is envisioned two main applications for the process investigated:

1. integrated in conventional wastewater treatment plants could be used as a pre-treatment stage for the abatement of organic contaminants before sending the waters to a standard biological treatment. Reducing the quantity of pollutant will reduce the timescale of the biological treatment and, consequently, costs. Also, decreased residue at 105 °C, as observed for both heterogeneous and homogeneous catalysis translates into less sludge, further reducing costs;
2. as a small-scale stand-alone treatment operated in situ by SMEs, it could reduce at the source the quantity of waste to be conferred at treatment plants, thus reducing costs for the company.

Further work can be aimed at better understanding the interplay of possible degradation mechanisms (direct photolysis, photo-Fenton, thermolysis) and toward performing the treatment at higher temperatures. This is expected [294] to increase the degradation yields and can be attained without cost with the solar concentrator. An upgraded reactor design, allowing for an increased illuminated area in heterogeneous catalysis, is also under study.

Chapter 7: Remediation of organo-lead compounds in wastewater by concentrated sunlight

Preview: This work is part of a convention between the University of Trento and *Agenzia Provinciale per la Protezione dell'Ambiente* (APPA – Trento province environmental protection agency), with the objective to investigate the feasibility of applying concentrated solar light to promote the remediation of organo-lead compound contaminated water. As a participant of the convention, I had the role to proceed the experimental campaign and draft the report with the results of the study. The content of this chapter was delivered and presented to APPA as the conclusion of the convention.

This chapter was developed based on the results of the convention: *Raccolta 5/2017 CONVENZIONE UNITN - APPA per la realizzazione del progetto di ricerca "Bonifica mediante radiazione solare concentrata di acque inquinate da composti organici di piombo"*

7.1 Introduction

Water sources contamination is certainly one of the main topics of discussion for the public health worldwide [295]. Among the distinct types of contamination, lead (Pb), a xenobiotic heavy metal is reported as one of the most aggressive to human health, with important studies correlating its presence and contact to groundwaters as potential causes to schizophrenia and psychosis [296–298]. Since the years of 1970s, many efforts were dedicated to discontinue the use of organo-lead compounds from the fuel market activities [299,300]. Organo-lead substances were employed consistently from the years of 1920 and 1970 in the form of tetraethyl lead (TEL), chemical formula $(CH_3CH_2)_4Pb$, a volatile substance used as an antiknock agent to improve the gasoline octane rating [301–303]. Inhalation and ingestion are the major routes for human exposure due to its high volatility (workers) and decomposition into sub products that penetrate in soil resulting in ground water sources contamination [304,305].

In different industrial facilities studied and reported, it was observed that the dealkylation route of TEL runs the chemical path starting from TEL to triethyl lead (TREL), then to diethyl lead (DEL), unstable forms of monoethyl lead (MONO) and in inorganic lead in the form of oxides (i.e. PbO, PbO_2 and Pb_3O_4), carbonate ($PbCO_3$) and sulfate ($PbSO_4$) compounds, represented in figure 7.1 and table 7.1, in which mono alkyl lead cations are assumed to be transient species [306]. After chemical decay and/or biological degradation of organic lead compounds, the inorganic, less toxic lead is immobilized by precipitation [307–310]. Also, every dealkylation step implies a reduction in toxicity. However, while TEL is an insoluble, highly volatile compound, TREL is a moderately soluble cation, which can percolate into soil and underground water and become persistent in the absence of light and oxygen.

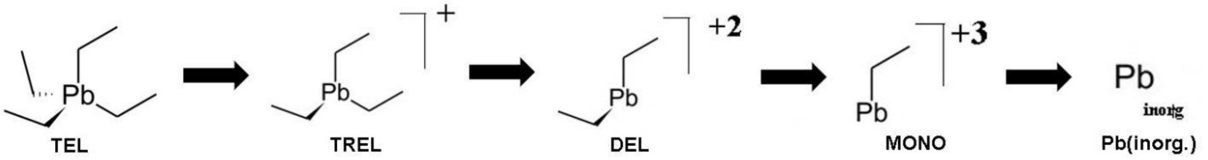

Figure 7.1: dealkylation route of organolead compounds.

Table 7.1: chemical formulas to the lead compounds in discussion

Lead compound	**Chemical Formula**
TEL	$(CH_3CH_2)_4Pb$
TREL	$(CH_3CH_2)_3Pb^+$
DEL	$(CH_3CH_2)_2Pb^{2+}$
MONO	$(CH_3CH_2)Pb^{3+}$
Pb(inorg.)	PbO, PbO_2, Pb_3O_4, $PbCO_3$, $PbSO_4$

In scientific terms, the analysis of a contaminated sample is performed under the evaluation of total organic lead (TOL) present, which is the sum of all byproducts from the decomposition of TEL. In the atmosphere, the dealkylation route is promoted by a photocatalytic environmental process in the presence of natural light (UV - hν) and air (O_2) which takes place in a time scale from hours to months. On the other hand, if subjected to remediation treatments such as the employment of advanced oxidation processes (AOP) or ultra-violet light (UV) exposure, the dealkylation process can be accelerated to the time range of seconds to minutes respectively [311–313].

In the city of Trento, north of Italy, a phased-out lead products chemical factory that operated from the 1940’s until its closure in 1978 (Ex-SLOI) has still evidences reporting levels of TOL (total organic lead: TEL + TREL + DEL) above national limits (0.9 µg/L) present in a well on the underground water. Monitoring activities have been performed since the local environmental agency (APPA, Province of Trento) has been assigned as the responsible public observer entity for the area [314]. Initial studies were already performed in order to evaluate possibilities to remediate the TOL which is present in the area along the decades and is still persistent on the contaminated water source present in the land.

Considering the possibilities to employ low cost solar concentration systems to perform AOPs, in the framework of a convention set in 2017 between UNITN and APPA, an investigation is proposed to study photo-Fenton reactions, photocatalysis, direct photolysis and combinations thereof with the experimental solar parabolic dish concentrator (PDC) apparatus at UNITN to determine degradation from a model of TREL to its sub products DEL, MONO and inorganic lead as possible solutions to remediate the persistent levels of TOL from the *”Ex-SLOI”* area.

7.2 Experimental methodology

7.2.1 Model solutions

Triethyl lead chloride in 99%, analytical grade (Dr. Ehrenstorfer GmbH) was used as the reference substance for producing model solutions with the presence of TREL. Batches of 20 L were produced to simulate the wastewater. The concentration levels of TREL varied between 60 and 90 μg/L and were prepared by the chemistry specialists from APPA. The tap water used to produce the batch had a chlorine ion (Cl-) concentration of about 1.5 x 10^{-4} M. The decision of using TREL instead of TEL is based on the following reasons: (1) TEL is an insoluble volatile compound readily converted into TREL in the atmosphere: as such, TREL and not TEL can be considered a water pollutant; (2) TREL is safer to manipulate due to low volatility and low risk of explosion. Also, TREL is a commercially available product which can be used to design experimental investigations. From the batch of 20 L, samples of 2 L were used in every experiment run proposed.

A UV–Vis-NIR absorption spectra of the TREL model solution was to verify the light absorption behavior of the substance.

The analytical method to detect of organic lead species was developed by APPA and consists of the following steps: (a) TREL and DEL were determined with an internal method after extraction with hexane of the water sample in a pH 8.5 buffered environment and in the presence of Ethylenediaminetetraacetic acid (EDTA), sodium citrate and sodium dithiocarbamate, and subsequent derivatization with Grignard reagent propyl magnesium chloride [315]. (b) The derivatives were subsequently confirmed and quantified in gas chromatography with a single quadrupole mass spectrometry detector (GC-MS). The measurement uncertainty has been evaluated considering the contributions due to repeatability, calibration and recovery. The estimate is in line with the one calculated with the Horwitz method with estimate error of 20%. The method was confirmed in the range 0.1 ug/L - 30 mg/L [316].

Tetraethyl lead was determined after adsorption on Solid-phase microextraction (SPME) fiber assembly polydimethylsiloxane (PDMS) 100 μm on the headspace of the aqueous sample and subsequent confirmation and quantification in gas chromatography with single quadrupole mass spectrometry detector [317].

Metallic lead is quantified in inductively coupled plasma mass spectrometry (ICP-MS) after acidification with HNO_3.

7.2.2 Catalyst synthesis

Iron metallic (Fe) and boric acid (H_3BO_3) powders were mixed and compressed in the form of a disc to be used as a target for the deposition of 3D hierarchical nanostructured hematite (Fe_2O_3) coating by the pulsed laser deposition technique (PLD) following already established parameters in previous report [105]. The coatings were deposited at room temperature on glass slides with dimensions of 7.5 x 2.5 cm, the weight of the catalyst was approximately 2 mg on each glass slide. Thermal annealing of the deposited coating was carried out in air at 600ºC for 4 h with a heating rate of 5 ºC/min in order to grow hierarchical urchin-like structures. The motivation of employing a ferrous coating catalyst is to enable the photo-Fenton reaction.

7.2.3 Adsorption experiments

With the aim to exclude the possibility of undesirable effects, such as adsorption by the pipes employed on this research, a set of 10 meters of PA tubing were employed to circulate the TREL reference solution under dark, four experiments were performed circulating the solution by 30, 60, 90 and 360 minutes. The circulation was controlled by a diaphragm pump system.

7.2.4 H_2O_2 oxidation lab experiment (Quenching with sodium metabisulfite - $Na_2S_2O_5$)

Direct oxidation with H_2O_2 (concentration of 1.5×10^{-2} M) under dark was performed in order to establish a blank condition and reveal the time scale of the degradation reactions. Addition of H_2O_2 is followed by quenching with sodium metabisulfite ($Na_2S_2O_5$ – 99% purity, Sigma-Aldrich) to stop the H_2O_2 reaction. This experiment was also performed to evaluate the possibility of H_2O_2 to be "masking" the analytical method results and were performed under four different times: 5, 15, 30 and 60 minutes respectively. A second experiment was done inserting in an inverted order the sodium metabisulfite ($Na_2S_2O_5$) and H_2O_2 to confirm the effectiveness of the inhibition reaction.

7.2.5 Solar concentrator photocatalytic measurements

The solar campaign was performed by circulating samples of 2 L of the TREL model solution towards the focus of the PDC available. The following experimental trials were performed: 1) Concentrated sunlight exposure within the times of 30, 60 and 90 minutes, 2) Concentrated sunlight + Fe_2O_3 catalyst, 3) Concentrated sunlight + Fe_2O_3 catalyst + 3 ml of H_2O_2 (corresponding to a concentration of 1.5×10^{-2} M) as the oxidizing agent for photo-Fenton reaction and finally, 4) Concentrated sunlight + 3 ml of H_2O_2. Experiments 2, 3 and 4 were performed for 60 minutes. The glass slides with the PLD deposited Fe_2O_3 catalyst were inserted inside the quartz glass tube that was used as the reactor in the focus of the solar concentrator.

In this study, to compare the prevalence effects between the concentrated sunlight and the H_2O_2 concentration, only one module of mirror was mounted on the system. After being circulated, samples were kept in the dark and delivered with purposely non-informative labels to the APPA laboratories for analysis. All the experiments were performed at controlled temperature range between 20 and 30 °C.

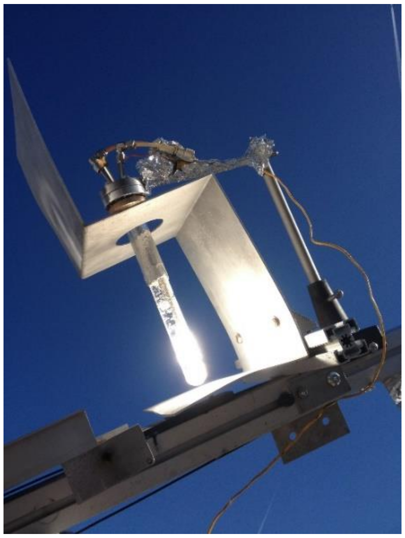

Figure 7.2: Solar apparatus employed in this work (IdEA group, department of physics, UNITN).

7.3 Results and discussions

7.3.1 UV-Vis spectra for TREL

With the aim to confirm the absorption range of TREL, a near UV-VIS spectrum was collected for a model solution with a concentration of 70 μg/L with the solvent in the reference beam using a quartz cuvette, the curve is presented in figure 7.3 and shows a sharp absorbance peak at a wavelength of 260 nm with a significant tail up to 500 nm: this allows for the direct absorption of sunlight by TREL.

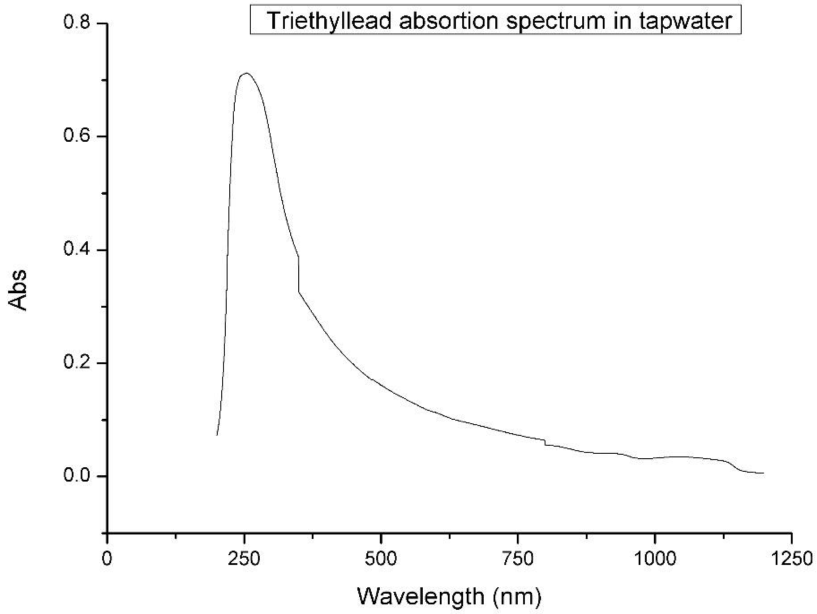

Figure 7.3: Absorption spectrum of TREL, concentration of 70 μg/L in tap water.

7.3.2 Fe_2O_3 catalyst: SEM

The surface morphology of the Fe_2O_3 catalyst coatings prepared with PLD sample was examined using scanning electron microscope (SEM-FEG, JSM 7001F, JEOL). Figure 7.4 presents the SEM image of Fe + H_3BO_3 coatings deposited. The coating shows morphological structure which tends to spherical particulates presenting an urchin-like structure with evolution of nanowires (NWs) vertical to the surface of the particulates.

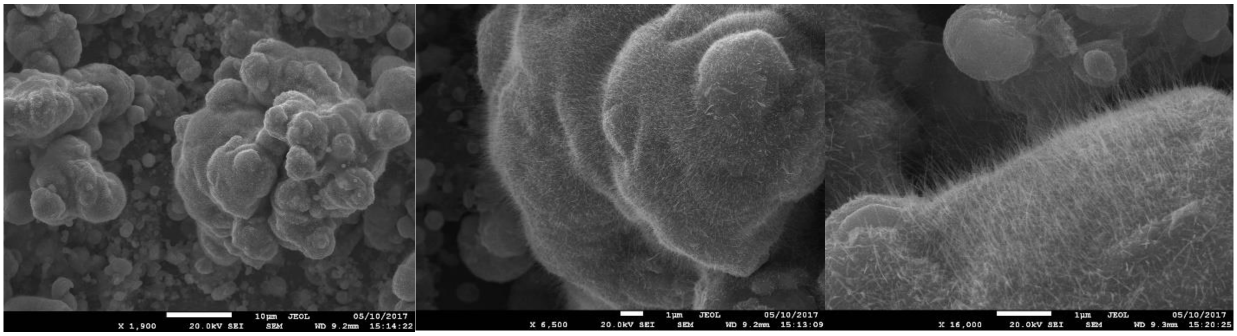

Figure 7.4: Fe_2O_3 catalyst SEM images, from left to right, 1.900x, 6.500x and 16.000x magnifications respectively.

7.3.3 Adsorption experiments

The different times of circulation on the PA tubes and the results achieved are shown in figure 7.5. It can be observed that there is some conversion from TREL to DEL and (to a minor extent) Pb (inorg.), but no net loss of TREL is detected. While the latter would indicate retention by the tube, the former can be ascribed to the natural dealkylation process occurring in contact with air, as expected from past literature works [17,18]. Hence, these results exclude the possible organic lead adsorption on the PA walls.

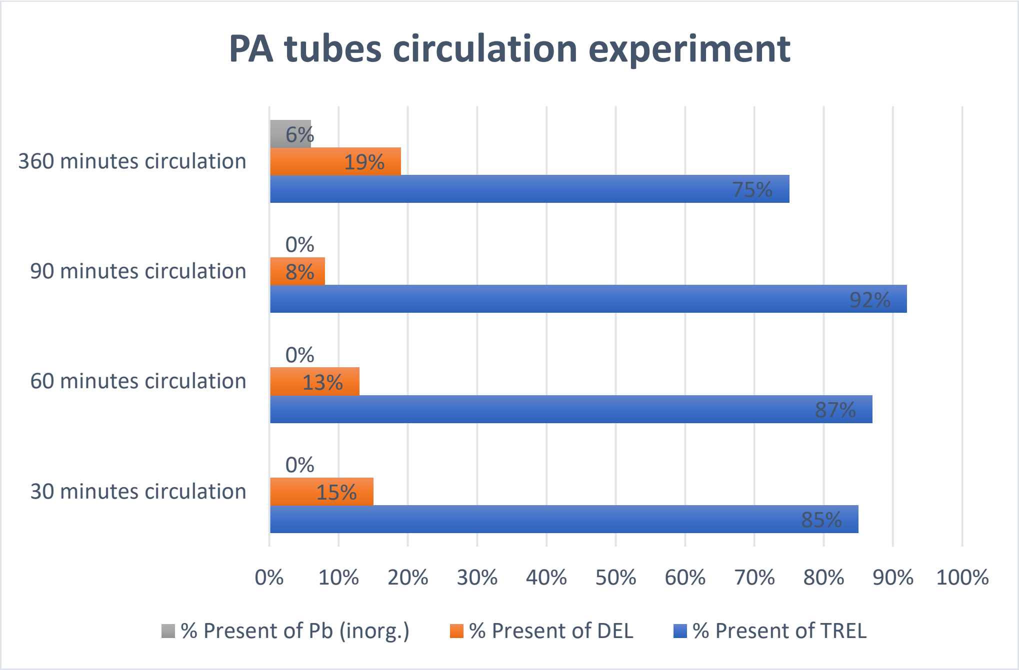

Figure 7.5: adsorption experiments.

7.3.4 H_2O_2 oxidation lab experiment (Quenching with sodium metabisulfite - $Na_2S_2O_5$)

Figure 7.6 presents the results regarding the in-lab H_2O_2 oxidation experiment under different quenching times. It can be observed that independently of the exposition time of the model solution to H_2O_2, its effective performance occurs in a time of less than 5 minutes. Thus, when comparing the results shown, H_2O_2 performs a partial dealkylation of TREL into DEL and Pb inorg. which reaches a limit in the range of 21%.

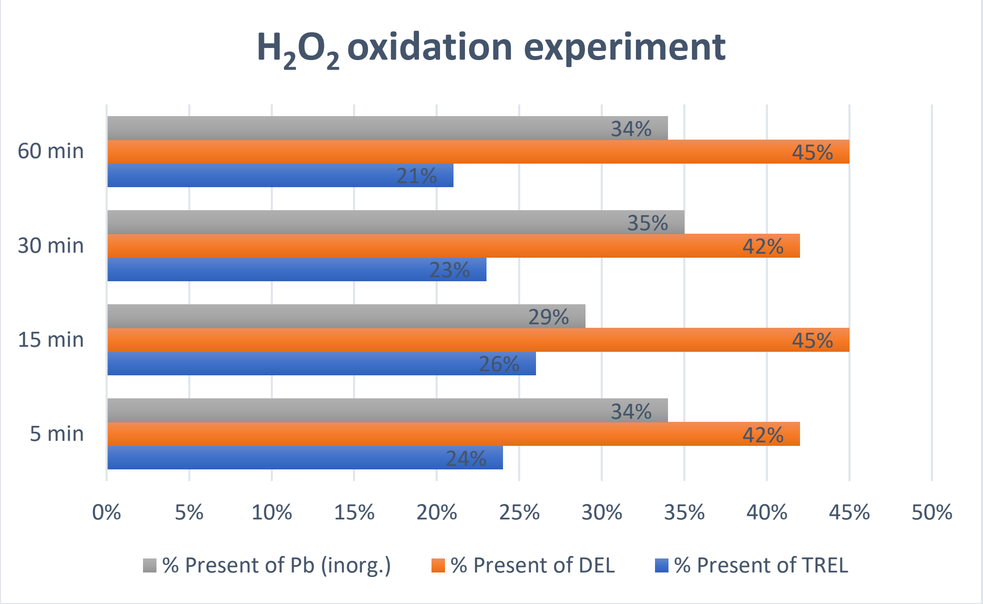

Figure 7.6: results achieved in different H_2O_2 reaction times.

Figure 7.7 confirms the inhibition of the reaction with H_2O_2 by sodium metabisulfite: when this is already present in solution (top) or added immediately after H_2O_2, the TREL conversion is effectively stopped.

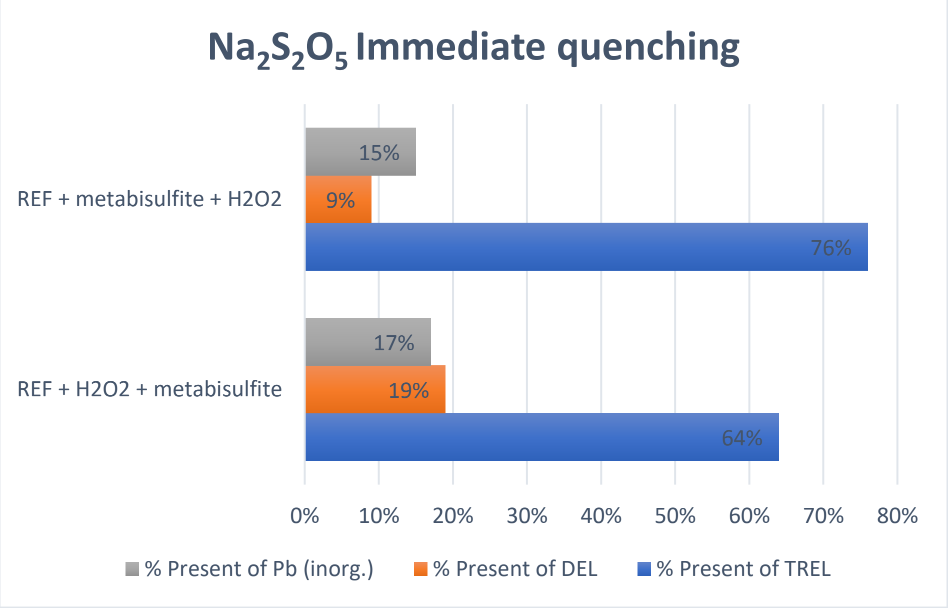

Figure 7.7: results achieved in time ZERO inverting the order of the chemical reactants.

7.3.5 Solar concentrator photocatalytic measurements

Results of the solar concentration experiment are showed in the graphic bars of figure 7.8. The data is presented in terms of TREL still present on the model solution after performing the experiment. Thus, higher values of percentage show less effectiveness of the experiment. Instead, low percentage values up to reaching value zero (0%) indicate that all TREL was converted under the dealkylation route to DEL and other forms of less hazardous forms of mono or inorganic lead. The results for the two cases of concentrated solar light and in the presence of H_2O_2 (with and without Fe_2O_3 catalyst), show a total conversion of TREL. On the other hand, when only concentrated sunlight is employed, a persistence of TREL is observed, for “60 min + Fe_2O_3 catalyst”, “90”, “60” and “30 minutes”, resulting values of 6%, 7%, 11% and 35% respectively. Hence, it can be observed that effectiveness along time show a relevant evolution from 30 to 60 minutes (35% to 11%), with less difference from 60 to 90 minutes (11% to 7%). Also, the use of an Fe_2O_3 catalyst in the 60 minutes condition shows photocatalytic activity with an increase of the effectiveness, enhancing the reaction rate. Finally, the employment of the Fe_2O_3 catalyst turns to an economy of time when comparing the same order of results achieved in 90 minutes (6% and 7%).

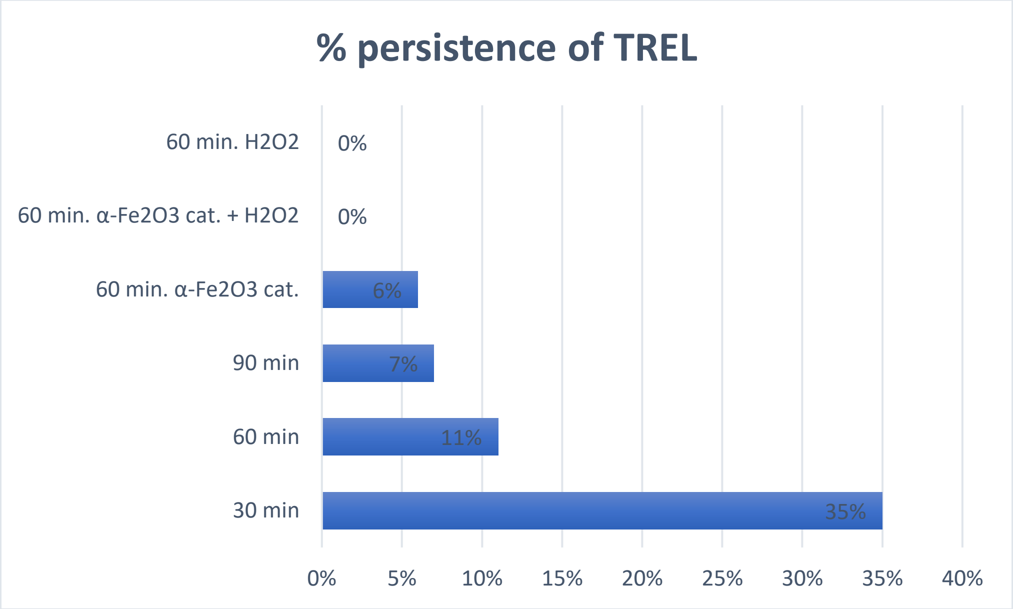

Figure 7.8: results achieved in the concentrated sunlight experiment.

7.4 Conclusions

This work investigated the dealkylation process of a model solution of TREL with concentrations between 60 and 90 μg/L under concentrated sunlight photocatalysis. The possibility to employ concentrated solar light, photocatalysis, photo-Fenton reaction, adsorption, and H_2O_2 oxidation was assessed. Concentrated solar light demonstrated to be by itself effective to promote the starting dealkylation of TREL. The employment of the Fe_2O_3 photocatalyst coupled with concentrated sunlight enhances the dealkylation rate leading to a reduction in reaction time. In the experimental apparatus, the use of polyamide tube does not influence the analytical procedure. H_2O_2 presents a fast reaction rate, with time to completeness less than 5 minutes, when concentrations are in the order of 10^{-2} M. The combined effect of concentrated sunlight, Fe_2O_3 catalyst and H_2O_2 follows photo-Fenton reaction by generation of OH• radicals by dissociation of H_2O_2 and can dealkylate completely TREL in the concentration ranges tested.

On the basis of these preliminary results, two main directions are recommended for further investigation:

(a) the use of H_2O_2 only. H_2O_2 at low concentrations appears to be itself capable of TREL conversion in a timescale of minutes, which could be exploited for decontamination. However, in these conditions the reaction seems to largely stop after the TREL -> DEL conversion step. Further experiments would be needed to address this issue. Also, an evaluation of the cost associated with the perspective use of H_2O_2 should be performed;

b) the use of concentrated sunlight is also effective, although on a longer timescale (> 1hr). This could be vastly improved in two ways: using an ad-hoc designed photocatalyst and implementing a different concentrator configuration. As for the former, in this case we used a high-surface material which is known to be active in photo-Fenton mode, but not effective for direct photocatalysis, nevertheless the degradation yield was enhanced in presence of the catalyst: the enhancement could be much greater if a material with high efficiency in direct photocatalysis, is employed. In the latter case, it is known that the parabolic dish configuration is not optimal for photocatalysis of diluted solutions. The limitation of the small concentrator spot (5.8 cm) could be solved by using line-focus configurations such as the compound-parabolic-concentrator. In this case the concentration factor is lower but should still be sufficient for the photocatalysis process [38,39,44].

Chapter 8: Realization of a solar hydrothermal carbonization reactor: A zero-energy technology for waste biomass valorization

Preview: this chapter reports an alternative activity performed during the PhD cycle regarding the application of solar concentration for the promotion of hydrothermal carbonization. Despite it is not directly related to water treatment, it demonstrates an alternative approach for the valorization of biomasses. As one of the authors of the work, my contribution includes the validation tests regarding the usability and safety of the reactor, the experimental solar campaign assembling the apparatus and performing the tests to generate the biomass focus of the work.

The content of this chapter was adapted from:
Ischia, G.; Orlandi, M.; Fendrich, M.A..; Bettonte, M.; Merzari, F.; Miotello, A.; Fiori, L.. J. Environ. Manage. **2020**, *259*, 110067. https://doi.org/10.1016/j.jenvman.2020.110067

8.1 Introduction

Climate change and fossil fuel depletion call for the development of technologies and processes based on renewable energy. Biorefinery facilities are a smart strategy leading to a wide spectrum of products (such as biofuels, bioenergy, biomaterials, and biochemicals) starting from biomass residues, which are abundant in nature and renewable [318]. However, biorefineries need to improve their profitability to be competitive in the global market and face the current low price of oil [319]. A way to achieve progress would be developing a highly efficient facility, in which energy consumption for the enhancement of biomass is minimized.

Conversion of biomass into valuable carbon products can be achieved through hydrothermal carbonization (HTC), a thermochemical process that is acquiring a rising interest. HTC occurs in water and exploits the unique properties of liquid water under elevated temperatures to carbonize biomass into a carbonaceous material, referred to as hydrochar. Since the process is wet, HTC is well suited to enhance biomass with high moisture content, avoiding any energy-intensive pre-drying stage. The process occurs under subcritical conditions, with temperatures usually ranging between 180 and 250 °C, self-generated pressure from 10 to 50 bar, and reaction times from a few minutes to several hours [320]. A complex network of reactions takes place during HTC, involving solid-solid and solid-liquid conversions and including reactions such as hydrolysis, dehydration, decarboxylation, and polymerization [321,322].

Even if the HTC reactions are slightly exothermic as a whole [323–326], the energy release is lower than thermal requirements (i.e. the energy necessary to reach operating conditions and to tackle heat losses), making external energy sources mandatory.

Until now, many efforts have been made to understand the fundamentals of HTC (e.g. reaction pathways, effect of operating parameters, characterization and optimization of hydrochars [322,327,328] and towards scalability bringing to the first pilot and industrial scale plants [329,330]. Because of its coal-like properties, hydrochar is particularly suitable for combustion applications [331,332]. Furthermore, tunable surface properties of hydrochars make them useable as precursors for high-value carbon-based materials [333]. In that respect, post-treatments have been recently investigated to enhance hydrochar as an adsorbent for water remediation applications [334,335] and as an electrode material for batteries and fuel cells [322].

Nevertheless, there is a certain lack of research around the optimization of the technological process itself. In particular, despite the huge and established potential of concentrated solar energy, the usage of concentration solar systems combined with HTC has been little investigated and only a few works dealing with this topic have been reported in the literature. Among them, [336] simulated a pilot plant made by an HTC reactor coupled with solar panels, while [337] tested an HTC reactor working with parabolic trough collector.

Despite the scarcity of research around solar HTC systems, adopting solar concentration to sustain thermochemical processes has seen a rising development from the mid-2000s [338], driven by lower costs and improved design. These solutions conceptually derive from the consolidated concentrated solar power (CSP) systems used for electrical production. Among hydrothermal processes besides HTC, [339] proposed a commercial solution involving a concentrating solar power system combined with hydrothermal liquefaction, while several conceptual studies were carried out both on hydrothermal liquefaction [340,341] and hydrothermal gasification [342–344]. Recently, [345] proposed a direct solar-hydrolysis apparatus to pretreat microalgae slurry. Moreover, the adoption of solar systems for producing hydrogen and syngas (through methane reforming and gasification of carbonaceous feedstock) and for industrial commodities (such as zinc production) has been demonstrated successfully at plant scale [338,346].

Thus, to address the lack of research concerning solar HTC and disclose a novelty in the current state-of-art, we propose the realization of an innovative hybrid solution consisting of an HTC reactor coupled with a parabolic dish concentrator (PDC). Within the solar thermal systems, the parabolic dish technology is attractive for its high conversion efficiency and possible use in remote grids [347,348]. Through the proposed system, concentrated sunlight is converted into heat, which fully covers the thermal energy requirements of HTC and avoids the need for any external energy source. The coupling between the two technologies is direct, meaning that the reactor is directly illuminated and heated by the concentrated solar radiation. The experimental apparatus consists of a 300 ml HTC reactor placed on the focus of a PDC prototype, equipped with a mirror of 0.8 m^2, while a copper oxide coating allows the maximization of the solar radiation absorption.

In this chapter it is reported details on the solar-HTC experimental apparatus and the first experimental campaign performed to assess its effectiveness. Since the absorption process of solar light is a key factor for the overall performance, particular attention was given to the design of an efficient optically absorbent coating. Besides, HTC tests were carried out at 180, 220, and 250 °C (residence time of 2 h) on grape seeds, an agro-biomass residue resulting from the winemaking industry. Given their high moisture content of about 60–70% [349], grape seeds are excellent candidates for HTC. Properties of "solar hydrochars" obtained through our hybrid solution were compared with those from conventional HTC systems.

As a whole, this research work provides a proof of concept for the solar-HTC technology and demonstrates the feasibility and reliability of the concept. This research work stimulates future advancements in the solar-HTC field to be achieved, for instance, through life cycle assessment, equipment design scale-up, energy savings evaluations, and estimation of the costs involved in the technology in comparison with more standard technical approaches.

8.2 Materials and methods

8.2.1 Description of the system

The demonstrator system realized at the University of Trento consists of an HTC reactor coupled with the parabolic dish concentrator (PDC) described in detail on chapter 3, both developed in-house. The coupling between the two technologies is direct: the HTC reactor was positioned on the focus of the parabolic dish, as shown in figure 8.1(a) and (b). This configuration allows the achievement of high concentration ratios and the minimization of heat losses in comparison with indirectly heated systems. Moreover, it presents a good constructive simplicity and versatility. Previous tests proved that one module leads to a maximum peak concentration ratio of 870X and ensures a Gaussian distribution of the light focus, with 95% of the power contained in a spot diameter of 5.8 cm [57].

The HTC reactor was designed to match the solar concentrator specifications, according to the European standard on unfired pressure vessels (UNI EN 13455–3:2014) and was manufactured at the machine workshop of the Physics Department of the University of Trento. The HTC reactor is a batch type, is made of stainless steel AISI 316 and has an internal volume of 300 ml. It was designed to withstand pressures and temperatures up to 190 bar and 280 °C, respectively. Fig. 1 (c) shows the reactor schematic drawing. A Teflon gasket guarantees the sealing between the main body of the HTC reactor and its closing flange. The reactor closing flange is the focus facing the concentrator mirror and aims both to absorb the concentrated sunlight and transfer heat to the internal side of the reactor. To maximize the sunlight absorption, a thin layer of copper oxide was deposited on the flange surface. Two thermocouples pass through the top side of the HTC reactor body for the measurement of temperature at different heights (1 cm from the top and 1 cm from the bottom, respectively). From the same side, a rupture disk (calibrated at 120 bar) was positioned for safety reasons. Two pipes were predisposed to the purging with nitrogen. During the HTC tests, the internal temperature of the reactor was maintained at the set point value (accuracy of ± 5 °C) by raising and lowering a shield positioned between the reactor and the mirror.

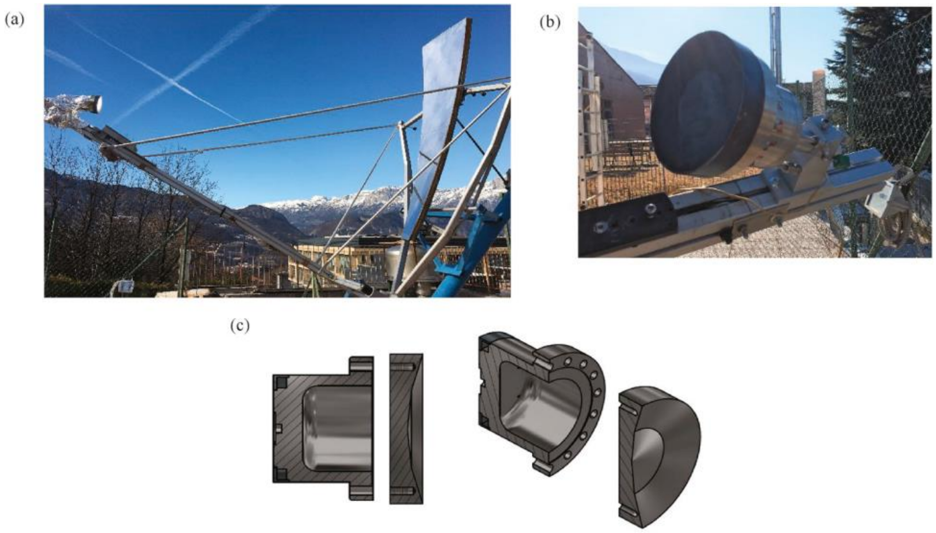

Figure 8.1: Solar-HTC system: (a) HTC reactor placed on the solar apparatus, made up of one parabolic module and a sun tracker; (b) HTC reactor: the coated closing flange; (c) technical drawings of the HTC reactor.

8.2.2 Realization and characterization of the coating

To maximize both the sunlight absorption and the heat transfer, the side of the HTC reactor on which sunlight is focused (i.e. the flange) was sandblasted and treated with a copper oxide coating. This consists of a 1.78 µm thin layer of copper oxide CuOx realized by combining electron beam deposition (EBD) with thermal oxidation in air. The coated flange can be appreciated in Fig. 1b, in which the HTC reactor is mounted on the solar collector.

Before the coating deposition, the flange was cleaned with acetone in an ultrasonic bath and sandblasted using silica particles of diameter in the range 90–150 µm for a duration of 120 s. Sandblasting allows to increase the roughness of steel, which influences the infrared emittance [350].

The deposition was performed through a laboratory-built evaporator system equipped with a 10 kV electron gun with a 10 mA average beam current. Copper powder (Alfa Aesar, 99%) was placed in a graphitic crucible on a water-cooled holder. Background pressure was maintained lower than 2.66×10^{-5} Pa before operation and at 9.33×10^{-4} Pa during evaporation. Deposition was performed at room temperature at a rate varied between 3.0 and 5.2° A/s, controlled with a quartz crystal transducer. After that, the coated steel was annealed in air at 450 °C for 12 h to ensure the oxidation of copper.

For characterization purposes, the same deposition procedure followed by thermal oxidation was repeated on stainless steel and glass slides (1.5 mm x 25 mm x 75 mm). Total reflectance (R_{tot}, specular plus diffuse), diffuse reflectance (Rd) and transmittance (T) of the coated samples were measured through a UV–Vis–NIR spectrophotometer (Varian Cary 5000), equipped with an integrating sphere. A Labsphere Spectralon SRS 99 white standard was used as reference material, while the data acquisition was carried out over a wavelength range between 300 and 800 nm. For comparison purposes, measures were performed also on an uncoated sandblasted stainless-steel sample.

T of the blasted steel was assumed equal to zero, both with and without the coating. Indeed, the fraction of light transmitted through the coating is likely absorbed by the steel substrate or reflected back and absorbed by the coating. Furthermore, the T of the coating itself was assumed equal to that of the coated sandblasted glass sample. In this case, the effect of a sandblasted substrate is approximated by the underlying glass.

Absorptance (A) and specular reflectance (Rs) were determined by difference at each wavelength, according to Equations (1) and (2).

$$A\ (\%) = 100 - R_{tot} - T \qquad (1)$$

$$R_s\ (\%) = R_{tot} - R_d \qquad (2)$$

The composition of the coating was established by X-ray Diffractometer using the Cu Kα radiation in Bragg-Brentano configuration. The morphology of the coating was investigated by scanning electron microscopy.

8.2.3 Experimental campaign

To show the effectiveness of the solar-HTC reactor, an experimental campaign was carried out for the treatment of grape seeds. The substrate derives from the wet sieving of grape marc and was provided by an alcohol producer company in the North-East of Italy (province of Trento), already dry and with a residual moisture content of about 5 wt %. Solar HTC tests were performed at temperatures of 180, 220, and 250 °C, while residence time and dry biomass to water weight ratio (B/W) were maintained fixed at 2 h and about 0.3, respectively. Each test was performed twice to address reproducibility.

For each run, 28.6 ± 0.1 g of dried grape seeds and 95.6 ± 0.1 g of distilled water were introduced inside the reactor. The amounts of materials were chosen to guarantee a B/W of about 0.3 and to leave a free volume in the reactor of 60%. After positioning the *Teflon*® gasket and the rupture disk, the reactor was sealed and mounted on the frame of the solar concentrator at a relative angle of 45°, with its coated side facing the parabolic mirror. To improve insulation and protect cables from the solar radiation, the reactor was wrapped with an aluminum foil. Thus, the parabolic mirror was aligned with the sun to have the concentrated light spot contained into the coated side of the reactor. Fig. 1 (a) shows a picture of the system under operation. The heating phase began and the counting of residence time started when the reactor internal temperature reached the set point value. The internal temperature was maintained at the set point value through a shield, which was manually operated to ensure a maximum temperature variation of ±5 °C to the set point value. During the tests, direct radiation was recorded through the pyrheliometer. After the residence time was over, the shield was raised, the system misaligned with the sun and the reactor cooled down naturally until ambient temperature. Thereafter, the system was disassembled: the reactor was opened, the solid fraction recovered by filtration and dried in an oven at 105 °C overnight.

The hydrochar solid yield (SY) was computed as the ratio between the mass of dry hydrochar ($m_{HC,dry}$) and the mass of dry biomass ($m_{bio, dry}$), as reported in Eq. (3).

$$SY (\%) = (m_{HC,dry} / m_{bio,dry}) \text{ x } 100 \qquad (3)$$

8.2.4 Characterization of hydrochars

Ultimate analyses were performed by means of a Vario MACRO Cube (CHNS–O version) and applying the ASTM D-5373 standard method. The ash content of hydrochars was determined according to the ASTM D3174 -12 standard at 900 °C in a muffle, while the oxygen content was computed by difference (O = 100-C-H-N-S-Ash). All compositional data refers to a weight percentage (wt.%), on a dry basis.

An IKA C 2000 calorimeter was used to measure the higher heating values (HHVs) of dry hydrochars and dry grape seeds according to the CEN/TS 14918 standard. The energy yield (EY) was computed as shown in Eq. (4).

$$EY (\%) = (HHV_{HC,dry} / HHV_{bio.dry}) \text{ x } SY (\%) \qquad (4)$$

For each sample, analyses were performed at least twice and the average values with their relative errors were reported.

8.3 Results and discussion

8.3.1 Properties of the coating

The coating confers to the blasted steel good absorbing properties. Indeed, it leads to a maximum absorptance of 95.5% in the UV region and values always higher than 90.7% over the observed wavelength range. The effect of the coating on the substrate is significant, as shown in figure 8.2 (a) and (b). In correspondence of the solar radiation peak (at around 500 nm), the substrate total reflectance and absorptance pass from 45.0 to 5.7% and from 55.0 to 94.2%, respectively. Besides, the coating reduces the impact of the wavelength variation, flattening the curves. Either with or without the coating, reflectance mainly consists of the diffuse fraction, which occupies more than 92.6% of the total reflectance over the entire observed spectrum. In this regard, sandblasting is decisive because it increases the steel macroscopic roughness and therefore the light scattering. Moreover, previous studies demonstrated that roughness positively impacts the emittance and adhesion of the film with the substrate [350,351], making sandblasting an effective pre-treatment for the coating.

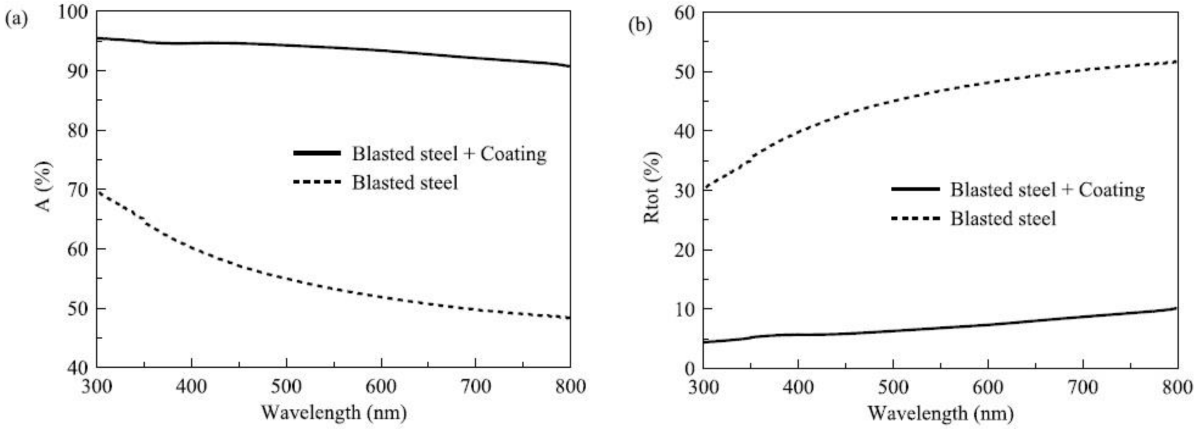

Figure 8.2: Trends of absorptance (A) (a) and total reflectance (Rtot) (b) of blasted steel, with and without the coating, at different wavelengths.

Table 8.1 summarizes the value ranges of the variables indicative of optical performances over the observed wavelength range (300–800 nm), for both the coating deposited on blasted steel and the coating itself. The difference among them is mainly due to transmittance, which is equal to zero for the coating deposited on the steel substrate. In the case of the coating itself, the amount of radiation transmitted is extremely low (maximum value of 0.1%). Interestingly, with an absorptance ranging between 95.6% (at 300 nm wavelength) and 89.8% (at 800 nm wavelength), the performances of the coating are comparable with commercial coatings. These are used in a variety of light absorption applications, such as in spacecraft, sensors and analyzer instruments for plasma and energy [350]. A list of commercial coatings with high absorptance (88.0–97.0%) can be found in literature [352].

XRD analysis demonstrates that the coating is a sub-stoichiometric mixture of copper oxides, consisting of CuO (cupric oxide) and a smaller fraction of Cu_2O (cuprous oxide). The XRD pattern of the coating deposited on blasted steel is shown in figure 8.3, where the presence of the steel phases (austenite and ferrite) of the substrate can be also detected. During oxidation, metallic Cu oxidizes to Cu_2O ($4Cu + O_2 \rightarrow 2Cu_2O$) which becomes the precursor to CuO ($2Cu_2O + O_2 \rightarrow 4CuO$), whose slow formation ensures a continuous and uniform growth for CuO nanowires [353].

Table 8.1: Value range of optical parameters of coating deposited on blasted steel and of coating itself, in the wavelength range 300–800 nm (A: absorptance, Rtot: total reflectance, Rd: diffuse reflectance, Rs: specular reflectance, T: transmittance).

	Blasted Steel + Coating	**Coating**
A (%)	95.5–90.7	95.6–89.8
R_{tot} (%)	4.5–9.3	4.4–10.1
R_d (%)	4.6–8.6	4.1–9.7
R_s (%)	0.1–0.7	0.2–0.4
T (%)	0	0.0–0.1

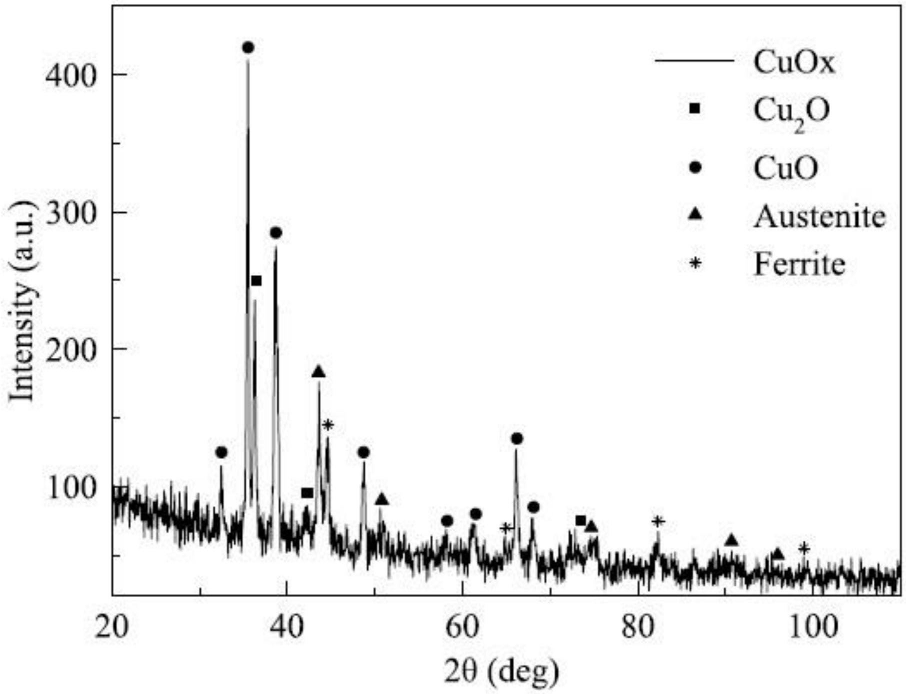

Figure 8.3: XRD pattern of the coating deposited on blasted stainless steel (θ: diffraction angle).

As shown in SEM images reported in figure 8.4 (a) and (b), CuO nanowires cover all the surface and have diameters between 20 and 100 nm. This kind of nanostructure is often found in transition metal oxides synthesized by physical vapor deposition methods followed by thermal annealing in oxidative conditions [353–355]. These have been employed in a broad field of applications in which a high surface is required, such as medical devices, sensors, solar cells, and catalysts [356].

Overall, the ordered nanostructured surface confers good absorption properties. The probability of the coating of trapping photons is positively affected by copper oxide nanowires, which allow multiple reflections of light inside the material. Moreover, sandblasting provides more sites for nucleation and then enhances the density and length of nanowires [356].

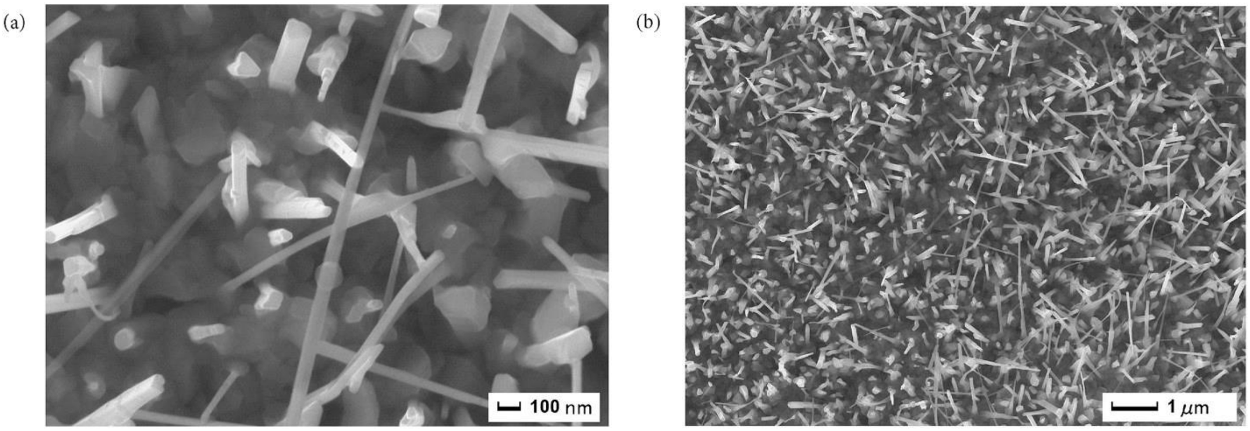

Figure 8.4: SEM images (a–b) at different magnifications of CuOx film deposited by EBD on blasted steel.

8.3.2 Effect of process parameters on heating times

As shown in table 8.3, as direct irradiance increases, the time required to reach the set point temperature decreases since more thermal power is supplied to the HTC reactor. In this respect, tests performed at 485 and 734 W/m^2 require the same time (40 min) to reach the HTC set point temperatures of 180 and 250 °C, respectively.

Heating times are comparable with those involving non-renewable heating sources, such as band heaters electrically powered, which amount to approximately 30 min [320,324,357]. However, a certain lack of investigation around heating times involved during HTC is observed in the current literature [358].

Figure 8.5 shows the trends of the HTC reactor internal temperature versus time during reactor heating-up. For all the investigated irradiances, trends are almost linear and can be approximated by two straight lines with two different slopes ($R^2 > 0.99$). Temperatures increase steeper in the first region (from 20 to 100 °C) than in the second one (from 100 °C to the set point value). Angular coefficients (*m*), computed through linear interpolation and summarized in table 8.2, mark this difference. Up to about 100 °C, energy is used to heat water and biomass, without any reaction occurring, and the amount of vaporized water is limited. In the second region, the heating phase slows down because HTC reactions progressively trigger, thermal losses to the environment increase, and the amount of water which vaporizes increases substantially (the vapor pressure of water at 180, 220, and 250 °C is equal to, respectively, 10, 23, and 40 bar (NIST Chemistry WebBook).

Table 8.2: Angular coefficients (m) and R^2 values of temperature-heating time interpolating lines in the intervals 0–100 °C and 100 °C-set point temperature (Id: direct irradiance).

	Id (W/m^2)					
	485	530	678	732	720	734
$m_{0–100\ °C}$	5.50	4.92	6.55	7.48	6.79	7.43
$R^2_{0-100\ °C}$	0.99	1.00	0.99	1.00	0.99	1.00
$m_{100\ °C\ -\ set}$	3.39	4.17	4.85	4.38	4.02	4.73
$R^2_{100\ °\ C\ -\ set}$	1.00	1.00	0.99	0.99	0.99	0.99

Table 8.3: Solar-HTC test details, ultimate analyses and HHVs of "solar hydrochars" (Relative errors ≤ 0.5% for ultimate analysis, ≤ 0.5% for ash, ≤ 0.6% for HHVs). All data are on a dry basis.

Sample	**Heating time (min)**	**Id (W/m^2)**	**SY (%)**	**Ultimate analysis (wt.%)**					**Ash (wt.%)**	**HHV (MJ/kg)**	**EY (%)**
				C	H	O[a]	N	S			
Raw biomass	-	-	-	53.2	6.7	36.2	1.7	0.3	1.9	22.5	-
180 °C - 1	40	485 ± 2	78.8	59.7	6.7	29.4	1.5	0.4	2.3	24.9	83.5
180 °C - 2	34	530 ± 8	80.1	60.1	6.7	29.1	1.6	0.4	2.2	25.1	85.6
220 °C - 1	36	678 ± 5	72.0	64.0	6.4	25.3	1.7	0.4	2.2	27.2	83.3
220 °C - 2	34	732 ± 9	70.1	64.5	6.4	24.8	2.0	0.3	2.0	27.7	82.6
250 °C - 1	45	720 ± 17	61.5	69.2	6.5	19.4	2.0	0.3	2.5	30.5	79.8
250 °C - 2	40	734 ± 14	61.1	69.1	6.3	19.8	2.0	0.3	2.7	30.0	78.0

[a] Computed by difference.

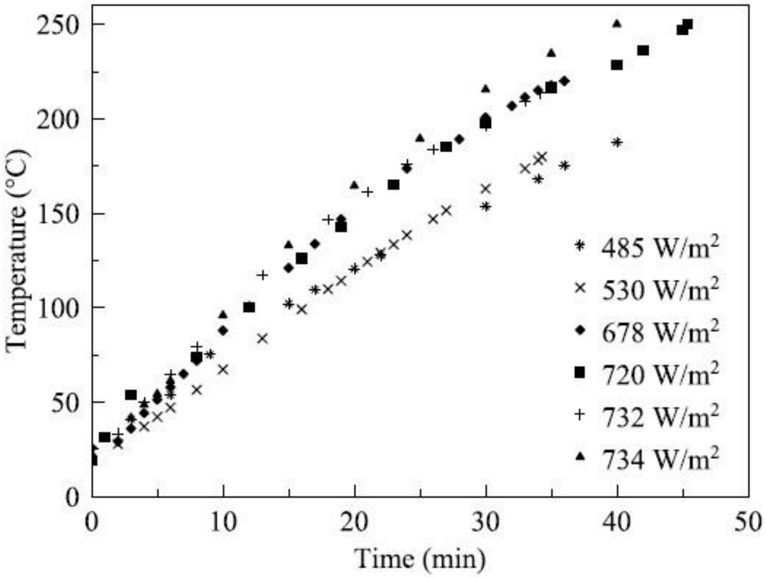

Figure 8.5: Trends of HTC reactor internal temperature as a function of time, at different direct irradiances.

As shown by temperature trends and angular coefficients, tests performed under higher irradiances show steeper slopes. Indeed, a higher irradiance means a higher amount of heat provided to the system, which determines a faster heating phase. Moreover, temperature trends measured at similar irradiances (720, 732, and 734 W/m^2) show relative differences in angular coefficients lower than 10%, which ensures a good reproducibility of the tests in terms of the operating conditions.

8.3.3 Properties of "solar hydrochars"

Higher HTC temperatures enhance the conversion degree of biomass into hydrochar, as demonstrated by the decreasing trend of solid yields reported in table 8.3. Indeed, harsher conditions favor the mass transfer of the starting biomass into the gas and liquid phases [359]. Biomass directly decomposes into gas molecules (mainly CO_2 and CO) through decarboxylation and decarbonylation reactions, whilst into organic molecules in the liquid phase [334,360]. Meanwhile, some of these organics further decompose to CO_2, react and possibly polymerize in the liquid phase.

Table 8.3 also reports the elemental composition of the raw biomass and hydrochars, in terms of carbon (C), hydrogen (H), oxygen (O), nitrogen (N) and sulfur (S). As expected, the HTC operating temperature has a positive effect on the carbonization process. Elemental C increases along with a decrease in O, reaching values of 69.2 and 19.4% (at 250 °C), respectively. H and N do not vary significantly among the tests, while the presence of sulfur is almost negligible (0.3–0.4%).

H/C and O/C atomic ratios were computed and visualized on a Van Krevelen diagram shown in figure 8.6, in which raw biomass and "solar hydrochars" are compared with typical coals (anthracite, bituminous coal, lignite and peat). HTC lowers both the H/C and O/C ratios, making hydrochars close to low-rank coals, like lignite and peat, and indicating that dehydration is a dominant reaction during the process.

The ash relative content (wt.%) in the hydrochars slightly varies with temperature and is slightly higher than that in the raw biomass (Table 8.3). However, the ash absolute amounts decrease compared to raw biomass and exhibit loss ratios ranging between 4 and 28%. This confirms the HTC capability of dissolving some inorganics (especially Na^+ and K^+) from the parent biomass into water [361,362].

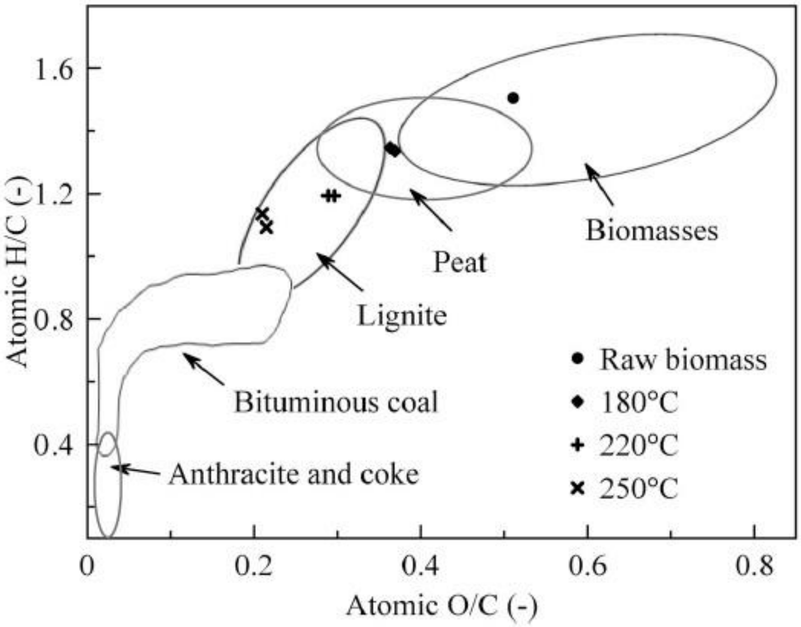

Figure 8.6: Van Krevelen diagram of raw biomass and "solar hydrochars" (Van Krevelen, 1950).

The effect of temperature on the carbonization degree is reflected in the energy properties of hydrochars (Table 8.3). Through HTC, the higher heating value (HHV) of grape seeds passes from 22.5 up to a 30.5 MJ/kg (at 250 °C). The energy yield (EY) slightly decreases with temperature mainly due to the counterbalance between mass loss and HHV enhancement.

Properties of hydrochars obtained at the same operating conditions and different irradiances are fully comparable: the differences in solid yields, composition, and energy properties (Table 8.3) are very small. Irradiance variations in the investigated range (from 485 to 734 W/m^2) do not affect hydrochar properties, proving the reproducibility of the experimental procedure. Moreover, hydrochar data resemble those obtained in previous works when using traditional HTC equipment and starting from the same feedstock. In particular, [363] report a carbon content in the hydrochars of 60.2, 63.6, and 69.5% (at 180, 220, and 250 °C, respectively), which implies a percentage difference with solar hydrochar lower than 1.4%. This is valid also for oxygen and hydrogen contents, as well as for hydrochar yields. Besides, the ash content of solar hydrochars is slightly lower than the ash content of the conventional hydrochars (ranging from 3.5 to 4.5% [363], likely due to the different temperature used during the ash measuring procedure (900 °C here against 550 °C in [363]. Therefore, the similarity in the composition of solar and conventional hydrochars demonstrates the effectiveness of the proposed apparatus and, more in general, of the solar-HTC technology.

8.4 Conclusions

This work provided a successful proof-of-concept for a hybrid solar- HTC technology. This solution represents a zero-energy process capable to enhance waste biomass into valuable carbonaceous materials. The HTC energy needs are fully covered by concentrated sunlight and the use of traditional energy sources is avoided. This system represents an innovative biorefinery concept in an actual context in which the combination of HTC with renewable energy sources has been little investigated, thus providing a step-forward towards an environmentally sustainable HTC process.

Technical details of the components forming the system (i.e. the HTC reactor and the parabolic dish concentrator) were provided. Particular attention was paid to the characterization of the coating, which was realized to maximize the absorption of the solar radiation. In particular, the coating showed very satisfactory light absorption properties (absorptance up to 95.6%) and an interesting nanostructured surface made up of copper oxide nanowires.

An experimental campaign performed on grape seeds (treated at 180, 220, and 250 °C, for 2 h) proved the operational effectiveness of the technology. Indeed, heating time, solid yields, chemical and thermal properties (elemental composition and heating values) of “solar hydrochars” obtained through our hybrid solution resemble well those of traditional HTC systems.

Future developments linked to the solar-HTC prototype include the realization of a more sophisticated control system, able to handle the shield positioned between the reactor and mirror as a function of the internal HTC temperature. In a wider perspective to fully develop the solar-HTC technology, further research is necessary: design scale-up, estimation of the costs involved in the combined technology in relation to those of more standard approaches, parametric analysis, life cycle assessment.

Chapter 9 – Conclusions and suggestions for future works

9.1 Conclusions

This thesis presented the results of an extensive 3-years scientific research to push forward applications of solar concentration for the decontamination of wastewater, suitable for the sustainable development. The research accomplished a deep discussion of the possibilities to apply the combination of concentrated sunlight with photocatalytic materials and direct photolysis applications. In particular, improvements on reaction speeds using novel photocatalysts and approaches regarding the treatment of real contaminated water sources were studied.

In this perspective, chapter 1 introduced the state-of-the art of the topic and positioned the social and economic impact of developing solar concentrators for green applications.

Chapter 2 highlights the lack of photocatalyst materials capable to operate under near UV-Visible irradiation, the necessity to improve heterogeneous photocatalysis routes proposing novel supported thin films, the process design using commercial silver coated mirrors for solar collectors and the open possibilities to shift applications from model pollutants to real wastewaters.

Chapter 3 describes the experimental methodology and characterizations used for the development of this work, the parabolic dish collector and the pulsed laser deposition as an important fabrication technique to synthesize thin films in nanostructured stable materials.

Specifically, regarding photocatalytic materials development, presented in chapters 4 and 5, WO_3 thin film coatings were successfully produced by PLD and, for the first time were employed for applications with concentrated sunlight wastewater treatment. Also, green-synthesized ZnO nanoparticles were successfully employed in solar wastewater remediation. The improvements on the photocatalyst as coatings can push forward applications on environmental-friendly wastewater remediation. Both above approaches demonstrated satisfactory results on a PDC configuration with commercial silver coated mirrors. This result paves the way to continue dedicating efforts to develop photocatalyst materials with the following features: a) coating catalysts, b) operating the near UV-Visible range and c) resistant to aggressive environments.

Regarding application of solar wastewater remediation technologies presented in chapters 6 and 7, surfactant-rich industrial wastewaters were successfully treated with concentrated sunlight. The application to real wastewaters after tests on model pollutants, was demonstrated.

Significative differences between heterogeneous and homogeneous routes could be observed leading the choice between them to individual evaluations on each industrial condition. On the work with organolead contaminated wastewaters, a possible vision for a local case on wastewater treatment was established, and the feasibility of using concentrated sunlight to degrade such contaminants was confirmed.

Regarding solar hydrothermal carbonization presented in chapter 8, the approach of coupling a PDC solar concentrator with a hydrothermal carbonization reactor was proposed for the first time. The carbonization effects obtained in this work have been demonstrated to be comparable with other thermal carbonization techniques described in literature. The activation for the reactions promoted by the solar system can drive to a zero-cost energy for this application.

9.2 Suggestions for future works

With the aim to improve the success of the application of solar concentration on the environment industry, it could be suggested for future works:

a) Related to the solar concentrator apparatus:

- Update the electronic controls from the tracking system in order to increase the operational reliability;
- Design and build a CPC or a V-through solar system with line focus in order to propose treatment comparisons, also in modular structure to be employed in SMEs for technological transfer;
- Improve the circulation conditions and data acquisition in form of a modular transportable installation, comprising the pumps, the computer and temperature controls.

b) Related to the photocatalyst material:

- Continue the investigations of WO_3 proposing composites, in order to shift absorption rates in values superior than 472 nm, improve acidic resistance together with in-depth mechanistic study;
- In the “green-synthesized” ZnO, study in depth the fixing of the films and consequent repeatability of the process on the circulation system.

c) Related to applications on real wastewaters:

- Extend the applications to novel contaminants of emerging concern (CEC), i.e. PFAS, antibiotics and pesticides contaminated water sources;

- Propose the integration of modular solar wastewater treatment into the value chain of industry 4.0 for implementation on eco-friendly processes.

d) Related to solar hydrothermal carbonization:

- Develop an automatic temperature control by means of balancing the solar radiation;
- Test different biomasses for comparisons of the carbonization rates;
- Increase the volume of the prototype tests;
- Propose a study on an application for the resulting carbonized biomass.

References

[1] B. Sinclair-Desgagné, The Environmental Goods and Services Industry, Int. Rev. Environ. Resour. Econ. 2 (2008) 69–99. doi:10.1561/101.00000012.

[2] Integrated Environmental and Economic Accounting, Handbook, UN / European Commission / IMF / OECD / World Bank, 2003. https://unstats.un.org/unsd/environment/seea2003.pdf.

[3] OECD, The environmental Goods & Services Industry, 1999. https://unstats.un.org/unsd/envaccounting/ceea/archive/EPEA/EnvIndustry_Manual_for_data_collection.PDF.

[4] M. Mazzucato, G. Semieniuk, Financing renewable energy: Who is financing what and why it matters, Technol. Forecast. Soc. Change. 127 (2018) 8–22. doi:https://doi.org/10.1016/j.techfore.2017.05.021.

[5] A. Acra, Y. Karahagopian, Z. Raffoul, R. Dajani, Disinfection of oral rehydration solutions by sunlight, Lancet (London, England). 2 (1980) 1257–1258. doi:10.1016/s0140-6736(80)92530-1.

[6] P. Pichat, Photocatalysis and Water Purification: From Fundamentals to Recent Applications, 2013. doi:10.1002/9783527645404.

[7] M.N. Chong, B. Jin, C.W.K. Chow, C. Saint, Recent developments in photocatalytic water treatment technology: A review, Water Res. 44 (2010) 2997–3027. doi:10.1016/j.watres.2010.02.039.

[8] J. Rodríguez-Chueca, M.I. Polo-López, R. Mosteo, M.P. Ormad, P. Fernández-Ibáñez, Disinfection of real and simulated urban wastewater effluents using a mild solar photo-Fenton, Appl. Catal. B Environ. 150–151 (2014) 619–629. doi:10.1016/j.apcatb.2013.12.027.

[9] A. Barwal, R. Chaudhary, Feasibility study for the treatment of municipal wastewater by using a hybrid bio-solar process, J. Environ. Manage. 177 (2016) 271–277. doi:10.1016/j.jenvman.2016.04.022.

[10] A.R. Ribeiro, O.C. Nunes, M.F.R. Pereira, A.M.T. Silva, An overview on the advanced oxidation processes applied for the treatment of water pollutants defined in the recently launched Directive 2013/39/EU, Environ. Int. 75 (2015) 33–51. doi:10.1016/j.envint.2014.10.027.

[11] O. Legrini, E. Oliveros, A.M. Braun, Photochemical processes for water treatment, Chem. Rev. 93 (1993) 671–698. doi:10.1021/cr00018a003.

[12] G. Ruppert, R. Bauer, G. Heisler, The photo-Fenton reaction — an effective photochemical wastewater treatment process, J. Photochem. Photobiol. A Chem. 73 (1993) 75–78. doi:https://doi.org/10.1016/1010-6030(93)80035-8.

[13] J. Kiwi, C. Pulgarin, P. Peringer, Effect of Fenton and photo-Fenton reactions on the degradation and biodegradability of 2 and 4-nitrophenols in water treatment, Appl. Catal. B Environ. 3 (1994) 335–350. doi:https://doi.org/10.1016/0926-3373(94)00008-5.

[14] D. Robert, S. Malato, Solar photocatalysis: a clean process for water detoxification, Sci. Total Environ. 291 (2002) 85–97. doi:https://doi.org/10.1016/S0048-9697(01)01094-4.

[15] M. Schiavello, Heterogeneous Photocatalysis, Wiley, Hoboken, NJ, USA, 2016.

[16] Environmental Protection Agency, Design Manual: Constructed Wetlands and Aquatic Plant Systems for Municipal Wastewater Treatment, Washington, DC, USA, 1998.

[17] A. Rabl, Active solar collectors and their applications, Oxford University Press, New York, 1985. http://www.gbv.de/dms/bowker/toc/9780195035469.pdf.

[18] J. Calkins, J.D. Buckles, J.R. Moeller, THE ROLE OF SOLAR ULTRAVIOLET RADIATION IN ‘NATURAL’ WATER PURIFICATION, Photochem. Photobiol. 24 (1976) 49–57. doi:10.1111/j.1751-1097.1976.tb06796.x.

[19] D. Spasiano, R. Marotta, S. Malato, P. Fernandez-Ibañez, I. Di Somma, Solar photocatalysis: Materials, reactors, some commercial, and pre-industrialized applications. A comprehensive approach, Appl. Catal. B Environ. 170–171 (2015) 90–123. doi:10.1016/j.apcatb.2014.12.050.

[20] S. Gutiérrez-Alfaro, J.J. Rueda-Márquez, J.A. Perales, M.A. Manzano, Combining sun-based technologies (microalgae and solar disinfection) for urban wastewater regeneration, Sci. Total Environ. 619–620 (2018) 1049–1057. doi:10.1016/j.scitotenv.2017.11.110.

[21] S. Sukkasi, W. Terdthaichairat, Improving the efficacy of solar water disinfection by incremental design innovation, Clean Technol. Environ. Policy. 17 (2015) 2013–2027. doi:10.1007/s10098-015-0926-9.

[22] A. Gallego-Schmid, R.R.Z. Tarpani, S. Miralles-Cuevas, A. Cabrera-Reina, S. Malato, A. Azapagic, Environmental assessment of solar photo-Fenton processes in combination with nanofiltration for the removal of micro-contaminants from real wastewaters, Sci. Total Environ. 650 (2019) 2210–2220. doi:10.1016/j.scitotenv.2018.09.361.

[23] H. Haider, W. Ali, S. Haydar, S. Tesfamariam, R. Sadiq, Modeling exposure period for solar disinfection (SODIS) under varying turbidity and cloud cover conditions, Clean Technol. Environ. Policy. 16 (2014) 861–874. doi:10.1007/s10098-013-0677-4.

[24] N. Yahya, F. Aziz, N.A. Jamaludin, M. A. Mutalib, A.F. Ismail, W.N. W. Salleh, J. Jaafar, N. Yusof, N. A. Ludin, A review of integrated photocatalyst adsorbents for wastewater treatment, J. Environ. Chem. Eng. (2018) 0–1. doi:10.1016/j.jece.2018.06.051.

[25] S.M. Rodríguez, J.B. Gálvez, M.I.M. Rubio, P.F. Ibáñez, D.A. Padilla, M.C. Pereira, J.F. Mendes, J.C. De Oliveira, Engineering of solar photocatalytic collectors, Sol. Energy. 77 (2004) 513–524. doi:10.1016/j.solener.2004.03.020.

[26] D.A. Baharoon, H.A. Rahman, W.Z.W. Omar, S.O. Fadhl, Historical development of concentrating solar power technologies to generate clean electricity efficiently – A review, Renew. Sustain. Energy Rev. 41 (2015) 996–1027. doi:10.1016/j.rser.2014.09.008.

[27] Y.-C. Tsao, T. Søndergaard, E. Skovsen, L. Gurevich, K. Pedersen, T.G. Pedersen, Pore size dependence of diffuse light scattering from anodized aluminum solar cell backside reflectors, Opt. Express. 21 (2013) A84. doi:10.1364/OE.21.000A84.

[28] G. Jorgensen, Ultraviolet Refle Solar Detoxificati Waste Materials for of Hazardous, (1991). https://www.nrel.gov/docs/legosti/old/4418.pdf.

[29] T. Wendelin, Outdoor Testing of Advanced Optical Materials for Solar Thermal Electric Applications, Natl. Renew. Energy Lab. Golden, CO (1992).

[30] C. Kutscher, R. Davenport, R. Farrington, G. Jorgensen, A. Lewandowski, C. Vineyard, Low-cost collectors. System development progress report, Sol. Energy Res. Inst. (1984). http://infohouse.p2ric.org/ref/20/19443.pdf.

[31] ALANOD, Alanod Aluminium-Veredlung GmbH & Co, (2018). https://www.alanod.com/ (accessed October 25, 2018).

[32] M. Tanveer, G. Tezcanli Guyer, Solar assisted photo degradation of wastewater by compound parabolic collectors: Review of design and operational parameters, Renew. Sustain. Energy Rev. 24 (2013) 534–543. doi:10.1016/j.rser.2013.03.053.

[33] A. Poullikkas, G. Kourtis, I. Hadjipaschalis, Parametric analysis for the installation of solar dish technologies in Mediterranean regions, Renew. Sustain. Energy Rev. 14 (2010) 2772–2783. doi:10.1016/j.rser.2010.07.021.

[34] J. V Anderson, H. Link, M. Bohn, B. Gupta, Development of solar detoxification technology in the USA - an introduction, Sol. Energy Mater. 24 (1991) 538–549. doi:https://doi.org/10.1016/0165-1633(91)90089-4.

[35] E. Ortega-Gómez, M.M.B. Martín, B.E. García, J.A.S. Pérez, P.F. Ibáñez, Wastewater disinfection by neutral pH photo-Fenton: The role of solar radiation intensity, Appl. Catal. B Environ. 181 (2016) 1–6. doi:10.1016/j.apcatb.2015.06.059.

[36] C. Sichel, J. Tello, M. de Cara, P. Fernández-Ibáñez, Effect of UV solar intensity and dose on the photocatalytic disinfection of bacteria and fungi, Catal. Today. 129 (2007) 152–160. doi:10.1016/j.cattod.2007.06.061.

[37] J. Ndounla, S. Kenfack, J. Wéthé, C. Pulgarin, Relevant impact of irradiance (vs. dose) and evolution of pH and mineral nitrogen compounds during natural water disinfection by photo-Fenton in a solar CPC reactor, Appl. Catal. B Environ. 148–149 (2014) 144–153. doi:10.1016/j.apcatb.2013.10.048.

[38] R.J. Braham, A.T. Harris, Review of major design and scale-up considerations for solar photocatalytic reactors, Ind. Eng. Chem. Res. 48 (2009) 8890–8905. doi:10.1021/ie900859z.

[39] S.A. Waghmare, N.P. Gulhane, Optical evaluation of compound parabolic collector with low acceptance angle, Optik (Stuttg). 149 (2017) 359–371. doi:10.1016/j.ijleo.2017.09.039.

[40] A. Fernández-García, E. Rojas, M. Pérez, R. Silva, Q. Hernández-Escobedo, F. Manzano-Agugliaro, A parabolic-trough collector for cleaner industrial process heat, J. Clean. Prod. 89 (2015) 272–285. doi:10.1016/j.jclepro.2014.11.018.

[41] N.B. Desai, S. Bandyopadhyay, Optimization of concentrating solar thermal power plant based on parabolic trough collector, J. Clean. Prod. 89 (2015) 262–271. doi:10.1016/j.jclepro.2014.10.097.

[42] M.J. Montes, A. Rovira, M. Muñoz, J.M. Martínez-Val, Performance analysis of an Integrated Solar Combined Cycle using Direct Steam Generation in parabolic trough collectors, Appl. Energy. 88 (2011) 3228–3238. doi:https://doi.org/10.1016/j.apenergy.2011.03.038.

[43] M.S. Al-Soud, E.S. Hrayshat, A 50 MW concentrating solar power plant for Jordan, J. Clean. Prod. 17 (2009) 625–635. doi:10.1016/j.jclepro.2008.11.002.

[44] A. Valan Arasu, T. Sornakumar, Design, manufacture and testing of fiberglass reinforced parabola trough for parabolic trough solar collectors, Sol. Energy. 81 (2007) 1273–1279. doi:10.1016/j.solener.2007.01.005.

[45] S. Kalogirou, Use of parabolic trough solar energy collectors, Appl. Energy 60. 60 (1998) 65–88.

[46] H. Jafari Mosleh, S.J. Mamouri, M.B. Shafii, A. Hakim Sima, A new desalination system using a combination of heat pipe, evacuated tube and parabolic through collector, Energy Convers. Manag. 99 (2015) 141–150. doi:10.1016/j.enconman.2015.04.028.

[47] R. Bigoni, S. Kötzsch, S. Sorlini, T. Egli, Solar water disinfection by a Parabolic Trough Concentrator (PTC): Flow-cytometric analysis of bacterial inactivation, J. Clean. Prod. 67 (2014) 62–71. doi:10.1016/j.jclepro.2013.12.014.

[48] M. Chafie, M.F. Ben Aissa, A. Guizani, Energetic end exergetic performance of a parabolic trough collector receiver: An experimental study, J. Clean. Prod. 171 (2018) 285–296. doi:10.1016/j.jclepro.2017.10.012.

[49] D.J. Alpert, J.L. Sprung, J.E. Pacheco, M.R. Prairie, H.E. Reilly, T.A. Milne, M.R. Nimlos, Sandia National Laboratories' work in solar detoxification of hazardous wastes, Sol. Energy Mater. 24 (1991) 594–607. doi:10.1016/0165-1633(91)90093-Z.

[50] P. Fernández, J. Blanco, C. Sichel, S. Malato, Water disinfection by solar photocatalysis using compound parabolic collectors, Catal. Today. 101 (2005) 345–352. doi:10.1016/j.cattod.2005.03.062.

[51] CADOX PROJECT, CADOX Project Website, (2006). https://www.psa.es/en/projects/cadox/ (accessed October 25, 2018).

[52] O. Sacco, V. Vaiano, L. Rizzo, D. Sannino, Photocatalytic activity of a visible light active structured photocatalyst developed for municipal wastewater treatment, J. Clean. Prod. 175 (2018) 38–49. doi:10.1016/j.jclepro.2017.11.088.

[53] J. Coventry, C. Andraka, Dish systems for CSP, Sol. Energy. 152 (2017) 140–170. doi:10.1016/j.solener.2017.02.056.

[54] H. Hijazi, O. Mokhiamar, O. Elsamni, Mechanical design of a low cost parabolic solar dish concentrator, Alexandria Eng. J. 55 (2016) 1–11. doi:10.1016/j.aej.2016.01.028.

[55] R.R.Z. Tarpani, A. Azapagic, Life cycle costs of advanced treatment techniques for wastewater reuse and resource recovery from sewage sludge, J. Clean. Prod. 204 (2018) 832–847. doi:10.1016/j.jclepro.2018.08.300.

[56] R.S. Bettonte, M.; Miotello, A.; Brusa, Solar Concentrator, Method and Equipement for Its Achievement, 2008. http://www.sumobrain.com/patents/wipo/ Solar-concentrator-method-equipmentits/WO2008074485A1.pdf.

[57] M. Eccher, S. Turrini, A. Salemi, M. Bettonte, A. Miotello, R.S. Brusa, Construction method and optical characterization of parabolic solar modules for concentration systems, Sol. Energy. 94 (2013) 19–27. doi:10.1016/j.solener.2013.04.028.

[58] S. Pauletta, A Solar Fresnel Collector Based on an Evacuated Flat Receiver, Energy Procedia. 101 (2016) 480–487. doi:10.1016/j.egypro.2016.11.061.

[59] M.J. Montes, C. Rubbia, R. Abbas, J.M. Martínez-Val, A comparative analysis of configurations of linear fresnel collectors for concentrating solar power, Energy. 73 (2014) 192–203. doi:10.1016/j.energy.2014.06.010.

[60] P. Boito, R. Grena, Optimization of the geometry of Fresnel linear collectors, Sol. Energy. 135 (2016) 479–486. doi:10.1016/j.solener.2016.05.060.

[61] J.M. Monteagudo, A. Durán, Fresnel lens to concentrate solar energy for the photocatalytic decoloration and mineralization of orange II in aqueous solution, Chemosphere. 65 (2006) 1242–1248. doi:10.1016/j.chemosphere.2006.04.057.

[62] A. Durán, J.M. Monteagudo, Solar photocatalytic degradation of reactive blue 4 using a Fresnel lens, Water Res. 41 (2007) 690–698. doi:10.1016/j.watres.2006.06.042.

[63] J.M. Monteagudo, A. Durán, J. Guerra, F. García-Peña, P. Coca, Solar TiO2-assisted photocatalytic degradation of IGCC power station effluents using a Fresnel lens, Chemosphere. 71 (2008) 161–167. doi:10.1016/j.chemosphere.2007.10.067.

[64] A.K. Ray, A new photocatalytic reactor for destruction of toxic water pollutants by advanced oxidation process, Catal. Today. 44 (1998) 357–368. doi:10.1016/S0920-5861(98)00210-7.

[65] R. De Sun, A. Nakajima, I. Watanabe, T. Watanabe, K. Hashimoto, TiO2-coated optical fiber bundles used as a photocatalytic filter for decomposition of gaseous organic compounds, J. Photochem. Photobiol. A Chem. 136 (2000) 111–116. doi:10.1016/S1010-6030(00)00330-0.

[66] A. Danion, J. Disdier, C. Guillard, N. Jaffrezic-Renault, Malic acid photocatalytic degradation using a TiO2-coated optical fiber reactor, J. Photochem. Photobiol. A Chem. 190 (2007) 135–140. doi:10.1016/j.jphotochem.2007.03.022.

[67] N.J. Peill, M.R. Hoffmann, Solar-Powered Photocatalytic Fiber-Optic Cable Reactor for Waste Stream Remediation, J. Sol. Energy Eng. 119 (1997) 229. doi:10.1115/1.2888024.

[68] R. Dillert, A.E. Cassano, R. Goslich, D. Bahnemann, Large scale studies in solar catalytic wastewater treatment, Catal. Today. 54 (1999) 267–282. doi:10.1016/S0920-5861(99)00188-1.

[69] Z. Tian, B. Perers, S. Furbo, J. Fan, Annual measured and simulated thermal performance analysis of a hybrid solar district heating plant with flat plate collectors and parabolic trough collectors in series, Appl. Energy. 205 (2017) 417–427. doi:10.1016/j.apenergy.2017.07.139.

[70] Y. Zhang, M. Sivakumar, S. Yang, K. Enever, M. Ramezanianpour, Application of solar energy in water treatment processes: A review, Desalination. 428 (2018) 116–145. doi:10.1016/j.desal.2017.11.020.

[71] Sutisna, M. Rokhmat, E. Wibowo, Khairurrijal, M. Abdullah, Prototype of a flat-panel photoreactor using TiO2nanoparticles coated on transparent granules for the degradation of Methylene Blue under solar illumination, Sustain. Environ. Res. 27 (2017) 172–180. doi:10.1016/j.serj.2017.04.002.

[72] O.M. Alfano, D. Bahnemann, A.E. Cassano, R. Dillert, R. Goslich, Photocatalysis in water environments using artificial and solar light, 2000. doi:10.1016/S0920-5861(00)00252-2.

[73] C. Minero, E. Pelizzetti, S. Malato, J. Blanco, Large solar plant photocatalytic water decontamination: Degradation of pentachlorophenol, Chemosphere. 26 (1993) 2103–2119. doi:https://doi.org/10.1016/0045-6535(93)90337-5.

[74] G. Li Puma, Dimensionless analysis of photocatalytic reactors using suspended solid photocatalysts, Chem. Eng. Res. Des. 83 (2005) 820–826. doi:10.1205/cherd.04336.

[75] Y.K. Abdel-Maksoud, E. Imam, A.R. Ramadan, TiO2 water-bell photoreactor for wastewater treatment, Sol. Energy. 170 (2018) 323–335. doi:10.1016/j.solener.2018.05.053.

[76] W.H. Glaze, J.-W. Kang, D.H. Chapin, The Chemistry of Water Treatment Processes Involving Ozone, Hydrogen Peroxide and Ultraviolet Radiation, Ozone Sci. Eng. 9 (1987) 335–352. doi:10.1080/01919518708552148.

[77] N.N. Misra, The contribution of non-thermal and advanced oxidation technologies towards dissipation of pesticide residues, Trends Food Sci. Technol. 45 (2015) 229–244. doi:10.1016/j.tifs.2015.06.005.

[78] J. Casado, Brillas 1998 Aniline mineralization by AOP's.pdf, 16 (1998) 31–42.

[79] K. Park, I. Ali, J.O. Kim, Photodegradation of perfluorooctanoic acid by graphene oxide-deposited TiO2 nanotube arrays in aqueous phase, J. Environ. Manage. 218 (2018) 333–339. doi:10.1016/j.jenvman.2018.04.016.

[80] F. Fu, Q. Wang, Removal of heavy metal ions from wastewaters: A review, J. Environ. Manage. 92 (2011) 407–418. doi:10.1016/j.jenvman.2010.11.011.

[81] M. Mehos, C. Turchi, A.J. Boegel, T. Merrill, R. Stanley, Pilot-Scale Stu of the Solar Detoxification o Groundwater Jim Pacheco Sandia National Laboratories, (1992).

[82] J.E.F. Moraes, F.H. Quina, C.A.O. Nascimento, D.N. Silva, O. Chiavone-Filho, Treatment of Saline Wastewater Contaminated with Hydrocarbons by the Photo-Fenton Process, Environ. Sci. Technol. 38 (2004) 1183–1187. doi:10.1021/es034217f.

[83] N. Negishi, Y. Miyazaki, S. Kato, Y. Yang, Effect of HCO3− concentration in groundwater on TiO2 photocatalytic water purification, Appl. Catal. B Environ. 242 (2019) 449–459. doi:10.1016/j.apcatb.2018.10.022.

[84] B. Wang, Z. Yang, H. An, J. Zhai, Q. Li, H. Cui, Photocatalytic activity of Pt-TiO2films supported on hydroxylated fly ash cenospheres under visible light, Appl. Surf. Sci. 324 (2015) 817–824. doi:10.1016/j.apsusc.2014.11.046.

[85] N. Negishi, M. Sugasawa, Y. Miyazaki, Y. Hirami, S. Koura, Effect of dissolved silica on photocatalytic water purification with a TiO2 ceramic catalyst, Water Res. 150 (2019) 40–46. doi:https://doi.org/10.1016/j.watres.2018.11.047.

[86] F.E. Osterloh, Inorganic nanostructures for photoelectrochemical and photocatalytic water splitting, Chem. Soc. Rev. 42 (2013) 2294–2320. doi:10.1039/c2cs35266d.

[87] T.L. Thompson, J.T. Yates, Surface Science Studies of the Photoactivation of TiO2New Photochemical Processes, Chem. Rev. 106 (2006) 4428–4453. doi:10.1021/cr050172k.

[88] F. Parrino, V. Loddo, V. Augugliaro, G. Camera-Roda, G. Palmisano, L. Palmisano, S. Yurdakal, Heterogeneous photocatalysis: guidelines on experimental setup, catalyst characterization, interpretation, and assessment of reactivity, Catal. Rev. - Sci. Eng. 61 (2019) 163–213. doi:10.1080/01614940.2018.1546445.

[89] R. Edla, N. Patel, M. Orlandi, N. Bazzanella, V. Bello, C. Maurizio, G. Mattei, P. Mazzoldi, A. Miotello, Highly photo-catalytically active hierarchical 3D porous/urchin nanostructured Co3O4 coating synthesized by Pulsed Laser Deposition, Appl. Catal. B Environ. 166–167 (2015) 475–484. doi:10.1016/j.apcatb.2014.11.060.

[90] M. Zimbone, M.A. Buccheri, G. Cacciato, R. Sanz Gonzàlez, G. Rappazzo, S. Boninelli, R. Reitano, L. Romano, V. Privitera, M.G. Grimaldi, {P}hotocatalytical and antibacterial activity of {T}i{O}2 nanoparticles obtained by laser ablation in water, Appl. Catal. B Environ. 165 (2015) 487–494. doi:doi:10.1016/j.apcatb.2014.10.031.

[91] D. Bahnemann, Photocatalytic water treatment: Solar energy applications, Sol. Energy. 77 (2004) 445–459. doi:10.1016/j.solener.2004.03.031.

[92] A. Mecha, M. Onyango, A. Ochieng, M. Momba, UV and solar photocatalytic disinfection of municipal wastewater: inactivation, reactivation and regrowth of bacterial pathogens, 2018. doi:10.1007/s13762-018-1950-1.

[93] R.K. Upadhyay, N. Soin, S.S. Roy, Role of graphene/metal oxide composites as photocatalysts{,} adsorbents and disinfectants in water treatment: a review, RSC Adv. 4 (2014) 3823–3851. doi:10.1039/C3RA45013A.

[94] N. Miranda-García, M.I. Maldonado, J.M. Coronado, S. Malato, Degradation study of 15 emerging contaminants at low concentration by immobilized TiO2 in a pilot plant, Catal. Today. 151 (2010) 107–113. doi:10.1016/j.cattod.2010.02.044.

[95] O. Youn-Chul, Photocatalytic degradation of organic contaminants in water, (2004). https://lib.dr.iastate.edu/rtd/1115.

[96] U.I. Gaya, A.H. Abdullah, Heterogeneous photocatalytic degradation of organic contaminants over titanium dioxide: A review of fundamentals, progress and problems, J. Photochem. Photobiol. C Photochem. Rev. 9 (2008) 1–12. doi:10.1016/j.jphotochemrev.2007.12.003.

[97] N. Patel, R. Jaiswal, T. Warang, G. Scarduelli, A. Dashora, B.L. Ahuja, D.C. Kothari, A. Miotello, Efficient photocatalytic degradation of organic water pollutants using V-N-codoped TiO2 thin films, Appl. Catal. B Environ. 150–151 (2014) 74–81. doi:10.1016/j.apcatb.2013.11.033.

[98] R. Jaiswal, J. Bharambe, N. Patel, A. Dashora, D.C. Kothari, A. Miotello, Copper and Nitrogen co-doped TiO2 photocatalyst with enhanced optical absorption and catalytic activity, Appl. Catal. B Environ. 168–169 (2015) 333–341. doi:10.1016/j.apcatb.2014.12.053.

[99] R. Jaiswal, N. Patel, A. Dashora, R. Fernandes, M. Yadav, R. Edla, R.S. Varma, D.C. Kothari, B.L. Ahuja, A. Miotello, Efficient Co-B-codoped TiO2 photocatalyst for degradation of organic water pollutant under visible light, Appl. Catal. B Environ. 183 (2016) 242–253. doi:10.1016/j.apcatb.2015.10.041.

[100] R.S. Varma, N. Thorat, R. Fernandes, D.C. Kothari, N. Patel, A. Miotello, Dependence of photocatalysis on charge carrier separation in Ag-doped and decorated TiO2 nanocomposites, Catal. Sci. Technol. 6 (2016) 8428–8440. doi:10.1039/c6cy01605g.

[101] H.Y. Jing, T. Wen, C.M. Fan, G.Q. Gao, S.L. Zhong, A.W. Xu, Efficient adsorption/photodegradation of organic pollutants from aqueous systems using Cu2O nanocrystals as a novel integrated photocatalytic adsorbent, J. Mater. Chem. A. 2 (2014) 14563–14570. doi:10.1039/c4ta02459a.

[102] S. Leong, A. Razmjou, K. Wang, K. Hapgood, X. Zhang, H. Wang, TiO2based photocatalytic membranes: A review, J. Memb. Sci. 472 (2014) 167–184. doi:10.1016/j.memsci.2014.08.016.

[103] S. Malato, M.I. Maldonado, P. Fernández-Ibáñez, I. Oller, I. Polo, R. Sánchez-Moreno, Decontamination and disinfection of water by solar photocatalysis: The pilot plants of the Plataforma Solar de Almeria, Mater. Sci. Semicond. Process. 42 (2016) 15–23. doi:10.1016/j.mssp.2015.07.017.

[104] J. Niu, L. Yin, Y. Dai, Y. Bao, J.C. Crittenden, Design of visible light responsive photocatalysts for selective reduction of chlorinated organic compounds in water, Appl. Catal. A Gen. 521 (2016) 90–95. doi:10.1016/j.apcata.2015.11.018.

[105] R. Edla, A. Tonezzer, M. Orlandi, N. Patel, R. Fernandes, N. Bazzanella, K. Date, D.C. Kothari, A. Miotello, 3D hierarchical nanostructures of iron oxides coatings prepared by pulsed laser deposition for photocatalytic water purification, Appl. Catal. B Environ. 219 (2017) 401–411. doi:10.1016/j.apcatb.2017.07.063.

[106] J. Fenoll, P. Hellín, C.M. Martínez, P. Flores, S. Navarro, Semiconductor oxides-sensitized photodegradation of fenamiphos in leaching water under natural sunlight, Appl. Catal. B Environ. 115–116 (2012) 31–37. doi:10.1016/j.apcatb.2011.12.023.

[107] M.B. Tahir, G. Nabi, M. Rafique, N.R. Khalid, Nanostructured-based WO3 photocatalysts: recent development, activity enhancement, perspectives and applications for wastewater treatment, Int. J. Environ. Sci. Technol. 14 (2017) 2519–2542. doi:10.1007/s13762-017-1394-z.

[108] M.E. Borges, M. Sierra, P. Esparza, Solar photocatalysis at semi-pilot scale: wastewater decontamination in a packed-bed photocatalytic reactor system with a visible-solar-light-driven photocatalyst, Clean Technol. Environ. Policy. 19 (2017) 1239–1245. doi:10.1007/s10098-016-1312-y.

[109] T. Sano, N. Negishi, K. Takeuchi, S. Matsuzawa, Degradation of toluene and acetaldehyde with Pt-loaded TiO2 catalyst and parabolic trough concentrator, Sol. Energy. 77 (2004) 543–552. doi:10.1016/j.solener.2004.03.018.

[110] N. Vela, M. Calín, M.J. Yáñez-Gascón, I. Garrido, G. Pérez-Lucas, J. Fenoll, S. Navarro, Solar reclamation of wastewater effluent polluted with bisphenols, phthalates and parabens by photocatalytic treatment with TiO2/Na2S2O8at pilot plant scale, Chemosphere. 212 (2018) 95–104. doi:10.1016/j.chemosphere.2018.08.069.

[111] E.M. Rodríguez, G. Fernández, N. Klamerth, M.I. Maldonado, P.M. Álvarez, S. Malato, Efficiency of different solar advanced oxidation processes on the oxidation of bisphenol A in water, Appl. Catal. B Environ. 95 (2010) 228–237. doi:10.1016/j.apcatb.2009.12.027.

[112] N. Muradov, Solar detoxification of nitroglycerine-contaminated water using immobilized titania, Sol. Energy. 52 (1994) 283–288. doi:10.1016/0038-092X(94)90495-2.

[113] L. Villén, F. Manjón, D. García-Fresnadillo, G. Orellana, Solar water disinfection by photocatalytic singlet oxygen production in heterogeneous medium, Appl. Catal. B Environ. 69 (2006) 1–9. doi:https://doi.org/10.1016/j.apcatb.2006.05.015.

[114] P. Bansal, A. Verma, S. Talwar, Detoxification of real pharmaceutical wastewater by integrating photocatalysis and photo-Fenton in fixed-mode, Chem. Eng. J. 349 (2018) 838–848. doi:10.1016/j.cej.2018.05.140.

[115] J.J. Pignatello, E. Oliveros, A. MacKay, Advanced Oxidation Processes for Organic Contaminant Destruction Based on the Fenton Reaction and Related Chemistry, Crit. Rev. Environ. Sci. Technol. 36 (2006) 1–84. doi:10.1080/10643380500326564.

[116] K. Soo-Myung, V. Alfons, Degradation of Organic Pollutants by the Photo-Fenton-Process, Chem. Eng. Technol. 21 (1999) 187–191. doi:10.1002/(SICI)1521-4125(199802)21:2<187::AID-CEAT187>3.0.CO;2-H.

[117] C. Ruales-Lonfat, J.F. Barona, A. Sienkiewicz, M. Bensimon, J. Vélez-Colmenares, N. Benítez, C. Pulgarín, Iron oxides semiconductors are efficients for solar water disinfection: A comparison with photo-Fenton processes at neutral pH, Appl. Catal. B Environ. 166–167 (2015) 497–508. doi:10.1016/j.apcatb.2014.12.007.

[118] I. García-Fernández, S. Miralles-Cuevas, I. Oller, S. Malato, P. Fernández-Ibáñez, M.I. Polo-López, Inactivation of E. coli and E. faecalis by solar photo-Fenton with EDDS complex at neutral pH in municipal wastewater effluents, J. Hazard. Mater. (2018) 0–1. doi:10.1016/j.jhazmat.2018.07.037.

[119] R. Edla, S. Gupta, N. Patel, N. Bazzanella, R. Fernandes, D.C. Kothari, A. Miotello, Enhanced H2 production from hydrolysis of sodium borohydride using Co3O4 nanoparticles assembled coatings prepared by pulsed laser deposition, Appl. Catal. A Gen. 515 (2016) 1–9. doi:10.1016/j.apcata.2016.01.031.

[120] M. Orlandi, N. Dalle Carbonare, S. Caramori, C.A. Bignozzi, S. Berardi, A. Mazzi, Z. El Koura, N. Bazzanella, N. Patel, A. Miotello, Porous versus Compact Nanosized Fe(III)-Based Water Oxidation Catalyst for Photoanodes Functionalization, ACS Appl. Mater. Interfaces. 8 (2016) 20003–20011. doi:10.1021/acsami.6b05135.

[121] M. Schenato, C.L.A. Ricardo, P. Scardi, R. Edla, A. Miotello, M. Orlandi, R. Morrish, Effect of annealing and nanostructuring on pulsed laser deposited WS2 for HER catalysis, Appl. Catal. A Gen. 510 (2016) 156–160. doi:10.1016/j.apcata.2015.11.009.

[122] C. Maurizio, R. Edla, N. Michieli, M. Orlandi, A. Trapananti, G. Mattei, A. Miotello, Two-step growth mechanism of supported Co3O4-based sea-urchin like hierarchical nanostructures, Appl. Surf. Sci. 439 (2018) 876–882. doi:10.1016/j.apsusc.2018.01.121.

[123] S. Malato, J. Blanco, D.C. Alarcón, M.I. Maldonado, P. Fernández-Ibáñez, W. Gernjak, Photocatalytic decontamination and disinfection of water with solar collectors, Catal. Today. 122 (2007) 137–149. doi:10.1016/j.cattod.2007.01.034.

[124] P. Fernandez-Ibanez, S. Malato, O. Enea, Photoelectrochemical reactors for the solar decontamination of water, 1999. doi:10.1016/S0920-5861(99)00194-7.

[125] M. Klare, J. Scheen, K. Vogelsang, H. Jacobs, J.A.C. Broekaert, Degradation of short-chain alkyl- and alkanolamines by TiO2- and Pt/TiO2-assisted photocatalysis, Chemosphere. 41 (2000) 353–362. doi:10.1016/S0045-6535(99)00447-6.

[126] T. Oyama, A. Aoshima, S. Horikoshi, H. Hidaka, J. Zhao, N. Serpone, Solar photocatalysis, photodegradation of a commercial detergent in aqueous TiO2 dispersions under sunlight irradiation, Sol. Energy. 77 (2004) 525–532. doi:https://doi.org/10.1016/j.solener.2004.04.020.

[127] C. Minero, E. Pelizzetti, S. Malato, J. Blanco, Large solar plant photocatalytic water decontamination: Effect of operational parameters, Sol. Energy. 56 (1996) 421–428. doi:https://doi.org/10.1016/0038-092X(96)00029-1.

[128] E.R. Bandala, C.A. Arancibia-Bulnes, S.L. Orozco, C.A. Estrada, Solar photoreactors comparison based on oxalic acid photocatalytic degradation, Sol. Energy. 77 (2004) 503–512. doi:https://doi.org/10.1016/j.solener.2004.03.021.

[129] S. Malato, J. Blanco, C. Richter, D. Curcó, J. Giménez, Low-concentrating CPC collectors for photocatalytic water detoxification: comparison with a medium concentrating solar collector, Water Sci. Technol. 35 (1997) 157–164. doi:10.2166/wst.1997.0109.

[130] M. Noorjahan, M. Pratap Reddy, V. Durga Kumari, B. Lavédrine, P. Boule, M. Subrahmanyam, Photocatalytic degradation of H-acid over a novel TiO2 thin film fixed bed reactor and in aqueous suspensions, J. Photochem. Photobiol. A Chem. 156 (2003) 179–187. doi:https://doi.org/10.1016/S1010-6030(02)00408-2.

[131] A.J. Feitz, B.H. Boyden, T.D. Waite, Evaluation of two solar pilot scale fixed-bed photocatalytic reactors, Water Res. 34 (2000) 3927–3932. doi:https://doi.org/10.1016/S0043-1354(00)00153-6.

[132] A.H.C. Chan, C.K. Chan, J.P. Barford, J.F. Porter, Solar photocatalytic thin film cascade reactor for treatment of benzoic acid containing wastewater, Water Res. 37 (2003) 1125–1135. doi:10.1016/s0043-1354(02)00465-7.

[133] M. van Well, R.H.G. Dillert, D.W. Bahnemann, V.W. Benz, M.A. Mueller, A Novel Nonconcentrating Reactor for Solar Water Detoxification, J. Sol. Energy Eng. 119 (1997) 114–119. doi:10.1115/1.2887888.

[134] J. Xu, Y. Ao, D. Fu, J. lin, Y. Lin, X. Shen, C. Yuan, Z. Yin, Photocatalytic activity on TiO2-coated side-glowing optical fiber reactor under solar light, J. Photochem. Photobiol. A Chem. 199 (2008) 165–169. doi:https://doi.org/10.1016/j.jphotochem.2008.05.019.

[135] M. Kositzi, I. Poulios, S. Malato, J. Caceres, A. Campos, Solar photocatalytic treatment of synthetic municipal wastewater, Water Res. 38 (2004) 1147–1154. doi:10.1016/j.watres.2003.11.024.

[136] V. Augugliaro, C. Baiocchi, A.B. Prevot, E. García-López, V. Loddo, S. Malato, G. Marcí, L. Palmisano, M. Pazzi, E. Pramauro, Azo-dyes photocatalytic degradation in aqueous suspension of TiO2 under solar irradiation, Chemosphere. 49 (2002) 1223—1230. doi:10.1016/s0045-6535(02)00489-7.

[137] L. Selva Roselin, G.R. Rajarajeswari, R. Selvin, V. Sadasivam, B. Sivasankar, K. Rengaraj, Sunlight/ZnO-Mediated photocatalytic degradation of reactive red 22 using thin film flat bed flow photoreactor, Sol. Energy. 73 (2002) 281–285. doi:10.1016/S0038-092X(02)00065-8.

[138] H.B. Thu, M. Karkmaz, E. Puzenat, C. Guillard, J.-M. Herrmann, From the fundamentals of photocatalysis to its applications in environment protection and in solar purification of water in arid countries, Res. Chem. Intermed. 31 (2005) 449–461. doi:10.1163/1568567053956671.

[139] A. Cabrera-Reina, S. Miralles-Cuevas, G. Rivas, J.A. Sánchez Pérez, Comparison of different detoxification pilot plants for the treatment of industrial wastewater by solar photo-Fenton: Are raceway pond reactors a feasible option?, Sci. Total Environ. 648 (2019) 601–608. doi:10.1016/j.scitotenv.2018.08.143.

[140] J.M. Monteagudo, A. Durán, I. San Martín, M. Aguirre, Effect of continuous addition of H2O2 and air injection on ferrioxalate-assisted solar photo-Fenton degradation of Orange II, Appl. Catal. B Environ. 89 (2009) 510–518. doi:10.1016/j.apcatb.2009.01.008.

[141] J. García-Montaño, L. Pérez-Estrada, I. Oller, M.I. Maldonado, F. Torrades, J. Peral, Pilot plant scale reactive dyes degradation by solar photo-Fenton and biological processes, J. Photochem. Photobiol. A Chem. 195 (2008) 205–214. doi:https://doi.org/10.1016/j.jphotochem.2007.10.004.

[142] C. Berberidou, V. Kitsiou, D.A. Lambropoulou, A. Antoniadis, E. Ntonou, G.C. Zalidis, I. Poulios, Evaluation of an alternative method for wastewater treatment containing pesticides using solar photocatalytic oxidation and constructed wetlands, J. Environ. Manage. 195 (2017) 133–139. doi:10.1016/j.jenvman.2016.06.010.

[143] V. Augugliaro, E. García-López, V. Loddo, S. Malato-Rodríguez, I. Maldonado, G. Marcì, R. Molinari, L. Palmisano, Degradation of lincomycin in aqueous medium: Coupling of solar photocatalysis and membrane separation, Sol. Energy. 79 (2005) 402–408. doi:https://doi.org/10.1016/j.solener.2005.02.020.

[144] O.A. McLoughlin, S.C. Kehoe, K.G. McGuigan, E.F. Duffy, F. Al Touati, W. Gernjak, I.O. Alberola, S.M. Rodríguez, L.W. Gill, Solar disinfection of contaminated water: a comparison of three small-scale reactors, Sol. Energy. 77 (2004) 657–664. doi:https://doi.org/10.1016/j.solener.2004.07.004.

[145] H. Freudenhammer, D. Bahnemann, L. Bousselmi, S.-V. Geissen, A. Ghrabi, F. Saleh, A. Si-Salah, V. Siemon, A. Vogelpohln, Detoxification and recycling of wastewater by solar-catalytic treatment, Water Sci. Technol. 35 (1997) 149–156. doi:https://doi.org/10.1016/S0273-1223(97)00020-6.

[146] M.I. Polo-López, I. García-Fernández, T. Velegraki, A. Katsoni, I. Oller, D. Mantzavinos, P. Fernández-Ibáñez, Mild solar photo-Fenton: An effective tool for the removal of Fusarium from simulated municipal effluents, Appl. Catal. B Environ. 111–112 (2012) 545–554. doi:10.1016/j.apcatb.2011.11.006.

[147] S. Nahim-Granados, J.A. Sánchez Pérez, M.I. Polo-Lopez, Effective solar processes in fresh-cut wastewater disinfection: Inactivation of pathogenic E. coli O157:H7 and Salmonella enteritidis, Catal. Today. 313 (2018) 79–85. doi:10.1016/j.cattod.2017.10.042.

[148] Y. Aguas, M. Hincapie, P. Fernández-Ibáñez, M.I. Polo-López, Solar photocatalytic disinfection of agricultural pathogenic fungi (Curvularia sp.) in real urban wastewater, Sci. Total Environ. 607–608 (2017) 1213–1224. doi:10.1016/j.scitotenv.2017.07.085.

[149] Y. Ruzmanova, M. Ustundas, M. Stoller, A. Chianese, Photocatalytic treatment of olive mill wastewater by n-doped titanium dioxide nanoparticles under visible light, Chem. Eng. Trans. 32 (2013) 2233–2238. doi:10.3303/CET1332373.

[150] A. Durán, J.M. Monteagudo, J. Gil, A.J. Expósito, I. San Martín, Solar-photo-Fenton treatment of wastewater from the beverage industry: Intensification with ferrioxalate, Chem. Eng. J. 270 (2015) 612–620. doi:10.1016/j.cej.2015.02.069.

[151] M. Brienza, M. Mahdi Ahmed, A. Escande, G. Plantard, L. Scrano, S. Chiron, S.A. Bufo, V. Goetz, Use of solar advanced oxidation processes for wastewater treatment: Follow-up on degradation products, acute toxicity, genotoxicity and estrogenicity, Chemosphere. 148 (2016) 473–480. doi:10.1016/j.chemosphere.2016.01.070.

[152] L. Onotri, M. Race, L. Clarizia, M. Guida, M. Alfè, R. Andreozzi, R. Marotta, Solar photocatalytic processes for treatment of soil washing wastewater, Chem. Eng. J. 318 (2017) 10–18. doi:10.1016/j.cej.2016.04.053.

[153] D.R. Manenti, P.A. Soares, A.N. Módenes, F.R. Espinoza-Quiñones, R.A.R. Boaventura, R. Bergamasco, V.J.P. Vilar, Insights into solar photo-Fenton process using iron(III)-organic ligand complexes applied to real textile wastewater treatment, Chem. Eng. J. 266 (2015) 203–212. doi:10.1016/j.cej.2014.12.077.

[154] M. Gar Alalm, A. Tawfik, S. Ookawara, Comparison of solar TiO2photocatalysis and solar photo-Fenton for treatment of pesticides industry wastewater: Operational conditions, kinetics, and costs, J. Water Process Eng. 8 (2015) 55–63. doi:10.1016/j.jwpe.2015.09.007.

[155] P. Pichat, S. Vannier, J. Dussaud, J.-P. Rubis, Field solar photocatalytic purification of pesticides-containing rinse waters from tractor cisterns used for grapevine treatment, Sol. Energy. 77 (2004) 533–542. doi:https://doi.org/10.1016/j.solener.2004.03.023.

[156] F. Méndez-Arriaga, M.I. Maldonado, J. Gimenez, S. Esplugas, S. Malato, Abatement of ibuprofen by solar photocatalysis process: Enhancement and scale up, Catal. Today. 144 (2009) 112–116. doi:10.1016/j.cattod.2009.01.028.

[157] S. Foteinis, J.M. Monteagudo, A. Durán, E. Chatzisymeon, Environmental sustainability of the solar photo-Fenton process for wastewater treatment and pharmaceuticals mineralization at semi-industrial scale, Sci. Total Environ. 612 (2018) 605–612. doi:10.1016/j.scitotenv.2017.08.277.

[158] G. Ferro, A. Fiorentino, M.C. Alferez, M.I. Polo-López, L. Rizzo, P. Fernández-Ibáñez, Urban wastewater disinfection for agricultural reuse: effect of solar driven AOPs in the inactivation of a multidrug resistant E. coli strain, Appl. Catal. B Environ. 178 (2015) 65–73. doi:10.1016/j.apcatb.2014.10.043.

[159] F. Almomani, R. Bhosale, A. Kumar, M. Khraisheh, Potential use of solar photocatalytic oxidation in removing emerging pharmaceuticals from wastewater: A pilot plant study, Sol. Energy. 172 (2018) 128–140. doi:10.1016/j.solener.2018.07.041.

[160] S. Miralles-Cuevas, I. Oller, A. Agüera, J.A. Sánchez Pérez, S. Malato, Strategies for reducing cost by using solar photo-Fenton treatment combined with nanofiltration to remove microcontaminants in real municipal effluents: Toxicity and economic assessment, Chem. Eng. J. 318 (2017) 161–170. doi:10.1016/j.cej.2016.06.031.

[161] E. Ortega-Gómez, B. Esteban García, M.M. Ballesteros Martín, P. Fernández Ibáñez, J.A. Sánchez Pérez, Inactivation of natural enteric bacteria in real municipal wastewater by solar photo-Fenton at neutral pH, Water Res. 63 (2014) 316–324. doi:10.1016/j.watres.2014.05.034.

[162] M.I. Polo-López, M. Castro-Alférez, I. Oller, P. Fernández-Ibáñez, Assessment of solar photo-Fenton, photocatalysis, and H2O2 for removal of phytopathogen fungi spores in synthetic and real effluents of urban wastewater, Chem. Eng. J. 257 (2014) 122–130. doi:10.1016/j.cej.2014.07.016.

[163] S. Turrini, M. Bettonte, M. Eccher, M. Grigiante, A. Miotello, R.S. Brusa, An innovative small-scale prototype plant integrating a solar dish concentrator with a molten salt storage system, Renew. Energy. 123 (2018) 150–161. doi:10.1016/j.renene.2018.02.053.

[164] N. Filosa, Treatment of organic pollutants in water with concentrated sunlight: towards a solar wastewater remediation process, University of Trento, 2017.

[165] P.B. Allen, Theory of thermal relaxation of electrons in metals, Phys. Rev. Lett. 59 (1987) 1460–1463. doi:10.1103/PhysRevLett.59.1460.

[166] R.W. Schoenlein, W.Z. Lin, J.G. Fujimoto, G.L. Eesley, Femtosecond studies of nonequilibrium electronic processes in metals, Phys. Rev. Lett. 58 (1987) 1680–1683. doi:10.1103/PhysRevLett.58.1680.

[167] R.F. Haglund, Laser Physics for Materials Scientists: A Primer BT - Lasers in Materials Science, in: M. Castillejo, P.M. Ossi, L. Zhigilei (Eds.), Springer International Publishing, Cham, 2014: pp. 1–28. doi:10.1007/978-3-319-02898-9_1.

[168] J. Reif, Material Response to Laser Energy Deposition (Thermal and Hyperthermal Processes) BT - Lasers in Materials Science, in: M. Castillejo, P.M. Ossi, L. Zhigilei (Eds.), Springer International Publishing, Cham, 2014: pp. 29–41. doi:10.1007/978-3-319-02898-9_2.

[169] R. Kelly, A. Miotello, Contribution of vaporization and boiling to thermal-spike sputtering by ions or laser pulses, Phys. Rev. E. 60 (1999) 2616–2625. doi:10.1103/PhysRevE.60.2616.

[170] A. Mazzi, F. Gorrini, A. Miotello, Liquid nanodroplet formation through phase explosion mechanism in laser-irradiated metal targets, Phys. Rev. E. 92 (2015) 31301. doi:10.1103/PhysRevE.92.031301.

[171] A. Miotello, R. Kelly, Critical assessment of thermal models for laser sputtering at high fluences, Appl. Phys. Lett. 67 (1995) 3535–3537. doi:10.1063/1.114912.

[172] R.F. Wood, J.N. Leboeuf, D.B. Geohegan, A.A. Puretzky, K.R. Chen, Dynamics of plume propagation and splitting during pulsed-laser ablation of Si in He and Ar, Phys. Rev. B. 58 (1998) 1533–1543. doi:10.1103/PhysRevB.58.1533.

[173] M. Bonelli, C. Cestari, A. Miotello, Pulsed laser deposition apparatus for applied research, Meas. Sci. Technol. 10 (1999) N27–N30. doi:10.1088/0957-0233/10/3/024.

[174] J.A. Greer, History and current status of commercial pulsed laser deposition equipment, J. Phys. D. Appl. Phys. 47 (2013) 34005. doi:10.1088/0022-3727/47/3/034005.

[175] J.I. Goldstein, D.E. Newbury, J.R. Michael, N.W.M. Ritchie, J.H.J. Scott, D.C. Joy, Scanning electron microscopy and X-ray microanalysis, Springer, 2017.

[176] A. Santini, Synthesis and characterization of nanostructures for catalysis, University of Trento, 2012.

[177] X-ray Diffraction (XRD) Academy, (2020). https://www.thermofisher.com/it/en/home/industrial/spectroscopy-elemental-isotope-analysis/spectroscopy-elemental-isotope-analysis-learning-center/elemental-structural-analysis-information/xrd-academy.html (accessed September 25, 2020).

[178] J. Grebenkemper, Powder X-Ray Diffraction, (2020). https://chem.libretexts.org/link?314 (accessed September 25, 2020).

[179] Z. El Koura, Solar water splitting for hydrogen production: development of photocatalysts based on earth abundant and biocompatible materials (TiO2 and Fe2O3), University of Trento, 2016.

[180] T. Schmid, P. Dariz, Raman Microspectroscopic Imaging of Binder Remnants in Historical Mortars Reveals Processing Conditions, Heritage. 2 (2019) 1662–1683. doi:10.3390/heritage2020102.

[181] T. Owen, Fundamentals of modern UV-visible spectroscopy, Hewlett-Packard, 1996.

[182] K. Gopalakrishnan, H.M. Joshi, P. Kumar, L.S. Panchakarla, C.N.R. Rao, Selectivity in the photocatalytic properties of the composites of TiO 2 nanoparticles with B- and N-doped graphenes, Chem. Phys. Lett. 511 (2011) 304–308. doi:10.1016/j.cplett.2011.06.033.

[183] W. Jin, H. quan Zhang, S. shuang Liu, H. bo Zhang, Technological innovation, environmental regulation, and green total factor efficiency of industrial water resources, J. Clean. Prod. 211 (2019) 61–69. doi:10.1016/j.jclepro.2018.11.172.

[184] X.Y. Zhou, B. Zheng, S.T. Khu, Validation of the hypothesis on carrying capacity limits using the water environment carrying capacity, Sci. Total Environ. 665 (2019) 774–784. doi:10.1016/j.scitotenv.2019.02.146.

[185] A.C. Mecha, M.S. Onyango, A. Ochieng, M.N.B. Momba, Ultraviolet and solar photocatalytic ozonation of municipal wastewater: Catalyst reuse, energy requirements and toxicity assessment, Chemosphere. 186 (2017) 669–676. doi:10.1016/j.chemosphere.2017.08.041.

[186] J. Willet, K. Wetser, J. Vreeburg, H.H.M. Rijnaarts, Review of methods to assess sustainability of industrial water use, Water Resour. Ind. 21 (2019) 100110. doi:10.1016/j.wri.2019.100110.

[187] A. Gupta, I.S. Thakur, Treatment of Organic Recalcitrant Contaminants in Wastewater, in: R. Farooq, Z. Ahmad (Eds.), Biol. Wastewater Treat. Resour. Recover., IntechOpen, Rijeka, 2017. doi:10.5772/66346.

[188] F.S. Manciu, J.L. Enriquez, W.G. Durrer, Y. Yun, C. V. Ramana, S.K. Gullapalli, Spectroscopic analysis of tungsten oxide thin films, J. Mater. Res. 25 (2010) 2401–2406. doi:10.1557/jmr.2010.0294.

[189] V.I. Shapovalov, A.E. Lapshin, A.G. Gagarin, L.P. Efimenko, Chemical composition and crystal structure of tungsten oxide films, Glas. Phys. Chem. 40 (2014) 553–569. doi:10.1134/S1087659614050150.

[190] L.H. Jin, Y. Bai, C.S. Li, Y. Wang, J.Q. Feng, L. Lei, G.Y. Zhao, P.X. Zhang, Growth of tungsten oxide nanostructures by chemical solution deposition, Appl. Surf. Sci. 440 (2018) 725–729. doi:10.1016/j.apsusc.2018.01.251.

[191] E. Besozzi, D. Dellasega, V. Russo, C. Conti, M. Passoni, M.G. Beghi, Thermomechanical properties of amorphous metallic tungsten-oxygen and tungsten-oxide coatings, Mater. Des. 165 (2019) 107565. doi:10.1016/j.matdes.2018.107565.

[192] H. Na, Y. Eun, M.O. Kim, J. Choi, J. Kim, Low-Temperature Selective Growth of Tungsten Oxide Nanowires by Controlled Nanoscale Stress Induction, Sci. Rep. 5 (2015) 1–8. doi:10.1038/srep18265.

[193] M.I. Nave, K.G. Kornev, Complexity of Products of Tungsten Corrosion: Comparison of the 3D Pourbaix Diagrams with the Experimental Data, Metall. Mater. Trans. A Phys. Metall. Mater. Sci. 48 (2017) 1414–1424. doi:10.1007/s11661-016-3888-6.

[194] T. Kikuchi, J. Kawashima, S. Natsui, R.O. Suzuki, Fabrication of porous tungsten oxide via anodizing in an ammonium nitrate/ethylene glycol/water mixture for visible light-driven photocatalyst, Appl. Surf. Sci. 422 (2017) 130–137. doi:10.1016/j.apsusc.2017.05.256.

[195] S. Salmaoui, F. Sediri, N. Gharbi, C. Perruchot, S. Aeiyach, I.A. Rutkowska, P.J. Kulesza, M. Jouini, Hexagonal nanorods of tungsten trioxide: Synthesis, structure, electrochemical properties and activity as supporting material in electrocatalysis, Appl. Surf. Sci. 257 (2011) 8223–8229. doi:10.1016/j.apsusc.2011.04.077.

[196] M. Visa, C. Bogatu, A. Duta, Tungsten oxide - fly ash oxide composites in adsorption and photocatalysis, J. Hazard. Mater. 289 (2015) 244–256. doi:10.1016/j.jhazmat.2015.01.053.

[197] M. Aslam, I.M.I. Ismail, S. Chandrasekaran, A. Hameed, Morphology controlled bulk synthesis of disc-shaped WO3 powder and evaluation of its photocatalytic activity for the degradation of phenols, J. Hazard. Mater. 276 (2014) 120–128. doi:10.1016/j.jhazmat.2014.05.022.

[198] I. Aslam, C. Cao, W.S. Khan, M. Tanveer, M. Abid, F. Idrees, R. Riasat, M. Tahir, F.K. Butt, Z. Ali, Synthesis of three-dimensional WO3 octahedra: Characterization, optical and efficient photocatalytic properties, RSC Adv. 4 (2014) 37914–37920. doi:10.1039/c4ra05724d.

[199] W. Chen, L. Chang, S. Bin Ren, Z.C. He, G.B. Huang, X.H. Liu, Direct Z-scheme 1D/2D WO2.72/ZnIn2S4 hybrid photocatalysts with highly-efficient visible-light-driven photodegradation towards tetracycline hydrochloride removal, J. Hazard. Mater. 384 (2020) 121308. doi:10.1016/j.jhazmat.2019.121308.

[200] S. Chen, Y. Xiao, W. Xie, Y. Wang, Z. Hu, W. Zhang, H. Zhao, Facile strategy for synthesizing non-stoichiometric monoclinic structured tungsten trioxide (WO 3−x) with plasma resonance absorption and enhanced photocatalytic activity, Nanomaterials. 8 (2018). doi:10.3390/nano8070553.

[201] F. Barreca, N. Acacia, S. Spadaro, G. Currò, F. Neri, Tungsten trioxide (WO3 - X) nanoparticles prepared by pulsed laser ablation in water, Mater. Chem. Phys. 127 (2011) 197–202. doi:10.1016/j.matchemphys.2011.01.059.

[202] K.J. Lethy, D. Beena, R. Vinod Kumar, V.P. Mahadevan Pillai, V. Ganesan, V. Sathe, D.M. Phase, Nanostructured tungsten oxide thin films by the reactive pulsed laser deposition technique, Appl. Phys. A Mater. Sci. Process. 91 (2008) 637–649. doi:10.1007/s00339-008-4492-4.

[203] H. Wu, K. Yin, W. Qi, X. Zhou, J. He, J. Li, Y. Liu, J. He, S. Gong, Y. Li, Rapid Fabrication of Ni/NiO@CoFe Layered Double Hydroxide Hierarchical Nanostructures by Femtosecond Laser Ablation and Electrodeposition for Efficient Overall Water Splitting, ChemSusChem. 12 (2019) 2773–2779. doi:10.1002/cssc.201900479.

[204] A. Bailini, F. Di Fonzo, M. Fusi, C.S. Casari, A.L. Bassi, V. Russo, A. Baserga, C.E. Bottani, Pulsed laser deposition of tungsten and tungsten oxide thin films with tailored structure at the nano- and mesoscale, Appl. Surf. Sci. 253 (2007) 8130–8135. doi:10.1016/j.apsusc.2007.02.145.

[205] G. Soto, W. De La Cruz, J.A. Díaz, R. Machorro, F.F. Castillón, M.H. Farías, Characterization of tungsten oxide films produced by reactive pulsed laser deposition, Appl. Surf. Sci. 218 (2003) 281–289. doi:10.1016/S0169-4332(03)00677-9.

[206] S. Shuntaro, T. Suzuki, M. Hirai, H. Suematsu, C. Grigoriu, C. Sima, I. Nicolae, W. Waldhauser, M. Lackner, Synthesis and optimization of tungsten and tungsten oxide films produced by laser ablation, J. Phys. Conf. Ser. 59 (2007) 297–300. doi:10.1088/1742-6596/59/1/062.

[207] A. Mazzi, A. Miotello, Simulation of phase explosion in the nanosecond laser ablation of aluminum, J. Colloid Interface Sci. 489 (2017) 126–130. doi:10.1016/j.jcis.2016.08.016.

[208] Q. Hao, W. Chen, G. Xiao, Beta (β) tungsten thin films: Structure, electron transport, and giant spin Hall effect, Appl. Phys. Lett. 106 (2015). doi:10.1063/1.4919867.

[209] S.C. Cifuentes, M.A. Monge, P. Pérez, On the oxidation mechanism of pure tungsten in the temperature range 600-800°C, Corros. Sci. 57 (2012) 114–121. doi:10.1016/j.corsci.2011.12.027.

[210] C. Fan, C. Liu, F. Peng, N. Tan, M. Tang, Q. Zhang, Q. Wang, F. Li, J. Wang, Y. Chen, H. Liang, S. Guan, K. Yang, J. Liu, Phase stability and incompressibility of tungsten boride (WB) researched by in-situ high pressure x-ray diffraction, Phys. B Condens. Matter. 521 (2017) 6–12. doi:10.1016/j.physb.2017.06.028.

[211] J. Chrzanowska, L. Kurpaska, M. Giżyński, J. Hoffman, Z. Szymański, T. Mościcki, Fabrication and characterization of superhard tungsten boride layers deposited by radio frequency magnetron sputtering, Ceram. Int. 42 (2016) 12221–12230. doi:10.1016/j.ceramint.2016.04.166.

[212] S.A. Aly, A.A. Akl, D.H. Mahmoud, Microstructural and electrical characteristics of sprayed Tungsten oxide thin films, Int. J. New Horizons Phys. 2 (2015) 47. doi:10.12785/ijnhp/020202.

[213] R. Ponnusamy, A. Gangan, B. Chakraborty, C. Sekhar Rout, Tuning the pure monoclinic phase of WO3 and WO3-Ag nanostructures for non-enzymatic glucose sensing application with theoretical insight from electronic structure simulations, J. Appl. Phys. 123 (2018). doi:10.1063/1.5010826.

[214] J. Zhang, Z. Liu, Z. Liu, Novel WO3/Sb2S3 Heterojunction Photocatalyst Based on WO3 of Different Morphologies for Enhanced Efficiency in Photoelectrochemical Water Splitting, ACS Appl. Mater. Interfaces. 8 (2016) 9684–9691. doi:10.1021/acsami.6b00429.

[215] S. Yamamoto, A. Inouye, M. Yoshikawa, Structural and gasochromic properties of epitaxial WO3 films prepared by pulsed laser deposition, Nucl. Instruments Methods Phys. Res. Sect. B Beam Interact. with Mater. Atoms. 266 (2008) 802–806. doi:10.1016/j.nimb.2007.12.092.

[216] F. Tavakoli Foroushani, H. Tavanai, M. Ranjbar, H. Bahrami, Fabrication of tungsten oxide nanofibers via electrospinning for gasochromic hydrogen detection, Sensors Actuators, B Chem. 268 (2018) 319–327. doi:10.1016/j.snb.2018.04.120.

[217] Y. Djaoued, S. Balaji, R. Brüning, Electrochromic devices based on porous tungsten oxide thin films, J. Nanomater. 2012 (2012) 1–9. doi:10.1155/2012/674168.

[218] M. Desseigne, N. Dirany, V. Chevallier, M. Arab, Shape dependence of photosensitive properties of WO 3 oxide for photocatalysis under solar light irradiation, Appl. Surf. Sci. 483 (2019) 313–323. doi:10.1016/j.apsusc.2019.03.269.

[219] H. Guo, N. Jiang, H. Wang, N. Lu, K. Shang, J. Li, Y. Wu, Pulsed discharge plasma assisted with graphene-WO3 nanocomposites for synergistic degradation of antibiotic enrofloxacin in water, Chem. Eng. J. 372 (2019) 226–240. doi:10.1016/j.cej.2019.04.119.

[220] A. Houas, H. Lachheb, M. Ksibi, E. Elaloui, C. Guillard, J.M. Herrmann, Photocatalytic degradation pathway of methylene blue in water, Appl. Catal. B Environ. 31 (2001) 145–157. doi:10.1016/S0926-3373(00)00276-9.

[221] A. Katafias, M. Lipińska, K. Strutyński, Alkaline hydrogen peroxide as a degradation agent of methylene blue-kinetic and mechanistic studies, React. Kinet. Mech. Catal. 101 (2010) 251–266. doi:10.1007/s11144-010-0234-7.

[222] S.G. Kumar, K.S.R.K. Rao, Tungsten-based nanomaterials (WO 3 & Bi 2 WO 6): Modifications related to charge carrier transfer mechanisms and photocatalytic applications, Appl. Surf. Sci. 355 (2015) 939–958. doi:10.1016/j.apsusc.2015.07.003.

[223] D.P. Depuccio, P. Botella, B. O’Rourke, C.C. Landry, Degradation of methylene blue using porous WO3, SiO2-WO3, and their Au-loaded analogs: Adsorption and photocatalytic studies, ACS Appl. Mater. Interfaces. 7 (2015) 1987–1996. doi:10.1021/am507806a.

[224] M. Pourbaix, Atlas of electrochemical equilibria in aqueous solutions, Pergamon Press, Oxford; New York, 1966.

[225] M. Kummu, J.H.A. Guillaume, H. De Moel, S. Eisner, M. Flörke, M. Porkka, S. Siebert, T.I.E. Veldkamp, P.J. Ward, The world’s road to water scarcity: Shortage and stress in the 20th century and pathways towards sustainability, Sci. Rep. 6 (2016) 1–16. doi:10.1038/srep38495.

[226] Y. Sharma, Water Pollution Control - A Guide to the Use of Water Quality Management Principles: Case Study I - The Ganga , India, 1997.

[227] M. Stan, A. Popa, D. Toloman, T.D. Silipas, D.C. Vodnar, Antibacterial and antioxidant activities of ZnO nanoparticles synthesized using extracts of Allium sativum, Rosmarinus officinalis and Ocimum basilicum, Acta Metall. Sin. (English Lett. 29 (2016) 228–236. doi:10.1007/s40195-016-0380-7.

[228] H.S. Kibombo, A.S. Weber, C.M. Wu, K.R. Raghupathi, R.T. Koodali, Effectively dispersed europium oxide dopants in tio2 aerogel supports for enhanced photocatalytic pollutant degradation, J. Photochem. Photobiol. A Chem. 269 (2013) 49–58. doi:10.1016/j.jphotochem.2013.07.006.

[229] D.S. Bhatkhande, V.G. Pangarkar, A.A.C.M. Beenackers, Photocatalytic degradation for environmental applications - A review, J. Chem. Technol. Biotechnol. 77 (2002) 102–116. doi:10.1002/jctb.532.

[230] M. Samadi, M. Zirak, A. Naseri, E. Khorashadizade, A.Z. Moshfegh, Recent progress on doped ZnO nanostructures for visible-light photocatalysis, Thin Solid Films. 605 (2016) 2–19. doi:10.1016/j.tsf.2015.12.064.

[231] N.S. Lewis, Toward cost-effective solar energy use, Science (80-.). 315 (2007) 798–801. doi:10.1126/science.1137014.

[232] R. Vinu, G. Madras, Environmental remediation by photocatalysis, J. Indian Inst. Sci. 90 (2010) 189–230.

[233] X. Li, J. Yu, M. Jaroniec, Hierarchical photocatalysts, Chem. Soc. Rev. 45 (2016) 2603–2636. doi:10.1039/c5cs00838g.

[234] M. Belhaj, C. Dridi, R. Yatskiv, J. Grym, The improvement of UV photodetection based on polymer/ZnO nanorod heterojunctions, Org. Electron. 77 (2020) 105545. doi:https://doi.org/10.1016/j.orgel.2019.105545.

[235] G. Yi, X. Li, Y. Yuan, Y. Zhang, Redox active Zn/ZnO duo generating superoxide (O 2−) and H 2 O 2 under all conditions for environmental sanitation, Environ. Sci. Nano. 6 (2019) 68–74. doi:10.1039/c8en01095a.

[236] C.B. Ong, L.Y. Ng, A.W. Mohammad, A review of ZnO nanoparticles as solar photocatalysts: Synthesis, mechanisms and applications, Renew. Sustain. Energy Rev. 81 (2018) 536–551. doi:10.1016/j.rser.2017.08.020.

[237] D. Jemmeli, M. Belhaj, B. Ben Salem, N. Jaballah, R. Yatskiv, C. Dridi, J. Grym, M. Majdoub, PPV derivative/ZnO nanorods heterojunction: Fabrication, Characterization and Near-UV light sensor development, Mater. Res. Bull. 106 (2018) 28–34. doi:10.1016/j.materresbull.2018.05.017.

[238] D. Suresh, R.M. Shobharani, P.C. Nethravathi, M.A. Pavan Kumar, H. Nagabhushana, S.C. Sharma, Artocarpus gomezianus aided green synthesis of ZnO nanoparticles: Luminescence, photocatalytic and antioxidant properties, Spectrochim. Acta - Part A Mol. Biomol. Spectrosc. 141 (2015) 128–134. doi:10.1016/j.saa.2015.01.048.

[239] T. Jan, J. Iqbal, M. Ismail, A. Mahmood, Synthesis of highly efficient antibacterial agent Ag doped ZnO nanorods: Structural, Raman and optical properties, J. Appl. Phys. 115 (2014) 154308–1. doi:10.1063/1.4869736.

[240] Y. Lai, M. Meng, Y. Yu, One-step synthesis, characterizations and mechanistic study of nanosheets-constructed fluffy ZnO and Ag/ZnO spheres used for Rhodamine B photodegradation, Appl. Catal. B Environ. 100 (2010) 491–501. doi:10.1016/j.apcatb.2010.08.027.

[241] C.A. Soto-Robles, O.J. Nava, A.R. Vilchis-Nestor, A. Castro-Beltrán, C.M. Gómez-Gutiérrez, E. Lugo-Medina, A. Olivas, P.A. Luque, Biosynthesized zinc oxide using Lycopersicon esculentum peel extract for methylene blue degradation, J. Mater. Sci. Mater. Electron. 29 (2018) 3722–3729. doi:10.1007/s10854-017-8305-4.

[242] S. Jebril, R. Khanfir Ben Jenana, C. Dridi, Green synthesis of silver nanoparticles using Melia azedarach leaf extract and their antifungal activities: In vitro and in vivo, Mater. Chem. Phys. 248 (2020). doi:10.1016/j.matchemphys.2020.122898.

[243] S. Das, J. Chakraborty, S. Chatterjee, H. Kumar, Prospects of biosynthesized nanomaterials for the remediation of organic and inorganic environmental contaminants, Environ. Sci. Nano. 5 (2018) 2784–2808. doi:10.1039/C8EN00799C.

[244] M. Hosseini-Sarvari, Z. Razmi, Highly active recyclable heterogeneous Pd/ZnO nanoparticle catalyst: Sustainable developments for the C-O and C-N bond cross-coupling reactions of aryl halides under ligand-free conditions, RSC Adv. 4 (2014) 44105–44116. doi:10.1039/c4ra06486k.

[245] H. Deng, D.A. Clausi, Unsupervised segmentation of synthetic aperture radar sea ice imagery using MRF models, in: Proc. - 1st Can. Conf. Comput. Robot Vis., 2004: pp. 43–50. doi:10.1016/j.tsf.2003.11.288.

[246] T.E. Park, B.H. Kong, H.K. Cho, D.J. Park, J.Y. Lee, Influence of gas atmosphere during growth interruption in the deposition of ZnO films by magnetron sputtering, in: Phys. B Condens. Matter, 2006: pp. 735–740. doi:10.1016/j.physb.2005.12.184.

[247] F. Peng, H. Wang, H. Yu, S. Chen, Preparation of aluminum foil-supported nano-sized ZnO thin films and its photocatalytic degradation to phenol under visible light irradiation, Mater. Res. Bull. 41 (2006) 2123–2129. doi:10.1016/j.materresbull.2006.03.029.

[248] Z.E. Vakulov, E.G. Zamburg, D.A. Khakhulin, O.A. Ageev, Thermal stability of ZnO thin films fabricated by pulsed laser deposition, Mater. Sci. Semicond. Process. 66 (2017) 21–25. doi:10.1016/j.mssp.2017.03.006.

[249] P. Rajiv, S. Rajeshwari, R. Venckatesh, Bio-Fabrication of zinc oxide nanoparticles using leaf extract of Parthenium hysterophorus L. and its size-dependent antifungal activity against plant fungal pathogens, Spectrochim. Acta - Part A Mol. Biomol. Spectrosc. 112 (2013) 384–387. doi:10.1016/j.saa.2013.04.072.

[250] D. Suresh, Udayabhanu, P.C. Nethravathi, K. Lingaraju, H. Rajanaika, S.C. Sharma, H. Nagabhushana, EGCG assisted green synthesis of ZnO nanopowders: Photodegradative, antimicrobial and antioxidant activities, Spectrochim. Acta - Part A Mol. Biomol. Spectrosc. 136 (2015) 1467–1474. doi:10.1016/j.saa.2014.10.038.

[251] P.C. Nethravathi, G.S. Shruthi, D. Suresh, Udayabhanu, H. Nagabhushana, S.C. Sharma, Garcinia xanthochymus mediated green synthesis of ZnO nanoparticles: Photoluminescence, photocatalytic and antioxidant activity studies, Ceram. Int. 41 (2015) 8680–8687. doi:10.1016/j.ceramint.2015.03.084.

[252] A.K. Zak, M.E. Abrishami, W.H.A. Majid, R. Yousefi, S.M. Hosseini, Effects of annealing temperature on some structural and optical properties of ZnO nanoparticles prepared by a modified sol-gel combustion method, Ceram. Int. 37 (2011) 393–398. doi:10.1016/j.ceramint.2010.08.017.

[253] T. Dayakar., K. Venkateswara Rao., K. Bikshalu., V. Rajendar., S.H. Park, Novel synthesis and structural analysis of zinc oxide nanoparticles for the non enzymatic glucose biosensor, Mater. Sci. Eng. C. 75 (2017) 1472–1479. doi:10.1016/j.msec.2017.02.032.

[254] X. Zhang, Y. Chen, S. Zhang, C. Qiu, High photocatalytic performance of high concentration Al-doped ZnO nanoparticles, Sep. Purif. Technol. 172 (2017) 236–241. doi:https://doi.org/10.1016/j.seppur.2016.08.016.

[255] M. Sajid, M.S. Butt, A. Shehzad, S. Tanweer, Chemical and mineral analysis of garlic: a golden herb, Pakistan J. Food Sci. 24 (2014) 108–110.

[256] S. Kaviya, E. Prasad, Biogenic synthesis of ZnO-Ag nano custard apples for efficient photocatalytic degradation of methylene blue by sunlight irradiation, RSC Adv. 5 (2015) 17179–17185. doi:10.1039/c4ra15293j.

[257] A. Moulahi, F. Sediri, Pencil-like zinc oxide micro/nano-scale structures: Hydrothermal synthesis, optical and photocatalytic properties, Mater. Res. Bull. 48 (2013) 3723–3728. doi:10.1016/j.materresbull.2013.05.116.

[258] T.R. Gordon, M. Cargnello, T. Paik, F. Mangolini, R.T. Weber, P. Fornasiero, C.B. Murray, Nonaqueous synthesis of TiO 2 nanocrystals using TiF 4 to engineer morphology, oxygen vacancy concentration, and photocatalytic activity, J. Am. Chem. Soc. 134 (2012) 6751–6761. doi:10.1021/ja300823a.

[259] S. Wang, L. Pan, J.J. Song, W. Mi, J.J. Zou, L. Wang, X. Zhang, Titanium-defected undoped anatase TiO2 with p-type conductivity, room-temperature ferromagnetism, and remarkable photocatalytic performance, J. Am. Chem. Soc. 137 (2015) 2975–2983. doi:10.1021/ja512047k.

[260] F. Zuo, L. Wang, T. Wu, Z. Zhang, D. Borchardt, P. Feng, Self-doped Ti3+ enhanced photocatalyst for hydrogen production under visible light, J. Am. Chem. Soc. 132 (2010) 11856–11857. doi:10.1021/ja103843d.

[261] L. Saikia, D. Bhuyan, M. Saikia, B. Malakar, D.K. Dutta, P. Sengupta, Photocatalytic performance of ZnO nanomaterials for self sensitized degradation of malachite green dye under solar light, Appl. Catal. A Gen. 490 (2015) 42–49. doi:10.1016/j.apcata.2014.10.053.

[262] Q. Li, X. Li, S. Wageh, A.A. Al-Ghamdi, J. Yu, CdS/Graphene Nanocomposite Photocatalysts, Adv. Energy Mater. 5 (2015) 1–28. doi:10.1002/aenm.201500010.

[263] P. Taylor, S. Lam, J. Sin, A.Z. Abdullah, A.R. Mohamed, Degradation of wastewaters containing organic dyes photocatalysed by zinc oxide : a review, Desalin. Water Treat. (2012) 37–41. doi:10.1080/19443994.2012.664698.

[264] B. Weng, S. Liu, Z.R. Tang, Y.J. Xu, One-dimensional nanostructure based materials for versatile photocatalytic applications, RSC Adv. 4 (2014) 12685–12700. doi:10.1039/c3ra47910b.

[265] F.H. Abdullah, N.H.H. Abu Bakar, M. Abu Bakar, Low temperature biosynthesis of crystalline zinc oxide nanoparticles from Musa acuminata peel extract for visible-light degradation of methylene blue, Optik (Stuttg). 206 (2020) 164279. doi:https://doi.org/10.1016/j.ijleo.2020.164279.

[266] O.J. Nava, C.A. Soto-Robles, C.M. Gómez-Gutiérrez, A.R. Vilchis-Nestor, A. Castro-Beltrán, A. Olivas, P.A. Luque, Fruit peel extract mediated green synthesis of zinc oxide nanoparticles, J. Mol. Struct. 1147 (2017) 1–6. doi:10.1016/j.molstruc.2017.06.078.

[267] D. Wu, W. Wang, F. Tan, F. Sun, H. Lu, X. Qiao, Fabrication of pit-structured ZnO nanorods and their enhanced photocatalytic performance, RSC Adv. 3 (2013) 20054–20059. doi:10.1039/c3ra42874e.

[268] A. Balcha, O.P. Yadav, T. Dey, Photocatalytic degradation of methylene blue dye by zinc oxide nanoparticles obtained from precipitation and sol-gel methods, Environ. Sci. Pollut. Res. 23 (2016) 25485–25493. doi:10.1007/s11356-016-7750-6.

[269] N.S. Pavithra, K. Lingaraju, G.K. Raghu, G. Nagaraju, Citrus maxima (Pomelo) juice mediated eco-friendly synthesis of ZnO nanoparticles: Applications to photocatalytic, electrochemical sensor and antibacterial activities, Spectrochim. Acta - Part A Mol. Biomol. Spectrosc. 185 (2017) 11–19. doi:10.1016/j.saa.2017.05.032.

[270] J. Osuntokun, D.C. Onwudiwe, E.E. Ebenso, Green synthesis of ZnO nanoparticles using aqueous Brassica oleracea L. var. italica and the photocatalytic activity, Green Chem. Lett. Rev. 12 (2019) 444–457. doi:10.1080/17518253.2019.1687761.

[271] H.R. Madan, S.C. Sharma, Udayabhanu, D. Suresh, Y.S. Vidya, H. Nagabhushana, H. Rajanaik, K.S. Anantharaju, S.C. Prashantha, P. Sadananda Maiya, Facile green fabrication of nanostructure ZnO plates, bullets, flower, prismatic tip, closed pine cone: Their antibacterial, antioxidant, photoluminescent and photocatalytic properties, Spectrochim. Acta Part A Mol. Biomol. Spectrosc. 152 (2016) 404–416. doi:https://doi.org/10.1016/j.saa.2015.07.067.

[272] R. Ishwarya, B. Vaseeharan, S. Kalyani, B. Banumathi, M. Govindarajan, N.S. Alharbi, S. Kadaikunnan, M.N. Al-anbr, J.M. Khaled, G. Benelli, Facile green synthesis of zinc oxide nanoparticles using Ulva lactuca seaweed extract and evaluation of their photocatalytic, antibiofilm and insecticidal activity, J. Photochem. Photobiol. B Biol. 178 (2018) 249–258. doi:10.1016/j.jphotobiol.2017.11.006.

[273] R. Vinayagam, R. Selvaraj, P. Arivalagan, T. Varadavenkatesan, Synthesis, characterization and photocatalytic dye degradation capability of Calliandra haematocephala-mediated zinc oxide nanoflowers, J. Photochem. Photobiol. B Biol. 203 (2020) 111760. doi:https://doi.org/10.1016/j.jphotobiol.2019.111760.

[274] S. Harish, M. Navaneethan, J. Archana, A. Silambarasan, S. Ponnusamy, C. Muthamizhchelvan, Y. Hayakawa, Y.H. S. Harisha, M. Navaneethanb, J. Archanab, A. Silambarasana S. Ponnusamya, C. Muthamizhchelvana, Controlled synthesis of organic ligand passivated ZnO nanostructures and their photocatalytic activity under visible light irradiation, Dalt. Trans. 44 (2015) 10490–10498. doi:10.1039/C5DT01572C.

[275] A. Di Mauro, M.E. Fragalà, V. Privitera, G. Impellizzeri, ZnO for application in photocatalysis: From thin films to nanostructures, Mater. Sci. Semicond. Process. 69 (2017) 44–51. doi:10.1016/j.mssp.2017.03.029.

[276] M. Kuru, The Effect of Thickness on Photocatalytic Performance in MgZnO Thin Films, Sak. Univ. J. Sci. 16 (2020) 575–584. doi:10.16984/saufenbilder.645104.

[277] A.M. Ali, E.A.C. Emanuelsson, D.A. Patterson, Photocatalysis with nanostructured zinc oxide thin films: The relationship between morphology and photocatalytic activity under oxygen limited and oxygen rich conditions and evidence for a Mars Van Krevelen mechanism, Appl. Catal. B Environ. 97 (2010) 168–181. doi:10.1016/j.apcatb.2010.03.037.

[278] A. Azam, S.S. Babkair, Low-temperature growth of well-aligned zinc oxide nanorod arrays on silicon substrate and their photocatalytic application, Int. J. Nanomedicine. 9 (2014) 2109–2115. doi:10.2147/IJN.S60839.

[279] S. An, B.N. Joshi, M.W. Lee, N.Y. Kim, S.S. Yoon, Electrospun graphene-ZnO nanofiber mats for photocatalysis applications, Appl. Surf. Sci. 294 (2014) 24–28. doi:10.1016/j.apsusc.2013.12.159.

[280] V. Mata, A. Maldonado, M. de la Luz Olvera, Deposition of ZnO thin films by ultrasonic spray pyrolysis technique. Effect of the milling speed and time and its application in photocatalysis, Mater. Sci. Semicond. Process. 75 (2018) 288–295. doi:10.1016/j.mssp.2017.11.038.

[281] M. Rivera, Z. R. Alvarez, A. M. Amador, Mexico City, Mexico,., in: 16th Int. Conf. Electr. Eng. Comput. Sci. Autom. Control, Mexico City, 2019.

[282] W. Vallejo, A. Cantillo, C. Díaz-Uribe, Methylene Blue Photodegradation under Visible Irradiation on Ag-Doped ZnO Thin Films, Int. J. Photoenergy. 2020 (2020) 1627498. doi:10.1155/2020/1627498.

[283] I.-H. Acir, K. Guenther, Endocrine-disrupting metabolites of alkylphenol ethoxylates – A critical review of analytical methods, environmental occurrences, toxicity, and regulation, Sci. Total Environ. 635 (2018) 1530–1546. doi:https://doi.org/10.1016/j.scitotenv.2018.04.079.

[284] F.-J. Zhu, W.-L. Ma, T.-F. Xu, Y. Ding, X. Zhao, W.-L. Li, L.-Y. Liu, W.-W. Song, Y.-F. Li, Z.-F. Zhang, Removal characteristic of surfactants in typical industrial and domestic wastewater treatment plants in Northeast China, Ecotoxicol. Environ. Saf. 153 (2018) 84–90. doi:https://doi.org/10.1016/j.ecoenv.2018.02.001.

[285] D.H. Everett, Manual of Symbols and Terminology for Physicochemical Quantities and Units, Appendix II: Definitions, Terminology and Symbols in Colloid and Surface Chemistry, Pure Appl. Chem. 31 (1972) 577–638. doi:https://doi.org/10.1351/pac197231040577.

[286] G. Dave, G. Herger, Determination of detoxification to Daphnia magna of four pharmaceuticals and seven surfactants by activated sludge, Chemosphere. 88 (2012) 459–466. doi:https://doi.org/10.1016/j.chemosphere.2012.02.070.

[287] M.J. Scott, M.N. Jones, The biodegradation of surfactants in the environment, Biochim. Biophys. Acta - Biomembr. 1508 (2000) 235–251. doi:https://doi.org/10.1016/S0304-4157(00)00013-7.

[288] G.-G. Ying, Fate, behavior and effects of surfactants and their degradation products in the environment, Environ. Int. 32 (2006) 417–431. doi:https://doi.org/10.1016/j.envint.2005.07.004.

[289] E. Olkowska, Ż. Polkowska, J. Namieśnik, Analytics of Surfactants in the Environment: Problems and Challenges, Chem. Rev. 111 (2011) 5667–5700. doi:10.1021/cr100107g.

[290] The European Parliament and The Council of the European Union, REGULATION (EC) No 648/2004 OF THE EUROPEAN PARLIAMENT AND OF THE COUNCIL, 2004.

[291] A.G. Trovó, A.K. Hassan, M. Sillanpää, W.Z. Tang, Degradation of Acid Blue 161 by Fenton and photo-Fenton processes, Int. J. Environ. Sci. Technol. 13 (2016) 147–158. doi:10.1007/s13762-015-0854-6.

[292] B. Beverskog, I. Puigdomenech, Revised pourbaix diagrams for iron at 25–300 °C, Corros. Sci. 38 (1996) 2121–2135. doi:https://doi.org/10.1016/S0010-938X(96)00067-4.

[293] D. Marchand, J.-F. Rontani, Characterisation of photo-oxidation and autoxidation products of phytoplanktonic monounsaturated fatty acids in marine particulate matter and recent sediments, Org. Geochem. 32 (2001) 287–304. doi:https://doi.org/10.1016/S0146-6380(00)00175-3.

[294] J.A. Zazo, G. Pliego, S. Blasco, J.A. Casas, J.J. Rodriguez, Intensification of the Fenton Process by Increasing the Temperature, Ind. Eng. Chem. Res. 50 (2011) 866–870. doi:10.1021/ie101963k.

[295] F. Edition, I. The, F. Addendum, WHO - Guidelines on drinking water quality - fourth edition, 2017. http://apps.who.int/iris/bitstream/handle/10665/254637/9789241549950-eng.pdf;jsessionid=B7A8C40C69D1C876A6809D9572C6B29C?sequence=1.

[296] L. Attademo, F. Bernardini, R. Garinella, M.T. Compton, Environmental pollution and risk of psychotic disorders: A review of the science to date, Schizophr. Res. 181 (2017) 55–59. doi:10.1016/j.schres.2016.10.003.

[297] S. Cairney, P. Maruff, C. Burns, B. Currie, The neurobehavioural consequences of petrol (gasoline) sniffing, Neurosci. Biobehav. Rev. 26 (2002) 81–89. doi:10.1016/S0149-7634(01)00040-9.

[298] S. Cairney, P. Maruff, C.B. Burns, J. Currie, B.J. Currie, Neurological and cognitive impairment associated with leaded gasoline encephalopathy, Drug Alcohol Depend. 73 (2004) 183–188. doi:10.1016/j.drugalcdep.2003.10.010.

[299] M. Lovei, Phasing out lead from gasoline, World Bank Tech. Pap. (1998) 57.

[300] The Case for Banning Lead in Gasoline, (1998). http://www.meca.org/galleries/files/111698_lead.pdf.

[301] P.T. Mulroy, L.-T. Ou, Degradation of tetraethyllead during the degradation of leaded gasoline hydrocarbons in soil, Environ. Toxicol. Chem. 17 (1998) 777–782. doi:https://doi.org/10.1002/etc.5620170502.

[302] D. Seyferth, The Rise and Fall of Tetraethyllead. 2., Organometallics. 22 (2003) 5154–5178. doi:10.1021/om030621b.

[303] H.L. Needleman, Clamped in a straitjacket: The insertion of lead into gasoline, Environ. Res. 74 (1997) 95–103. doi:10.1006/enrs.1997.3767.

[304] M. Lu, X.J. Wu, D.C. Zeng, Y. Liao, Distribution of PCDD/Fs and organometallic compounds in sewage sludge of wastewater treatment plants in China, Environ. Pollut. 171 (2012) 78–84. doi:10.1016/j.envpol.2012.07.035.

[305] T.A. Ioannidis, A.I. Zouboulis, Detoxification of a highly toxic lead-loaded industrial solid waste by stabilization using apatites, J. Hazard. Mater. 97 (2003) 173–191. doi:10.1016/S0304-3894(02)00258-3.

[306] C. Gallert, J. Winter, Bioremediation of soil contaminated with alkyllead compounds, Water Res. 36 (2002) 3130–3140. doi:10.1016/S0043-1354(01)00543-7.

[307] Y. Ouyang, R.S. Mansell, R.D. Rhue, A microemulsification approach for removing organolead and gasoline from contaminated soil, J. Hazard. Mater. 46 (1996) 23–35. doi:10.1016/0304-3894(95)00100-X.

[308] K. Bergmann, B. Neidhart, Speciation of organolead compounds in water samples by GC-AAS after in situ butylation with tetrabutylammonium tetrabutylborate, Fresenius J. Anal. Chem. 356 (2004) 57–61. doi:10.1007/s0021663560057.

[309] W. Shotyk, D. Weiss, M. Heisterkamp, A.K. Cheburkin, P.G. Appleby, F.C. Adams, New peat bog record of atmospheric lead pollution in Switzerland: Pb concentrations, enrichment factors, isotopic composition, and organolead species, Environ. Sci. Technol. 36 (2002) 3893–3900. doi:10.1021/es010196i.

[310] A.N. Alshawabkeh, E. Ozsu-Acar, R.J. Gale, S.K. Puppal, Remediation of Soils Contaminated with Tetraethyl Lead by Electric Fields, Transp. Res. Rec. 1615 (1998) 79–85. doi:10.3141/1615-11.

[311] F. Unob, A. Hageége, D. Lakkis, M. Leroy, Degradation of organolead species in aqueous solutions by electron beam irradiation, Water Res. 37 (2003) 2113–2117. doi:10.1016/S0043-1354(02)00620-6.

[312] L.-T. Ou, W. Jing, J.E. Thomas, Biological and chemical degradation of ionic ethyllead compounds in soil, Environ. Toxicol. Chem. 14 (1995) 545–551. doi:10.1002/etc.5620140401.

[313] Y. Song, N. Wang, L. Yang, Y. Wang, D. Yu, X. Ouyang, Facile Fabrication of ZIF-8/Calcium Alginate Microparticles for Highly Efficient Adsorption of Pb(II) from Aqueous Solutions, Ind. Eng. Chem. Res. 58 (2019) 6394–6401. doi:10.1021/acs.iecr.8b05879.

[314] G. Andreottola, L. Dallago, E. Ferrarese, Feasibility study for the remediation of groundwater contaminated by organolead compounds, J. Hazard. Mater. 156 (2008) 488–498. doi:10.1016/j.jhazmat.2007.12.044.

[315] C. Nerin, P. Begona, Speciation of alkyllead in water sample, in: Quim. Anal., 1994: pp. 209–213.

[316] V. Minganti, R. Capelli, R. De Pellegrini, Evaluation of different derivatization methods for the multi-element detection of Hg, Pb and Sn compounds by gas chromatography-microwave induced plasma-atomic emission spectrometry in environmental samples, Fresenius. J. Anal. Chem. 351 (1995) 471–477. doi:10.1007/BF00322922.

[317] R.D. Rhue, R.S. Mansell, L.T. Ou, R. Cox, S.R. Tang, Y. Ouyang, The fate and Behavior of Lead Alkyls in the Environment: A Review, Crit. Rev. Environ. Control. 22 (1992) 169–193. doi:10.1080/10643389209388435.

[318] Y. Wang, L. Qiu, M. Zhu, G. Sun, T. Zhang, K. Kang, Comparative Evaluation of Hydrothermal Carbonization and Low Temperature Pyrolysis of Eucommia ulmoides Oliver for the Production of Solid Biofuel, Sci. Rep. 9 (2019) 5535. doi:10.1038/s41598-019-38849-4.

[319] H.C. Ho, M. Goswami, J. Chen, J.K. Keum, A.K. Naskar, Amending the Structure of Renewable Carbon from Biorefinery Waste-Streams for Energy Storage Applications, Sci. Rep. 8 (2018) 1–13. doi:10.1038/s41598-018-25880-0.

[320] M. Lucian, M. Volpe, L. Fiori, Hydrothermal Carbonization Kinetics of Lignocellulosic Agro-Wastes: Experimental Data and Modeling, Energies. 12 (2019) 516. doi:10.3390/en12030516.

[321] A. Funke, F. Ziegler, Hydrothermal carbonization of biomass: A summary and discussion of chemical mechanisms for process engineering, Biofuels, Bioprod. Biorefining. 4 (2010) 160–177. doi:10.1002/bbb.198.

[322] A. Kruse, A. Funke, M.M. Titirici, Hydrothermal conversion of biomass to fuels and energetic materials, Curr. Opin. Chem. Biol. 17 (2013) 515–521. doi:10.1016/j.cbpa.2013.05.004.

[323] J.A. Libra, K.S. Ro, C. Kammann, A. Funke, N.D. Berge, Y. Neubauer, M.-M. Titirici, C. Fühner, O. Bens, J. Kern, K.-H. Emmerich, Hydrothermal carbonization of biomass residuals: a comparative review of the chemistry, processes and applications of wet and dry pyrolysis, Biofuels. 2 (2011) 71–106. doi:10.4155/bfs.10.81.

[324] F. Merzari, M. Lucian, M. Volpe, G. Andreottola, L. Fiori, Hydrothermal carbonization of biomass: Design of a bench-Scale reactor for evaluating the heat of reaction, Chem. Eng. Trans. 65 (2018) 43–48. doi:10.3303/CET1865008.

[325] M. Pecchi, F. Patuzzi, V. Benedetti, R. Di Maggio, M. Baratieri, Thermodynamics of hydrothermal carbonization: Assessment of the heat release profile and process enthalpy change, Fuel Process. Technol. 197 (2020) 106206. doi:https://doi.org/10.1016/j.fuproc.2019.106206.

[326] M. Titirici, Chapter 12 - Hydrothermal Carbons: Synthesis, Characterization, and Applications, in: J.M.D.B.T.-N.C.A. Tascón (Ed.), Nov. Carbon Adsorbents, Elsevier, Oxford, 2012: pp. 351–399. doi:https://doi.org/10.1016/B978-0-08-097744-7.00012-0.

[327] M. Lucian, M. Volpe, L. Gao, G. Piro, J.L. Goldfarb, L. Fiori, Impact of hydrothermal carbonization conditions on the formation of hydrochars and secondary chars from the organic fraction of municipal solid waste, Fuel. 233 (2018) 257–268. doi:10.1016/j.fuel.2018.06.060.

[328] M. Volpe, L. Fiori, From olive waste to solid biofuel through hydrothermal carbonisation: The role of temperature and solid load on secondary char formation and hydrochar energy properties, J. Anal. Appl. Pyrolysis. 124 (2017) 63–72. doi:10.1016/j.jaap.2017.02.022.

[329] M. Lucian, L. Fiori, Hydrothermal carbonization of waste biomass: Process design, modeling, energy efficiency and cost analysis, Energies. 10 (2017). doi:10.3390/en10020211.

[330] T. Weide, E. Brügging, C. Wetter, Anaerobic and aerobic degradation of wastewater from hydrothermal carbonization (HTC) in a continuous, three-stage and semi-industrial system, J. Environ. Chem. Eng. 7 (2019) 102912. doi:10.1016/j.jece.2019.102912.

[331] P. Biller, A.B. Ross, Production of biofuels via hydrothermal conversion, in: Handb. Biofuels Prod. Process. Technol. Second Ed., Elsevier Ltd, 2016: pp. 509–547. doi:10.1016/B978-0-08-100455-5.00017-5.

[332] L. Gao, M. Volpe, M. Lucian, L. Fiori, J.L. Goldfarb, Does hydrothermal carbonization as a biomass pretreatment reduce fuel segregation of coal-biomass blends during oxidation?, Energy Convers. Manag. 181 (2019) 93–104. doi:10.1016/j.enconman.2018.12.009.

[333] M.-M. Titirici, Green Carbon, Sustain. Carbon Mater. from Hydrothermal Process. (2013) 1–36. doi:doi:10.1002/9781118622179.ch1.

[334] F. Benstoem, G. Becker, J. Firk, M. Kaless, D. Wuest, J. Pinnekamp, A. Kruse, Elimination of micropollutants by activated carbon produced from fibers taken from wastewater screenings using hydrothermal carbonization, J. Environ. Manage. 211 (2018) 278–286. doi:10.1016/j.jenvman.2018.01.065.

[335] J.T. Petrović, M.D. Stojanović, J. V. Milojković, M.S. Petrović, T.D. Šoštarić, M.D. Laušević, M.L. Mihajlović, Alkali modified hydrochar of grape pomace as a perspective adsorbent of Pb2+ from aqueous solution, J. Environ. Manage. 182 (2016) 292–300. doi:10.1016/j.jenvman.2016.07.081.

[336] S. Bertolucci, B. Bressan, F. Caspers, S. Pauletta, Using solar energy to convert biomass to fossil fuel analogs, (2014) 16–19.

[337] P. Khongkrapan, T. Chinpensawat, Solar energy-assisted activated carbon production, in: Proc. ISER 148th Int. Conf., Solar Energy-assisted Activated Carbon Production, Melbourne, Australia, 2018.

[338] D. Yadav, R. Banerjee, A review of solar thermochemical processes, Renew. Sustain. Energy Rev. 54 (2016) 497–532. doi:10.1016/j.rser.2015.10.026.

[339] M. Pearce, X. Tonnellier, N. Sengar, C. Sansom, Commercial development of bio-combustible fuels from hydrothermal liquefaction of waste using solar collectors, in: AIP Conf. Proc., 2018. doi:10.1063/1.5067145.

[340] A. Giaconia, L. Turchetti, A. Ienna, D. Mazzei, B. Schiavo, O. Scialdone, G. Caputo, A. Galia, Conceptual study of the coupling of a biorefinery process for hydrothermal liquefaction of microalgae with a concentrating solar power plant, 2017. doi:10.1063/1.4984464.

[341] M. Pearce, M. Shemfe, C. Sansom, Techno-economic analysis of solar integrated hydrothermal liquefaction of microalgae, Appl. Energy. 166 (2016) 19–26. doi:10.1016/j.apenergy.2016.01.005.

[342] S. Viereck, J. Keller, A. Haselbacher, Z.R. Jovanovic, A. Steinfeld, Assessment of Heat Exchangers for the Integration of Concentrated Solar Energy into the Catalytic Hydrothermal Gasification of Biomass, Energy Technol. 5 (2017) 2086–2099. doi:10.1002/ente.201700405.

[343] J. Chen, W. Xu, F. Zhang, H. Zuo, J. E, K. Wei, G. Liao, Y. Fan, Thermodynamic and environmental analysis of integrated supercritical water gasification of coal for power and hydrogen production, Energy Convers. Manag. 198 (2019) 111927. doi:https://doi.org/10.1016/j.enconman.2019.111927.

[344] J. Chen, W. Xu, H. Zuo, X. Wu, J. E, T. Wang, F. Zhang, N. Lu, System development and environmental performance analysis of a solar-driven supercritical water gasification pilot plant for hydrogen production using life cycle assessment approach, Energy Convers. Manag. 184 (2019) 60–73. doi:https://doi.org/10.1016/j.enconman.2019.01.041.

[345] C. Xiao, Q. Liao, Q. Fu, Y. Huang, H. Chen, H. Zhang, A. Xia, X. Zhu, A. Reungsang, Z. Liu, A solar-driven continuous hydrothermal pretreatment system for biomethane production from microalgae biomass, Appl. Energy. 236 (2019) 1011–1018. doi:https://doi.org/10.1016/j.apenergy.2018.12.014.

[346] J. E, G. Liu, T. Liu, Z. Zhang, H. Zuo, W. Hu, K. Wei, Harmonic response analysis of a large dish solar thermal power generation system with wind-induced vibration, Sol. Energy. 181 (2019) 116–129. doi:https://doi.org/10.1016/j.solener.2019.01.089.

[347] Y. Li, G. Liu, X. Liu, S. Liao, Thermodynamic multi-objective optimization of a solar-dish Brayton system based on maximum power output, thermal efficiency and ecological performance, Renew. Energy. 95 (2016) 465–473. doi:https://doi.org/10.1016/j.renene.2016.04.052.

[348] X. Zhao, J. E, G. Wu, Y. Deng, D. Han, B. Zhang, Z. Zhang, A review of studies using graphenes in energy conversion, energy storage and heat transfer development, Energy Convers. Manag. 184 (2019) 581–599. doi:https://doi.org/10.1016/j.enconman.2019.01.092.

[349] L. Fiori, L. Florio, Gasification and combustion of grape marc: Comparison among different scenarios, Waste and Biomass Valorization. 1 (2010) 191–200. doi:10.1007/s12649-010-9025-7.

[350] D. Prasanth, K.P. Sibin, H.C. Barshilia, Optical properties of sputter deposited nanocrystalline CuO thin films, Thin Solid Films. 673 (2019) 78–85. doi:10.1016/j.tsf.2019.01.037.

[351] X. Xiao, L. Miao, G. Xu, L. Lu, Z. Su, N. Wang, S. Tanemura, A facile process to prepare copper oxide thin films as solar selective absorbers, Appl. Surf. Sci. 257 (2011) 10729–10736. doi:10.1016/j.apsusc.2011.07.088.

[352] L. Kauder, Spacecraft thermal control coatings design, NASA/TP–2005–212792, 2005. https://ntrs.nasa.gov/archive/nasa/casi.ntrs.nasa.gov/20070014757.pdf.

[353] X. Jiang, T. Herricks, Y. Xia, CuO Nanowires Can Be Synthesized by Heating Copper Substrates in Air, Nano Lett. 2 (2002) 1333–1338. doi:10.1021/nl0257519.

[354] R.S. Devan, R.A. Patil, J.H. Lin, Y.R. Ma, One-dimensional metal-oxide nanostructures: Recent developments in synthesis, characterization, and applications, Adv. Funct. Mater. 22 (2012) 3326–3370. doi:10.1002/adfm.201201008.

[355] D. Zappa, E. Comini, R. Zamani, J. Arbiol, J.R. Morante, G. Sberveglieri, Copper oxide nanowires prepared by thermal oxidation for chemical sensing, in: Procedia Eng., Elsevier B.V., 2011: pp. 753–756. doi:10.1016/j.proeng.2011.12.185.

[356] L. Yuan, G. Zhou, The Growth of One-Dimensional Oxide Nanostructures by Thermal Oxidation of Metals, Int. J. Nano Sci. Nano Eng. Nanotechnol. 4 (2012) 2229–7383. http://citeseerx.ist.psu.edu/viewdoc/download?doi=10.1.1.718.4194&rep=rep1&type=pdf.

[357] L. Fiori, D. Basso, D. Castello, M. Baratieri, Hydrothermal carbonization of biomass: Design of a batch reactor and preliminary experimental results, Chem. Eng. Trans. 37 (2014) 55–60. doi:10.3303/CET1437010.

[358] S. Román, J. Libra, N. Berge, E. Sabio, K. Ro, L. Li, B. Ledesma, A. Alvarez, S. Bae, Hydrothermal carbonization: Modeling, final properties design and applications: A review, Energies. 11 (2018) 1–28. doi:10.3390/en11010216.

[359] M. Volpe, J.L. Goldfarb, L. Fiori, Hydrothermal carbonization of Opuntia ficus-indica cladodes: Role of process parameters on hydrochar properties, Bioresour. Technol. 247 (2018) 310–318. doi:10.1016/j.biortech.2017.09.072.

[360] M. Heidari, S. Salaudeen, A. Dutta, B. Acharya, Effects of Process Water Recycling and Particle Sizes on Hydrothermal Carbonization of Biomass, Energy & Fuels. 32 (2018) 11576–11586. doi:10.1021/acs.energyfuels.8b02684.

[361] Z. Liu, R. Balasubramanian, Upgrading of waste biomass by hydrothermal carbonization (HTC) and low temperature pyrolysis (LTP): A comparative evaluation, Appl. Energy. 114 (2014) 857–864. doi:10.1016/j.apenergy.2013.06.027.

[362] M.T. Reza, R. Emerson, M.H. Uddin, G. Gresham, C.J. Coronella, Ash reduction of corn stover by mild hydrothermal preprocessing, Biomass Convers. Biorefinery. 5 (2015) 21–31. doi:10.1007/s13399-014-0122-x.

[363] D. Basso, E. Weiss-Hortala, F. Patuzzi, M. Baratieri, L. Fiori, In Deep Analysis on the Behavior of Grape Marc Constituents during Hydrothermal Carbonization, Energies. 11 (2018) 1379. doi:10.3390/en11061379.

[364] J. Giménez, S. Esplugas, S. Malato, J. Peral, Chapter 8 - Economic Assessment and Possible Industrial Application of a (Photo)catalytic Process: A Case Study, in: G. Marcì, L.B.T.-H.P. Palmisano (Eds.), Elsevier, 2019: pp. 235–267. doi:https://doi.org/10.1016/B978-0-444-64015-4.00008-0.

Appendix A – Evaluation of H_2O_2 concentrations on solar photocatalytic experiments (chapter 4)

Figure A.1 shows the data results regarding the use of 1M concentration of H_2O_2. It is evidenced that the use of this concentration of H_2O_2 promotes a prevalence effect of direct photocatalysis in the solar concentrator experiment condition. This is due to the high density of photons reflected by the mirror and the high absorption of the H_2O_2 in visible light condition (Concentrated power density of 720 W/m^2). In this case it is not possible to evidence a photocatalytic improvement promoted by the WO_3 material.

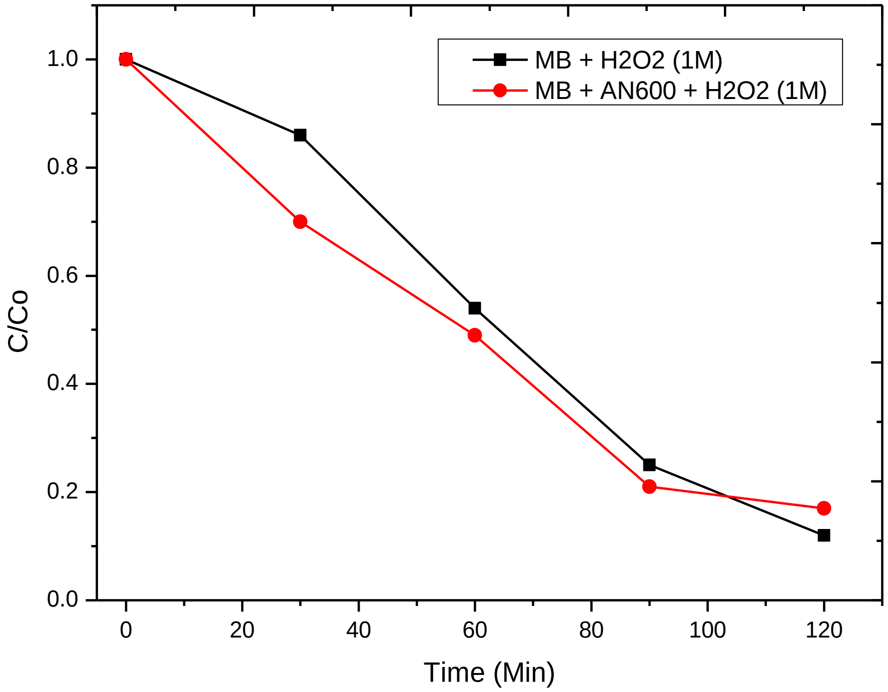

Figure A.1**:** Relative degradation of MB dye up to 120mins under concentrated sunlight in presence of H_2O_2 (1M) solely and AN600 coating with H_2O_2 (1M).

For this reason, in figure A.2 the experiment was also performed with 0.1 M H_2O_2 concentration to focus the solar photocatalytic performance of the WO_3 material. After this test it was decided to adopt for the solar experiment a concentration of 0.1M. Finally, figure A.3 confirms a decrease in the kinetic activity by using 0.1 M H_2O_2 concentration.

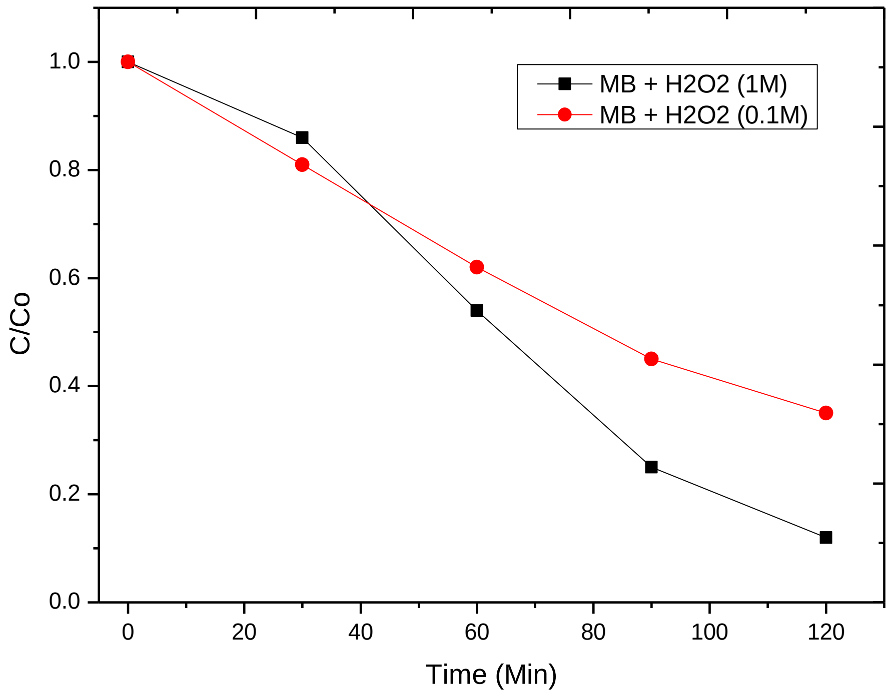

Figure A.2**:** Relative degradation of MB dye up to 120mins under concentrated sunlight in presence of 1M and 0.1M H_2O_2 concentrations.

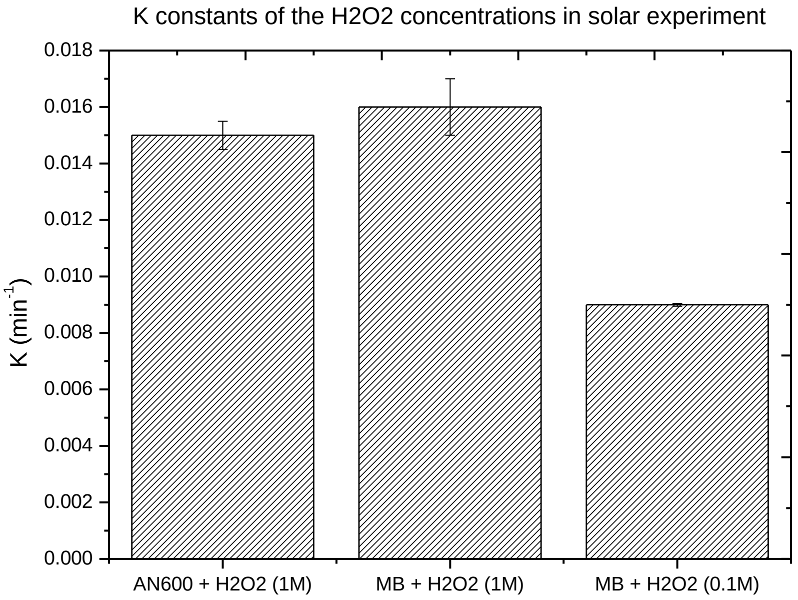

Figure A.3**:** Kinetic constants for the experiments performed in figures A.1 and A.2.

Appendix B – Cost analysis of PDC solar concentrator to wastewater purification

Economic considerations follow below for the PDC prototype, consisting of a parabolic dish (area of 0.76 m^2) and a quartz tube reactor with a volume of 150 mL as resulting from calculations. These data just want to provide preliminary insights into the cost evaluation of the PDC solar wastewater purification prototype apparatus.

The costs of the prototype were estimated on the base of the incurred expenditures we sustained to build the PDC system at our university mechanical workshop and lab facilities.

Table B.1 reports the main results with total cost of EUR 10.180 for the PDC apparatus, pumping system, cooling system, quartz glass lid and catalyst.

Table B.1: Technical details and initial costs of the PDC wastewater purification apparatus.

Technical details	
PDC projected area (m^2)	0.76
Illuminated volume (L)	0.15
Total volume (L)	2
Power PDC (W/m^2)	800
Incident Power @ the catalyst (W/m^2)	720 (90%)

Costs	
Total PDC system cost (Euro)	**10180**
PDC (Euro)	9500
Quartz glass reactor (Euro)	165
Pump and circulation system (Euro)	300
Cooling system (Euro)	15
Catalyst price estimate (Euro)	200

Appendix C – Economic analysis of ZnO applications (chapter 5)

An economic assessment was carried out with the objective to compare the costs between ZnO-Green and ZnO-Chem colloidal photocatalysis in the PDC system. The catalyst concentration of 0.6 g/L for the time interval of 2 hours that resulted in the highest degradation rates (94%) for ZnO-Green and ZnO-Chem was considered. The calculations were guided using as reference a previous work for applications of photocatalytic processes in experimental setups [364]. In this approach, the calculations took into consideration the costs of installation, the electrical power consumption and the photocatalysts synthesis. Table C.1 presents the items of the installation and summarizes the experimental conditions. For this assessment, one year of use of the system was considered, corresponding to 50 experiment runs, each with 2 liters volume and a concentration of 10 ppm of MB as the model pollutant.

Table C.1: Components and experimental conditions assumed for the economic evaluation.

Solar PDC apparatus
PDC solar concentrator
quartz glass tube
diaphragm pump
thermometer
feeding tank
pump tubing (10m)

Experimental Conditions	**Value**
Total volume (L)	2
Illuminated volume (L)	0.15
Power PDC	Sunlight
Initial concentration of pollutant (ppm)	10
Conversion (%)	94
Experiments by year (hypothesis)	50
Concentration of catalyst per experiment (g/L)	0.6
Total volume treated by year (L)	100

Table C.2 shows the yearly costs of the facility, to every component is attributed the fabrication costs. A 5% of use was defined to the experimental setup taking into consideration the concomitance with other experiments along the same time period. For each item the lifetime was specified a therefore the calculation resulted in a yearly cost value of €28.65 for the PDC system.

Table C.2: Yearly costs of the solar PDC apparatus for photocatalysis.

Components of device	**Price (€)**	**Use (%)**	**Cost of use (€)**	**Lifetime (years)**	**Yearly cost (€/year)**
PDC solar concentrator	9500	5%	475	20	23.75
quartz glass tube	165	5%	8.25	3	2.75
diaphragm pump	280	5%	14	10	1.40
thermometers	15	5%	0.75	5	0.15
feeding tank	10	5%	0.50	5	0.10
pump tubing (10 m)	10	5%	0.50	1	0.50
Total	**9980**		**499**		**28.65**

The second evaluation performed are the costs related to electrical power consumption. Table C.3 presents the calculus expressing the amount of time used for every experiment (2 hours) individualizing the electrical power consumption of every electrical component from the apparatus expressed in KWh. The result of the sum of the consumption was multiplied by the quantity of 50 experiments along 12 months. An average value of electricity price of 0.12 €/KWh was assumed, and the electrical costs resulted in €7.80/year for the solar PDC.

Table C.3: Yearly electricity costs for the solar PDC installation.

Solar PDC	**Use Equipment (h/exp)**	**Power (KW)**	**Consumption (KWh)**
PDC gearmotors and controls	2	0.4	0.8
diaphragm pump	2	0.2	0.4
Thermometer	2	0.05	0.1
Total consumption per experiment			**1.3**
Yearly number of experiments			**50**
Total consumption per year (KWh/year)			**65**
KWh cost (€)			**0.12**
Electricity costs (€/year)			**7.80**

Table C.4 presents the costs related to the synthesis of both ZnO-Green and ZnO-Chem catalysts. In this approach, only the raw materials cost was considered due to the assumption to be the major contribution in the cost and a yield of 10% for the synthesis methods was rated. For each 2 L experiment, the weight of 1.2 g of catalyst was employed in the colloidal suspension. The cost per gram of the ZnO-Green resulted in 10.80 €/g, starting from $Zn(NO_3)_2.6H_2O$ (Sigma-Aldrich 98%, 0.27 €/g) and fresh garlic bulbs (8 €/Kg). The ZnO-Chem cost is 16.50 €/g due to the employment of $Zn(NO_3)_2.6H_2O$ (Sigma-Aldrich 98%, 0.27 €/g) and Oxalic Acid (Sigma-Aldrich

>99%, 0.74 €/g). For the yearly duration of experiments (50 runs), the cost resulted in € 648 and € 990 for the ZnO-Green and ZnO-Chem respectively. The relevance in difference on the cost for ZnO-Green is regarding the employment of garlic instead of oxalic acid.

Table C.4: ZnO photocatalyst synthesis comparison costs.

Photocatalyst	**ZnO-Green**	**ZnO-Chem**
Concentration (g/L)	0.6	0.6
Volume of experiment (L)	2	2
Total amount / experiment (g)	1.2	1.2
Price (€/g) (only reagents and 10% yield)	10.8	16.5
Cost / experiment	12.96	19.8
Exp/year	**50**	**50**
Yearly cost reagents / exp (€/Year)	**648**	**990**

Table C.5 presents the condensed yearly and unitary experiment costs for the studied case. The numbers are the values from sum of the three factor costs evaluation: yearly cost of the facility, electrical power consumption and photocatalysts synthesis. The resulting value for the ZnO-Green catalyst experiment is €684.45/year and of €1026.45/year with ZnO-Chem on the solar PDC configuration. If considered the unitary costs: the values are of €13.69 with ZnO-Green and €20.53 with ZnO-Chem per experiment.

Table C.5: Total costs for operating the solar PDC apparatus.

Solar PDC	**ZnO-Green**		**ZnO-Chem**	
Cost by Year	**€/year**	**%**	**€/year**	**%**
Yearly costs of facility (YCF)	28.65	4%	28.65	3%
Electricity costs	7.8	1%	7.8	1%
Catalyst costs	648	95%	990	96%
Total annual costs (TAC)	**684.45**	**100%**	**1026.45**	**100%**
Total costs per experiment (50)	**13.69**	**100%**	**20.53**	**100%**

The above evaluation put in evidence the stronger influence on the costing composition of the experiment given by the catalyst synthesis, corresponding to 95% and 96% for the ZnO-Green and ZnO-chem respectively. In the other hand, the costs of electricity and installation of the solar PDC do not represent remarkable influence in the short term, but for medium and long terms the solar PDC can play in favor by long lasting lifetime of the system if for example comparing with illumination by artificial sources.

Scientific Production

Fendrich, M., Popat, Y., Orlandi, M., Quaranta, A., Miotello, A., 2020. Pulsed laser deposition of nanostructured tungsten oxide films: A catalyst for water remediation with concentrated sunlight. Mater. Sci. Semicond. Process. 119, 105237. https://doi.org/10.1016/j.mssp.2020.105237

Ischia, G., Orlandi, M., **Fendrich, M.A.**, Bettonte, M., Merzari, F., Miotello, A., Fiori, L., 2020. Realization of a solar hydrothermal carbonization reactor: A zero-energy technology for waste biomass valorization. J. Environ. Manage. 259, 110067. https://doi.org/10.1016/j.jenvman.2020.110067

Fendrich, M, Quaranta, A., Orlandi, M., Bettonte, M., Miotello, A., 2019. Solar Concentration for Wastewaters Remediation: A Review of Materials and Technologies. Appl. Sci. 9, 118. https://doi.org/10.3390/app9010118

Orlandi, M., Filosa, N., Bettonte, M., **Fendrich, M.**, Girardini, M., Battistini, T., Miotello, A., 2019. Treatment of surfactant-rich industrial wastewaters with concentrated sunlight: toward solar wastewater remediation. Int. J. Environ. Sci. Technol. 16, 2109–2114. https://doi.org/10.1007/s13762-018-2099-7

El Golli, A., **Fendrich, M.**, Bazzanella, N., Dridi, C., Miotello, A., Orlandi, M., 2020. Wastewater remediation with ZnO photocatalysts: green synthesis and solar concentration as an economically and environmentally viable route to application was submitted to the *Journal of Environmental Management* on November 18th, 2020 and at the date this thesis was published the manuscript was *Under Review*.

Workshops and congress participations

SP7 – Milano – 2019 – Poster

Energy day, university of Trento 2018 - Poster

EIT Raw Materials alumni association foundation, Berlin 2018 – Discussion meeting

EIT Alumni connect event, Budapest 2018 – Discussion meeting

EIT Raw Materials winter school, Trento 2017 - Course

Acknowledgements

During these three years living in Trentino and working at the University of Trento I had a unique, intense and fruitful time. The decision of moving overseas and to integrate in a new country with the family is a tremendous challenge and undoubtedly a remarkable experience. Through learning to deal with life in a new society and scientific discussions with colleagues I was able to extend my horizons, develop new insights and overcome smoothly the difficulties faced along the way.

I am primarily grateful to my tutors, professors Alberto Quaranta and Antonio Miotello for the confidence in my work through providing the financial support and invaluable advices.

I want to express my sincere gratitude to Dr. Michele Orlandi, for sharing the office with me during these years and be always available to develop the utmost honest professional discussions, not limited to only science, but sharing opinions and perspectives.

A special thanks I would like to direct to Marco Bettonte for the relevant help with the setup and maintenance of the solar concentrator, Nicola Bazzanella for the detailed insights and experience in SEM images acquisition. The same thanks I would like to say to Claudio Cestari, Massimo Cazzanelli and Luigino Vivaldi.

My acknowledgements are also extended to my PhD colleagues during this period, Dr. Yaksh Popat, Giulia Ischia, Asma El Golli, Luca Basso, Jacopo Terragni and Pietro Battocchio.

I am very grateful for my parents Wilson and Janir for their support and confidence that pursuing the PhD would be a tremendous advance in my career. I thank my sister, Patrícia and my brother, Wilson Junior, to be always close of our parents during this time.

Last but not least, I could never reach this goal without the unconditional support from my wife Taciara and our son Pedro. They jumped in this journey with me, independent of taking the advantages and the drawbacks of going out of the comfort zone in a different country, the goal was achieved, and the merit is yours.

Grazie a tutti!